Novel neuro-microphysiological system (nMPS) for multiple characterisations of 3D neuronal networks co-cultured with astrocytes and microglia

Dissertation

zur Erlangung des Grades eines
Doktors der Naturwissenschaften
der Mathematisch-Naturwissenschaftlichen Fakultät
und
der Medizinischen Fakultät
der Eberhard-Karls-Universität Tübingen

vorgelegt von

Laura-Victoria Jentsch
aus Madrid, Spanien

2021

Tag der mündlichen Prüfung: 18. Oktober 2021

Dekan der Math.-Nat. Fakultät: Prof. Dr. Thilo Stehle
Dekan der Medizinischen Fakultät: Prof. Dr. Bernd Pichler

1. Berichterstatter: Dr. Paolo Cesare
2. Berichterstatter: Prof. Dr. Peter Heutink

Prüfungskommission: Dr. Paolo Cesare

Prof. Dr. Peter Heutink

Dr. Jonas Neher

Prof. Dr. Stefan Liebau

Erklärung / Declaration:

Ich erkläre, dass ich die zur Promotion eingereichte Arbeit mit dem Titel:
„Novel neuro-microphysiological system (nMPS) for multiple characterisations of 3D neuronal networks co-cultured with astrocytes and microglia" selbständig verfasst, nur die angegebenen Quellen und Hilfsmittel benutzt und wörtlich oder inhaltlich übernommene Stellen als solche gekennzeichnet habe. Ich versichere an Eides statt, dass diese Angaben wahr sind und dass ich nichts verschwiegen habe. Mir ist bekannt, dass die falsche Abgabe einer Versicherung an Eides statt mit Freiheitsstrafe bis zu drei Jahren oder mit Geldstrafe bestraft wird.

I hereby declare that I have produced the work entitled "Novel neuro-microphysiological system (nMPS) for multiple characterisations of 3D neuronal networks co-cultured with astrocytes and microglia ", submitted for the award of a doctorate, on my own (without external help), have used only the sources and aids indicated and have marked passages included from other works, whether verbatim or in content, as such. I swear upon oath that these statements are true and that I have not concealed anything. I am aware that making a false declaration under oath is punishable by a term of imprisonment of up to three years or by a fine.

Tübingen, den ....

Datum / Date Unterschrift /Signature

“Las neuronas son células de formas delicadas y elegantes, las misteriosas mariposas del alma, cuyo batir de alas quién sabe si esclarecerá algún día el secreto de la vida mental."

-Ramón y Cajal

Summary

Neurological disorders constitute over 6% of the global burden of disease and are believed to increase in society over time. Therefore, pharmacy companies aim to develop novel therapies that minimise the effect of such disorders. However, the former has proved challenging as the efficacy and safety issues are not accurately estimated in pre-clinical studies due to the lack of physiologically relevant models. Therefore, neuro-microphysiological systems (nMPS) aim to bridge the gap from the less relevant two-dimensional (2D) *in vitro* platforms and animal models to three-dimensional (3D) models that mimic more closely the brain's physiological phenomena.

Nevertheless, most novel nMPS cannot precisely evaluate neuronal networks or brain structures due to the lack of diverse readouts implemented in their devices. This study presents a novel transparent high-throughput *in vitro* platform with the capability of simultaneously recording the electrophysiological activity of up to 18 individual 3D neuronal networks through insulating caps on substrate-integrated microelectrode arrays (MEA) (capped microelectrodes, CμE). Additionally, this nMPS allows the characterisation of morphological and proteomic traits.

To evaluate the accuracy of this system, multiple readouts were performed. Firstly, the physiological growth of three different brain cells (neurons, astrocytes, and microglia) introduced in the 3D cell culture was corroborated via live-cell imaging and immunocytochemistry (ICC). Secondly, synaptic circuits of the 3D growing neurons were confirmed via calcium imaging, and optogenetics performed simultaneously to electrophysiological recordings. The network's functionality was evaluated using reference compounds picrotoxin (PTX), tetrodotoxin (TTX), and rotenone, demonstrating an exceptional sensitivity and experimental reproducibility among various devices. Furthermore, the application of rotenone demonstrated the toxicity of the compound at lower concentrations and the earlier detection of neuronal alterations by electrophysiological recordings compared to traditional morphological studies, demonstrating the former's superior susceptibility. This sensitivity was corroborated after evaluating the effect of pro-inflammatory compounds interferon-γ (IFNγ) and tumour necrosis factor-α (TNFα) in co-cultured neurons, microglia and astrocytes at a morphological, proteomic and electrophysiological level.

In conclusion, a novel, high-physiologically relevant neuro-microphysiological device was developed, which captures the electrical activity of 3D growing neurons in co-culture with astrocytes and microglia with high efficiency and reproducibility by additionally relying on cellular morphological and proteomic characterisation. Through its versatility, this platform

qualified as a new standard approach for disease modelling and a new tool for screening of compounds targeting the central nervous system (CNS). This work was funded by the Baden-Württemberg Stiftung GmbH under grant agreement MIVT-7 (NEWRON-3D) and sent for publication to a journal (Molina-Martínez and Jentsch et al., 2021). The second part of this work is being prepared for a further publication.

Zusammenfassung

Neurologische Erkrankungen machen mehr als 6 % der globalen Krankheitslast aus und es wird angenommen, dass sie mit der Zeit in der Gesellschaft zunehmen. Daher ist es das Ziel von Pharmaunternehmen, neuartige Therapien zu entwickeln, die die Auswirkungen solcher Krankheiten minimieren. Ersteres erweist sich jedoch als Herausforderung, da die Wirksamkeit und Sicherheit in präklinischen Studien mangels physiologisch relevanter Modelle nicht genau abgeschätzt werden kann. Daher zielen neuro-mikrophysiologische Systeme (nMPS) darauf ab, die Lücke von den weniger relevanten zweidimensionalen (2D) In-vitro-Plattformen und Tiermodellen zu dreidimensionalen (3D) Modellen zu schließen, die die Eigenschaften des menschlichen Gehirns besser nachahmen.

Dennoch können die meisten neuartigen nMPS neuronale Netzwerke oder Hirnstrukturen nicht präzise auswerten, da in ihren Geräten nicht genügend Auslesefunktionen implementiert sind. In dieser Studie wird ein neuartiges transparentes In-vitro-System vorgestellt, das die elektrophysiologische Aktivität von bis zu 18 individuellen 3D-Neuronennetzwerken durch integrierte Mikroelektroden-Arrays (MEA) aufzeichnen kann. Darüber hinaus erlaubt dieses nMPS die Charakterisierung von morphologischen und proteomischen Merkmalen.

Um die Genauigkeit dieses Systems zu evaluieren, wurden mehrere Auslesungen durchgeführt. Erstens wurde das physiologische Wachstum von drei verschiedenen Gehirnzellen (Neuronen, Astrozyten und Mikroglia), die in die 3D-Zellkultur eingebracht wurden, mittels Live-Cell-Imaging und Immunzytochemie bestätigt. Zweitens wurden die synaptischen Schaltkreise der in 3D wachsenden Neuronen durch Kalzium-Imaging und Optogenetik bewiesen, die gleichzeitig mit elektrophysiologischen Ableitungen durchgeführt wurden. Die Funktionalität des Netzwerks wurde mit den Referenzsubstanzen Picrotoxin (PTX), Tetrodotoxin (TTX) und Rotenon evaluiert, wobei sich eine außergewöhnliche Sensitivität und experimentelle Reproduzierbarkeit zwischen verschiedenen Geräten zeigte. Nach der Anwendung von Rotenon zeigten zusätzliche morphologische Auswertungen dessen Wirkung zu späteren Zeitpunkten im Vergleich zu elektrophysiologischen Ableitungen, was die überlegene Empfindlichkeit der letzteren demonstrierte. Diese Empfindlichkeit wurde bestätigt, nachdem die Wirkung der pro-inflammatorischen Moleküle Interferon-γ (IFNγ) und Tumornekrosefaktor-α (TNFα) in ko-kultivierten Neuronen, Mikroglia und Astrozyten auf morphologischer, proteomischer und elektrophysiologischer Ebene ausgewertet wurde.

Schlussendlich wurde ein neuartiges, hochphysiologisch relevantes mikrophysiologisches Gerät entwickelt, das die elektrische Aktivität von 3D wachsenden Neuronen mit hoher Effizienz und Reproduzierbarkeit erfasst, indem es sich zusätzlich auf die zelluläre

morphologische und proteomische Charakterisierung stützt. Durch ihre Vielseitigkeit qualifiziert sich diese Plattform als neuer Standardansatz für die Krankheitsmodellierung und als neues Werkzeug für das Screening von Substanzen, die auf das zentrale Nervensystem abzielen. Diese Arbeit wurde von der Baden-Württemberg-Stiftung GmbH unter dem Fördervertrag MIVT-7 (NEWRON-3D) gefördert und an eine Fachzeitschrift mit der Absicht zur Veröfffentlichung geschickt (Molina-Martínez and Jentsch et al., 2021). Der andere Teil der Arbeit wird für eine weitere Veröffentlichung zur Zeit vorbereitet.

Acknowledgements

I firstly want to thank all my colleagues of the NMS group, but especially Dr Cesare, for his advice, suggestions and fruitful scientific discussions throughout my thesis. My eternal gratitude goes to my friend and former colleague Bea, who suggested that I apply for this worthwhile and cutting-edge research position and made my time in the lab and Tübingen much more special and joyful (therefore, I also thank her parents for her existence). I am also grateful to my colleagues Fulya and Matt for their great work in the clean room facility.

My gratitude extends to the NMI for giving me the opportunity of working in a multidisciplinary institute. I highly acknowledge all the help my group and I have received from Dr Peter D. Jones for technical challenges in the microfabrication processes, Dr Simge Yüz for supporting me with everything related to the cell sorting of microglia, and Ricarda Stock for helping me with understanding the bipolar FACS machine. My special gratitude goes to Dr Nicole Schneiderhan-Marra and Meike Jakobi for the quantitative analysis of pro-inflammatory compounds. I also want to thank Martin Gaier, Joana Hummel and Clara Daab for their assistance with previous bonding experiments. I am also grateful to Kathrin Stadelmann for the SEM images she took and Karl Reuter and Frank Machnow for taking care of the animal facility.

I highly acknowledge all the external collaborators who participated in this project, especially Prof Dr Peter Heutink, for his always very useful and wise advice and suggestions related to my work. I also thank Dr Stella Donato and Dr Joachim Träger for their assistance with the automated microscopy system and Dr Jonas Neher for his insightful comments related to neuroinflammation. I want to express my deep gratitude to Dr Fernández Agudo-García, or Laura (as I like to call her), not only for her friendship but also for her well-received help with everything concerning the microglia cell culture. I would also like to thank Alexander Kirillov for his assistance with the electrophysiological data analysis and Dr Christian Feldhaus, Aurora Panzera and Vanessa Carlos from the MPI for their remarkable help they provided with the microscope to take the beautiful 3D images of brain cells.

As much as I am thankful for all the colleagues who have helped me achieve my goal, I want to express my deep gratitude to those outside of my workplace who have knowingly or unknowingly made this journey so much easier and joyful. Therefore, I want to start by thanking Bob Marley, Freddy Mercury and Fito & Fitipaldis for their excellent music and lyrics, which are not only great for road trips but also will put you in a good mood no matter how grumpy or tense you feel. I continue by acknowledging all my older friends around the globe, especially my travel friends Esther, Ana, Patri and Megha, for inspiring and motivating me to forget about

work for a few weeks a year and explore new cultures and food. I thank Alb, Bea, Gabi, Magín, Curly Laura, Tullio, Carol, Dapen, Lams, Luis, Chedar, Bru and Tiago for your friendship and support in distance or proximity and joyful memories before and during my thesis. Moreover, I want to thank my Tübinger friends, especially Albane, Sara, Andrea, Leo, Magda and Nils, for your empathy and unforgettable parties, hikings and trips during my time here. I am sure that my experience in Tübingen has been as exciting and unique as it has, thanks to you.

Als letztes will ich mich bei denen bedanken, die mir am nächsten stehen. Ich danke dir, Cri, für deine Liebe und deinen außerordentlichen Humor. Du bist mein Fels in der Brandung. Os doy las gracias a vosotros, Cari y Mati, por vuestro apoyo incondicional y por una hermandad envidiable que ha llenado mi infancia y mi vida adulta de risas, aventuras y alguna que otra resaca. Mi vida y este logro no serían lo mismo sin vosotros. Lieben Dank, Paps und Mams, dafür, dass ihr mir eine vorbildliche und aufgeschlossene Erziehung geboten habt, sowie die Ermutigung im Leben. Ohne euch hätte ich alle meine Ziele nicht erreicht. Ich bin stolz Teil dieser Familie zu sein. Os quiero!

P.D.: Creo que esto es una ocasión perfecta para esa aclamada paella, Paps!

Abbreviations

%BinNB	Percentage of bursts in network bursts
%SiB	Percentage of spikes in bursts
µG	Microglia
12nMPS	12-well nMPS
18nMPS	18-well nMPS
2D	Two-dimensional
3D	Three-dimensional
AAV	Adenovirus
AC	Astrocytes
AD	Alzheimer’s disease
AMPA	α-amino-3-hydroxyl-5-methyl-4-isoxazole-propionate
AP	Action potential
BD	Burst duration
BFR	Burst frequency rate
BiC -/-	Bi-culture without IL-34 and TGFβ2
BiC +/+	Bi-culture supplemented with IL-34 and TGFβ2
BiC	Bi-culture
BoC	Brain-on-a-chip
CµE	Capped microelectrode
Ca^{2+}	Calcium
CCL5	CC-chemokine ligand 5
ChR2	Channelrhodopsin
Cl^-	Chloride
CNS	Central nervous system
CXCL2	C-X-C motif chemokine 2
DIV	Days in vitro
EM -/-	Enhancing medium without IL-34 and TGFβ2
EM +/+	Enhancing medium with IL-34 and TGFβ2
EPSP	Excitatory postsynaptic potential
FACS	Fluorescent-activated cell sorting
FSC	Forward scatter channel
GABA	γ-aminobutyric acid

GFP	Green fluorescent protein
GL	Gel layer
Glu	Glutamine
hSC	Human stem cells
HTS	High-throughput screening
ICC	Immunocytochemistry
IFNR	Interferon-γ receptor
IFNγ	Interferon-γ
IL-1β	Interleukin-1β
IL-34	Interleukin-34
IL-6	Interleukin 6
iPSC	induced pluripotent stem cell
IPSP	Inhibitory postsynaptic potential
ISI CoV	Inter-spike interval coefficient of variance
LL	Liquid layer
LL	Liquid layer
LMA	Luminex multiplex assay
LTD	Long-term depression
LTP	Long-term potentiation
MEA	Microelectrode array
MF	Microfluidic
MFR in NB	Mean firing rate in network bursts
MFR	Mean firing rate
mGluRs	Metabotropic glutamate receptors
MMP9	Matrix metallopeptidase 9
MPS	Microphysiological system
mRNA	Messenger RNA
N+AC	Neurons and astrocytes
Na^+	Sodium
NB	Network bursts
NB+	Neurobasal +
NBF	Network burst frequency
NME	New molecular entities

NMDA	N-methyl-d-aspartate
nMPS	Neuro-microphysiological system
NO	Nitric oxide
NT	Neurotransmitter
OoC	Organ-on-a-chip
PAI-1	Plasminogen activator inhibitor-1
PD	Parkinson's disease
PDMS	Polydimethylsiloxane
PM -/-	Plating medium without IL-34 and TGFβ2
PM +/+	Plating medium with IL-34 and TGFβ2
PTX	Picrotoxin
RANTES	Regulated and normal T cell expressed and secreted
ROS	Reactive oxygen species
SLE	Selective laser-induced etching
SSC	Side scatter channel
TGFβ2	Transforming growth factor-β2
TNFR	Tumour necrosis factor receptors
TNFα	Tumour necrosis factor α
TriC 1:4	Tri-culture; 4 neurons per microglia
TriC 1:8	Tri-culture; 8 neurons per microglia
TriC	Tri-culture
TTX	Tetrodotoxin

Contents

List of figures

List of tables

List of videos

1 Introduction

Neurological disorders are among the most common origin of health loss and are the second largest cause of death worldwide (GBD 2015 Neurological Disorders Collaborator Group). After stroke, Alzheimer's disease (AD) and Parkinson's disease (PD) are the most prevalent brain disorders in Europe (Deuschl et al., 2020). Therefore, pharmaceutical industries have focused on producing novel treatments to reduce the outcome of such disorders. However, due to the brain's complexity and all the mechanisms involved in such diseases, few medicinal compounds exist that deplete neurodegeneration in AD and PD. The leading cause for the lack of treatments is the low predictability of efficacy and safety during primary clinical stages (Mohs and Greig, 2017). The former arises due to the use of experimental models, such as animal models or 2D *in vitro* platforms, which cannot accurately mimic human physiological traits. To fill this gap, 3D microphysiological systems (MPS) that recapitulate brain-like neuronal networks or structures *in vitro* have emerged in recent years (Park et al., 2018; Soscia et al., 2020; Park et al., 2021, Shin et al., 2021).

Neuronal 3D MPS have propelled beyond conventional monolayers by allowing basic neuroscience research. The latter, however, has only been possible via the synergy of molecular and cellular biology, bioengineering, material sciences, and computer modelling. Through those, novel nMPS have been designed to characterise brain cells growing in 3D by combining morphological readouts of multiple cell types, histoarchitecture and cell-to-cell interactions. To understand those further, some platforms allow traditional studies of transcriptomics or proteomics (Kim et al., 2015, Papadimitriou et al., 2018, Park et al., 2018). Moreover, functional readouts through electrophysiological recordings or calcium imaging, and neuromodulation via optogenetics, have further increased the value of nMPS, not only for basic research purposes but also to overcome challenges during the drug discovery pipeline (Park et al., 2021; Shin et al., 2021).

To this day, the most challenging feature to be implemented in nMPS is the characterisation of synaptic circuits in a non-invasive and reproducible manner. To address this issue, this study presents a reproducible and high-throughput system compatible with functional, morphological, and proteic quantitative readouts. This platform enables the characterisation of morphological properties from subcellular resolution and the quantification of released molecules, harming or enhancing neuronal functionality. More importantly, this device's novelty is the assessment of non-invasive extracellular recordings of up to 18 neuronal networks of dissociated neurons simultaneously to calcium imaging or optogenetics. Through the combination of the multiple possible readouts, this nMPS proves to be suitable to give insights into basic research studies of the central nervous system (CNS), such as neuroinflammation,

progression of neurological disorders, long-term potentiation or blood-brain barrier permeability, but also drug testing and toxicity screening.

2 Background

As part of the CNS, the brain is one of the most relevant organs in the human being. Most of the sensations perceived during life are selected and sorted by the cerebrum through the brain's key component, the nerve cells. Those are highly organised into networks and specialised in transforming stimuli into electrical discharges. It is fundamental to understand this unique communication ability based on molecular and cellular mechanisms to identify the processes that compromise its function, such as neuronal pathologies. Responses to harmful stimuli caused in unhealthy brains are translated into the release of specific factors and further evaluated by neighbouring brain cells, such as neurons, astrocytes and microglia. The interaction of glial and neuronal cells is crucial for novel therapies of prevalent neurological diseases.

Nonetheless, due to the elaborate and broad interplay of many units (blood-brain-barrier, lymphatic system, axon-myelin, etc.) with the CNS immune system, the origin of many neurological diseases remains puzzling to this day. Indeed, animal experiments have demonstrated to be decisive. Much of the neurons' physiological behaviour and their interaction with glia cells have been discovered via the latter, mainly through the development of several neurobiological techniques. Neurobiological techniques range from optical approaches to electrophysiological methods and aid in defining cellular and molecular traits.

2.1 Neurophysiology

The brain is composed of two main cell types, neurons and glial cells. Together, they comprise about 171 billion cells only in the human brain (von Bartheld et al., 2016). Nerve cells form half of that amount (86 billions). Neurons are discrete and independent entities that communicate via unique contacts. The transmission of information between neurons was first described in the late 19th century by Spanish histologist Ramón y Cajal as the "neuron doctrine" (Cajal and May, 1928). Neurophysiologist Charles Sherrington corroborated this theory by examining the nature of neuronal communication. He described it as a transfer of electrical signals, later known as an action potential (AP), between two neurons occurring through functional connections, which he termed synapses (Foster and Sherrington, 1897). Synapses are categorised into electrical and chemical synapses and evoke the direct or indirect influx of ions into the postsynaptic membrane, respectively (figure 2.1) (Towlson et al., 2018).

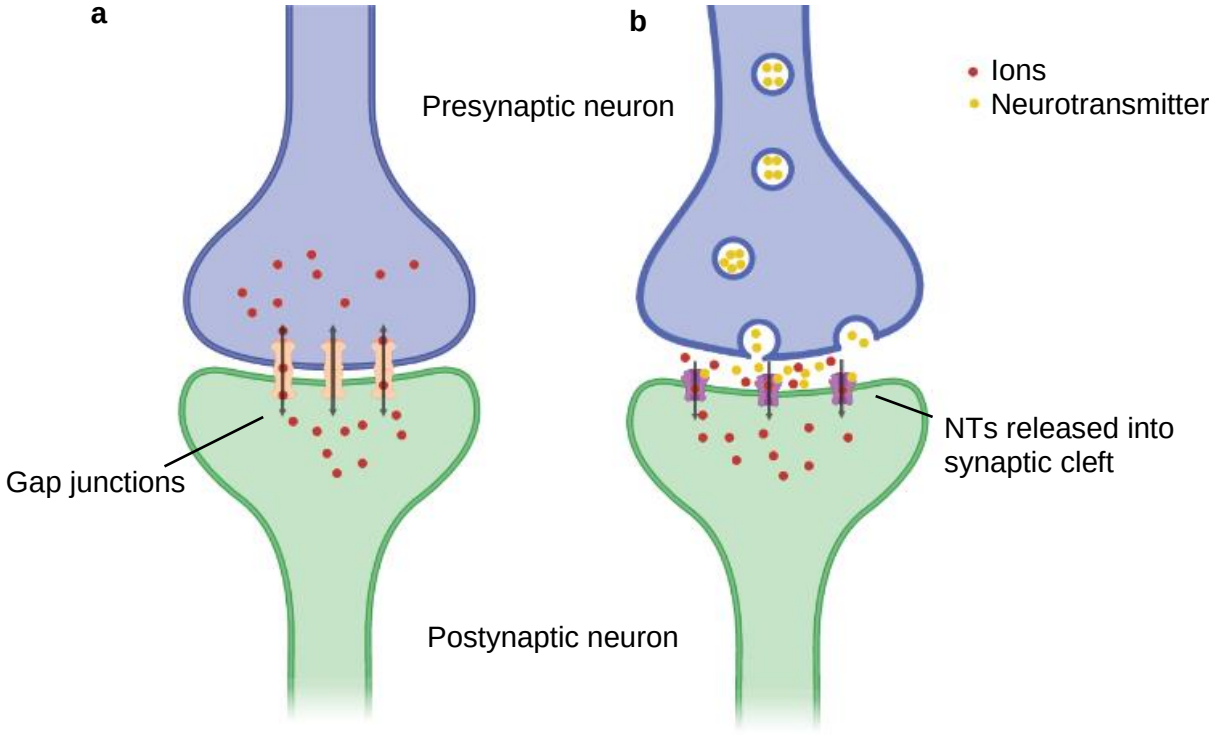

Figure 2.1: Electrical and chemical synapses. Ions may pass in both directions through gap junctions (a) while neurotransmitters are released into the synaptic cleft of the chemical synapse (b) to bind to inactive receptors in the postsynaptic membrane that open to allow the flow of ions. (Created with Biorender.com).

Electrical synapses are mechanically linked through the presence of gap- junctions containing connexon channels in both the pre- and postsynaptic membranes that cause the direct flow of positively charged ions (sodium, Na^+) (Kandell et al., 2021). The influx of sodium elicits a change in the membrane potential of the postsynaptic neuron. Its resting potential is approximately -70 mV but increases through the influx of Na^+, leading to the depolarisation of the membrane (Purves et al., 2004). The latter may cause an action potential to travel down the neuron by evoking the opening of contiguous Na^+-channels. The AP travels down the myelinated axon and dendrites of the neuron until the next synapse is affected. This type of synapses comprises the minority in the brain and allows the migration of AP in a bi-directional manner (Kandell et al., 2021).

On the contrary, as described in Purves et al. (2004), in chemical synapses, the travelling of AP is unidirectional. Here, once the AP reaches the axon terminal, it evokes the opening of Calcium (Ca^{2+})-channels. The entry of calcium causes the synaptic vesicles in the presynaptic button to release their containing neurotransmitters (NT) into the synaptic cleft (figure 2.1b). Neurotransmitters reversibly bind to the postsynaptic NT-specific receptors causing either an excitatory or an inhibitory response by opening certain ion channels (Purves et al., 2004). The

excitatory response, also known as excitatory postsynaptic potential (EPSP), causes the opening of postsynaptic channels that allow the influx of positively charged ions (Na^+, Ca^{2+}) into the postsynaptic neuron (Takagi, 2000). This process again causes the depolarisation of the membrane, which may lead to an AP travelling down the neuron. Instead, an inhibitory postsynaptic potential (IPSP) induces the opening of ion-gated channels that mainly permit the entrance of negatively charged ions, leading to hyperpolarisation (Coombs et al., 1955).

The most common neurotransmitters in the brain are amino acids glutamate (Glu) and γ-aminobutyric acid (GABA). According to Purves et al. (2004), the former is estimated to be the excitatory amino acid released in half of the brain's synapses. When glutamate is released into the synaptic cleft, a rapid response is evoked in the postsynaptic neurons by binding to ionotropic glutamate receptors AMPA (α-amino-3-hydroxyl-5-methyl-4-isoxazole-propionate) and NMDA (N-methyl-d-aspartate). AMPA permits the influx of Na^+, while NMDA additionally permits the entrance of Ca^{2+} when amino acid glycine is simultaneously bound to the receptor (Purves et al., 2004). Calcium influx into the postsynaptic neuron might activate several intracellular signalling cascades, leading to synaptic enhancement (Regehr et al., 1994). As stated by Brodal et al. (2010), a slower postsynaptic reaction is caused when Glu activates metabotropic glutamate receptors (mGluRs). The binding to mGluRs induces the uncoupling of a G-protein from the receptor, which subsequently initiates the direct interaction with other ion channels. Metabotropic receptors are also found in GABAergic synapses ($GABA_b$), although those cause an inhibitory response when active. Moreover, GABA may also bind to an ionotropic receptor ($GABA_a$), which permits the entry of negatively charged ions causing the hyperpolarisation of the postsynaptic neuron (Brodal et al., 2010).

Neurotransmitters and receptors in the synaptic cleft are highly diverse. Indeed, the communication between neurons can be easily modulated through the increase or decrease of NT release or receptor expression. These processes may be modified through external or intrinsic factors and may also be influenced by neighbouring glial cells (Suzumura and Ikenaka, 2013).

2.2 Neuroglia

As aforementioned, glia cells sum up to 85 billion cells in the human brain (von Bartheld et al., 2016), from which 10-15 % are microglia (Lawson et al., 1992) while 20-40% account for astrocytes (Filiano et al. 2015). Spanish neuroscientist Pio del Río-Hortega first described microglia (μG) at the beginning of the 20th century (del Rio Hortega and Penfield, 1892). Since then, several functions have been attributed to this cell type, such as scavenging, phagocytosis

of developing and adult neurons and synapses, the latter's monitoring, and extracellular signalling (Wake and Fields, 2011). As summarised by Suzumura and Fields (2013), among their wide range of functions, the one that has gained more attention from researchers is the secretion of signalling molecules that help maintain the brain's homeostasis and respond to cues implying an external pathogen's intrusion. Indeed, those cues activate microglia, which modulate an immune response to remove noxious agents to limit their detrimental effects, making this cell a key element of the CNS immune system (Suzumura and Ikenaka, 2013). Microglia activation is rapid and reversible and affects its surveillance, motility, morphology, and ramification (Ling and Wong, 1993). Microglia have shown to be more motile in an active state and to alter their ramified morphology into an amoeboid form (Kreutzberg, 1996). Moreover, they secrete specific molecules that affect neighbouring glial cells, such as astrocytes (AC).

Astrocytes are star-like cells involved in forming the blood-brain barrier and its permeability condition (Siracusa et al., 2019). Moreover, they play a critical regulatory role in neurogenesis and synaptogenesis while they also maintain an appropriate chemical environment for neuronal signalling by, for instance, regulating the uptake of NTs (Patel et al., 2005). As previously mentioned, NT glutamate is released by neurons. After an action potential, it is taken up by astrocytes to be metabolised into glutamine. Then, glutamine is released again and is broken down to either glutamate or GABA inside the neuron (Bak et al., 2006) (figure 2.2). In the presence of signalling molecules, such as tumour necrosis factor-α (TNFα) or interferon-γ (IFNγ), the uptake of glutamate by AC may be altered through the possible change in astrocytic reactivity. This modification may lead to astrogliosis, where the extensively ramified astrocyte reduces its extensions and develops thicker and shorter branches, finally becoming hypertrophic (Kakh et al., 2017). Surely, astrocytic activation leads to modifications in synaptic transmission and neuronal health and influences the state of the microglia, which responds accordingly through signals received by astrocytes and neurons, maybe leading to an inflammatory response. This interplay between neurons, microglia, and astrocytes is the most relevant to keep the homeostasis in the brain, but also to respond to noxious agents. Together, they form the "quad-partite synapse", a functional structure consisting of pre- and postsynaptic neurons, astrocytes, and microglia (Araque et al., 1999; Schafer et al., 2013; Pittaluga, 2017).

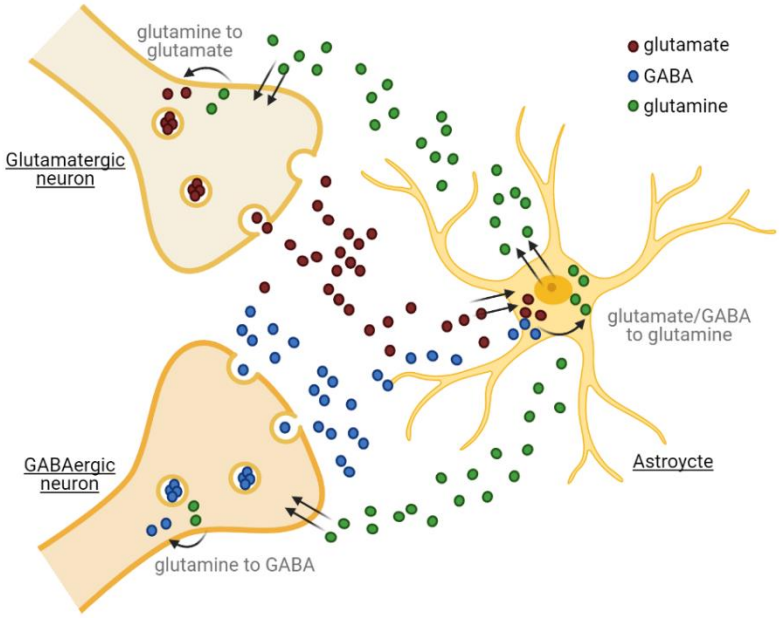

Figure 2.2: Simplified uptake of neurotransmitters GABA and glutamate by astrocyte. Glutamate and/or GABA are taken up by astrocytes and metabolised into glutamine via different pathways. Glutamine is released to the extracellular milieu and converted to glutamate and GABA by glutamatergic and GABAergic neurons, respectively. (Figure was created with Biorender.com).

2.2.1 The "quad-partite synapse" in neuroinflammation

The CNS response to an inflammatory stimulus is very complex. The activation of the CNS immune system is mainly translated into the release of pro-inflammatory molecules, such as TNFα and IFNγ (Beneveniste and Benos, 1995).

TNFα is a small multifunctional protein secreted by neurons, astrocytes and microglia, but primarily by the latter two (Strohmeyer and Rogers, 2001). It is required for neuronal survival as it plays a key role in forming neuronal circuits and the accurate functioning of synapses, mainly resulting in increasing AMPA receptors and reducing GABA receptors during neuronal development (Matejuk and Ransohoff, 2020). However, an imbalance may occur due to injuries, brain damage, infections, or certain neuropathologies, such as Alzheimer's disease or Parkinson's disease, where in both cases, neurons degenerate over time (Burns and Iliffe, 2009; Kalia and Lang, 2015). As neurodegeneration has recently been associated with inflammation processes promoted by glia cells (Amor et al., 2010), scientists aim to develop targeting therapies to treat or reduce the outcome of neurodegenerative diseases. However, due to the complex dynamics of patient-specific characteristics (ageing, genetic background), inflammatory mediators, and environmental factors, the development of effective therapies for

brain diseases affected by the CNS immune system remains challenging (Lucas et al., 2006, Chen and Pan, 2015). To enhance the success rate of treatments, the influence of inflammatory processes on physiological, biochemical, and behavioural characteristics is a critical aspect that needs to be studied more in detail. Therefore, several studies focus on the neurotoxic effects of TNFα (Lock et al., 1999; McCoy and Tansey, 2008; Probert, 2015). This is also the case for cytokine IFNγ, which is recently thought to play an essential role in neurodegenerative diseases, such as multiple sclerosis (Arellano et al., 2015). This cytokine was thought to be mainly secreted by lymphocytes T for many years. Nonetheless, current research has proven that it is not only released by T cells but is also produced by astrocytes and microglia (Lau and Yu, 2001; Wang et al., 2007). Although the production of IFNγ in glia cells is yet not well understood, it is clear that an imbalanced concentration of both IFNγ and TNFα leads to direct or indirect neuronal cell death and exacerbates the inflammatory response through the release of additional molecules, such as IL-1β (Interleukin-1β), IL-6 (Interleukin-6), CCL5/Rantes (CC-chemokine ligand 5/ regulated on activation, normal T cell expressed and secreted), CXCL2/MIP-2 (C-X-C motif chemokine/2 Macrophage Inflammatory Protein 2), MMP9 (Matrix metallopeptidase 9), Serpin E1/PAI-1 (Plasminogen activator inhibitor-1) (Sallés and Strickland, 2002; de Paola, 2007; Semple et al., 2009; Suzumura and Ikenaka, 2013; Mehra et al., 2016; Wang et al., 2014; Rempe et al., 2016).

By initiating the immune response in the CNS, the pathways of IFNγ or TNFα may be activated. Both, eventually, cause specific effects on microglia, neurons, or astrocytes (figure 2.3). When bound to the interferon-gamma receptor (IFNR) in microglia, IFNγ activates the latter, resulting in the release of microglial TNFα. Subsequently, TNFα molecules bind to tumour necrosis factor receptors (TNFR), present on microglia and both astrocytes and neurons (Probert et al., 2015). TNFα retroactively binds to microglia as well as to astrocytes and provokes the secretion of glutamate. Then, glutamate binds to neuronal glutamatergic receptors and elicits the entrance of Na^+ and Ca^{2+} (Purves et al., 2004). When entering the cell in large quantities, Ca^{2+} results in oxidative stress (nitric oxide, NO and reactive oxygen species, ROS), leading to a decrease in ATP production caused by mitochondrial dysfunction. This leads to a lower axonal flow, neuritic beading, and finally, neuronal cell death (Suzumura and Ikenaka, 2013).

As summarised in Suzumura and Ikenaka (2013), simultaneously with TNFα, NO and ROS avoid the uptake of glutamate by astrocytes, which increments the presence of glutamate in the synaptic cleft and the extracellular milieu. As glutamate uptake is blocked, the NT may also bind to glutamatergic metabotropic receptors (mGluR2) present in microglia, triggering more TNFα release enhancing the inflammatory response in the CNS. Moreover, the binding of TNFα to the neuronal TNFR induces the decrease of GABA receptors but increases AMPA

and NMDA ones, again permitting the entrance of more Ca^{2+} into the neuron. This cascade leads to a more effective blocking of processes that take up glutamate and increases neuronal cell death (Suzumura and Ikenaka, 2013). Additionally, the presence of IFNγ may significantly accelerate neuronal cell death. Recently, researchers found that IFNγ activates AMPA receptors by forming receptor complexes that allow the entrance of Ca^{2+}, leading to an exacerbation of glutamate neurotoxicity and cell death (Mizuno et al. 2008).

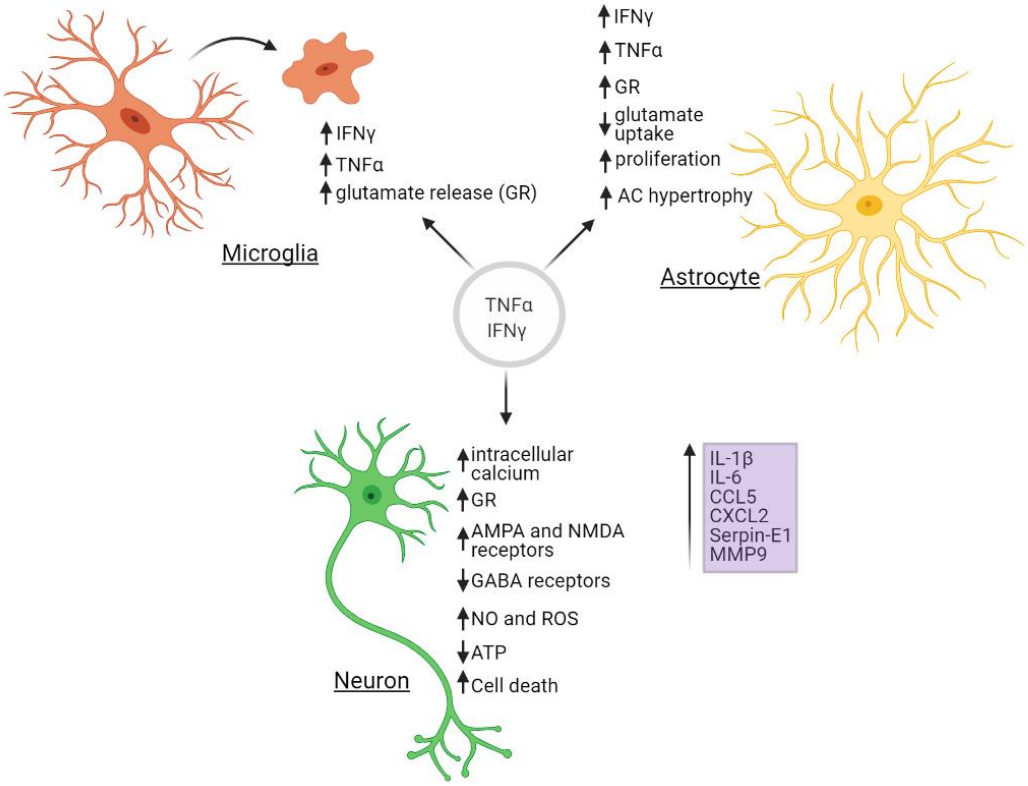

Figure 2.3: Effect of TNFα and IFNγ in the CNS. Cross-talk between neurons, microglia, and astrocytes in an abnormally high concentration of TNFα and IFNγ. Inflammation results in neurotoxicity via glutamate, finally inducing cell death. The presence of TNFα and IFNγ exacerbates the release of additional pro-inflammatory compounds IL-1β, IL-6, CCL5, CXCL2, Serpin E1, and MMP9, enhancing the inflammatory response of glial cells and neurons. (Figure created with BioRender.com).

Moreover, inflammation processes are augmented by releasing additional molecules, such as IL-1β, IL-6, CCL5/RANTES, CXCL2/MIP-2, Serpin E1/PAI-1, and MMP9. Interleukins-1β and 6, and MMP9 (Basu et al., 2004; Erta et al., 2012; Fujioka et al., 2012; Bronisz and Kurkowska-Jastrzębska, 2016) are well known to be released by neurons, astrocytes and microglia, while CXCL2 primarily by the latter two (Semple et al., 2009). On the other hand, Serpin E1 is thought

to be predominantly secreted by astrocytes and is relevant in increasing axonal fibrin digestion leading to neurodegeneration (Buisson et al., 1998; Kim et al., 2011; Mehra et al., 2016). Indeed, CCL5 has been demonstrated to be released by microglia, astrocytes, and neurons, enhancing the release of glutamate, and therefore, promoting neurotoxicity and, finally, cell death (Pittaluga, 2017; Lanfranco et al., 2018). Although also anti-inflammatory molecules are released to diminish detrimental effects related to neuroinflammation, during this study, only the pro-inflammatory response was considered and studied via several neurobiological methodologies.

The enhancement of an inflammatory response in the CNS is very complex; however, the mentioned simplified process highlights the neuron-glia cross-talk through specific molecules' production, primarily via TNFα and IFNγ. Both are known to be increased in many neurodegenerative disorders and are therefore the focus of many studies (Barcia et al., 2011; Zheng et al., 2016; Göbel et al., 2018). Moreover, this interplay may be reinforced via physical links, i.e. gap junctions, between neurons and glia cells, defining a pathway for bidirectional electrical and metabolic signalling (Fróes et al., 1999; Dobrenis et al., 2005). Time has proven the challenges to define and characterise the importance of intercellular gap junctions in the CNS. However, studies have demonstrated that malfunctions in the former may lead to neurological disorders, such as hereditary deafness (Martínez et al., 2009) or uncorrelated motor neuron firing (Personius et al., 2007). By applying diverse neurobiological techniques, this and other features of the CNS may be understood better.

2.3 Neurobiological techniques

Neurobiological techniques are the pillar to unfold the complexity of the brain. Methodologies to study the latter have only been possible thanks to the considerable advances in technologies related to physics, chemistry, engineering, and others. Consequently, the analysis of cellular and molecular processes in the CNS is possible and has led to a better understanding of the brain's underlying mechanisms in the last century. For *in vitro* studies, neuroscientists favour using technologies that allow the analysis of single brain cells or a group of brain cells to simplify the brain structure. Eventually, gained information can be correlated to the entire organ. Those studies usually combine morphological, functional, or proteomic analysis.

2.3.1 Morphological readout

The analysis of cellular structures requires the visualisation of the former. One of the most common *in vitro* techniques utilised for acquiring detailed cellular information is immunocytochemistry (ICC), where samples are permeabilised and fixed to allow the labelling of structures with target-specific antibodies conjugated to a fluorophore. Those structures may then be visualised in high-resolution through a microscope. As useful as this technique is to study several components at once, it only provides already-fixed cells and proves to be more complex when analysing three-dimensional (3D) structures. Therefore, modern technologies were developed for a more successful visualisation of samples in real-time by using viruses (adenovirus, lentivirus). Viruses containing fluorescent proteins (GFP, RFP, YFP, etc.) transduce targeted cells, leading to fluorescence-expressing cell types easily visible via a microscope, which allows monitoring cellular outgrowth health in real-time. Both techniques are widely used depending on the addressed question of the study.

2.3.2 Functional readout

Neurobiological techniques focused on functional readouts are mainly designed to capture neuronal activity. The first-ever employed method to capture electrophysiological information was, in fact, developed to determine the propagation of action potentials in neurons (Hodgkin and Huxley, 1952). This type of technique corresponded to an invasive intracellular recording, in which an electrode is introduced into the cell while a reference electrode is placed in the extracellular space to detect small changes in the voltage of the neuronal membrane. Since then, researchers have developed new methodologies to address more detailed processes, such as patch-clamp. The mentioned, developed in the late 1970s (Neher and Sakmann, 1976), might be one of the most used techniques to study ion channels and was actually fundamental to understanding channels' involvements in neuronal electrical processes. Although this technique is necessary to study ionic currents in single cells, it is rather inappropriate for studying neuronal circuits. Therefore, to assess information about neuronal circuits' dynamics and reduce the aforementioned intracellular recordings' invasiveness, extracellular recordings are performed.

In extracellular recordings, both the recording and reference electrodes are integrated into the extracellular space. Here, the recorded changes in the neuron's membrane potential correspond to the difference between the potentials identified by the recording and reference electrodes. Consequently, in order to be able to detect any signal during an AP, neuronal somas need to be in very close contact with the recording electrode (Molina-Martínez et al., 2021). Hence, platforms employed to study neuronal circuits integrate multiple recording

microelectrodes, also known as microelectrode arrays (MEA), not only to increase the chance of functional readout but also to assess information about numerous neurons simultaneously (Thomas et al.,1972; Johnston et al., 2010). Thus, more details about the network, and, if necessary, about single neurons, can be acquired (Carter and Shieh, 2010).

As the MEAs are generally incorporated in the platform, the functional readout is much more straightforward and non-invasive than the previously mentioned intracellular recordings and patch-clamp. Therefore, neuronal activity can be recorded over several periods, providing information about the development of neuronal networks and spatiotemporal properties (Gurney, 2004). Although this approach is thought to be the most appropriate and productive technique to acquire electrical information from neuronal networks, it is still not the most cost-efficient. Therefore, in the late 1980s, scientists developed an optical technique that allows cellular activity measurement (Cannell et al., 1987).

Imaging methods are widely utilised for acquiring neuronal activity in a non-invasive manner (Mofazzal et al., 2019). Scientists commonly employ techniques that rely on calcium (Ca^{2+}) indicators that change their fluorescence properties when bound to Ca^{2+}. Calcium indicators are categorised into chemical indicators (dyes) or genetically encoded calcium indicators (adenovirus). Both guarantee the measurement of neuronal transient calcium, which, in neurons, is correlated to the firing of an action potential as the main influx of Ca^{2+} takes place in the axon terminal in the chemical synapses (see section 2.1). Moreover, they permit the observation of the neuronal activity of various cells simultaneously in real-time.

Nonetheless, these measurements depend on the spatial and temporal resolution, which is limited to the sensitivity of the Ca^{2+}-indicator and the type of cell culture and microscopy employed. Although advances in light field microscopy (Prevedel et al., 2014) allowed the recording of Ca^{2+}-transients in 3D *in vivo*, calcium indicators serve as a surrogate marker and can therefore not be considered for direct assessments of actions potentials. Furthermore, calcium is involved in cellular signalling, not only in neurons but also in microglia and astrocytes. Consequently, astrocyte- and microglia-specific Ca^{2+}-indicators are also employed to clarify glia cells' functionality in the brain (Umpierre et al., 2020; Wang et al., 2009).

In order to demonstrate the maturity of the neuronal networks and their physiological relevance, studies employing either of the mentioned functional assessments employ gold standard compounds, such as picrotoxin or tetrodotoxin. PTX, a poisonous plant compound (Boullay, 1812), is an antagonist of GABA that interrupts the inhibitory dynamics between GABAergic and excitatory neurons, causing a seizure-like behaviour in mature neuronal networks (Ehrenberger et al., 1982). Likewise, in immature neuronal cultures, GABA has the

same effect, the activation of excitatory neurons via the inhibition of inhibitory GABAergic neurons (Obata et al., 1978). Instead, TTX blocks Na^+-channels, causing a decrease in neuronal activity. The inhibition of neuronal activity demonstrates the presence of Na^+-channels in all neuronal cell types. Eventually, for more detailed information about neuronal networks and glia processes, scientists employ a biological technique, optogenetics, which genetically modifies cells to express light-sensitive ion channels, giving the possibility to modulate cellular activity (Zemelman et al., 2002).

2.3.3 Neuromodulation

Optogenetics is a modern methodology employed to genetically modify cells to express light-gated ion channels that are ultimately sensitive to light stimuli (Zemelman et al., 2002). Through the stimulation with a specific wavelength, ion channels undergo a conformation allowing the influx of cations or anions, leading to depolarisation or hyperpolarisation of the cell. The specificity of ion influx is dependent on the optogenetic actuators, such as channelrhodopsin, which can cause light-induced excitability or inhibition in the cell. Moreover, through the integration of a specific promoter, cell-type specific manipulation of activity can be performed. Modulation of cellular activity is mainly applied to neurons to identify neuronal networks (Schmieder et al., 2018) or study synaptic plasticity (Xie et al., 2013), but recent studies also show applications of optogenetics for astrocytes and microglia (Adamsky et al., 2018; Laprell et al., 2021), making this technique relevant for biological interrogations.

Although the modulation of various cell types is possible, the effect of such alteration needs to be monitored either via animal behaviour in *in vivo* studies (Sidor et al., 2015) or via Ca^{2+}-imaging or electrophysiological recordings in *in vitro* platforms (Renault et al., 2015; Shin et al. 2021). However, to fully understand the molecular pathways in neuronal networks, signalling cues in the "quad-partite synapse" need to be evaluated in parallel.

2.3.4 Protein expression

A relevant and very accepted technique to understand molecular pathways is the study of up-regulated or expressed proteins. For this, scientists employ two main methods: the detection of messenger RNA (mRNA) or already synthesised proteins.

mRNA can be detected via several methodologies, such as reverse transcription-polymerase chain reaction (RT-PCR) (Temin and Mizutani, 1970; Baltimore, 1970), northern blot analysis (Alwine et al., 1977), in situ hybridisation (Gall and Pardue, 1969; Pardue et al., 1969), or

nuclease protection assays (NPA) (Sambrook et al., 2001). Each of them gives different information about the mRNA. NPA, for example, is the most suitable for multi-target analysis and mapping studies, while in situ hybridisation detects gene expression within tissues or cells. The most straightforward detection strategy is northern blot, where endogenous transcript information and multigene family members are identified. However, it also counts as the least sensitive method among the ones mentioned. On the contrary, RT-PCR is the most sensitive detection technique in which uncommon mRNA levels can be exposed. Nonetheless, it also entails the most technical challenges, especially in regard to the retrieval of the cells in different cell culture types. As all these methods provide different information, researchers mostly employ more than one technique to confirm the detected mRNA levels.

Levels of already synthesised proteins can be detected by employing numerous techniques, such as Western blot (Renart et al., 1979), enzyme-linked immunosorbent assays (ELISA) (Engvall et al., 1971), or Luminex multiplex assays (LMA) (Elshal and McCoy, 2006). Equal to the detection of mRNA levels, the mentioned approaches all have their advantages and disadvantages. Both Western blot and ELISA are prevalent methods to detect a single protein's presence or levels. These are informative for diagnostics or research but not the most appropriate approach if several proteins want to be detected simultaneously, as more sample volume is needed. Therefore, multiplex immunoassays, such as LMA, give the possibility to quantify multiple proteins at once. In LMA, colour-coded microspheres are internally marked with different proportions of red and infrared fluorophores corresponding to a distinct spectral signature or bead region. Analyte-specific antibodies are coupled to a unique bead region that becomes fluorescent when coupled to the protein of interest. The main advantage of this system is the detection of up to 100 proteins at once.

Although the expression of proteins reveals a substantial amount of molecular processes, the effect of those needs to be analysed in combination with morphological and functional readouts. With the synergy of those, more relevant information about neuronal and glial cells can be assessed. Therefore, microphysiological systems aim to integrate as maximum assays as possible.

3 Microphysiological systems (MPS)

To carry out basic research and drug discovery, traditional two-dimensional (2D) *in vitro* models are widely used to mimic pathological conditions (Marx U. et al., 2016). Although these models present very low experimental variation, they are limited in representing structural and functional *in vivo* complexities (Kamei et al., 2016; Tekin et al., 2018; Cuní-López et al., 2021). To better understand physiological processes, recently, novel microphysiological *in vitro* models holding more complex 3D cell components have been developed. For example, organ-on-a-chip (OoC) is an emerging technology in which artificial 3D organs simulate *in vivo* dynamic, functional, and physiological responses (Cirit and Stokes, 2018). To achieve this, advanced microphysiological OoC platforms merge human-derived cells, microfluidics and microfabrication techniques. Through this combination, the OoC technology intends to support the 3R principle, which aims to reduce, redefine and replace the use of experimental animals (Mastrangeli et al., 2019).

Moreover, this approach provides more accurate information about cellular or organ-specific processes than traditional 2D models or other 3D platforms. It represents an improvement for drug development, as the latter's major challenge is the employment of highly physiologically-relevant *in vitro* models during drug testing. In fact, this is why federal institutions and pharmaceutical companies fund projects for more predictive OoC models. Indeed, in the next five years, this novel *in vitro* system is predicted to reduce the time cost to develop new approved molecular entities (NME) (Franzen et al., 2019). Hence, OoC is forecasted to decrease between 10 and 26 % of the total research and development (RandD) costs spent for NME, which nowadays lays between 600 million and 2 billion dollars (Marx et al., 2016; Mosig et al., 2017). Furthermore, by supporting the growth of human-derived cells, this system aims to fill the gap of performing studies that are ethically questionable in humans or experimental animals. Most importantly, OoC seeks to reduce the translational challenges that emerge from pathophysiological variations among species (Hackam and Redelmeier, 2006, Low et al., 2020).

Lately, physiological aspects of multiple organs, such as lung, heart, liver, or kidney, have been mimicked in OoC platforms (Huh et al., 2010; Grosberg et al., 2011; Bavli et al., 2016; Jang et al., 2013). Moreover, scientists aim to develop body-on-a-chip, also known as multi-organ microphysiological systems, in which multiple organs are imitated and operated in parallel (Esch et al., 2016; Chen et al., 2018). Certainly, neuro-microphysiological systems (nMPS) aiming to imitate the brain (brain-on-a-chip, BoC) (Koo et al., 2018) or the spinal cord (spinal cord-on-a-chip, SCC) (Shin et al., 2021) also represent an emerging field, especially because

of the harmful effect of neurological disorders and diseases is increasing continuously in our society (Deutschl et al., 2020).

3.1 Neuro-microphysiological systems (nMPS)

The main goal of developing *in vitro* models targeting the CNS is to bridge the gap from monolayer cell cultures to 3D forms that mimic the brain's architecture. The most physiologically relevant models, such as the brain-on-a-chip, could imply a significant decrease of the costs in the development of new CNS drugs, especially by exposing toxicity and efficacy failures in pre-clinical studies (Dowden et al., 2019). Indeed, the development of CNS drugs is the most expensive if compared to other drugs because neurological agents usually fail in Phase III of clinical trials, which implies an expensive investment for companies, as the latest phases are the costliest (Fogel, 2018). Moreover, the success rate of neuropsychiatric diseases is low compared to others (8.2% vs 15%, respectively) (Mohs and Greig 2017). For instance, the attrition rate of drugs focused toward AD progression has so far been 99.6% (Pistollato et al., 2016; Mohs and Greig 2017). The main reason for such a low success rate is that the CNS conditions, especially AD, tend to be chronic and complex and therefore hinder an accurate estimation of drug efficacy in pre-clinical trials. Additionally, AD is not naturally occurring in mice, but is imitated by creating mouse models (Götz et al., 2018). Thus, nMPS aims to optimise CNS drugs' success rate by developing more physiologically relevant systems that potentially permit the identification of early effects of NME. For a higher physiological relevance and translatability, nMPS tend to employ human-derived cells.

Nonetheless, the development of an nMPS that supports the growth of human-derived brain structures is rather complex. It needs to fulfil certain requirements to assess information about the morphology, functionality, neurotoxicity, cell-to-cell interaction, and the brain's histoarchitecture. Thus, multiple types of research focus on creating 3D neuronal cell cultures to produce 3D *in vitro* platforms in line with the OoC principles, however, by employing diverse neuronal cell types, cell culture systems, and technical approaches for the validation of the system.

3.1.1 State of the art

In an effort to develop neuro-microphysiological systems that target the CNS, researchers employ diverse cell types, such as primary cells from rats or mice, immortalised cell lines, human-induced pluripotent stem cells, or embryonic human stem cells. Those can be either embedded in a gel in a dissociated or self-organised fashion or grow in a hydrogel-

free environment (tables 3.1 and 3.2). One of the biggest challenges is the materials employed for the production of an nMPS. Materials range from silicon-like components to glass.

Table 3.1: Current nMPS employed for dissociated cell culture types.

Cell culture system	Cell type	Technical approach	Scaffold	Readout possibilities	Throughput	References
Dissociated cells	Rat primary cells (neurons, astrocytes)	Custom-made cell culture chambers	Matrigel	Imaging, patch-clamp	1 replicate	Irons et al., 2008
	Murine immortalized cell line (fibroblasts), murine primary cells (neurons)	Polymide MF chip, ring	PEG hydrogel	Imaging, planar MEA	1 replicate	Lin et al., 2009
	Rat primary cells (neurons)	Custom-made cell culture chamber	Collagen type I	Imaging, patch-clamp	1 replicate	Xu et al., 2009
	Rat primary cells (neurons)	PDMS MF chip	Hydrogel mix (agarose, alginate)	Imaging	1 replicate	Kunze et al., 2011
	Rat primary cells (neurons), human iPSCs (neurons)	PDMS microchambers	Collagen type I	Imaging, calcium imaging, planar MEA	2 replicate	Odawara et al., 2013
	Primary rat cells (neurons)	MEA well plate, area defined by PDMS	Transwell suppport (microbead monolayer)	Imaging, planar MEA	1 replicate	Frega et al., 2014
	Primary rat cells (neurons)	Multi-well plate	Silk collagen scaffold	Imaging, quantitative and qualitative assays, local field potential measurement (LMF)	24 replicates	Chwalek et al., 2015
	Human primary cells (endothelial cells), iPSCs (neurons), primary cell lines (astrocytes, pericytes)	PDMS MF chip	Collagen type I	Imaging, TEER measurements (impedance)	1 replicate	Brown et al, 2015
	Human immortalized cell line (neurons)- *AD model*	Multi-well plate	Matrigel	Imaging, quantitative and qualitative assay	1-96 replicates	Kim et al., 2015
	Human-derived cell lines (astrocytes, pericytes, endothelial cells)	PDMS MF chip	Collagen type I	Imaging, quantitative assay	1 replicate	Herland et al., 2016
	Murine embyrionic stem cells	PDMS MF chip	PEG hydrogel, GelMa hydrogel	Imaging	12 replicates	Bae et al., 2016
	Human neural progenitor cells (hNPCs)- *AD model*	Multi-well plate	Matrigel	Imaging	1-96 replicates	Choi et al., 2016
	Human iPSC-derived cells (neurons, astrocytes)	OrganoPlate®	Matrigel	Imaging, calcium imaging	96 replicates	Wevers et al., 2016
	Rat primary cells (neurons, astrocytes) HUVEC (endothelial cells), immortalized cell line (endothelial cells)	PDMS MF chip	Collagen type I	Imaging, calcium imaging	1 replicate	Adriani et al., 2017
	Rat primary cells (neurons)	PDMS MF chip	Collagen type I	Imaging, quantitative assay, calcium imaging, patch-clamp	1 replicate	Kim et al., 2017
	Human immortalized cell lines (neurons, astrocytes, microglia, endothelial cells)	OrganoPlate®	Matrigel	Imaging, quantitative assay	96 replicates	Koo et al., 2018
	Human immortalized cell lines (astrocytes, pericytes, endothelial cells)	OrganoPlate®	Collagen type I	Imaging, quantitative assay	40 replicates	Wevers et al., 2018
	Rat primary cells (neurons)	MEA ring	Collagen type I	Imaging, planar MEA	1 replicate	Bourke et al., 2018
	Human primary cells (astrocytes), iPSCs (neurons)- *AD model*	Multi-well plates	StarPEG-heparin hydrogel, Matrigel	Imaging, quantitative and qualitative assay, calcium imaging, patch-clamp, electron microscopy	24 replicates	Papadimitriou et al., 2018
	Human iPSC-derived cells (neurons, astrocytes) human immortalized cell line (microglia) *AD model, Neuroinflammation*	PDMS MF chip	Matrigel	Imaging, quantitative and qualitative assays calcium imaging	1 replicate	Park et al., 2018
	Human iPSC-derived cells (neurons, astrocytes)	Polymide MF chip, ring	Collagen type I	Imaging, 3D MEA	3 replicates	Soscia et al. 2020

Table 3.2: Current nMPS employed for assembled culture types.

Cell culture system	Cell type	Technical approach	Scaffold	Readout possibilities	Throughput	References
Assembled cells	Aggregates of human iPSC-derived cells (neuron)	Multi-well plates	Free-floating	Imaging, quantitative analysis	8 replicates	Mariania et al. 2012
	Spheroids from primary murine cells	Multi-well plates	Free-floating	Imaging, calcium imaging	6 replicates	Todd et al., 2013
	Organoids from patient-derived iPSCs- *Microcephaly*	Spinning bioreactor	Matrigel	Imaging, quantitative assays, calcium imaging	1 replicate	Lancaster et al., 2013
	Spheroids from primary rat cells	PDMS MF chip	Free-floating	Imaging	50 replicates	Park et al., 2015
	Neurospheres of human-derived cells	Multi-well plates	Free-floating	Imaging, patch-clamp, quantitative analysis	N/A	Paşca et al., 2015
	Aggregates of human cell lines (neurons and astrocytes)	Spinner vessels	Free-floating	Imaging	1 replicate	Terraso et al., 2016
	Neuroclusters of human-derived cells (adhered to bottom)	PDMS MF chip	Free-floating	Imaging	1 replicate	Kilic et al., 2016
	Spheroid from human-derived cell line B*rain cancer*	PDMS MF chip	PEGDA hydrogel	Imaging	1 replicate	Fan et al., 2016
	Spiral ganglion from murine primary cells	Multi-well plate	Matrigel	Imaging, quantitative analysis	4 replicates	Sun et al. 2016
	Spheroids of human derived cell-lines	Multi-well plate	Matrigel	Imaging, patch-clamp	6 replicates	Jo et al., 2016
	Brain organioids from human iPSCs- *Zika virus*	SpinΩ bioreactor	Matrigel, floating	Imaging, quantitative analysis	12 replicates	Qian et al., 2016
	Neurospheres of murine embryonic stem cell line	PDMS MF chip	Collagen, Matrigel	Imaging, quantitative assays, patch-clamp, optogenetics	1 replicate	Uzel et al., 2016
	Neurospheres of Neural progenitor cell	MEA multi-well plate	Free-floating	Imaging, quantitative assay, electron microscopy, planar MEA	48 replicates	Pamies et al., 2017
	Neurospheres of Neural progenitor cell	Multi-well plates	Free-floating	Imaging, quantitative assays	6 replicates	Pamies et al., 2018
	Organoids from human iPSCs	PDMS MF chip	Matrigel	Imaging, quantitative analysis, patch-clamp	1 replicate	Wang et al., 2018
	Neural organoids from human iPSCs	Mesh MEA device	Attached to mesh in medium	Imaging, MEA mesh	4 replicates	McDonald et al. 2020
	Human spinal cord organoid	PDMS MF chip	Collagen type I	Imaging, quantitative assay, calcium imaging, 3D MEA, optogenetics	1 replicate	Shin et al., 2021
	Spheroids from human cortical neural cells	3D multifunctional mesoscale framework (MMF)	Free-floating	Imaging, calcium imaging, 3D MEA, optogenetics, temperature measurements	16 replicates	Park et al. 2021
	Rat primary cells (neurons)	PDMS MF chip	Collagen type I	Imaging, quantitative assay, calcium imaging, 3D MEA, optogenetics	1 replicate	Shin et al., 2021

3.1.1.1 Cell type

In vivo models are time-consuming and labour-intensive. Additionally, they raise ethical concerns. Therefore, they are not suited for large-scale studies necessary for the development of NME. In an effort to fill this gap, *in vitro* models seem to be a more compatible alternative to study details about brain cell cultures. Depending on the aim of the research, diverse brain cell types derived from few species may be utilised (tables 3.1 and 3.2).

Genetically and neuroanatomically, chimpanzees hold the most significant similarity to human beings (Suntsova and Buzdin, 2020). Therefore, this primate should be considered as the species to carry out various studies. However, behavioural studies or isolation of primate brain cells are challenging to gain due to the ethical and logistical constraints (Phillips et al., 2014). Thus, cellular studies are traditionally carried out employing primary cell cultures derived from rodents (Carbone, 2004). The latter share similar neuroanatomical features that are more accessible than in primates (Batzoglou et al., 2000). *In vitro*, they may retain *in vivo* features related to morphology, functionality, and cellular interactions for weeks, making it possible to acquire detailed information for different neuroscientific research fields. Nonetheless, the level of brain complexity differs significantly from the human brain. Therefore, isolated cells from different rodent brain areas are not fully translatable to a human, and consequently, the effect of NME may vary when tested on humans in clinical trials.

With the aim of reducing the use of rodents, immortalised cell lines became popular. These type of cells are generated via senescence gene regulation, in which genes are mutated to preserve the regenerative potential (Scherer et al., 1953). Nonetheless, genetic alterations usually entail modifications in cellular morphology and functionality (Idris et al., 2018; Timmerman et al., 2018).

To avoid cellular alterations, human stem cells (hSC) may be employed. Those carry a self-renewal potential and the possibility to be differentiated into various cellular lineages while preserving the capability of forming synapses in neurons and the morphology of *in vivo* brain cells (Ylä-Outinen et al., 2004). Nonetheless, as with primate research, their accessibility is limited due to ethical constraints. As an alternative, Takahashi and Yamanaka (2006) developed reprogrammed cell lines derived from human fibroblasts, known as human-induced pluripotent stem cells (hiPSCs) (Takahashi and Yamanaka, 2006). Consequently, patient-specific brain cells may be generated while opening the possibility to closely model neuronal disorders *in vitro* (Brown et al., 2016; Pamies et al., 2017; Pamies et al., 2018; Papadimitriou et al., 2018; Park et al., 2018; Wand et al., 2018). However, similar to the immortalised cells, iPSCs may not fully preserve the cellular functionalities and show significant differences depending on the differentiation technique (Volpato and Webber, 2020). Furthermore,

reprogrammed cells might show genetic and protein variabilities, reducing the presence of intra-cell type homogeneity (Mertz et al., 2018).

Indeed, independently of what cell type is employed, the prediction capacity and the quality of the cell processes highly depend on the mono- or co-culture system in which the cells are seeded.

3.1.1.2 Culture systems

In the past years, *in vitro* models have proved relevant to further understand the CNS's underlying mechanisms. Traditional monolayers have been highly significant in recent years as they ensured higher throughput and lower experimental variation than *in vivo* models (Pan et al., 2011; Peyrin et al., 2011; Brunello et al., 2013; Habibey et al., 2015; Renault et al., 2015). Moreover, the low cost and more accessible and straightforward experimental analysis promoted an established and widespread methodology of 2D cell cultures. Specifically, for neuronal functionality, 2D neuronal cell cultures have been easily recorded as the neuronal somas attach to surfaces that might integrate recording electrodes. Despite the mentioned advantages, the simplistic monolayers do not recapitulate brain architecture because they lack fundamental physiological environments, such as the blood perfusion system or the extracellular matrix. Because of the latter, brain cells present a planar morphology as they expand only in two dimensions, limiting their inter- and intra-cell interaction. Moreover, the presence of growth factors produced may be decreased due to the fashion in which cell cultures are nurtured (media change), which may contribute to the difference in gene expression and spontaneous neuronal activity if compared to 3D models (Laplaca et al., 2010; Kim et al., 2015; Kamei et al., 2016; Papadimitriou et al., 2017; Chandrasekaran et al., 2017; Pamies et al., 2018; Papadimitriou, 2018; Tekin et al. 2018). Hence, 3D cell cultures systems have emerged with the purpose of better recapitulating brain processes.

Three-dimensional models vary among the purpose of research. Nonetheless, most of the studies are presented with the difficulty of including an ECM in their systems. The solution to this issue in most of the researches is the use of a hydrogel scaffold. Indeed, Matrigel is the most known hydrogel among scientists, as neurons' viability is the highest in that gel (Fang and Eglen, 2017; Molina-Martínez, 2020). For instance, dissociated brain cells embedded in hydrogels is the most employed technique for addressing neuronal circuits or specific pathways (table 3.1). Although crucial details may be acquired through the mentioned culture system, it still does not fully emulate brain structures. Instead, self-organised brain organoids derived from stem cells, or neurospheres (table 3.2) may be more appropriate to study brain

properties. Neurospheres are clusters of cells that adhere to each other and form a spheroid (Kempermann, 2006). Those may be or not grown in a scaffold (table 3.2). On the other hand, brain organoids are more complex clusters that self-assemble when given an extracellular environment (Lancaster et al., 2013; Amin and Paşca, 2018) such as Matrigel and are therefore more advanced than neurospheres.

All the mentioned culture systems may be used to address pathophysiological processes. However, only the brain organoid can be considered one of the narrowest interface between *in vitro* and *in vivo* neurobiology. They demonstrate a more advanced cell composition, maturation, and tissue architecture. Despite this, readout possibilities of brain organoids are somewhat limited when compared to dissociated cells. Surely, morphological readouts of the interior of compact organoids or neurospheres are challenging, and so is obtaining functional information. Therefore, readouts are mostly limited to the structures' surface, whereas with dissociated cells, morphological and functional assessments of entire networks prove to be more straightforward. Furthermore, through the 3D conformation, the cells in the core of the brain organoids or neurospheres may not be sufficiently or homogenously nurtured, leading to increased internal cell death. This issue is less relevant when employing dissociated brain cells, as the extracellular space leaves room for nutrient diffusion. Here, cells are mainly nurtured via perfusion systems or through gravity-driven flow (table 3.1).

3.1.1.3 Technical approaches for possible readouts

The development of a novel assay for the characterisation of 3D structures depends on the interrogation that wants to be addressed. Fact is that the platform in question has to provide biocompatibility, cellular outgrowth, nutrient diffusion, and a combination of diverse readouts to be considered an *in vitro* model. Undoubtedly, additional challenges, such as the design, the employed materials and the possibility of readouts, are conditioned to the cell culture system. For instance, a brain organoid that may grow up to 4 mm, cannot be supported in an nMPS compartment with a 1 mm width. Therefore, the device's design may be formatted following the width of the brain organoid. Moreover, the structure of the latter also carries specific implications for neuronal functional readouts.

3.1.1.3.1 Electrophysiology

As the hallmark of neurons is the communication via electrical signals, the biggest challenge employing any brain cell culture system may be the feasibility of neuronal functional readouts. As previously mentioned, several readouts are possible, such as intra- or

extracellular recordings, patch-clamp or Ca^{2+}-imaging (section 2.3.2). For this matter, the design of the MPS needs to be adapted. 2D nMPS are the simplest to adapt for this particular issue. Here, scientists tend to employ MEA integrated into the platform's substrate or do measurements via Ca^{2+}-imaging and sometimes even combine them (Chang et al., 2011). Moreover, the design may contain compartmentalised structures connected via microchannels (Cesare et al., 2017; Molina-Martínez, 2020), commonly utilised to study axonal transport (Uzel et al., 2016), unidirectional axonal growth (Peyrin et al., 2011; Malishev et al., 2015; Courte et a., 2018), axonal regeneration and injury (Taylor et al., 2005) or the neuronal network properties in neurological diseases (Ionescu et al., 2016; Coquinco and Cynader, 2015). Through compartmentalisation, extracellular recording electrodes may be found in the compartments themselves or inside the microchannels (Molina-Martínez, 2020). Through the latter, the sealing resistance increases, allowing the recording of electrophysiological activity from neurites instead of somas (Johnstone et al., 2010; Obien et al., 2014). Consequently, the acquired electrical information does not depend on the cell bodies' random distribution (Heuschkel et al., 2002; Soscia et al., 2020). This methodology may be applied to 3D nMPS systems (Molina-Martínez, 2020). Nonetheless, this design for recording electrical activity is not fully compatible with 3D assembled structures.

Brain organoid or spheroids can mostly be recorded from their surfaces or via invasive recordings like patch-clamp. The latter is a gold standard approach to record activity and acquire information about ion channels in neuronal cells. Certainly, it has been employed to obtain electrical findings of the core from organoids (Jo et al., 2016) or organoid slices (Paşca et al., 2015). Nonetheless, the feasibility of replication in high-performance via this technique is relatively low. Additionally, high expertise is required to carry out patch-clamp measurements. Moreover, the well in which cells are seeded needs to be wide enough to be compatible with the necessary machinery for patch-clamp, which generally reduces the device's throughput. Alternatively, a more user-friendly device produced by Shin et al. (2021) fabricated a 3D high-density multifunctional multi-shank MEA that allowed the recording of internal structures of a human spinal cord organoid via intracellular recordings (Shin et al., 2021). Nonetheless, to validate their system and study circuit dynamics, they employed dissociated rat neuronal cells embedded in a hydrogel. Ultimately, the presented device included high-density and large-scale electrical recording capability, a 3D volume, local optical stimulation, and drug delivery capabilities (Shin et al., 2021). However, the system also performed invasive recordings and showed a low reproducibility rate. On the contrary, Park et al. (2021) developed a novel high-throughput 3D "multifunctional mesoscale framework" (MMF) for studying broad aspects of neuronal assemblies. They produced a system able to record superficial electrophysiological activity, neuromodulate via optogenetics, identify the

culture media's and the neural spheroid's temperature via an integrated thermal actuator, and monitor oxygen concentration via an electrochemical sensor (Park et al., 2021). Although this design proves to be very advanced, it still does not support morphological or functional readouts from the assemblies' inner core.

Therefore, many kinds of research still focus on employing dissociated neurons to study network's properties. Also, those cell culture systems are less time consuming to grow than organoids. Although most of the available systems still rely on Ca^{2+}-imaging, some studies employ platforms with 3D MEAs. One example is the previously mentioned multi-shank MEA, where dissociated rat neurons prevail freely in a hydrogel scaffold (Shin et al., 2021). A less invasive technique was produced by Soscia et al. in 2020, where dissociated 3D neurons surrounded 3D vertically-positioned microelectrodes. However, the activity recorded depended on the somas' proximity to the electrodes and therefore showed a small percentage of active electrodes. Additionally, the reproducibility rate is relatively low.

The mentioned technical approaches were designed to acquire more information about neuronal assemblies and neuronal circuits and will probably contribute to the already broad studies focusing on disorders affecting the CNS employing these cell culture systems (Cugola et al., 2016; Garcez et al., 2016; Qian et al., 2016; Kim et al., 2019; Cairns et al., 2020) However, a factor that should be included to understand the CNS mechanisms is neuroinflammation, which plays a significant role in those diseases.

3.1.1.3.2 Neuroinflammation

Motility and phagocytosis are some of the hallmarks of microglia functionality. Therefore, most studies focus on microglial migration and the transformation of ramified resting µG to active and motile microglia. Those need to be studied in detail upon activation. Assembled cell types, such as organoids, carry the disadvantage of preventing morphological assessments from the inner core. Therefore some studies acquire brain organoid slices to determine the morphological alteration of microglia (Xu et al., 2020). However, the microglia motility in the inner core is rather complex to examine in assembled brain cells. Therefore, some studies focus on co-culturing dissociated brain cells with microglia.

For instance, in 2018, Park et al. designed a platform in which dissociated human-derived neurons and astrocytes were separated from immortalised human microglia through compartmentalisation (Park et al., 2018). However, both cultures were still connected via microchannels. Motility and phagocytosis of stained activated microglia could be observed quickly via a microscope, and increasing inflammatory cues were detected through ELISA kits.

By combining both readout techniques, custom-designed compartmentalisation and the analysis of morphological traits, the device has the potential to study human-like neuroinflammation. Although this system also allowed the measurement of transient Ca^{2+} in neurons, this platform's main drawback was the lack of electrophysiological recordings that could give more accurate and direct insights into the neuronal circuit dynamics in neuroinflammation. Moreover, for the platform's construction, they employed a silicon-based material (Polydimethylsiloxane, PDMS).

3.1.1.3.3 Materials

PDMS is commonly utilised due to its gas permeability, non-cytotoxicity, transparency, and low cost (Ren et al., 2013) (tables 3.1 and 3.2). Moreover, it is appropriate for the fast evaluation of suitable nMPS designs for specific studies. In this manner, any form of the platform may be estimated in a short time and modified accordingly. Additionally, PDMS structures can be easily attached to thin glass substrates, allowing high-resolution morphological studies or to thick glass integrating recording electrodes for neuronal functional readouts (Habibey et al., 2015; Martínez-Molina, 2020). However, previous studies have reported that cell cultures may behave differently in the presence of PDMS (Łopacińska et al., 2013; Mehling and Tay; 2014.). Moreover, it is known to absorb hydrophobic compounds, making its use unreliable when studying the effect of NME (Ren et al., 2013).

Surely, *in vitro* models need to employ transparent materials to be able to monitor cellular health. An alternative to the easily customisable PDMS on top of glass substrates is polystyrene (PS), a standard substrate for cell cultures for over 50 years (Rubin, 1966). PS may be formed via electrospinning or 3D printing and may be applied for angiogenesis, chemotaxis, super-resolution microscopy and others (Godbe et al., 2020; Zengel et al., 2011). However, this material is not the most appropriate material for producing micrometre resolution patterns for wells or compartments nor integrating recording electrodes. Therefore, substrates integrating MEAs are made of glass (Molina-Martínez, 2020). As glass does not absorb drug compounds, is biocompatible, stable, transparent, and has a low conductivity, it is highly suitable for drug screening, morphological and electrophysiological readouts and may be reused. Furthermore, for micrometre resolution patterns in the platform's compartments, selective laser-induced etching (SLE, FEMTOprint, Switzerland) can be applied to the microfluidic component. Nonetheless, no other 3D glass nMPS with integrated electrodes for extracellular recordings of neuronal circuits exists to this day. The reason for this may be the complex bonding procedure if, for instance, recording electrodes are contained in microtunnels connecting two compartments (Cesare, 2016; Molina-Martínez, 2020) or the cost to produce

glass microfluidic pieces. Also, MEA integrated into a glass substrate is not cost-efficient either and limits the throughput of the platforms to the number of recording electrodes. The latter may have a significant impact on large-scale studies, where high-throughput devices are preferred.

3.1.1.3.4 Throughput

For nMPS to be used in large-scale studies, the throughput to carry out multiple experiments simultaneously needs to be increased. Additionally, the device should be cost-efficient and compatible with multiple standard readouts. One of the companies that overcomes these issues is the company MIMETAS (Netherlands). They developed an *in vitro* system made of plastic that allows simultaneous cell seeding in 3D up to 96 times (Wevers et al., 2016), making the system appropriate for large-scale studies with multiple readouts. However, the functional neuronal readout relies on imaging techniques and not electrophysiological recordings. Furthermore, the cell types and cell culture systems seeded in this device are limited due to its design. Alternatively, the previously mentioned MMF (Park et al. 2021) seems to be appropriate for large-scale studies with the ability to monitor up to 16 spheroids in parallel and provide a more diverse range of readouts. Thanks to the latter and the possibility of characterizing neurospheroids and probably brain organoids, this *in vitro* platform may give a broader insight into CNS mechanisms.

To conclude, diverse platforms combine multiple readouts and designs for specific cell types and cell culture systems that could potentially serve as assays for drug screening, neuroinflammation, cellular interactions or neuronal circuit dynamics (see tables 3.1 and 3.2). Nonetheless, several challenges are still to be faced in this emerging field.

3.2 Challenges

The biggest challenge to be fulfilled is translating 2D *in vitro* readouts enhanced throughout the past decades into 3D models to obtain more accurate detailed information about brain processes and using those for drug development in large-scale studies, ultimately decreasing the CNS drug development failure rate. Compared to other failure rates, the one of CNS compounds is the largest (Dowden et al., 2019). The main reason for increased attrition rates is the limited understanding of the CNS that leads to lower efficacy and safety rates, demonstrating the inability to prove a significant effect of a compound and the presence of adverse consequences, respectively (Fogel, 2018). Due to the last mentioned, for NME to be accepted, additional controls must be performed to test a CNS compound's safety (Accardi et al., 2016).

Therefore, the pharmacological industry relies on predictive CNS models. As guidance, the European Organ on Chip Society (EuroOoC) encouraged specific requirements for the production and validation of OoC that are also fitting with other 3D neuronal models (Mastrangeli et al., 2019). One fundamental feature for the latter is the flexibility of the device for multiple applications. Electrophysiological recordings are significant as the decrease in neuronal networks' activity or malfunctioning ion channels in neurons is one of the first characteristics of neurodegenerative diseases exhibited as memory loss, tremor rigidity and others (Kalia and Lang, 2015). Moreover, mechanisms accountable for those outcomes need to be studied with human models to reduce the translation effect from animal models to humans. Here, variability responses arising through gender, genetic background or epigenetic modifications also need to be anticipated and, if possible, reduced via personalised medicine for single patients (Schork, 2015; Fogel, 2018). Furthermore, experiments in 3D *in vitro* models should be highly reproducible. They should be compatible with high-throughput screening (HTS) for performing large-scale studies, additionally sustaining samples for long-term measurements. To this day, systems including all recommendations are limited. Therefore, during this study, a neuro-microphysiological system was developed considering a diversity of cell types, cell culture systems, and technical approaches.

For the validation of the nMPS, murine embryonic dissociated neurons, astrocytes and microglia were embedded in a hydrogel scaffold. To support their survival, an open quartz microfluidic chip was designed and bonded on top of a glass substrate, which allowed the seeding of a controlled cell density and the supply of nutrients in a gravity-driven flow. Due to the transparency of the device, multiple imaging techniques may be applied. Cell cultures can be monitored via live-cell imaging or also labelled with antibody markers. Additionally, neuronal activity may be assessed via Ca^{2+}-imaging or modulated through optogenetic techniques.

More importantly, for greater insight into neuronal circuits, this device integrates MEA in the glass substrate. Here, the principle of the electrodes inside microchannels was applied. This technique was already examined in a previous study (Cesare, 2016; Molina-Martínez, 2020), in which two compartments of 3D neurons were connected via microtunnels containing recording electrodes. Neurites grew through the microtunnels and were ultimately recorded. Finally, to simplify the device and its production, instead of having microchannels connecting two compartmentalised 3D cell cultures, recording electrodes were integrated into the bottom of the 3D co-culture. As neuronal somas are homogeneously dispersed in 3D far away from the recording electrodes, the latter needed to be covered with a cap (capped microelectrode, CμE) containing microtunnels that allowed the growth of neurites close to the electrode. Through the increased sealing resistance provided by the microtunnels, 3D neuronal network

activity could be recorded from neurites. Accordingly, electrophysiological activity was able to be assessed simultaneously with Ca^{2+}-imaging or optogenetics. Moreover, neurotoxicity tests employing reference or inflammatory compounds could be performed. Furthermore, to study cues released from cells, retrieval of cells through the hydrogel degradation or collection of supernatant for protein analysis is feasible.

To employ this system for large-scale studies, the device was designed to simultaneously perform 12 or 18 independent experiments and is fully compatible with ANSI/SLAS standards. Consequently, this system was also employed for large-scale imaging in an automated system (Stella Donato, DZNE).

Although this system was validated with murine dissociated cells, this nMPS showed the possibility of recording neuronal activity from human iPSCs (Stella Donato, DZNE) and neurospheres (Dominik Loser, NMI). Therefore, the introduced 3D cell culture model counts as a multidisciplinary approach to model neuronal networks and potentially neuroinflammation, fulfilling most of the EuroOoC requirements.

4 Material and methods

4.1 Cell type

For the validation of this system, primary murine hippocampal and microglial cells were employed. For this purpose, pregnant Swiss strain mice were provided from Janvier Labs (France) and kept in the animal facility of the Natural and Medical Science Institute (NMI) until the day of the experiment. Mice were placed in individual cages (GM500 for Mice and DGM, Tecniplast Group, Germany) containing bedding, a toy house, food, water, soft paper and cotton balls. Simultaneously, a filter system monitored the ventilation system (Smart Flow AHU, Tecniplast Group, Germany) in a 12-h light-dark cycle. Cages were cleaned every 3 to 4 days, and mice were transferred into new, clean cages. Mice were treated following the European Union (EU) legislation for the care and use of laboratory animals (Directive 2010/63/EU, of the European Parliament on the protection of animals used for scientific purposes, German TierSchG (Tierschutzgesetz) with latest revision 2019 (TierSchG, 2019)).

4.1.1 Primary hippocampal neurons and astrocytes

Primary hippocampal neurons and astrocytes (N+AS) were isolated from embryonic Swiss mice (RjOrl:SWISS) at E16/17 based on previous protocols (Piondron et al., 2005; Kaech and Banker, 2006; Seibenhener and Wooten, 2012) and always under sterile conditions. Pregnant mice were euthanised with CO_2 and sprayed with ethanol 70% before placing it on the preparation bench. Subsequently, embryos were removed from the female's uterus after performing a mid-ventral opening using dissecting sterile scissors and tweezers. They were then placed in a Petri dish containing pre-cooled Hank's Balanced salt solution -/- (HBSS-/-) (14170112, Thermo Fisher Scientific, MA, US). Then, embryos were released from the embryonic sack and placed into a new Petri dish under the dissecting microscope (SMZ-171, Motic, Hong Kong) and were decapitated using a scalpel (0205, scalpel blades No.15, Swann-Morton, UK) (figure 4.1). Embryo's brains were thereafter dissected with tweezers and a scissor by performing a posterior-anterior cut in the embryo's skull. Brains were ventrally detached from the skull and then transferred into a new Petri dish with cooled HBSS -/- before cutting transversally in order to visualise the hippocampi after removing the cerebellum (figure 4.1). To visualise the dark and curved structure corresponding to the hippocampi in the apical part of the cerebral hemispheres, the meninges were removed with two micro tweezers. Then, hippocampi were extracted by cutting around the structure with two micro tweezers and were transferred into a 15 ml falcon tube containing pre-cooled HBSS -/- to proceed with the enzymatic digestion by following the protocol available in the Neural Dissociation Kit T (130-093-231, Miltenyi Biotec GmgH, Germany). Once N+AS were dissociated, they were filtered

(MAC SmartStrainer of 70 µm (130-098-462, Miltenyi Biotec GmgH, Germany) in a filtering medium containing Neurobasal + (NB+) (A3582901, Gibco), 0.5 % penicillin-streptomycin (P/S) (P4333, Sigma-Aldrich) and 10% of fetal bovine serum (FBS) (10082139, Thermo Fisher Scientific, MA, US) (table 4.1). Subsequently, cells were centrifuged at 300g for 5 min at RT.

Depending on the final cell culture type, the pellet was reconstituted in different media. For a bi-cultivation of neurons and astrocytes (BiC), a plating medium (PM -/-) containing NB+, 2 % of SM1 (5711, STEMCELL Technologies) and 0.5 % P/S was used (table 4.2). Cells were then counted with the Nucleocounter (NucleoCounter® NC-200TM, ChemoMetec A/S, Denmark) to proceed with the cell seeding into different devices.

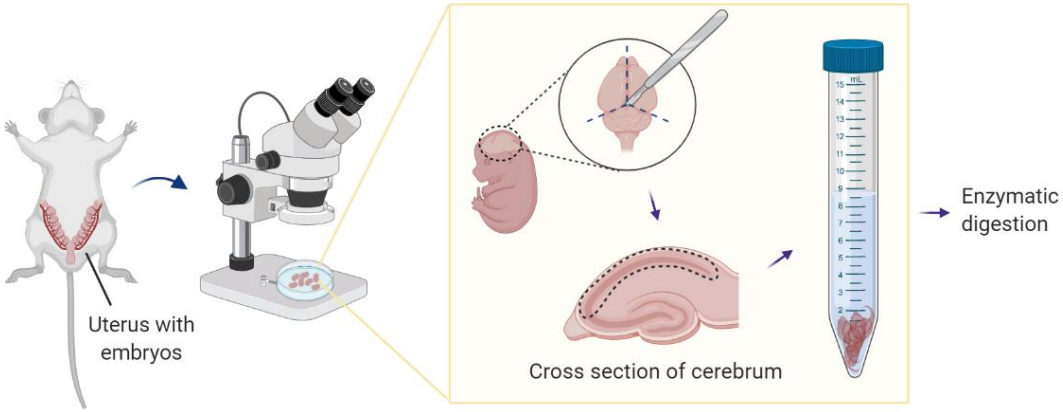

Figure 4.1: Isolation of murine hippocampi. Embryos of a pregnant mouse were transferred into a Petri dish with pre-cooled HBSS -/- to extract the brains. Cerebral hemispheres and their meninges were removed from the brain to visualise the hippocampus. Hippocampus was extracted and transferred into a 15 ml falcon tube to proceed with the enzymatic digestion (created with BioRender.com).

Table 4.1: Filtering medium. Medium employed during neuronal isolation.

Filtering medium	**Dilution/ concentration**	**Catalogue number**
Neurobasal Plus™ Medium		A3582901, Gibco, Thermo Fisher Scientific, MA, US
Fetal Bovine Serum	1:10	10082139, Thermo Fisher Scientific, MA, US
Penicillin-Streptomycin	1:200	P4333-20mL, Sigma-Aldrich, Merck KGaA, Germany

Table 4.2: Plating medium for bi-cultures. Medium employed for cell seeding in cultures only containing neurons and astrocytes.

Plating medium -/- (PM -/-)	**Dilution/ concentration**	**Catalogue number**
Neurobasal Plus™ Medium		A3582901, Gibco, Thermo Fisher Scientific, MA, US
SM1 Neuronal Supplment	1:50	5711, STEMCELL Technologies Inc., Germany
Penicillin-Streptomycin	1:200	P4333-20mL, Sigma-Aldrich, Merck KGaA, Germany

4.1.2 Primary microglia

Isolation of microglia was achieved by following the protocol of García-Agudo et al. (2019). Brains from postnatal day 1 or 2 were dissected, freed from meninges and minced before digestion with trypsin and EDTA 0.05% (T4049, Sigma). Brains were then transferred into a 50 ml tube and incubated for 10 minutes inside a water bath (37°C). Five minutes before and after the incubation, minced brains were vortexed (MS1 minishaker, IKA works inc., Wilmington, North Caroline, US) for 15 seconds to promote the dissociation of cells and avoid neurons' survival.

To stop the enzymatic digestion, microglia plating medium (MPM) (table 4.3) containing DMEM (41965039, Thermo Fisher Scientific) with 10% horse serum (HS) (26050070, Thermo Fisher Scientific) and 0.5% P/S was added to the brains besides 400 IU/ brain of DNase I (LS002139, Cell Systems). With the purpose of enhancing cell dissociation, samples were thereafter incubated for 2 to 3 minutes and then mechanically triturated using a 5 ml glass pipette (606-160, Greiner Bio-One GmbH, Germany). Once completed, cells were centrifuged (10 min, 150 g, RT) and plated in a Poly-D-Lysine (PDL)-coated (50 µg/ ml) (P7280, Sigma) 75 cm² flask (431464U, Corning Incorporated, MA, US). Cells were finally incubated at 37°C and 5 % CO_2. The medium was changed after 1 and 2 days in vitro (DIV). To promote microglial growth, cells were stimulated with L-929 conditioned medium (LCM) (1:3) after 4 DIV and 7 DIV. Cells were harvested after 9 or 11 DIV by manually shaking the flask. After sorting the cells via flow cytometry, pure microglia were seeded in culture together with neurons and astrocytes (ratios 1:4 and 1:8).

Table 4.3: Microglia plating medium. Medium employed during microglial isolation.

Microglia plating medium (MPM)	**Dilution/ concentration**	**Catalogue number**
DMEM, high glucose		41965039, Thermo Fisher Scientific, MA, US
Horse Serum	1:10	26050070, Thermo Fisher Scientific, MA, US
Penicillin-Streptomycin	1:200	P4333-20mL, Sigma-Aldrich, Merck KGaA, Germany

4.1.2.1 Flask coating

T 75 flasks were coated with 50 µg/ ml PDL for 30 minutes at 37°C and 5% CO_2. PDL was washed out once with 10 ml of ddH_2O per flask and left to dry for approximately 2 hours. Then, 10 ml of MPM was added into the flask and incubated at 37°C until cell seeding.

4.1.2.2 L929 fibroblasts

L-929 mouse fibroblasts (kindly provided by H. Ehrenreich's Laboratory at the Max Planck Institute of Experimental Medicine, Göttingen; L929/R (ECACC 04102001)) were seeded in 75 cm² flasks at a density of 470.000 cells and incubated in L-929 plating medium (LPM) (DMEM, 1% P/S, 10% FBS) (table 4.4) for seven days at 37°C and 5% CO_2. L-929 conditioned medium in flasks was collected, filtered through a 0.22 µm filter and stored at -20°C until used.

Table 4.4: L-929 plating medium. Medium employed for microglia proliferation.

L-929 plating medium (LPM)	**Dilution/ concentration**	**Catalogue number**
DMEM, high glucose		41965039, Thermo Fisher Scientific, MA, US
Fetal Bovine Serum	1:10	10082139, Thermo Fisher Scientific, MA, US
Penicillin-Streptomycin	1:100	P4333-20mL, Sigma-Aldrich, Merck KGaA, Germany

4.1.2.3 Fluorescence- activating cell sorting (FACS)

To ensure the purity of microglia, the latter were stained with a marker specific for microglia, CD11b (Invitrogen, 11-0112-81) (1:100), and finally filtered through a fluorescence-activating cell sorting (FACS) machine (BD FACSMelody Cell Sorter, BD Biosciences). For this purpose, cells were first shaken off the flask after 9 or 11 DIV and centrifuged (10 min, 150 g, RT). To avoid non-specific binding of the immunoglobulin to Fc receptors, samples were

incubated with CD16/32 (Invitrogen, 14-0161-82) (1:100) in staining buffer (table 4.5) composed of phosphate-buffered saline DPBS -/- (14190250, Gibco) with 3 % Bovine Serum Albumin (BSA) (A7979, Sigma-Aldrich) for 20 min at 4°C. After washing the sample with washing buffer (PBS -/-, 1 % BSA) (table 4.6), cells were centrifuged (10 min, 150 g, RT) and stained for microglia using antibody CD11b via a 20-minute incubation at 4°C (table 4.7). For dead cell exclusion, a 7-AAD viability staining solution (Biolegend, 420403) (5 µl per million cells) mixed in staining buffer was employed (10 min in the dark at RT). Before cell sorting, samples were washed and centrifuged again (5 min, 300 g, RT). Subsequently, samples were re-suspended in 300 µl staining buffer and ran through the cell sorting instrument. The latter was previously set up and started by following several steps. First, the fluidics start-up was carried out, and then the stream was optimised. After, the machine's performance was checked using beads (CSandT RUO Beads, 661414, BD Biosciences, (1:250); Accudrop beads, 345249, BD Biosciences, (1:500)). Then, experiments were set up to sort microglia stained with CD11b. For this, cells were categorized into several graphs. First, the area of the cells was defined by the forward scatter channels(FSC), and the side scatter channel (SSC). Singlets were defined with both FSC and SSC scatter plots characterizing the cells' width and height. Subsequently, a scatter plot excluded cells that were not stained with 7AAD (dead cells) and cells were then categorized into stained vs unstained histogram. Cells were finally sorted into a glass tube containing 500 µl of plating medium (PM +/+) for tri-cultures (TriC) (table 4.8), containing 2 % of SM1, 0.5 % P/S, interleukin-34 (IL-34) (100 ng/ ml, Peprotech, 200-34) and transforming growth factor-beta 2 (TGF-ß2) (2 ng/ ml, Peprotech, 100-35B). Ultimately, selected microglia were centrifuged for 5 min at 300 g, re-suspended in PM +/+ and counted with Nucelocounter.

Table 4.5: Staining buffer. Buffer employed to mark microglia with antibodies CD16/32 and CD11b, and dye 7-AAD.

Staining buffer	**Dilution/ concentration**	**Catalogue number**
DPBS -/-		14190250, Gibco, Thermo Fisher Scientific, MA, US
Bovine Serum Albumin	3:100	A7979, Sigma-Aldrich, Merck KGaA, Germany

Table 4.6: Washing buffer. Buffer used to wash out remaining antibodies and dye.

Washing buffer	**Dilution/ concentration**	**Catalogue number**
DPBS -/-		14190250, Gibco, Thermo Fisher Scientific, MA, US
Bovine Serum Albumin	1:100	A7979, Sigma-Aldrich, Merck KGaA, Germany

Table 4.7: Antibodies/dye for microglia sorting. Antibodies CD16/32 and CD11b, and dye 7-AAD employed for posterior microglia sorting. M= mouse, R= rat.

Antibodies/ dye	Clonality	Reactivity	Host	Concentration	Catalogue number
CD11b (M1/70), FITC, eBioscience™	monoclonal	M	R	1:100	11-0112-81, Thermo Fisher Scientific, MA, US
CD16/CD32, eBioscience™	monoclonal	M	R	1:100	14-0161-82, Thermo Fisher Scientific, MA, US
7-AAD Viability Staining Solution	N/A			5 µL/ 1 million cells	420403, 9 BioLegend Way, San Diego, CA, US

Table 4.8: Plating medium for Tri-cultures. Medium employed for cell seeding in cultures containing microglia.

Plating medium +/+ (PM +/+)	Dilution/ concentration	Catalogue number
Neurobasal Plus™ Medium		A3582901, Gibco, Thermo Fisher Scientific, MA, US
SM1 Neuronal Supplment	1:50	5711, STEMCELL Technologies Inc., Germany
Penicillin-Streptomycin	1:200	P4333-20mL, Sigma-Aldrich, Merck KGaA, Germany
Interleukin-34 (IL-34)	100 ng/ml	200-34, Peprotech, New Jersey, US
Tumour growth factor β2 (TGFβ2)	20 ng/ml	100-35B, Peprotech, New Jersey, US

4.2 The 3D cell culture system

In order to have a more physiologically relevant in-vitro cell culture, neurons, astrocytes and microglia were seeded in systems that allowed their outgrowth in 3D. For this purpose, cells were embedded in a hydrogel and cultured in two types of systems, the multi-well µ-slide plates and the nMPS.

4.2.1 3D cell seeding

For the 3D cultures, the hydrogel Matrigel Matrix (356230, Grow Factor Reduced Matrigel® matrix, Corning Incorporated, MA, US) was used to provide the cells with a scaffold necessary for their outgrowth. Additionally, this hydrogel has the advantage of remaining liquid when handled in cold temperatures but starts polymerising at temperatures above 10°C. Thus, to avoid an early polymerisation, Matrigel was thawed at 4 to 6°C and kept at this temperature

during the entire cell seeding process. For this purpose, a cooled metal rack (CoolRack® M30-PF, BioCision, CA, US) placed in an insulating box (CoolBox® 30 System, BioCision, CA, US) containing an ice block (Cool Rack M30 PF, BioCision, CA, US) was used. For the cell seeding, the cell solution was mixed with the hydrogel in 1.5 ml tubes at a ratio of 1 to 3 (75 % matrigel). Before plating the cells inside the device, the latter was placed on a metal block (CoolSink® XT 96F, BioCision, CA, US) under the binoculars (SMZ-171, Motic, Hong Kong) to maintain the cold temperatures.

All used 3D systems consisted of a minimum of two layers, the gel layer (GL) and the liquid layer (LL). Each gel lane was designed so that the liquid dispensed inside was subjected to surface tension, which avoided the liquid's overflow to the LL. In this manner, the cell solution could be pipetted into the GL of the utilised system and placed upside down inside a humidified Petri dish. This procedure ensured a homogeneous distribution of the cells inside the gel lane and avoided the cells settling down on the substrate of the devices. Subsequently, samples remained at 37°C for 10 min to promote the polymerisation of the gel. Immediately after, cells were nurtured with 50 µl of plating medium (PM -/- or PM +/+), and the device was incubated at 37°C.

Neurons and astrocytes were co-cultured at a total concentration of 3000 cells per µl. For the tri-culture, neurons and astrocytes were seeded at a density of 3000 cells per µl. Instead, microglia were co-cultured at either 750 or 375 cells per µl, achieving a final ratio of 4 or 8 N+AS per microglia, respectively. The plating medium was changed every 2 to 3 days and replaced by an enhancing medium after 4 or 5 DIV. Bi-culture enhancing Medium (EM -/-) (table 4.10) was composed of BrainPhys (05790, STEMCELL Technologies) containing 2 % of SM1 and 0.5 % of P/S and used for the co-culture of astrocytes and neurons. The same components were contained in the enhancing medium (EM +/+) (table 4.11) primarily employed for tri-cultures, however, in addition to IL-34 (100 ng/ml) and TGF-ß2 (2 ng/ml). This medium was only employed for tri-culture studies.

Table 4.9: Enhancing medium for bi-cultures. Medium employed after 4-6 DIV in cultures only containing neurons and astrocytes.

Enhancing medium -/- (EM -/-)	**Dilution/ concentration**	**Catalogue number**
BrainPhys™ Neuronal medium		05790, STEMCELL Technologies Inc., Germany
SM1 Neuronal Supplment	1:50	5711, STEMCELL Technologies Inc., Germany
Penicillin-Streptomycin	1:200	P4333-20mL, Sigma-Aldrich, Merck KGaA, Germany

Table 4.10: Enhancing medium for Tri-cultures. Medium employed after 4-6 DIV in cultures only containing neurons and astrocytes.

Enhancing medium +/+ (EM +/+)	**Dilution/ concentration**	**Catalogue number**
BrainPhys™ Neuronal medium		05790, STEMCELL Technologies Inc., Germany
SM1 Neuronal Supplment	1:50	5711, STEMCELL Technologies Inc., Germany
Penicillin-Streptomycin	1:200	P4333-20mL, Sigma-Aldrich, Merck KGaA, Germany
Interleukin-34 (IL-34)	100 ng/ml	200-34, Peprotech, New Jersey, US
Tumour growth factor β2 (TGFβ2)	20 ng/ml	100-35B, Peprotech, New Jersey, US

4.2.2 Ibidi Multi-well µ-Slide plates

The multi-well µ-slide plates (81506, ibidi GmbH, Germany) were mainly used to establish cell seeding protocols or study the morphology of the cultures before employing the nMPS. Using this system allowed to perform 15 independent experiments, each allowing a cell and medium volume of 10 and 50 µl, respectively (figure 4.2). The GL was 800 µm tall and 4 mm wide, and the LL was 2.5 mm high and 5 mm wide. Cells were kept at 37°C with 5% CO_2 until 7 to 8 DIV.

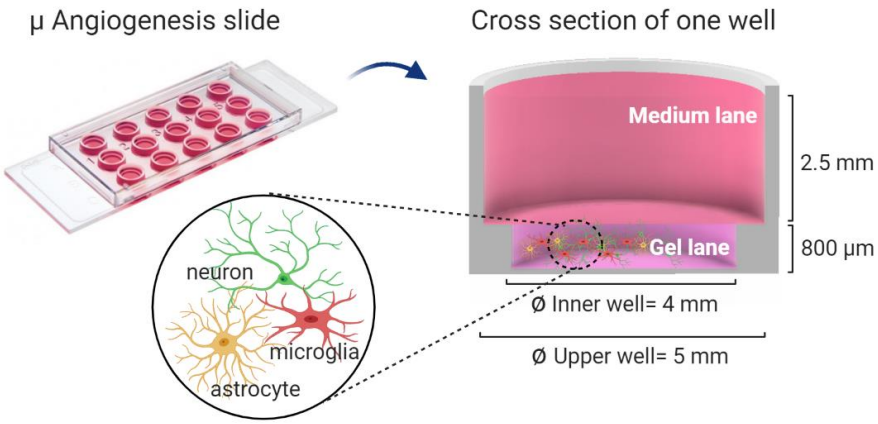

Figure 4.2: Multi-well µ-slide plate and cross-section of one well. The system used to perform 3D cell culture containing 15 independent experiments. A cross-section of one well shows neurons, astrocytes and microglia present in the inner well embedded in Matrigel and medium in the upper well. The inner well holds a volume of 10 µl, while the upper well is filled with 50 µl of the medium. Adapted from www.ibidi.com and created with BioRender.com

4.2.3 The nMPS

For the purpose of studying the cellular morphology and functionality, two nMPS were developed and designed in collaboration with Dr Peter Jones' laboratory at the NMI in Reutlingen (Biomedical Micro and Nano Engineering Group). The preceding version, 12-well nMPS (12nMPS), was primarily employed to validate the system, while 18-well nMPS (18nMPS) was mainly used for the tri-culture studies.

The devices are composed of two elements: a pre-designed microfluidic piece and a glass substrate containing the self-arranged microelectrode arrays connected to contact patches. Those link the MEA to the recording system (USB-MEA256System, Multi Channel Systems MCS GmbH, Germany). Both components are ultimately bonded and, together, they form the nMPS. The two final produced devices carried different features in each of the two components. In 12nMPS, 21 CµE were arranged in each of the 12 independent wells, whereas only 14 CµE were viable in the 18 separate channels of 18nMPS (figure 4.3). Despite these dissimilarities, both underwent the same microfabrication processes.

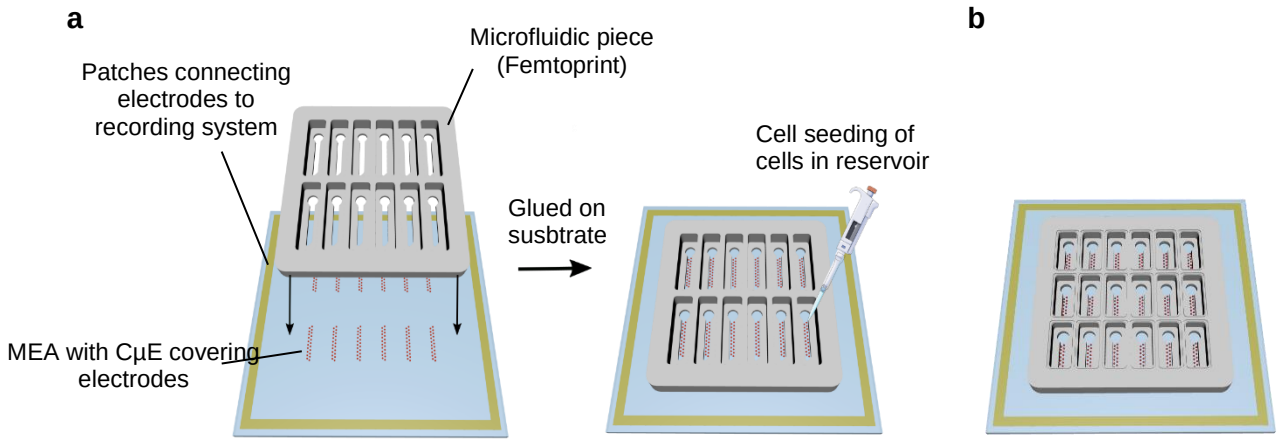

Figure 4.3: Devices 12nMPS and 18nMPS. 12 nMPS was used to perform functional and morphological analysis of 3D cell cultures holding 12 independent experiments. The microfluidic piece was glued on top of a glass substrate containing 21 CµE (a). 18nMPS englobes 18 independent experiments, each carrying 14 CµE (b). (Partly created with BioRender.com).

4.2.3.1 MEA design and production

The production of the MEAs was performed by the NMI TT (NMI Technologietransfer GmbH, Microdevices, Germany), while the electrode arrangement was designed with the CleWin 5 software (WieWeb software, the Netherlands) by colleagues from the NMS group at the NMI with the help of Dr Peter Jones from the Biomedical Micro and Nano Engineering

Group at the NMI (figure 4.4). 256 30 µm-long and round electrodes were based on a 49 x 49 mm glass substrate (1 mm thick) and arranged according to the device version. In the 12nMPS, electrode arrays were organised so that each of the independent experiments contained 21 recording electrodes, while in the 18nMPS, each well incorporated 14 electrodes (figure 4.4). Each of the latter was separated by a 200 µm pit. Electrodes were gold, whereas conduction paths and contact pads were made of indium tin oxide (ITO) and insulated with silicon nitride (SiNx) (Hämmerle et al., 1994).

All CµE components were designed (CleWin 5 software (WieWeb software, the Netherlands)) and manufactured by colleagues from the NMS group who performed in the NMI cleanroom facility. The caps were comprised of two epoxy photoresist materials, a 3 µm thick SU-8 structure (SU-8 2002 (MicroChem, MA, USA)) containing 5 µm wide microtunnels and a 20 µm thick ADEX cap (ADEX^{TM} TDFS A20 (Micro Resist Technology GmbH, Berlin, Germany)), posteriorly laminated on top of the SU-8 layer (figure 4.5). In order to produce these capping structures, the latter underwent steps of lamination and photolithography. Firstly, to activate the surface of the MEA substrate, they were pre-treated with oxygen plasma (2 min, 310-320 V, 1800 mPa) (PECVD, Piccolo, Plasma Electronic GmbH, Germany) and baked for 1 h at 150°C (Memmert GmgH and Co., KG, Germany). Then, a SU-8 layer was spin-coated (10 s at 500 rpm, then 30 s at 1000 rpm) (Spin-coater Convac 1001, ST 146) on top of the MEA and afterwards baked (5 min at 95°C on a hotplate, ramped up and down at 0.5°C/ min). To have a specific SU-8 pattern surrounding the electrodes on top of the MEA, a pre-designed chrome-on-glass photomask purchased from Delta Mask B.V. (Enschede, the Netherlands) was employed during the exposure period (250 mJ/cm², ca. 20 s, i-line, soft contact). Succeeding the exposure, a post-exposure bake, identical to the pre-exposure bake, was carried out to ensure the cross-linking of the structures. The SU-8 layer was developed for 15 s by employing a SU-8 developer (mr dev 600, Micro Resist Technology GmbH, Berlin, Germany) and finally rinsed with isopropanol. In order to avoid an overdevelopment of the SU-8 in successive steps consisting of more extended development periods and cyclohexanone, the SU-8 layer was further cross-linked by a final 30 min hard bake at 150°C.

Once the SU-8 layer was attached on top of the MEA, a dry film resist ADEX-foil was laminated on top of the substrate at 3 mm/s and 78°C and exposed at 600 mJ/cm^2 (i-line, 10 µm proximity exposure). Similar to the exposure of SU-8, a pre-designed chrome-on-glass photomask was utilized to acquire a specific pattern of ADEX on top of the SU-8 layer. After, substrates were baked for 1 h at 65°C and developed by rinsing in cyclohexanone twice for 4 minutes and twice for 2 and 1 minute in isopropanol. Subsequently, MEAs were dried with nitrogen gas. Lastly, to complete the cross-linking of epoxy-resins (Jones, 2017) and preventing toxicity (Baëtens

et al., 2020), substrates were hard-baked at 170°C for 30 min (ramping up and down at 0.5 °C/min).

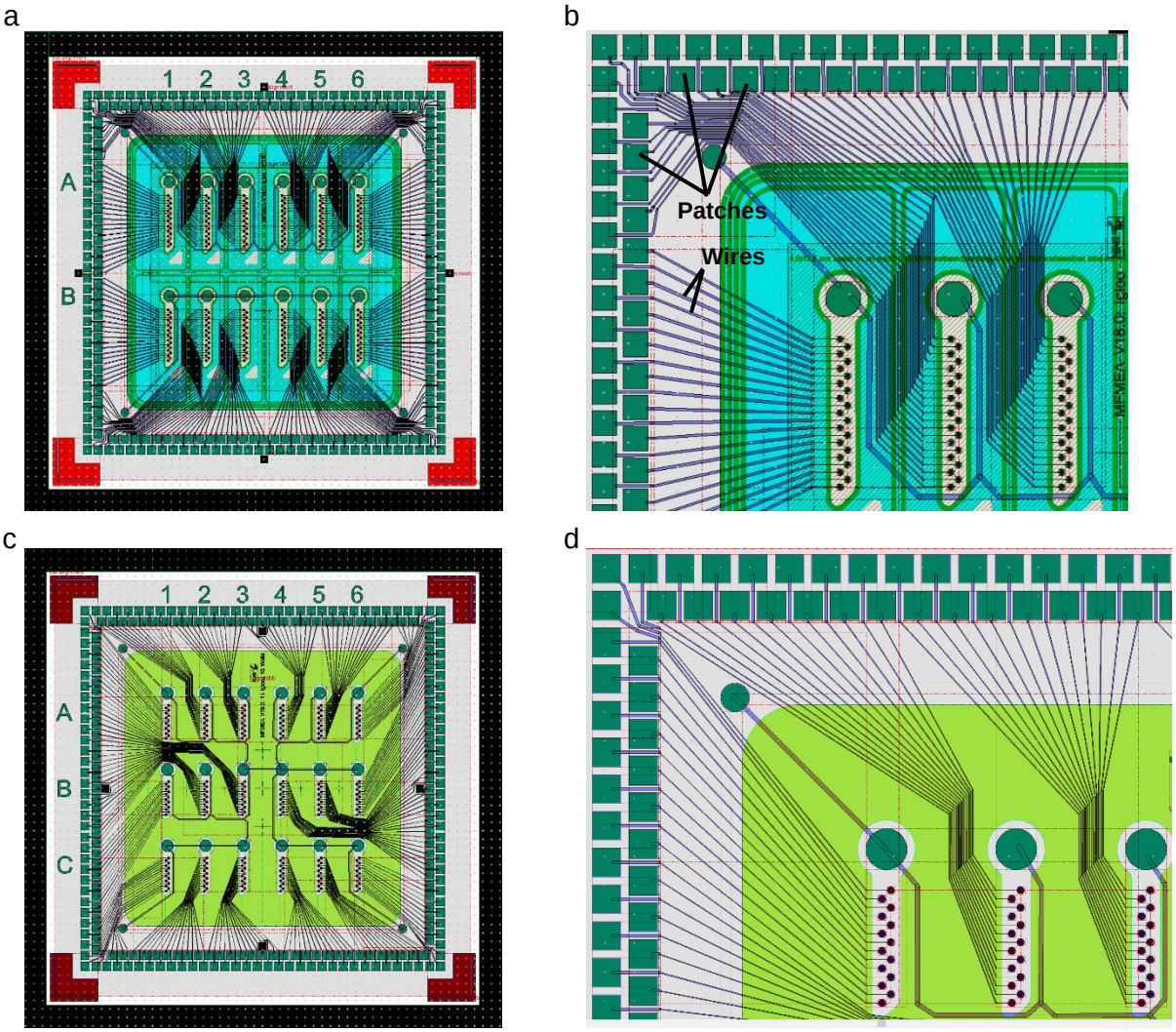

Figure 4.4: Wire map of electrodes connected to contact patches. Wires connect electrodes to patches located in the edge of the MEA in 12nMPS (a and b) and 18nMPS (c and d).

CµE production for both 12nMPS and 18nMPS was executed identically, but they carried different SU-8 patterns inside the CµE. In the 12nMPS, electrodes were surrounded by 6 microtunnels branching out to final 24 entries, whereas in the 18nMPS, electrodes were also surrounded by 6 microtunnels but branching out to final 12 entries (figure 4.6). Both CµE diameters were 250 µm wide.

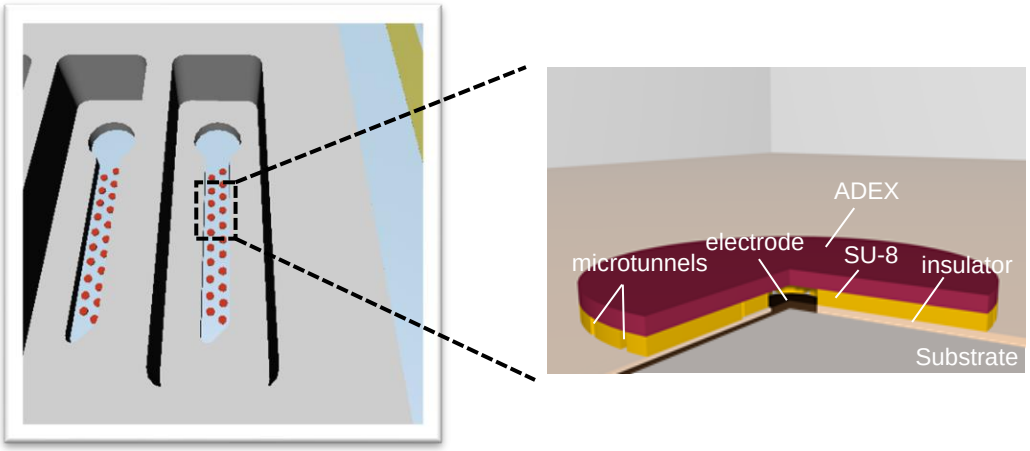

Figure 4.5: Capped microelectrodes. CµE are integrated into the substrate inside the gel lane. After lamination, the SU-8 structure surrounding the recording electrode is photolithographed to the surface and later laminated with an ADEX cap. Microtunnels are open on the edges of the CµE.

Figure 4.6: SU-8 structures. SU-8 structures in 12nMPS with 24 entries and two fractions (left) and 18nMPS comprising 12 entries and one fraction.

4.2.3.2 Microfluidic fabrication

Custom 3 mm thick and 32.5 mm wide square, quartz microfluidic (MF) pieces were designed with Autodesk Inventor Software (Autodesk Inc. CA, USA) and purchased from FEMTOprint SA (Switzerland). Here, monolithic pieces were modified at micrometre resolution by employing a technique called selective laser-induced etching process (ISLE). In the latter, the MF piece was modified by a high-energy laser that targeted defined areas, which were then chemically removed through wet-chemical etching (Gottman et al., 2012; Bellouard, 2012), ultimately leading to the desired MF pieces.

As mentioned above, a fundamental difference between both MF pieces was the number of independent wells incorporated in the MF piece. Nonetheless, both incorporated a minimum of two layers in each well, the bottom layer (900 µm tall), later to be filled with cells in hydrogel (gel layer) and the upper one (2.1 mm tall), present to supply cells with nurturing medium (liquid layer) (figure 4.7a, supplementary video 1, and table 4.12).

For a complete nMPS, the microfluidic piece was glued to the MEA with EPO-TEK® 301-2FL (Epoxy Technology Inc., Billerica, MA, USA) and aligned with a custom-made aluminium adapter (Weerg Srl., Italy). The biocompatible glue was distributed at 30 mPa on the MF piece's bonding surface by employing a fluid dispenser pump (Ultimus I, Nordson EFD, Germany). Drops were dispensed at a frequency of 0.01 Hz and ultimately created a 5 µm thin layer. Lastly, the device was cured for 3 h at 80°C (ramped, 0.5°C/min).

Once bonded, a cell volume of 7 µl and 9 µl fit into the GL of the 18nMPS and 12nMPS, respectively. As a result of the surface tension, liquid dispensed in the gel lane did not overflow, and the gel polymerized with homogeneously distributed cells (figure 4.7b). Subsequently, cells were nurtured with 50 µl plating medium. It is worth noting that media could be added on top of the gel by using a 125 µl multi pipette (VIAFLO 12 125µL, INTEGRA Bioscience AG., Switzerland) as the wells' distance was homologous to the distance between wells of a 96-well plate. Cells were incubated at 37°C with 5% CO_2. Readouts were performed at 10 DIV.

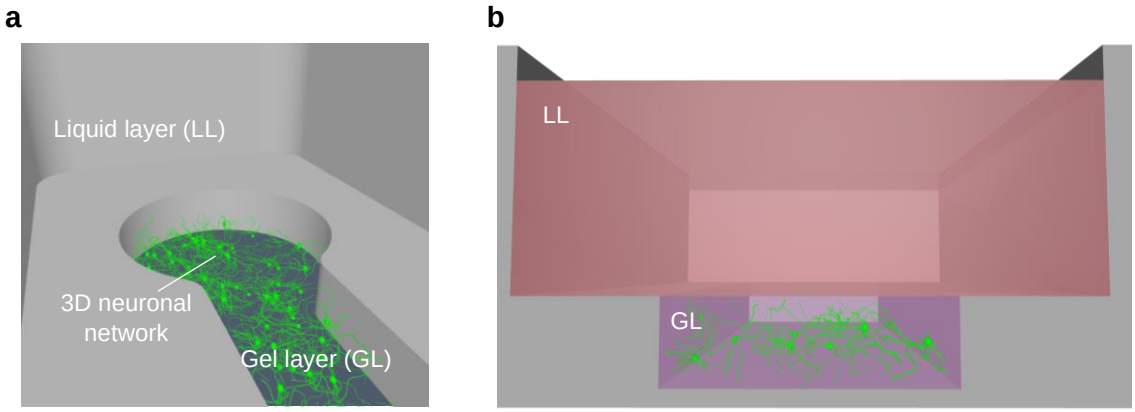

Figure 4.7: Compartmentalisation of one well. Neurons were embedded in liquid hydrogel and seeded into the gel layer (GL). After polymerization of the gel, the medium was added on top in the liquid layer (LL) (a). Cross-section of one well representing the GL with neurons under the LL (b). More details in suppl. video 1.

Table 4.11: Dimensions of the two versions of MF-MEA systems.

	12nMPS	18nMPS
Height (LL)	2.1 mm	2.1 mm
Width (LL)	3.5 mm	3.5 mm
Length (LL)	12.25 mm	7.8 mm
Volume (LL)	50 µL	50 µL
Height (GL)	0.9 mm	0.9 mm
Width (GL)	1 mm	1 mm
Length (GL)	Approx. 8 mm	Approx. 5.5 mm
Volume (GL)	9 µL	7 µL

Prior to each cell seeding, both manufactured nMPS versions were plasma-cleaned for two minutes at medium potency (Plasma cleaner/sterilizer PDC-32G, Harrick Plasma, Ithaca, US) with the aim of sterilisation. More importantly, this process favoured creating a hydrophilic surface, which avoided the clogging of the hydrogel in the GL during the cell seeding.

4.2.3.3 Reusability

The nMPS could be re-used up to 10 times without compromising the quality of the recordings or the cells' morphology. After every use, devices were washed with H_2O and subsequently rinsed with ddH_2O. Then, they were immersed in ddH_2O with tergazyme (1304, Alconox, Inc., NY, US) (0.01%) and left for 6 h or O/N. After, devices were washed out with ddH_2O and left in ddH_2O for 6 h or overnight (O/N). Lastly, nMPS were left under the hood for dry.

4.3 Readouts

Morphological read-outs were carried out with microscopes (Cell Observer® System with spinning disk head, Carl Zeiss, Germany; Zeiss LSM 780 NLO confocal equipped with Airyscan, Carl Zeiss, Germany). For the functional analysis, a recorder (USB-MEA256System, Multi Channel Systems MCS GmbH, Germany) from Multi Channel Systems was employed.

4.3.1 Morphological readout

Cell cultures were visually monitored every 2 days by utilizing a microscope (EVOS® FL microscope, Thermo Fisher Scientific, MA, US). For the high-resolution imaging of the neuronal network, cells were analysed in the facilities of Max- Planck- Institute (MPI) for Developmental Biology in Tübingen by employing a confocal microscope (Zeiss LSM 780 NLO) equipped with an Airyscan unit microscope stand. Other images were taken with the microscope at the NMI facilities (Cell Observer® System with spinning disk head, Carl Zeiss, Germany).

4.3.1.1 Live-cell imaging

For live visualisation and oversight of the neural network, neurons were transduced after 1 DIV with an adenovirus (50465 - AAV1, addgene, MA, US) (1:2000) (table 4.13) that carried human Synapsin 1 as a promoter and GFP as a gen of interest. After 4 or 5 DIV, GFP expression could be appreciated with the microscope (EVOS® FL microscope Thermo Fisher Scientific, MA, US). Neurons were also transduced to prove the neurites' growth inside the microtunnels and analyse the neural networks' health, especially after being treated with rotenone. Morphology of neurons was studied 20 min, 6h and 24 h after applying 0.05 µM, 0.5 µM and 5 µM of rotenone.

Table 4.12: Adenovirus employed to perform live-cell imaging

Adeno-associated virus (AAV)	**Promotor**	**Fluorescent protein**	**Application**	**Catalogue number**
pAAV.hSyn.eGFP.WPRE.bGH	Human synopsis 1	GFP	Live imaging	50465, addgene, MA, US

4.3.1.2 ICC

In order to study other cell types inside the 3D culture, an immunocytochemistry was carried out. Hence, cells were fixed with paraformaldehyde containing 4% sucrose for 20 min at 37°C. Then, samples were carefully washed out 5 times using a washing buffer (WB) consisting of PBS -/- and fish skin gelatine (G7765, Sigma-Aldrich) (0.2%) (table 4.14). Afterwards, cells were permeabilized for 1 h at RT on a rocker (infinity rocker™ pro, Next advance, NY, US) by employing a permeabilisation buffer (PB) comprising PBS -/- and 20 % Triton X (T9284, Sigma-Aldrich). Subsequently, PB was washed out 5 times with WB and replaced by blocking buffer (BB) containing donkey serum (017-000-121, Dianova GmbH) (0.1%) and PB. Samples were left in BB on a shaker O/N at 4°C. The day after, primary

antibodies were added at a ratio of 1:500 and left on the rocker (velocity 2) O/N at 4°C. Primary antibodies (table 4.15) that targeted specific molecules from different cell types were employed. Class III β-tubulin (β-tub III) (801201, BioLegend) stained neurons' dendrites and axons, glial fibrillary acidic protein (GFAP) (173011, Synaptic Systems GmbH) marked astrocytes, Homer-1 (160 003, Synaptic Systems GmbH, Germany) targeted postsynaptic proteins, Synaptophysin-1 marked presynaptic molecules (101 004, Synaptic Systems GmbH, Germany), microtubule-associated protein 2 (MAP2, NB300-213, Novus Biologicals, CO, US) stained dendrites, GAD67 enzyme (GAD67, MAB5406, Merck KgaA, Darmstadt, Germany) and allograft inflammatory factor 1 (IBA 1) (019-19741, FUJIFILM Wako Chemicals) targeted microglia. Samples were washed with WB and left on the shaker (velocity 2) at 4°C for 24 h. Then, all secondary antibodies (table 4.16) were added at a ratio of 1:200, while β-tub III was stained with the respective secondary antibody employing a ratio of 1:100. Afterwards, samples were washed out with WB 5 times and left O/N at 4°C. Fixed cultures were washed out again 5 times and replaced with SlowFade (2054439, Thermo Fisher Scientific, MA, US) that stained nuclei with DAPI. ICCs could be kept up to 4 months at 4°C.

Table 4.13: ICC buffers. Buffers employed to characterise 3D brain cells and structures.

ICC buffers	**Composition**	**Catalogue number**
Washing buffer	DPBS $^{-/-}$ with 0.2 %(w/v) Fish skin gelatin	14190250, Gibco, Thermo Fisher Scientific, MA, US G7765, Sigma-Aldrich, Merck KGaA, Germany
Permeabilisation buffer	Washing buffer with 0.3 %(w/v) Triton X-100	T9284, Sigma-Aldrich, Merck KGaA, Germany
Blocking buffer and Ab carrier solution	Washing buffer with 0.2 %(v/v) of normal donkey serum and 0.1%(v/v) of permeabilisation buffer	017-000-121, Dianova GmbH, Germany

Table 4.14: ICC primary antibodies. Primary antibodies employed to characterise 3D brain cells and structures. C= cow, Ch= chicken, F= frog, GP= guinea pig, Ha= hamster, H= human, M= mouse, R= rat, Rb= rabbit.

Primary antibodies	**Clonality**	**Reactivity**	**Host**	**Catalogue number**
Anti-glial fibrillary acidic protein (GFAP)	monoclonal	H, R, M	M	173011, Synaptic Systems GmbH, Germany

Anti-calcium binding adaptor molecule 1 (Iba1)	polyclonal	H, R, M	Rb	019-19741, FUJIFILM Wako Chemicals, Japan
Anti-Homer 1 (VesL, Syn 47)	polyclonal	H, R, M	Rb	160 003, Synaptic Systems GmbH, Germany
Anti-microtubule-associated protein 2 (MAP2)	polyclonal	H, R, M	Ch	NB300-213, Novus Biologicals, CO, US
Purified anti-Tubulin β3 (TUBβ3)	monoclonal	H, R, M	M	801201, BioLegend CNS Inc, CA, US
Anti-GAD 67	monoclonal	H, R, M	M	MAB5406, Merck KGaA, Darmstadt, Germany
Anti-Synaptophysin 1	polyclonal	H, R, M, Ha, C, Ch, F	GP	101 004, Synaptic Systems GmbH, Germany

Table 4.15: ICC secondary antibodies. Secondary antibodies employed to characterise 3D brain cells and structures. Ch= chicken, Dk= donkey, GP= guinea pig, M= mouse, Rb= rabbit.

Secondary antibodies	**Emission (nm)**	**Reactivity**	**Host**	**Catalogue number**
Alexa Fluor 488-conjugated AffiniPure Donkey Anti-Mouse IgG	488	M	Dk	715-545-150, Dianova GmbH, Germany
Alexa Fluor 488-conjugated AffiniPure Donkey Anti-Rabbit IgG	488	Rb	Dk	711-545-152, Dianova GmbH, Germany
Alexa Fluor 568-conjugated AffiniPure Donkey Anti-Mouse IgG	568	M	Dk	1917938, Thermo Fisher Scientific, MA, US
Alexa Fluor 647-conjugated AffiniPure Donkey Anti-Chicken IgG	647	Ch	Dk	703-605-155, Dianova GmbH, Germany
Alexa Fluor 647-conjugated AffiniPure Donkey Anti-Rabbit IgG	647	Rb	Dk	711-605-152, Dianova GmbH, Germany
Alexa Fluor 488-conjugated AffiniPure Donkey Anti-Guinea Pig IgG	488	GP	Dk	706-545-148, Dianova GmbH, Germany

4.3.1.3 Microscopy

After labelling cells in the 3D culture, either via viral transduction or ICC, the morphology of different cell types was assessed with different microscopes and objectives available at the NMI facilities and the MPI (table 4.17). The use of those depended on the thickness of the gel and the appropriate image resolution.

To study the different ratios of the N+AS and microglia, the confocal microscope with spinning disk head was employed (Cell Observer® System with spinning disk head, Carl Zeiss, Germany). The software used for taking the images was the ZEN 3.0 software (blue edition, ZEISS, Germany).

To be able to acquire a more detailed morphological assessment, a microscope (LSM 780 NLO, Zeiss, Germany) with higher resolution was employed. Imaging was performed by employing software ZEN 2.3 (black edition, ZEISS, Germany).

Table 4.16: Microscope characteristics for morphological readouts of 3D cell cultures.

Microscope facility	**Objectives**	**Working distance (mm)**	**Numerical aperture**	**Immersion / RI**	**Illumination Lasers wavelength (nm)**
Cell Observer® System with spinning disk head, Carl Zeiss, Germany **NMI Institute**	10x EC Plan-Neofluar	5.2	0.3	w/o	405, 488, 561, 639
	20x LD Plan-Neufluar	8.4	0.4	w/o	
	20x Plan-Apochromat	0.55	0.8	w/o	
	40x LD Plan-Neufluar	3.3	0.6	w/o	
	63x Plan-Apochromat	0.18	1.4	oil / 1.518	
LSM 780 NLO, Confocal System, with 32 channel GaAsP array + 2 GaAsP PMTs Carl Zeiss, Germany **Max Plank Institute, Light Microscopy facility**	10x C-Apochromat	1.8	0.45	water / 1.333	405, 458, 488, 514, 561, 633
	25x LD LCI Plan-Apochromat 25x	0.57	0.8	water, oil / 1.333, 1.518	
	40x LD C-Apochromat	0.62	1.1	water / 1.333	
	40x Plan-Apochromat	0.2	1.3	oil / 1.518	
	63x C-Apochromat	0.19	1.4	water / 1.333	
LSM 780 NLO, Confocal system with Airyscan unit on an AxioObserver Z.1 Microscope **Max Plank Institute, Light Microscopy facility**	10x C-Apochromat	1.8	0.45	water / 1.333	
	25x LD LCI Plan-Apochromat 25x	0.57	0.8	water, oil / 1.333, 1.518	
	40x LD C-Apochromat	0.62	1.1	water / 1.333	
	40x Plan-Apochromat	0.2	1.3	oil / 1.518	
	63x C-Apochromat	0.19	1.4	water / 1.333	

4.3.2 Functional readout

The nMPS used in this study provided the ability of recording neuron's electrical activity through CμE. However, several steps needed to be accomplished to verify the accuracy of the employed device. Firstly, the used nMPS had to be validated. Therefore, the electrical activity of the neuronal networks was recorded after being treated with reference compounds picrotoxin (PTX), tetrodotoxin (TTX) and rotenone. In addition to that, the formation of synaptic circuits was demonstrated by performing simultaneous calcium-imaging (Ca^{2+}-imaging) and optogenetic experiments. After the system was validated, the devices were used to study the effect of neuroinflammatory compounds interferon-γ (IFNg) and tumour necrosis factor α (TNFa).

4.3.2.1 Electrophysiological recordings

During the functional read-out, one device at a time was placed inside the recording system (USB-MEA256System, Multi Channel Systems MCS GmbH, Germany). At the same time, the environmental conditions (36°C, 5% CO_2 and 85% humidity) were constantly monitored and supervised with a control panel (Okotouch, Control Unit, 118-1924, Oko Srl, Italy). Values were kept stable and more sterile by placing a customized incubation chamber (Oko Srl, Italy) on top of the device (figure 4.8). Additionally, the recording system was connected to a temperature controller (TC01) (Multi Channel Systems MCS GmbH, Germany) set to 34.3°C.

Contact patches along the edges of the devices permitted the connection of the recording system to the computer screen. In order to appreciate the action potentials of the neural network, software MC Rack (MC_Rack v.4.6.2., Multi Channel Systems MCS GmbH, Germany) was utilized. Here, electrical activity was filtered with the Bessel 4th order IIR filter parameter at high pass and 100 Hz for its visualisation *in situ*.

To validate the system, reference compounds PTX, TTX and rotenone were employed. To study the effect of drugs, the study was designed to comprise 4 different conditions for each compound, one control and 3 different drug concentrations, each differing by a 10-fold. Final concentrations for PTX were 0.1 μM, 1 μM and 10 μM, for TTX 1 nM, 10nM and 100 nM, and ultimately for rotenone 0.05 μM, 0.5 μM and 5 μM. Generally, 3 wells per condition were defined in each device.

In pursuance of studying neuroinflammation, different ratios for microglia:N+AS (1:4 and 1:8) were tested. Typically, in one nMPS, 4 wells per ratio condition were used as a control, while the remaining 5 were treated with pro-inflammatory compounds IFNγ (20 ng/ml) and TNFα (50 ng/ml) (I+T).

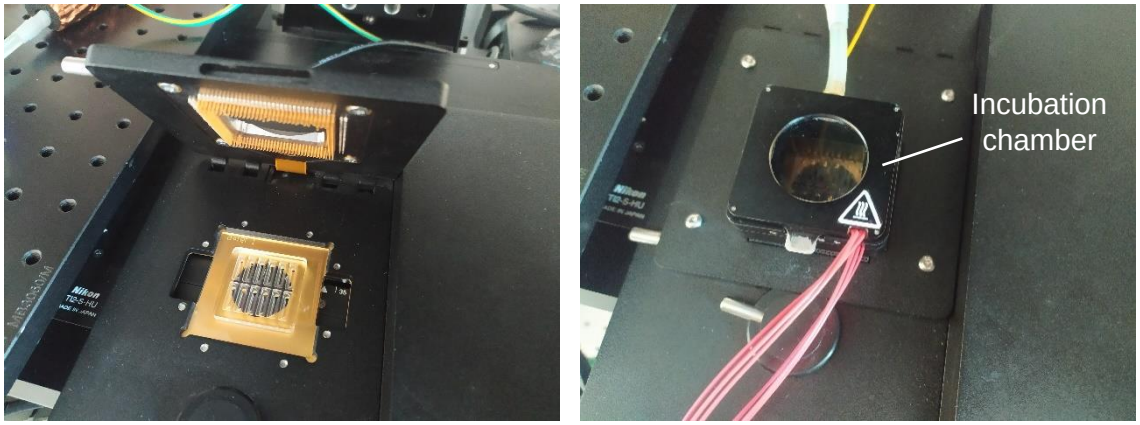

Figure 4.8: Recording system. nMPS is placed inside the open recording system (a). Closed recording system, including the customized incubation chamber.

In order to ensure the same conditions in each recording, a protocol for compound application was established. Before each recording, samples were left to adapt to the environment and then, the basal spontaneous activity of the neuronal network was recorded. After, compounds or bare medium, serving as a control, were added to the single wells by utilizing an automatic INTEGRA multi-pipette. Here, 5 µL were removed from each well and were replaced by 5 µl of the respective condition. To mix the latter homogenously, 5 µl were aspired and dispensed for two additional times on the bottom and the top part of the well, respectively (Molina-Martínez et al., 2020). Afterwards, samples were left until the effect of the drugs was recorded. Each step before and after the drug application consisted of 10 minutes. Recordings were performed after 10 DIV. Samples treated with neuroinflammatory compounds were recorded at 8 DIV (T= 0 h), 9 DIV (T= 24 h) and 10 DIV (T= 48 h) after compound application.

4.3.2.2 Calcium imaging

Ca^{2+}-imaging was performed simultaneously to recordings to ensure the capture of electrical activity originating from the entire neuronal network, therefore, excluding single-cell activity. For visualisation of the calcium influx in neurons, they were transduced with adenovirus pAAV.Syn.GCaMP6f.WPRE.SV40 (addgene, 100837) (table 4.18) after 1 DIV.

This virus carries a genetically encoded calcium indicator. Here, the latter's expression was supervised employing a microscope (EVOS® FL AMF 4300, Thermo Fisher Scientific, MA, US) every 2 days. Ten days after cell seeding, recordings were performed while simultaneously acquiring the Ca^{2+} influx in the neurons.

The fluorescence emitted by GCaMP6f was captured by the inverted microscope system ECLIPSE Ti2 (Nikon GmbH, Germany) and visualized with the NIS-Elements software (Nikon Instruments Inc., USA) by lightning the sample with a 470 nm LED. Ca^{2+}-imaging was performed for 1 min at the height of 560 µm. In order to be able to image and record electrical activity synchronously, the metal support in the recording system was perforated to obtain a 30 mm hole. In this manner, LED light could shine through the glass substrate of the chip into the gel scaffold. Only a 0.04 mm^2 (200 x 200 µm) square was imaged for the Ca^{2+}-imaging.

Table 4.17: Adenovirus employed to perform calcium imaging.

Adeno-associated virus (AAV)	**Promotor**	**Fluorescent protein**	**Application**	**Catalogue number**
pAAV.Syn.GCaMP6f.WPRE.SV40	Human synopsis 1	ultra sensitive protein calcium sensor (GCaMP6f)	Ca^{2+}-imaging	100837, addgene, MA, US

4.3.2.3 Optogenetics

To support the results acquired with Ca^{2+}-imaging, neurons were transduced with pAAV-hSyn-hChR2(H134R)-EYFP (AAV1) (addgene, 26973). This procedure ensured the presence of Channelrhodopsin-2 light-gated ion channels, which were activated when stimulated with blue light (470 nm) (CoolLED pE-300ultra, CoolLED, UK). The light-stimulated areas were set by a digital micro-mirror device system (MM-0436, Mosaic3, Andor, Oxford Instruments, UK) added to the inverted microscope system ECLIPSE Ti2 (Nikon GmbH, Germany). The response to this stimulation was synchronously recorded with the recording system MCsetup USB-MEA256 System and visualized with software MC_Stimulus II (Multi Channel Systems MCS GmbH, Germany). In each recording, the system gathered cellular activity 50 ms before each light stimulus and 200 ms after optical stimulation. The latter was 5 ms long and repeated every 10 s for 1 s at a frequency of 40 Hz. Light intensity was set to 1% (CoolLED pE-300ultra, CoolLED, UK) at a region of interest (ROI) of 0.04 mm^2 (200 x 200 µm).

Table 4.18: Adenovirus employed for optical stimulation.

Adeno-associated virus (AAV)	Promotor	Fluorescent protein	Application	Catalogue number
pAAV-hSyn-hChR2(H134R)-EYFP	Human synopsis 1	humanized channelrhodopsin 2 with H134R mutation fused to mCherry	optogenetic assessment	26973, addgene, MA, US

4.4 Data analysis

4.4.1 Image processing

Z-stacks of 3D images were processed and reconstructed by IMARIS 4.6 (Bitplane AG, Oxford Instruments, UK). Videos were exported at 250 frames per second. The resolution of the latter was set to 1920 x 1080 pixels.

4.4.2 Electrophysiological recordings

The recorded cell activity was imported to the software NeuroExplorer (version 5.1, Nex Technologies, Littleton, MA, USA) for conversion, filtering, spike detection, burst analysis and, ultimately, network synchronicity. For this purpose, customized scripts written in Python language were provided by Nex Technologies.

Before any analysis, single electrodes were named and organized into groups, that is, the wells they belonged to. This classification was necessary to identify the burst and network burst activity present in each individual well. Then, spikes for each electrode were detected by filtering electrophysiological data using a band-pass filter of 4th order with a minimum frequency of 60 Hz to a maximum of 6000 Hz. The detection of the action potentials was accomplished by utilizing the threshold crossing algorithm of 4*σn, where σ represents an essential standard deviation value by which the background noise is determined. The latter is calculated with the following formula, where x indicates the band-pass filter signal (Quiroga et al., 2004):

$$\sigma n = median\{\frac{|x|}{0.6745}\}$$

It should be emphasised that this algorithm only considered the negative peaks of the action potential present in all extracellular spikes recorded. The minimum time difference between each spike was set to 1 ms.

Moreover, the interval algorithm was applied to define the burst periods in a spike train. Therefore, certain parameters were specified (figure 4.9) (Cotterill et al., 2016; Neuroexplorer, 2019). For a train of events to be defined as a burst, the minimum duration of the latter was fixed to 10 ms. Each burst had to carry at least 5 spikes, where the time difference between the two beginning spikes and the spikes within the bursts was set to a maximum of 170 ms and 300 ms, respectively. For two bursts to be considered one single burst, the minimum time between those two signals was fixed to 200 ms. Once parameters were defined, data were exported and saved into an excel file (Microsoft® Excel®, 2016, Seattle, US).

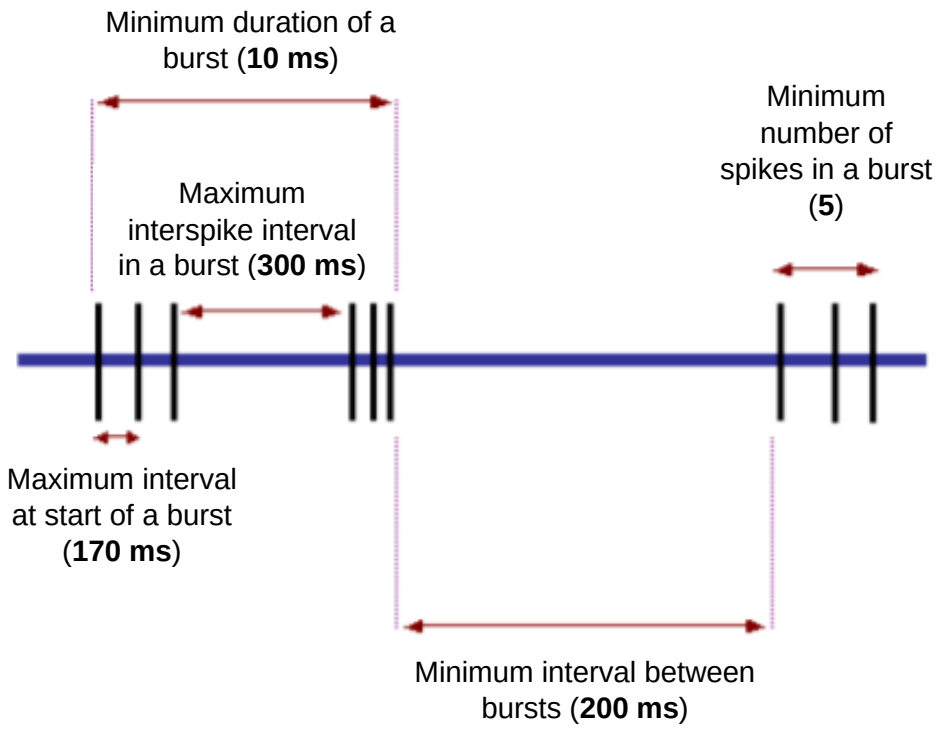

Figure 4.9: Parameters for burst analysis. Parameters were defined upon suggestions of Neuroexplorer software. The image was adapted from Neuroexplorer manual.

In order to study the interspike interval (ISI), the minimum interval was set to 0, and the maximal interval was set to 0.5 s. Additionally, the bin (s) was set to 0.005. Then, an excel file was exported and saved for further analysis.

Ultimately, the collected data were analysed for synchronicity by studying the network bursts (NB), which are bursts originating simultaneously in most electrodes in one well. For this purpose, a customized script (NeuroExplorer®, Nex Technologies, Littleton, MA, USA) containing an algorithm based on Poisson's surprise method (Legéndy and Salcmac, 1985) was employed. The latter is an algorithm widely used for burst detection, in which trains of spikes are distinguished from the baseline neuronal firing. Conclusively, bursts are defined as periods of deviation from neuronal firing that are assumed to follow Poisson's distribution (Legéndy and Salcmac, 1985). In this method, surprise (S) levels evaluate the unlikelihood for a fired burst at a given time to be a chance occurrence. This surprise value was defined by the following formula, where P is the probability that a given time interval of length T contains n or more spikes. The mean firing rate is represented by r:

$$S = -log\ log\ (P) \qquad P = e^{-rT} \sum_{i=n}^{\infty} \frac{(rT)^{-i}}{i!}$$

It is worth noting that this approach was also considered as a burst detection method for this study but proved to be unreliable when detecting bursts after applying certain drugs to the cell culture. However, it showed to work accurately for the network burst analysis. Here, medians of bursts in each electrode of single wells were identified and projected as single events in one timeline. Then, Poisson's surprise procedure was applied to that timeline. For a train of bursts to be identified as a network burst, at least 33% of the electrodes had to fire a burst synchronously. The beginning of an NB corresponded to the beginning of the first spike in a burst inside that NB, and the end of the NB was defined by the last spike of one burst inside the NB. The level of surprise was fixed to 3. Raw data were automatically exported to an excel file and saved.

4.4.3 Statistics

GraphPad software (Version 8.4.3, GraphPad Software, LLC) was employed to process the raw data. Performed analysis were focused on several variables that gave an insight into the network's activity. These variables corresponded to the mean firing rate (MFR), the burst frequency rate (BFR), the mean burst duration (BD), the percentage of spikes in bursts (%SiB), the coefficient of variance of inter-spike intervals (ISI CoV), mean network burst

frequency (NBF), the mean firing rate in network bursts (MFR in NB), and the percentage of bursts inside Network bursts (%B in NB) (table 4.20).

Table 4.19: Parameters selected for electrophysiological analysis.

Parameter	Unit	Description
Mean firing rate (MFR)	Hz	Number of spikes divided by the duration of the recording.
Burst frequency rate (BFR)	Hz	Number of burst detected divided by the duration of the recording.
Spikes in bursts (%SiB)	%	Percentage of detected spikes in a burst.
Bursts duration (BD)	s	Average time from the first to the last spike in a burst. Burst were defined by applying the Max Interval logarithm.
Interspike interval coefficient of variation (ISICoV)		Coefficient of variation of the inter-spike interval (duration of the interval between spikes), acquired by the division of standard deviation/mean. The closer the values are to 0, the more regular is the triggering of action potentials, while values >1 indicate bursting activity.
Network burst frequency (NBF)	Hz	Number of network bursts divided by the duration of the recording. Network bursts were defined via Poisson's surprise with a minimum surprise value of 3.
Mean firing rate in network bursts (MFR in NB)	Hz	Number of spikes detected in NB divided by the duration of the network burst.
Bursts in network bursts (%B in NB)	%	Percentage of detected bursts that are part of NB.

This study aimed to evaluate the effect of specific compounds on 3D cultures and validate if the used device was applicable for biological studies. For the latter, the basal spontaneous neuronal firing collected with 12nMPS were analysed to study the variability of this device model. In order to understand the different causes responsible for possible deviations in the data, three main possible external factors were considered and studied. First, the chip's fabrication could influence the outcome of the results. To test if this factor had a significant impact, collected data were grouped into the multiple employed devices. For the validation of this nMPS, five devices were employed, and each of the devices' mean was compared to a control group, which was composed of the mean of all collected data. Secondly, the cell culture condition based on the day in which it was isolated from the embryos might affect the results. Therefore, gathered data were classified into the different preparations. In total, 10 different days of preparations were contrasted with the control group. Lastly, another factor that might influence the recordings is the variable of human error. Here, errors may occur during the cell

isolation, the plating, cell counting, or handling the nMPS. To test this, results acquired from three to four devices of 3 preparations were evaluated. Devices of each preparation were compared to a control mean.

Another element that certainly affects the cell culture is the biological aspect. The latter may influence the neuronal outgrowth, which is detrimental to the projection of neurites inside the microtunnels. The more neurites grow in a 3D cell culture and, therefore, through a microtunnel, the more activity will be recorded. However, this may also not be only influenced by the biology of the cells but also by chance since no regulated factor dictated the neuron where to project its neurite. To study this element, the mean values of individual wells inside three out of seventeen randomly chosen recordings were compared to a control mean, which corresponded to the mean of all wells of the selected recording.

The second step of the validation of 12nMPS was to prove the viability and the forming of a reactive network of the neuronal cell culture. Thus, reference compounds PTX, TTX and rotenone were applied to the samples. The neural activity collected from individual electrodes before and after compound (treatment) or medium application (no treatment) was compared and represented in % change to investigate the drug effect. The average % change of each well was then defined and grouped into the 4 different drug concentrations for further comparison.

The 18nMPS was mainly used for testing the effect of pro-inflammatory compounds IFNγ and TNFα (I+T) after 24 and 48 h in 3D cell cultures containing microglia, astrocytes and neurons (TriC). Those were compared to two controls containing only N+AS (BiC). One control contained the same media conditions as the TriC (PM +/+) and another one the PM-/- to ensure the survival of only neurons and astrocytes. Single absolute values captured from electrodes of samples at T= 24 h (9 DIV) and T= 48 h (10 DIV) were transformed into the relative change (%) in reference to data acquired before any treatment (T= 0 h) (8 DIV). All conditions were classified into eight different groups. The first four groups corresponded to data obtained from BiC, where the first two groups (1 and 2) were not supplemented with IL-34 and TGFβ2 (BiC -/-), while groups 3 and 4 (BiC +/+) were. Groups 5 and 6 corresponded to TriC seeded at a ratio of 1 microglia per 4 neurons (1:4) (TriC 1:4), while groups 7 and 8 described data gained from cultures with 1 microglia per 8 neurons (1:8) (TriC 1:8). Furthermore, uneven groups remained unstimulated, while even groups were stimulated. The stimulation was carried out after the recordings at T= 0 h. Unstimulated samples were only supplied with fresh medium. Statistical differences were analysed between treated vs untreated samples (group 1 vs 2; group 3 vs 4, group 5 vs 6, group 7 vs 8), unstimulated groups (group 1 vs 3 vs 5 vs 7) and

stimulated groups (2 vs 4 vs 6 vs 8), always at 24 h or 48 h. Moreover, differences in activity between 24 and 48 h in each group were measured.

Basal values of each condition and parameter were first investigated for outliers employing the ROUT method (ROUT= 5 %). Subsequently, data were examined for normality by performing the Shapiro-Wilk test and compared to a frequency distribution histogram and a quantile-quantile plot (QQ-plot) (Thode, 2002; Elliott and Woodward, 2007). Assuming normality, data were analysed for significant differences between variances by using Bartlett's test. If the evaluated groups showed to have significant differences between variances, the Brown test was performed. Subsequently, groups were compared by performing a multiple comparison post hoc test. Otherwise, if variances did not significantly differ, the ordinary one-way ANOVA was employed, and subsequently, data were evaluated by performing either the Tukey test or the Dunnett test. The latter was used if data were compared to a control group. Significant differences were represented with asterisks (*p-value <0,05; **p-value <0.01; ***p-value <0.001; ****p-value <0.0001) unless indicated otherwise.

4.4.4 Calcium imaging

Live Ca^{2+}-imaging was visualised with the software NIS-Elements (Nikon Instruments Inc., USA). Videos were exported at 5 frames per second. Captured fluorescence in arbitrary units (a.u.) over time was illustrated in a histogram and later correlated with the captured electrical activity by employing the nMPS described in section 6.3.2.1.

4.4.5 Optogenetics

Electrical activity acquired during the optogenetics experiments was exported from MC_Rack to Neuroexplorer (see section 6.3.2.1). Image during light stimulation was exported from NIS-Elements software (Nikon Instruments Inc., USA). Light stimuli and respective electrical activity were displayed.

4.4.6 Automated imaging

A customized 384-plate adaptor was designed to standardize the imaging of nMPS devices with an automated system. This platform was produced by Weerg company (Weerg Srl., Italy) and supported the analysis of two nMPS devices at once. The robotic system contains a Microlab Star that performs all liquid handling and an integrated Cytomat-24 CO_2 incubator. The plates were transported within the system by a Rack runner. High-content screening of transduced neurons was performed with a high content fluorescent microscope

(PerkinElmer, Operetta) and an automated spinning disk confocal microscope (Yokogawa, CV7000). Images were then processed and exported using the Cell PathFinder software (Yokogawa, version 3.03.02.02). Images were taken and processed by Dr Stella Donato (DZNE).

4.4.7 Luminex Multiplex Assay (LMA)

Protein measurements were carried out by Meike Jakobi from the group of Multiplex Immunoassays at the NMI. For this purpose, supernatants (30 µl) of samples were collected and transferred into a multi-well plate (Mouse Magnetic Luminex Assay, LXSAMSM RandD Systems, Minneapolis, US) with integrated fluorophore-containing beads specific for IL-1β, IL-6, CCL5/Rantes, CXCL2, Serpin-E1/ PAI-1 and MMP9. To measure their concentration, the Luminex FlexMap® 3D analyzer system and Luminex xPONENT® 4.2 software (Luminex, Austin, TX, USA) system was employed. For data analysis, MasterPlex QT version 5.0 was used.

5 Results

5.1 System validation

As mentioned in the introductory section, the nMPS had to fulfil several requirements. It especially needs to be apt for functional and morphological readouts. Consequently, the devices' material should be biocompatible, thermally stable, solvent-compatible, and, if possible, reusable. Quartz is a material that fulfilled all these criteria. A monolithic piece of the former was thereupon organised into several microfluidic compartments forming multiple wells (figure 5.1). Twelve wells could be manufactured by employing the selective laser-induced etching (SLE) technique (LoTurco et al., 2013), in which a pattern was chemically etched at micron resolution. This monolithic piece was glued on top of a transparent substrate carrying the MEA, arranged equally inside the gel compartment of each well. By having a translucent device, the morphology of cells could be examined. This assessment was carried out via live imaging or immunocytochemistry. Additionally, the nMPS transparency allowed performing Ca^{2+}-imaging and optogenetics while capturing neuronal activity with the MEA. For this purpose, the nMPS was placed inside the recorder and imaged or optically stimulated, respectively.

Figure 5.1: In vitro platform 12nMPS. Final bioreactor carrying 12 independent experiments and 21 electrodes in each well.

5.1.1 Microfabrication of 12-well nMPS

Microfabrication processes were carried out in the cleanroom facilities to avoid the adhesion of dust or other materials usually present in the air. A SU-8 layer was laminated surrounding the electrode, followed by a second lamination with ADEX (figure 5.2a). The design enclosing the electrode (figure 5.2b) presented the double-branching of six microchannels, providing 24 final entries on the edge of the structure. Laminating ADEX on

top of the construction (figure 5.2c) established the final microtunnels (figure 5.2d) leading towards the electrode and forming the capped microelectrode.

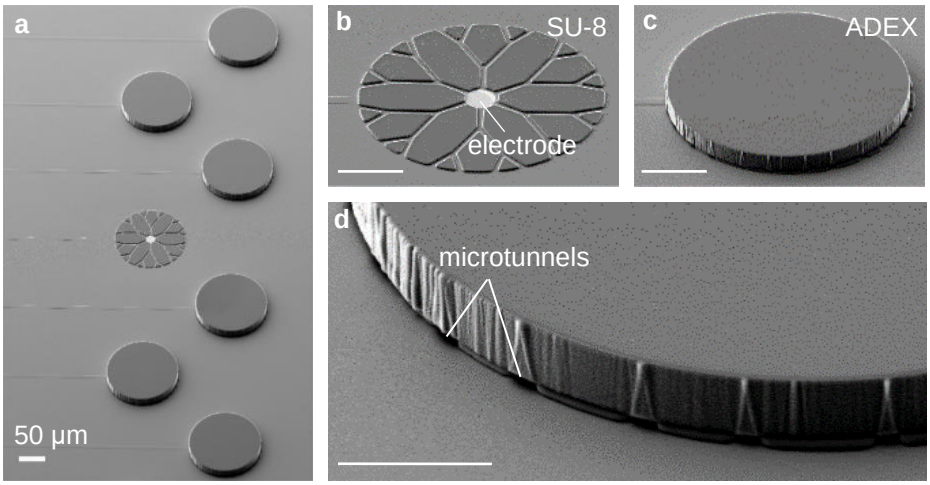

Figure 5.2: Microfabricated CµE. CµEs are integrated into the substrate (a). After lamination, the SU-8 structure shows 24 perfectly lithographed microchannels surrounding the electrode (b). By covering the SU-8 structure with ADEX (c), microchannels become microtunnels (d). SEM images were taken by Kathrin Stadelmann (NMI).

5.1.2 Morphology

The biocompatible nMPS guaranteed the survival of neurons for at least 10 days. The device allowed the outgrowth of neurons and dendritic spines in 3D (figure 5.3) within a 900 µm thick hydrogel, demonstrating biological neuronal characteristics featured in this nMPS. The neuronal projections were observed 4 or 5 DIV after transducing cells with an eGFP-coupled virus. Consequently, eGFP-transduced neurons facilitated the monitoring of the latter's viability between wells or even after applying certain compounds. More importantly, it certified the projection of neurites inside the microtunnels of the CµE (figure 5.4), which is decisive for evaluating the electrophysiology of the neuronal culture.

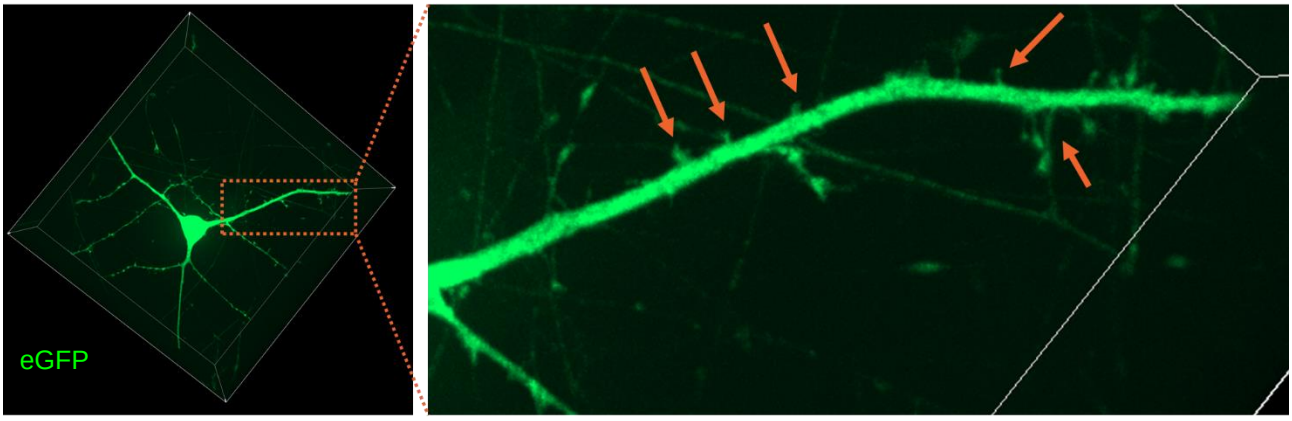

Figure 5.3: Live cell imaging of a neuron transduced with eGFP. Cell culture was labelled with GFP and imaged at 63X. Orange arrows indicate dendritic spines. Scale left: H= 57 µm; A= 124 µm x 127 µm.

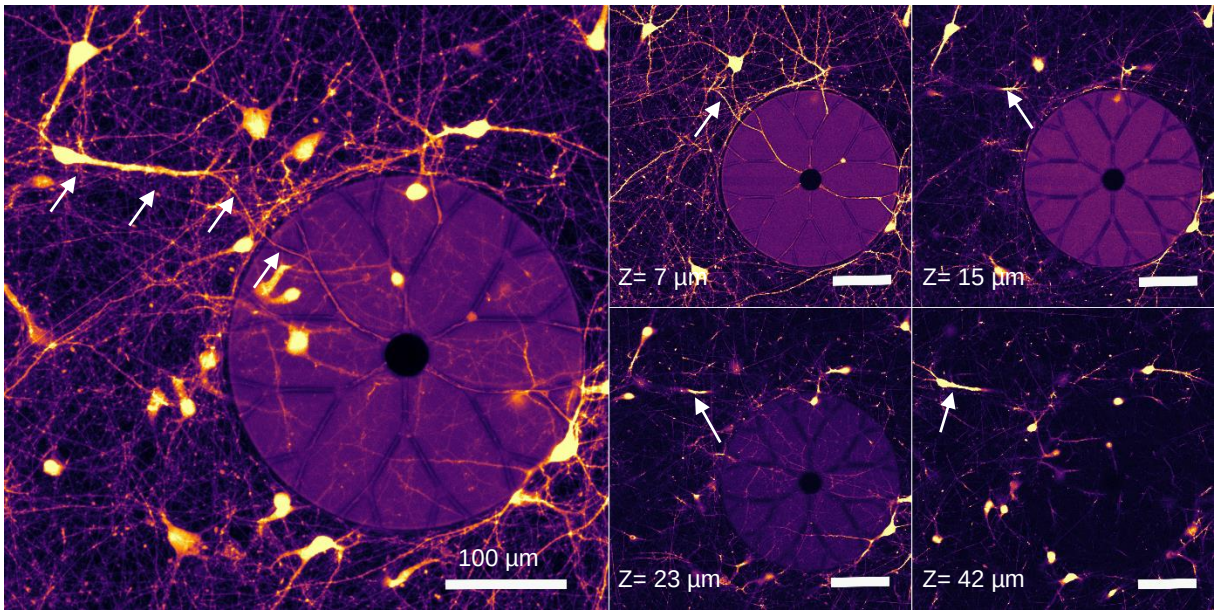

Figure 5.4: Neuronal projection into the microtunnel of the CµE. Different Z-planes are showing the growth of a neurite inside the microtunnel of a recording CµE. Neurons were transduced with a virus containing eGFP fluorophore and imaged with a 10X objective. Arrows illustrate the outgrowth of the neuronal projection into the microtunnel.

The presented nMPS becomes more valuable for disease and compound testing (Watson et al., 2017; Mastrangeli et al., 2019), thanks to the microfluidic piece's design structured to be compatible with automation (figure 5.5a). By producing a self-designed adapter compatible with a 384-well plate system (figure 5.5b), neurons transduced with eGFP could be imaged utilizing the Yokogawa system. By placing two nMPS at a time inside the adaptor, this high-content assay ensures the reduction of manual intervention.

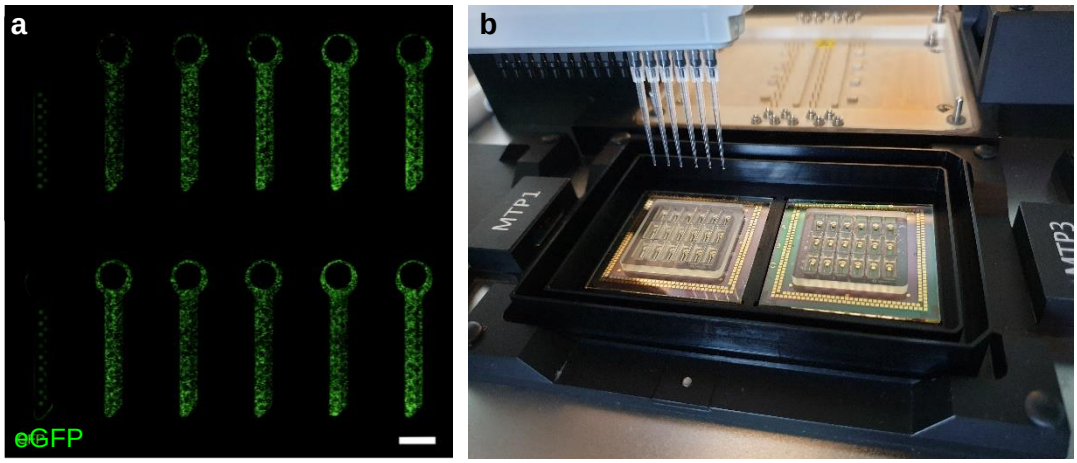

Figure 5.5: Automated imaging. Maximum intensity projection (MIP) (100 µm) of transduced eGFP neurons in 12nMPS were imaged with the Yokogawa system (scale bar= 2 mm) (a) while placed in a self-designed adaptor (b). Adaptor carries two 18nMPS (only used for representation). Images at the Yokogawa station were taken by Dr Stella Donato (DZNE).

The visualisation of neurites' growth through the microtunnels could only be achieved via live-imaging with eGFP-transduced neurons and not through other staining methods, such as immunolabelling. The reason for this is the trespassing of the staining antibodies through the microtunnels, especially since they are at the bottom of the thick gel. Since this nMPS is gravity-driven, antibodies most likely travel only in the z-plane. Placing the samples on a moving rocker promoted antibodies to advance in the xy-plane, although not enough to stain the entire neurite inside the microtunnel. Additionally, for this matter, completing an immunocytochemistry is much more laborious and less informative about the neurons' health throughout its outgrowth if compared to live-imaging with transduced cells. Despite the mentioned disadvantages, ICCs prove to be more favourable when more detailed information is required. Cell-to-cell interaction is more straightforward to evaluate by performing an ICC due to the lack of commercial AAV specific for certain molecules. For the same reason, it is more advantageous to employ immunolabelling techniques if more than one cell type is to be targeted or defined in a cell culture. ICCs should especially be considered when studying immune responses towards an agent, as utilisation of AAV may affect the results. In this study, ICC methodology was thoroughly examined for an almost 1 mm thick gel. In this manner, neurons, microglia, astrocytes (figure 5.6a, supplementary video 2) and inhibitory neurons (figure 5.6b) could be imaged. Most importantly, detailed information about pre- and postsynaptic features were acquired (figure 5.6c). This technique was highly relevant to evaluate the potential of utilizing this system as a device for studying neuroinflammation.

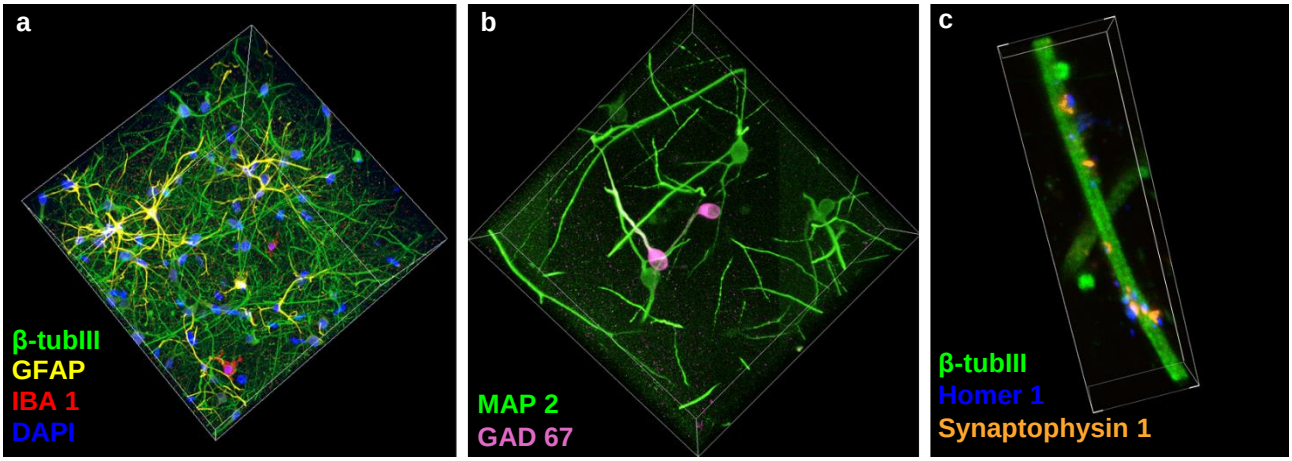

Figure 5.6: Cell imaging of immunostained primary cell culture. Cell culture was labelled with βtub III (neurons), GFAP (astrocytes), IBA1 (microglia) and DAPI (nuclei) and imaged at 25X. Scale: H= 249 µm; A= 262 µm x 262 µm (a). Inhibitory neurons were stained with GAD 67, while dendrites were marked with MAP 2 Scale: H= 66 µm; A= 225 µm x 225 µm (b). Labelling of pre- (synaptophysin), postsynaptic (Homer 1) and neuronal markers (β-tubulin III, β-tubIII). Scale: H= 6 µm; A= 11 µm x 36 µm (c).

5.1.3 Electrophysiology

The information of interconnected circuits propagates across the brain as electrical activity, being the most crucial characteristic as it determines cognitive, sensory and motor functions. Therefore, the microelectrode-based method was implemented to target electrophysiological activity. To insulate the neural activity, recording electrodes integrated into the substrate were covered by a cap (CμE) that contained pre-designed microtunnels, through which the neurites grew (figure 5.4 and 5.7a). It is worth noting that previous work has shown the importance of an insulating structure (Molina-Martínez, 2020; Molina-Martínez et al., 2021). These structures ensure the increase of the sealing resistance between the neurite's membrane and the electrode, ultimately allowing the recording of electrical impulses of lower amplitude travelling down the neurites (figure 5.7c). Conversely, an uncovered electrode does not record any activity (figure 5.7b) unless a neuron's cell body is not more than 15 μm far from the electrode (Molina-Martínez et al., 2021). Having 3D neurons in that proximity to an open electrode is improbable considering that all cell bodies are homogeneously dispersed in the 3D scaffold in a non-adherent manner. Therefore, CμEs are necessary to be able to perform any electrophysiological recordings.

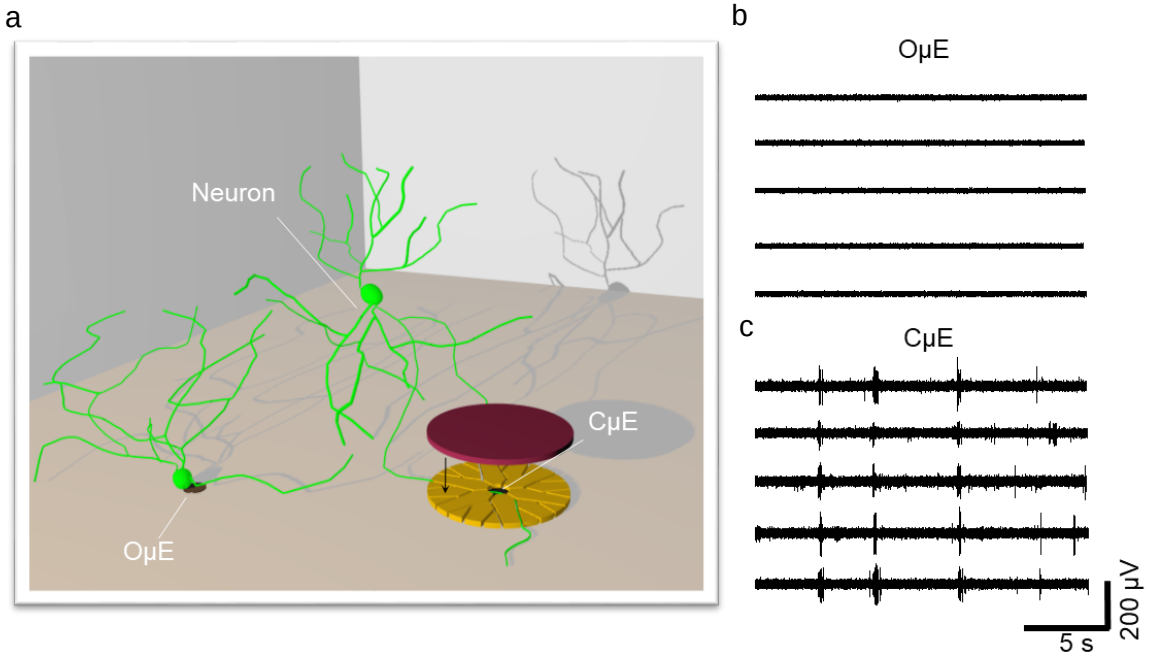

Figure 5.7: Schematic illustration of two neurons growing next to an open microelectrode (OμE) and the capped microelectrode (CμE). Neurons project their neurites through the microtunnels of the CμE towards the covered electrode (a). Activity measured by open (b) and covered electrodes (c) is represented as trace plots. Open electrode recordings were performed by Dr Beatriz Molina Martínez.

This system allows the measurement of neuronal activity in a direct, non-invasive and high-resolution approach. The latter was validated by applying reference compounds picrotoxin (PTX), tetrodotoxin (TTX) and rotenone, and was then quantified by diverse parameters, i.e., mean firing rate (MFR), burst frequency rate (BFR), percentage of spikes in bursts (%SiB), burst duration (BD), interspike interval of the coefficient of variance (ISI CoV), network burst frequency (NBF) (Hz), MFR in network bursts (MFR in NB) (Hz) and percentage of bursts in network bursts (B in NB) (%). Additionally, Ca^{2+}-imaging and optical stimulation demonstrated the assessment of excitability across the entire volume of the 3D neuronal network.

5.1.3.1 Variability

The evaluation of the reproducibility and consistency of the obtained results by employing this novel technology was fundamental. Consequently, the data variability was examined by estimating the differences across different wells, devices and cell seedings (table 5.1).

The low intrinsic variability was corroborated by studying the inter-well variation (figure 5.8). For this purpose, the innate variability between wells in 3 devices plated in one day was compared for various parameters (MFR, BFR, SiB, BD, ISICoV). Even though most of the values captured from electrodes were dispersed, the mean and median values lay among similar ranges across the diverse parameters (table 9.1). Some wells do present dissimilarities among each other, especially when considering the MFR and BFR in device C. Reasons for these variations can be assigned to uncontrollable biological or technical causes. The latter enclose materials utilized during cell isolation, such as pipetting. Inconsistencies arising during pipetting might affect the network's biology by providing an unequal cell density among wells. By holding a lower cell number, the synaptic connections may decrease, and, therefore, the transmitted electrical information might also be reduced. Consequently, the network’s maturity develops more moderately. A more likely fallout due to a lower cell concentration is a decreased number of neurites growing through the microtunnels of the CμE. This condition is not only correlated to the cell density but also chance. However, it is safe to say that the more neurites, the higher is the chance for neurites to grow through microtunnels. Nonetheless, this may not only depend on the neuronal cell number but also on the health of the cell culture, which is correlated to a more prominent neurite outgrowth (Hancock et al., 2015).

As a consequence, results suggest that even if cell cultures are seeded at the same time in a given device, the outcome may show slight dissimilarities. However, in most cases, those variations are not present and, hence, do not significantly affect the outcome of the results.

Therefore, this compilation can be considered as a homogeneous data set. Consequently, data were grouped into wells and tested for normality to compare devices and cell seedings.

Table 5.1: List of recordings. Seventeen recordings were registered at ten different experimental/preparation days by employing five different devices.

Preparation	Recording	MEA n°
1	1	A
1	2	B
1	3	C
2	4	B
3	5	A
3	6	B
3	7	C
3	8	D
4	9	A
4	10	C
4	11	D
5	12	C
6	13	A
7	14	A
8	15	A
9	16	E
10	17	E

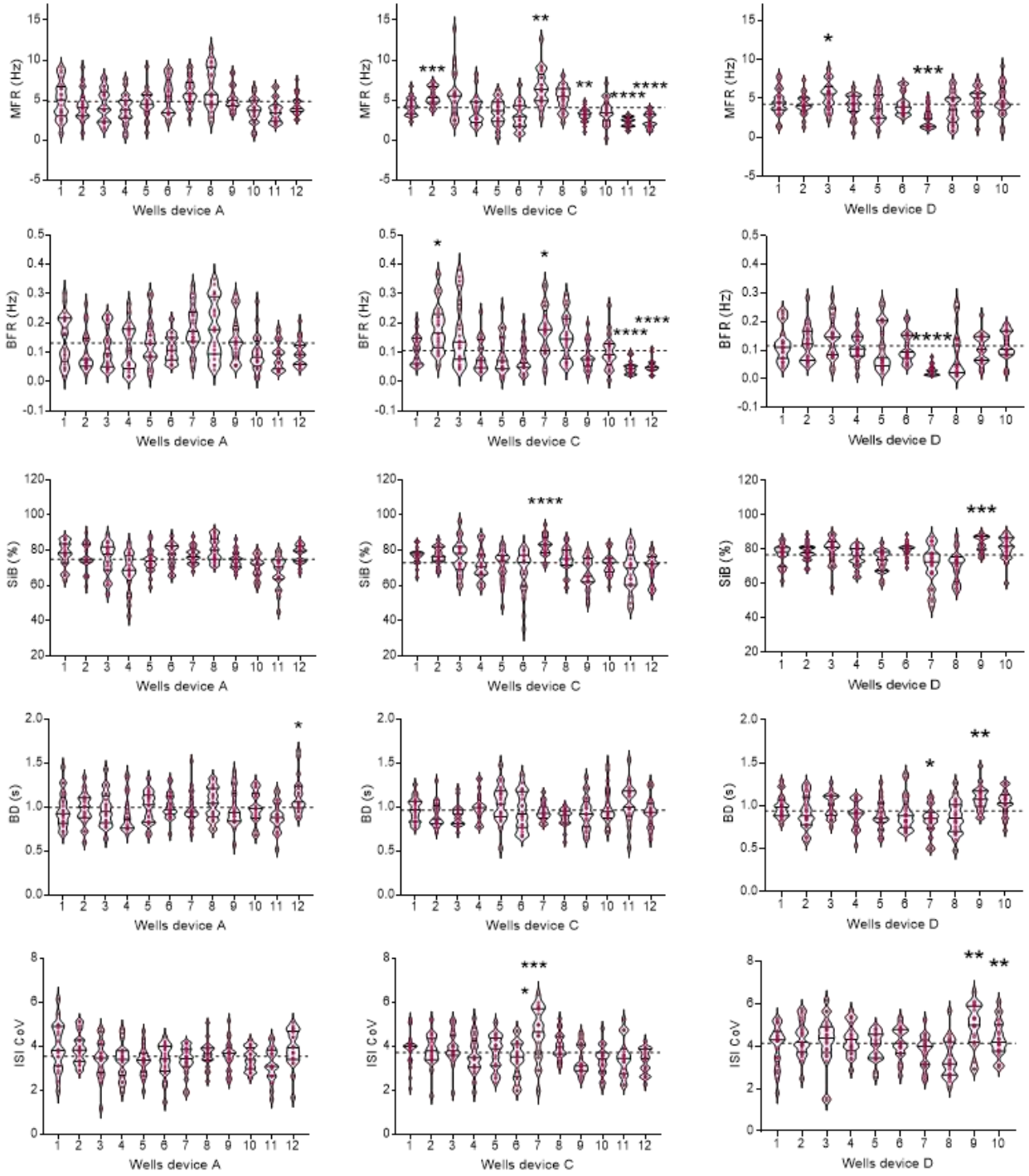

Figure 5.8: Data of single wells from 3 different devices (A, C and D) from preparation 4. Values of electrodes from wells were compared to the mean of all values of specific devices (A, C and D) collected on preparation day 4. The following data are represented in violin plots: mean firing rate (MFR) (Hz), burst frequency rate (BFR) (Hz), number of spikes in burst (SiB) (%), burst duration (BD) (s), and interspike interval of the coefficient of variance (ISI CoV). Values of electrodes are represented as red dots. The mean of all values from a certain device is represented as a discontinuous black line. Median and quartiles are illustrated inside the violin plots as a continuous black line. Asterisks indicate significant differences between a well with the mean of all values of a certain device: *p-value <0,05; **p-value <0.01; ***p-value <0.001; ****p-value <0.0001.

The dispersion of the data was estimated in combination with the Shapiro-Wilk test (SWT), QQ plots and frequency histograms (figure 5.9). Most of the collected data (N= 187 wells) demonstrated not being normally distributed according to the SWT (MFR, BFR, %SiB, BD, MFR in B and %B in NB). Indeed, by examining the visual normality tests, it becomes clear that some of the data are slightly left-skewed (MFR, BFR, BD, MFR in B). Nevertheless, this is a usual behaviour of neuronal dynamics indicating mature networks (Biffi et al., 2013; Negri J. et al., 2019), which is also corroborated by right-skewed data of SiB (%) and B in NB (%), as the higher their value is, the more mature the network is. Consequently, data were treated as normally distributed data.

Despite the symmetry observed in most of the examined variables, variations become apparent when comparing values from biological replicates obtained from cell isolations performed at different experimental days (figure 5.10) (table 9.2). These are most likely to be attributed to external issues affecting the quality of the animal-derived cells or the network's connectivity. Apart from the aforementioned technical and biological factors, here, additional elements may play a role. Additional technical causes may be using different Matrigel batches, which present different biological and technical properties from batch to batch (Kleinman et al., 2005; Huhges et al., 2010). Different Matrigel lots may improve or decrease the quality or outgrowth of neurites, causing dissimilarities among cell cultures. Further elements affecting the captured activity may be ambient conditions during incubation or while registering the neural information. Utilised media should not be a component affecting the neurons' health; however, evaporation of the mentioned could suppose a worse nurturing condition for the culture. Less nourished neuronal cultures may lead to a lower neurite outgrowth, reducing the chance of neurites growing towards a CµE. Furthermore, the data may also be influenced by the cell density present in the 3D scaffold, as mentioned in the section above. Those could be, again, related to the employed materials during the cell isolation.

Moreover, an additional source of disparity due to technical issues may play a determinant role for the observed variations, that is, the microfabrication of the employed devices. Therefore, values were grouped into utilized platforms and compared to each other to exclude variabilities arising during the device's fabrication (figure 5.11) (table 9.3). Some of the data imply that using certain devices could influence the outcome significantly, especially for BFR, %SiB and MFR in NB. However, those data might also be altered by the biological differences resulting from different preparations. The preparation's influence is corroborated when comparing the captured values of various nMPS plated the same day (figure 5.12). Very little significances imply a repercussion from employing various devices. Results demonstrate that the mean value for %SiB of recordings performed at preparation 1 (45.57 %) is almost half of the %SiB

registered at preparation day 3 and 4 (84.7 % and 74.04 %, respectively) (table 9.4). A similar tendency is observed for MFR in NB, where the average value from preparation 4 (221.5 Hz) is almost double as high as from preparations 1 and 3 (117.4 Hz and 132.3 Hz, respectively). Additionally, the BFR documented at preparations 1, 3 and 4 unveil, once more, the variation present between cell seedings at different days (0.09 Hz, 0.15 Hz and 0.13 Hz, respectively). The latter is also accurate for other variables, especially MFR and %B in NB (table 9.4).

Those data affirm the variability arising from isolating cells at different time points and not necessarily from using various devices. Nonetheless, as previously mentioned, certain factors do also affect the variability of recordings performed at the same time point, such as the cell density, network health and chance of neurites crossing the microtunnels. This is corroborated by a highly significant difference displayed for BFR in the first recording of preparation 3 (device A), which could be attributed to biological causes and not due to, for example, using different devices. This supposition is supported by the fact that the same device affecting in preparation 3, did not influence the outcome for performed recordings of preparation 1 and 4. Impactful variations between that device and others were only seen in preparation day 3.

Regarding the presented results, it is safe to say that causes arising from plating isolated neurons on different days are the most influential aspect of this study. Therefore, values collected in toxicology studies were analysed in percentage changes over a control. Ultimately, changes arising due to drug application were measured considering the basal activity before any drug application. In this manner, variations arising due to different preparations were reduced.

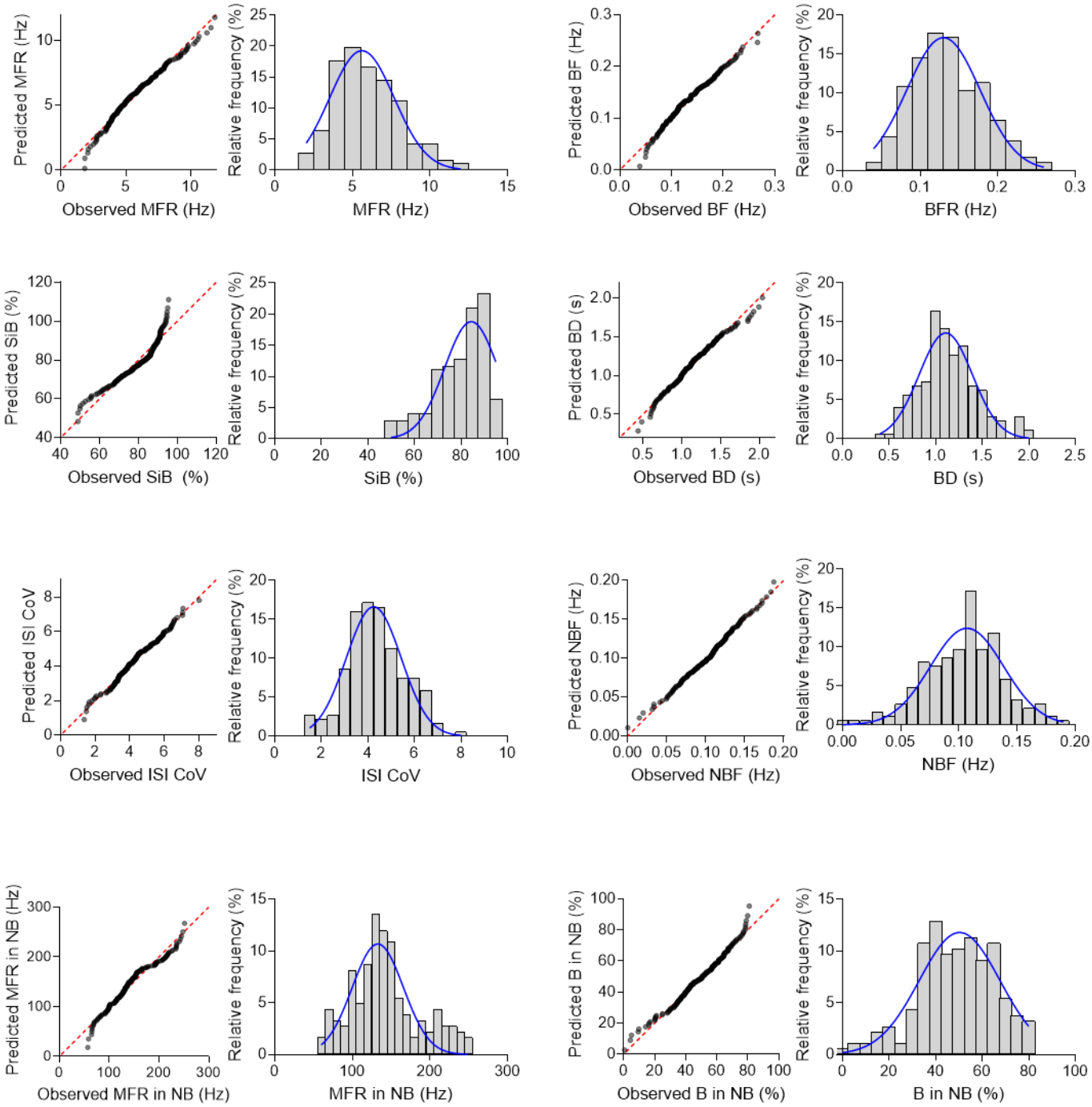

Figure 5.9: Distribution of the data. Collected data are represented in QQ plots and frequency histograms. QQ plots show the expected distribution vs a fictional perfect distribution of the means of all wells, while frequency histograms show the density of the data within a specific range. The red discontinued line represents a perfect fit for the data distribution. The blue line indicates the Gaussian curve fit. The following data are represented: MFR (Hz) (Shapiro-Wilk value $p < 0.05$), BFR (Hz) (Shapiro-Wilk value $p < 0.05$), SiB (%) (Shapiro-Wilk value $p < 0.05$), BD (s) (Shapiro-Wilk value $p < 0.0001$), ISI CoV (Shapiro-Wilk value $p = 0.24$), NBF (Hz) (Shapiro-Wilk value $p = 0.66$), MFR in NB (Hz) (Shapiro-Wilk value $p < 0.0001$) and B in NB (%) (Shapiro-Wilk value $p < 0.05$).

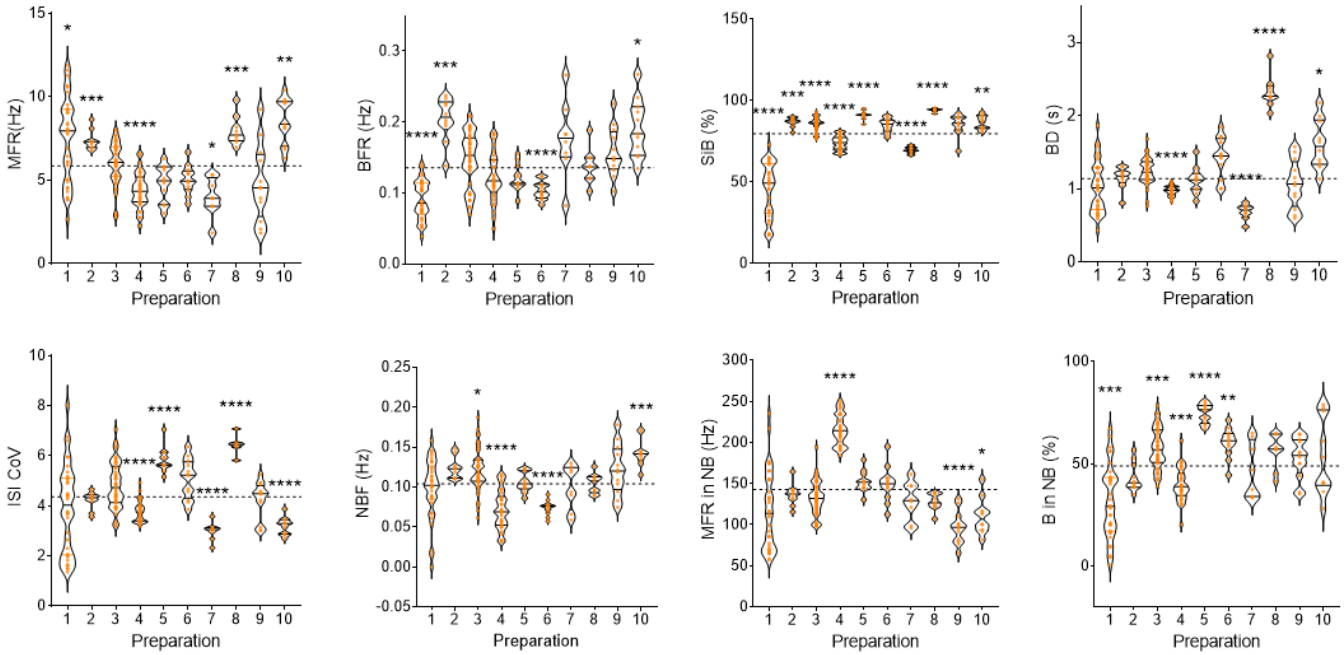

Figure 5.10: Data represented according to preparations. Means of all wells were categorized into preparations and analysed for significant differences between the sum of all values (N= 187). The following data are represented in violin plots: MFR (Hz), BFR (Hz), SiB (%), BD (s), ISI CoV, NBF (Hz), MFR in NB (Hz) and B in NB (%). Means of wells are represented as orange dots. The mean of all values is represented as a discontinuous black line. Median and quartiles are illustrated inside the violin plots as continuous black lines. Asterisks indicate significant differences between a certain day of preparation and the mean of all values: *p-value <0,05; **p-value <0.01; ***p-value <0.001; ****p-value <0.0001.

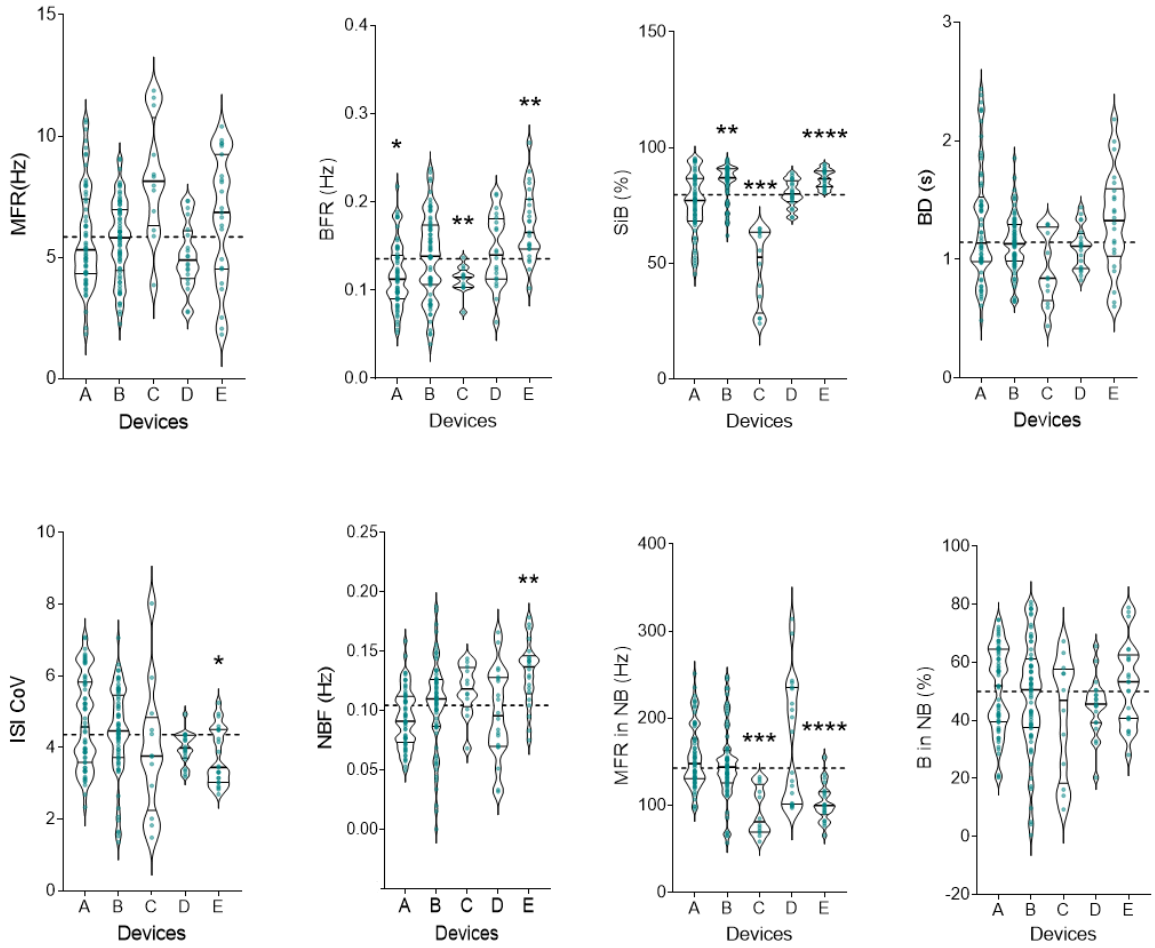

Figure 5.11: Data represented according to the five used devices. Means of all wells were categorized into the devices used for this study and analysed for significant differences between the mean of all values (N= 187). The following data are represented in violin plots: MFR (Hz), BFR (Hz), SiB (%), BD (s), ISI CoV, NBF (Hz), MFR in NB (Hz) and B in NB (%). Means of wells are represented as turquois dots. The mean of all values is represented as a discontinuous black line. Median and quartiles are illustrated inside the violin plots as a continuous black line. Asterisks indicate significant differences between a certain device and the mean of all values: *p-value <0,05; **p-value <0.01; ***p-value <0.001; ****p-value <0.0001.

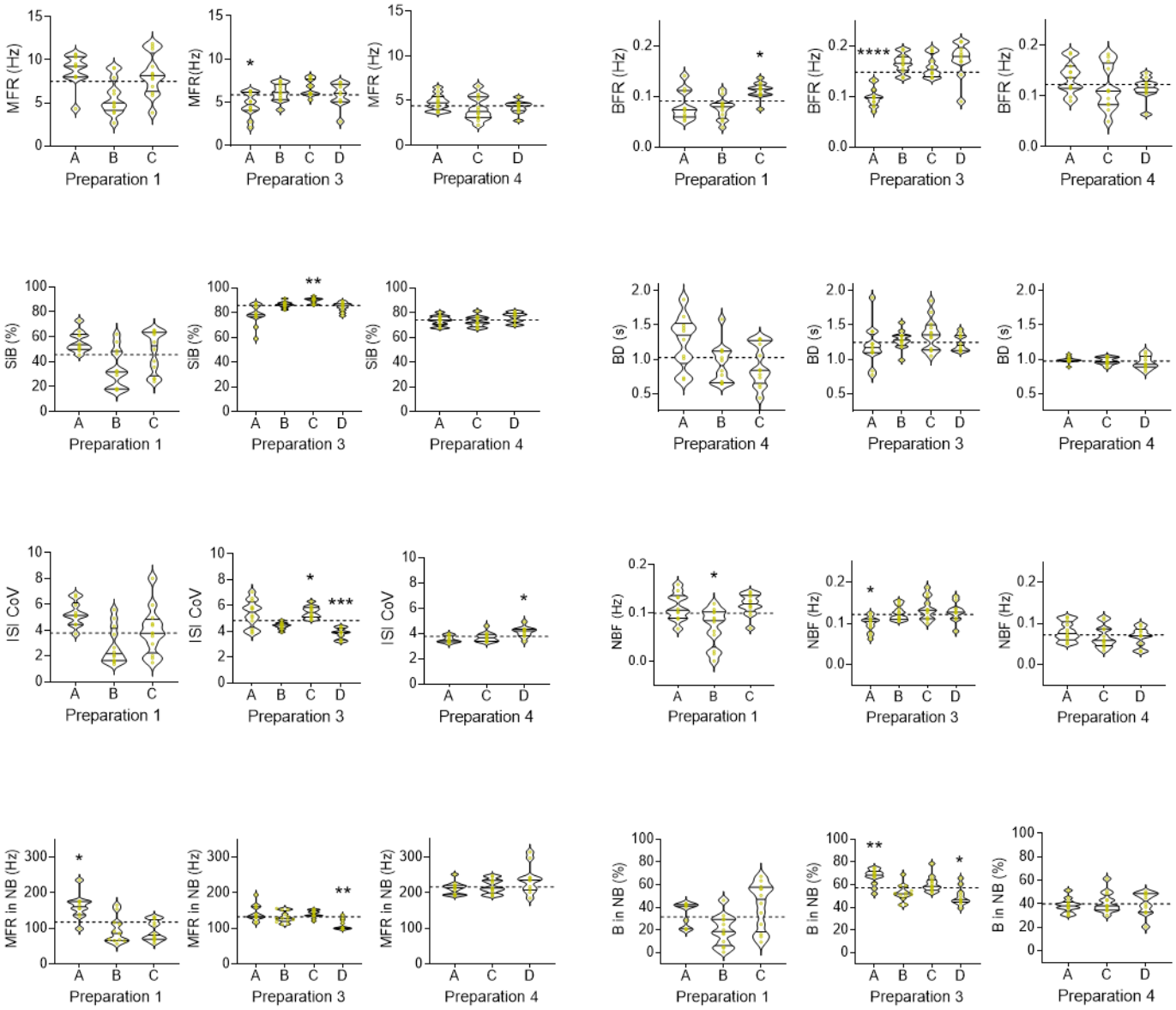

Figure 5.12: Data of single devices categorised into preparations. Means of wells of devices corresponding to three different preparations (1, 3 and 4) were compared to the mean of all the values of a certain preparation. The following data are represented in violin plots: MFR (Hz), BFR (Hz), SiB (%), BD (s), ISI CoV, NBF (Hz), MFR in NB (Hz) and B in NB (%). Means of wells are represented as yellow dots. The mean of values is represented as a discontinuous black line. Median and quartiles are illustrated inside the violin plots as a continuous black line. Asterisks indicate significant differences between a certain device of a certain day of preparation and the mean of all values collected that day: *p-value <0,05; **p-value <0.01; ***p-value <0.001; ****p-value <0.0001.

5.1.3.2 Toxicology

The advantage of employing this nMPS was reinforced by analysing the effect of reference compounds in a non-invasive, direct and detailed manner. The chemical stimulants used to strengthen the validation of this system were PTX, TTX and rotenone. The former is a GABA antagonist and causes a seizure-like activity in neurons. On the contrary, TTX and rotenone are known to decrease neural activity by blocking sodium channels and disturbing the electron transport chain in mitochondria, respectively. By applying these drugs for 10 minutes, the addition of each compound impacted as expected.

As the PTX causes the network's activity to be subjected to triggering electrical impulses without any inhibitory control, the firing trains of action potentials are incredibly high for a longer time. Moreover, the bursting becomes more regular throughout the recording since the time the network needs to recover from the seizure-like behaviour is constant throughout the recording. These characteristics are corroborated by the increase of BD, MFR, %SiB, MFR in NB and ISI CoV (figure 5.13). Furthermore, this outburst of activity causes the BFR, and consequently the NBF, to be reduced. Once more, these data demonstrate the diversity of neurons present in this nMPS, especially excitatory neurons and inhibitory GABAergic neurons. Moreover, they demonstrate the presence of synapses between excitatory and inhibitory neurons and, therefore, a biological neuronal behaviour.

Contrary to PTX, TTX shows a loss of activity. As the inhibition causes the blocking of activity, a decrease in all parameters mentioned above is demonstrated (figure 5.14). However, not a significant decrease. In most cases, the highest doses need to be applied to corroborate this statement, implying that a 1 nM concentration may be too low. It appears as TTX 1 nM does not impact significantly when present for only 10 minutes. Either the mechanism of action is not fast enough to notably affect, or insufficient sodium channels are blocked to collapse the neuronal network. If the latter was the case, this might affect cell cultures differently, as it might be correlated to biological factors. As previously mentioned, the time point at which cells were isolated might impact the viability and cell density of the cell cultures. Suppose it is true that a higher amount of TTX molecules is needed to block enough sodium channels to knockout the circuit's activity. In that case, it can be argued that a higher cell density implies a lower chance to block sufficient channels to affect the network's activity. Nevertheless, this can only be proved by replicating this assessment employing a lower cell density or increasing the sample size. Power analysis ($p= 80\%$; $\beta= 0.2$; $\alpha= 0.05$) indicated the need of more samples to see an effect. However, those analyses are tightly coupled to the variability (standard deviation) of the samples, which, as demonstrated, varies among preparations.

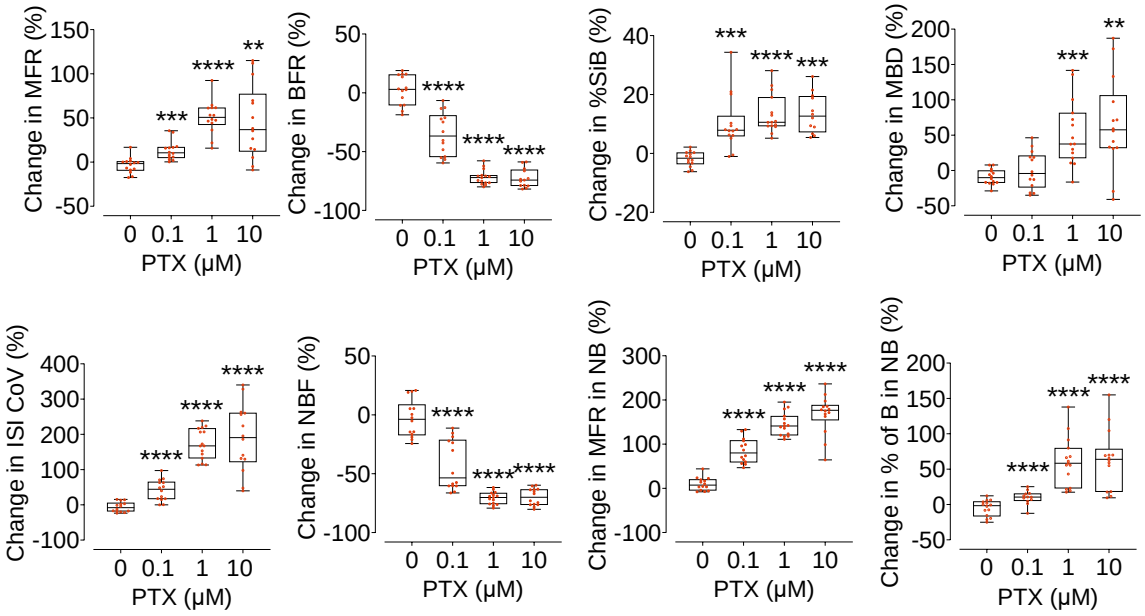

Figure 5.13: Response to PTX. 3D neuronal circuits were stimulated with different doses of PTX. Orange dots represent the means of wells to which a certain concentration was applied. The following data are represented: MFR (Hz), BFR (Hz), SiB (%), BD (s), ISI CoV, NBF (Hz), MFR in NB (Hz) and B in NB (%). Box plots indicate the median of each condition and its quartiles. Whiskers illustrate the minimum and maximum value. Asterisks indicate significant differences between the non-treated wells vs the treated wells: *p-value <0,05; **p-value <0.01; ***p-value <0.001; ****p-value <0.0001.

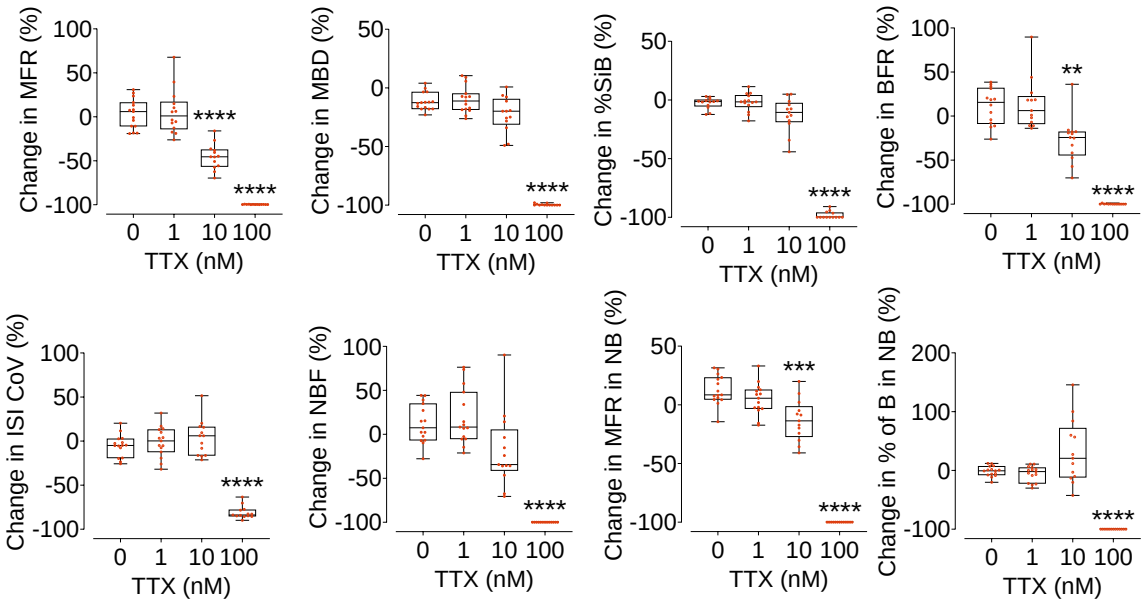

Figure 5.14: Response to TTX. 3D neuronal networks were stimulated with different doses of TTX. Black dots represent the means of wells to which a certain concentration was applied. The following data are represented: MFR (Hz), BFR (Hz), SiB (%), BD (s), ISI CoV, NBF (Hz), MFR in NB (Hz) and B in NB (%). Box plots indicate the median of each condition and its quartiles. Whiskers illustrate the minimum and maximum value. Asterisks indicate significant differences between the non-treated wells vs the treated wells: *p-value <0,05; **p-value <0.01; ***p-value <0.001; ****p-value <0.0001.

Interestingly, when treating the neuronal network with rotenone, the circuit's activity is disrupted rapidly. As mentioned, rotenone impairs the mitochondria's functionality, a critical organelle that supplies chemical energy to the cell (Pamies et al., 2018). Neurons depend on this source of energy to initiate the elaborate process of neurotransmission. Therefore, when this chain is disrupted by rotenone, the neuron's and network's activity is reduced (figure 5.15). The decrease is demonstrated by a reduction of the MFR, BFR, BD and NBF. The higher the dose, the higher the effect.

Moreover, a disruption of the network's synchronicity seems to increase, which is demonstrated by a lower burst triggering inside NB when compared to untreated circuits; however, not significantly. The effect on the mentioned parameter may be caused by the large variability inside each data set, more present in cultures treated with higher rotenone concentrations. These might be caused by several biological mechanisms possibly related to the mitochondrial fusion-fission dynamics (Bertholet et al., 2016) as well as previously mentioned dissimilarities caused by the network's viability. By increasing the sample size of wells treated with lower concentrations of rotenone, the effect of the latter may be more obvious.

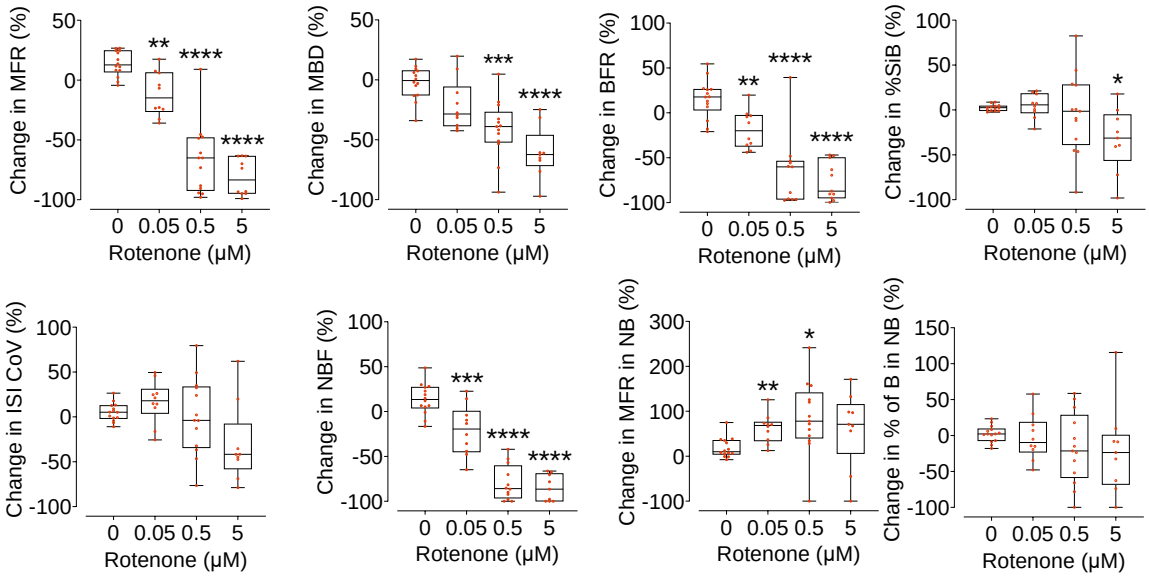

Figure 5.15: Response to rotenone. 3D neuronal circuits were stimulated with different doses of rotenone. Black dots represent the means of wells to which a certain concentration was applied. The following data are represented: MFR (Hz), BFR (Hz), %SiB (%), BD (s), ISI CoV, NBF (Hz), MFR in NB (Hz) and %B in NB (%). Box plots indicate the median of each condition and its quartiles. Whiskers illustrate the minimum and maximum value. Asterisks indicate significant differences between the non-treated wells vs the treated wells: *p-value <0,05; **p-value <0.01; ***p-value <0.001; ****p-value <0.0001.

The immediate functional effect of rotenone was also evident visually during the recordings, where the reduced activity became obvious by fewer firing APs (figure 5.16). However, apparent morphological impact on the neuron's health could be observed only at the highest doses (0.5 and 5 µM) after 6 or 24 h (figure 5.17). Nonetheless, no significant morphological differences were seen when treating neurons with 0.05 µM of rotenone. Certainly, this supports the importance of acquiring detailed information about the electrical information transmitted through neurons to understand better any compound's phenomena affecting neuronal circuits' physiology.

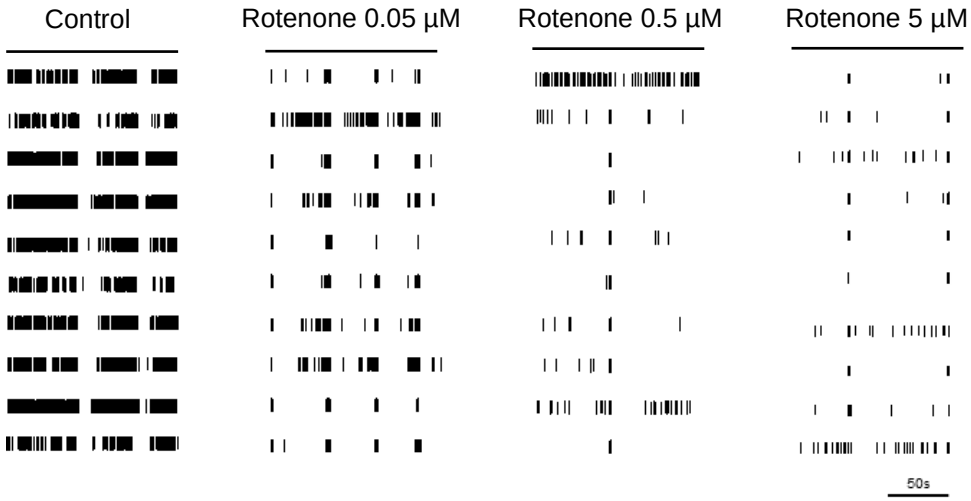

Figure 5.16: Raster plot of electrophysiological activity from neurons treated with rotenone. Spontaneous activity of 4 wells after a 10-minute treatment of rotenone at different concentrations. Black lines represent one spike. Only 10 out of 21 electrodes are shown here for simplicity.

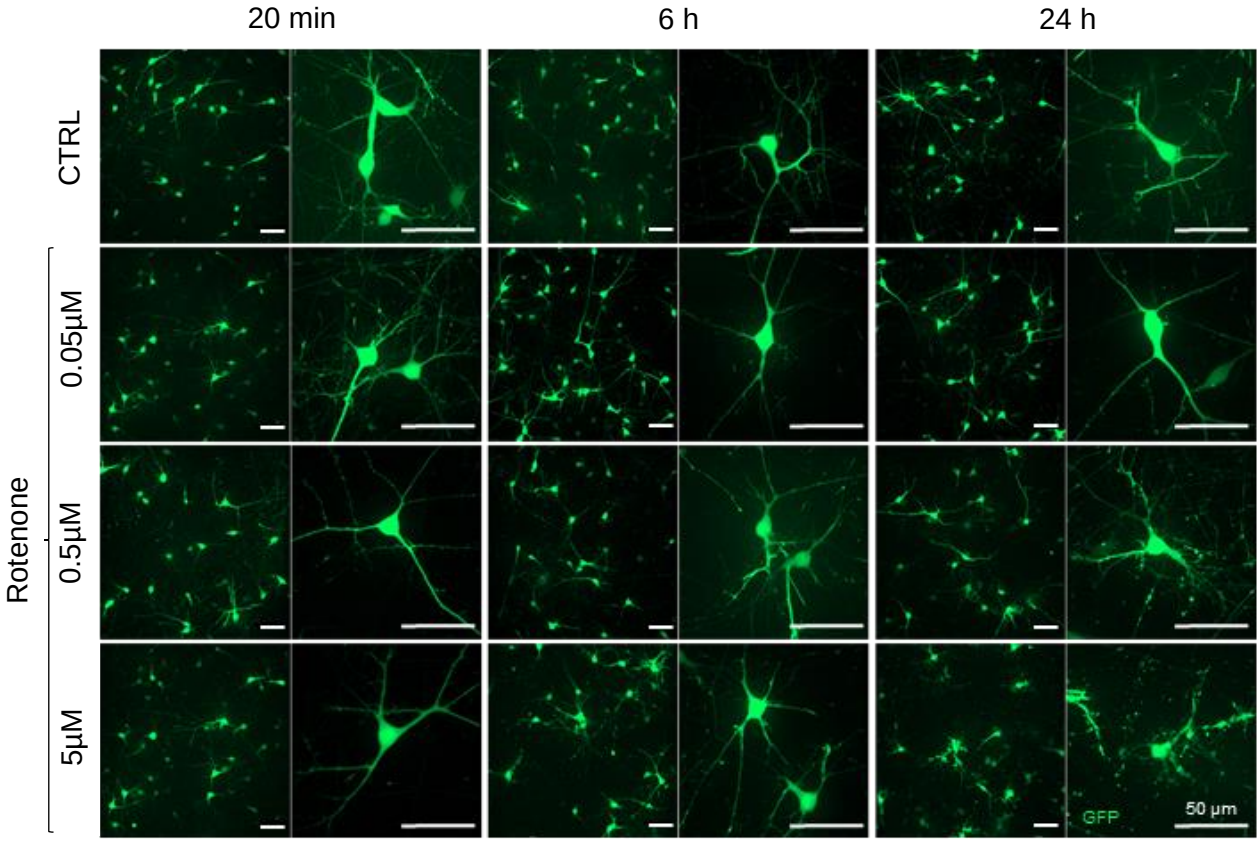

Figure 5.17: Morphological assessment of time and dose-dependent response to rotenone. 3D neuronal circuits were stimulated with different doses of rotenone and imaged at different time points. Neurons were transduced with eGFP. Illustrations represent maximum intensity projections of images taken with objective 20X and 63X. 20x images represent maximum intensity projections (MIP) of 253 to 458 µm sections; 63x images indicate MIPs of 34 to 120 µm.

5.1.3.3 Synaptic circuits

Another relevant characteristic that needed to be verified was the confirmation of registering a whole-network activity. As electrodes are integrated into the bottom part of the gravity-driven device, it is fair to argue the assumption of synchronous activity from an entire network and not from neurons growing close to the bottom and inside the CµE forming synapses between them. Therefore, two independent methodologies were employed while simultaneously recording electric signals from the neurites.

5.1.2.3.1 Calcium imaging

Firstly, the reinforcement of the nMPS was approached by measuring the calcium influx of the neurons. Hence, nerve cells were transduced with an adenovirus containing GCaMPf6. Calcium transients of neural cell bodies embedded in the hydrogel at a single z-plane of 560 µm were registered while simultaneously recording the basal neuronal activity that was

later chemically altered with PTX 10 µM and TTX 10 nM (figure 5.18). Network bursts identified with electrophysiological recordings (figure 5.18a) were synchronous with an increase of the intracellular calcium, represented as peaks in the fluorescence charts (figure 5.18b, supplementary videos 3, 4 and 5). Moreover, those calcium transients became larger after applying PTX, demonstrating its characteristic feature of a higher activity rate in represented NB, as well as in the previous section (figure 5.13). These data corroborate the communication taking place between neurons in lower and higher sections of the 3D scaffold. More importantly, short network bursts captured with CµE after applying TTX are not gained by the Ca^{2+}-imaging approach. The low detection efficiency substantiates the importance and necessity for a more efficient platform to ease the exhaustive documentation of neuronal circuits.

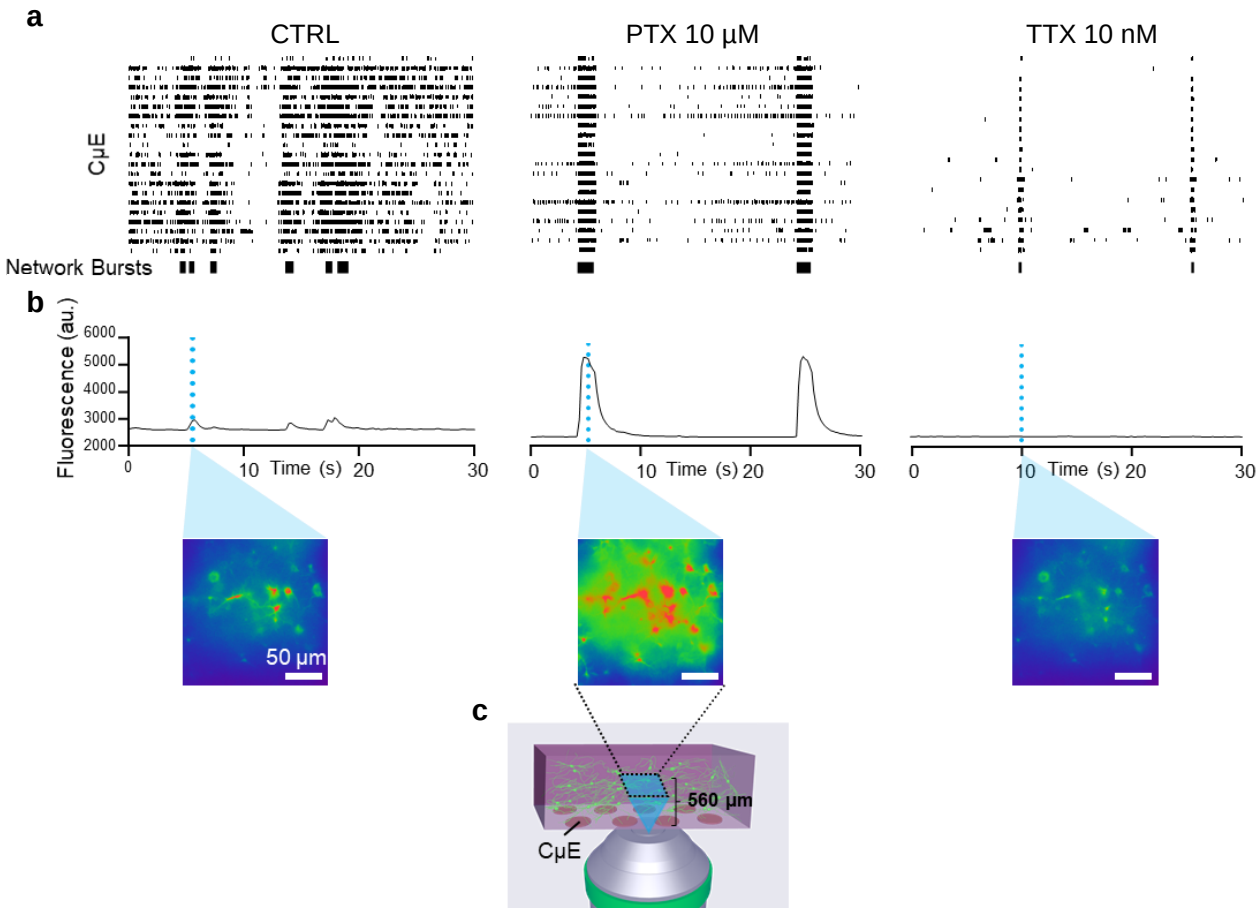

Figure 5.18: Simultaneous Ca^{2+}- imaging and recordings of GcaMP6f- transduced neurons. Recorded electrophysiological activity of a neuronal network subsequently treated with PTX (10 µM) and TTX (10 nM) (a). Fluorescence charts of the Ca^{2+} indicator (au., arbitrary units) over time (s). Suppl. videos 3, 4 and 5) (b). Cells were imaged simultaneously at one Z-plane at the height of 560 µm of the hydrogel (c).

5.1.2.3.2 Optogenetics

Secondly, a supplementary optical technique to electrophysiological recordings was employed. Neurons were transduced with foreign DNA incorporating channelrhodopsin-2 (hChR2) fused with YFP to express light-sensitive ion channels that open when stimulated by short pulses of blue light (470 nm), leading to cell depolarisation. Digital micromirror device (DMD) technology was used to reflect light onto the sample, obtaining patterned illumination of digitally defined regions. The latter was set to illuminate an area of 0.04 mm^2 between two electrodes at the height of 100 µm. The small area was stimulated every 10 seconds for 1 second with 5 ms pulses at 40 Hz. (figure 5.19a). It should be noted that the stimulation light goes through the gel. Therefore, it is not possible to accurately define the Z-plane or which exact neurons were triggered. Nonetheless, xy-planes remained defined as explained.

Optical activation of hChR2, although limited to only those neurons in the illuminated area, triggered activation of action potentials that were detected by individual electrodes as synchronized network bursts (figure 5.19b). More importantly, trains of spikes were primarily fired when stimulated with light (figure 5.19c). These data suggest that neurons are not only synaptically connected in the z-plane as calcium-imaging demonstrated in the previous section (section 5.1.2.3.1) (figure 5.18) but also in a xy-plane, ultimately corroborating the formation of synaptic circuits in the entire well. Therefore, CµE, even if integrated into the substrate of the device, proved to be suitable to record 3D neuronal networks. Additionally, data indicate that the current device could be used to explore synaptic plasticity mechanisms (long-term potentiation and depression, LTP and LTD, respectively) in 3D neuronal circuits.

To further explore this possibility with a throughput compatible with drug discovery, all wells were stimulated simultaneously by placing the optic fibre on top of the device while continuously monitoring electrophysiological activity captured with CµE (figure 5.19d). Network bursts identified in all wells were independent of each other until wells were optically stimulated in parallel (figure 5.19e), demonstrating, once more, the robustness and reproducibility of the nMPS for high-throughput studies.

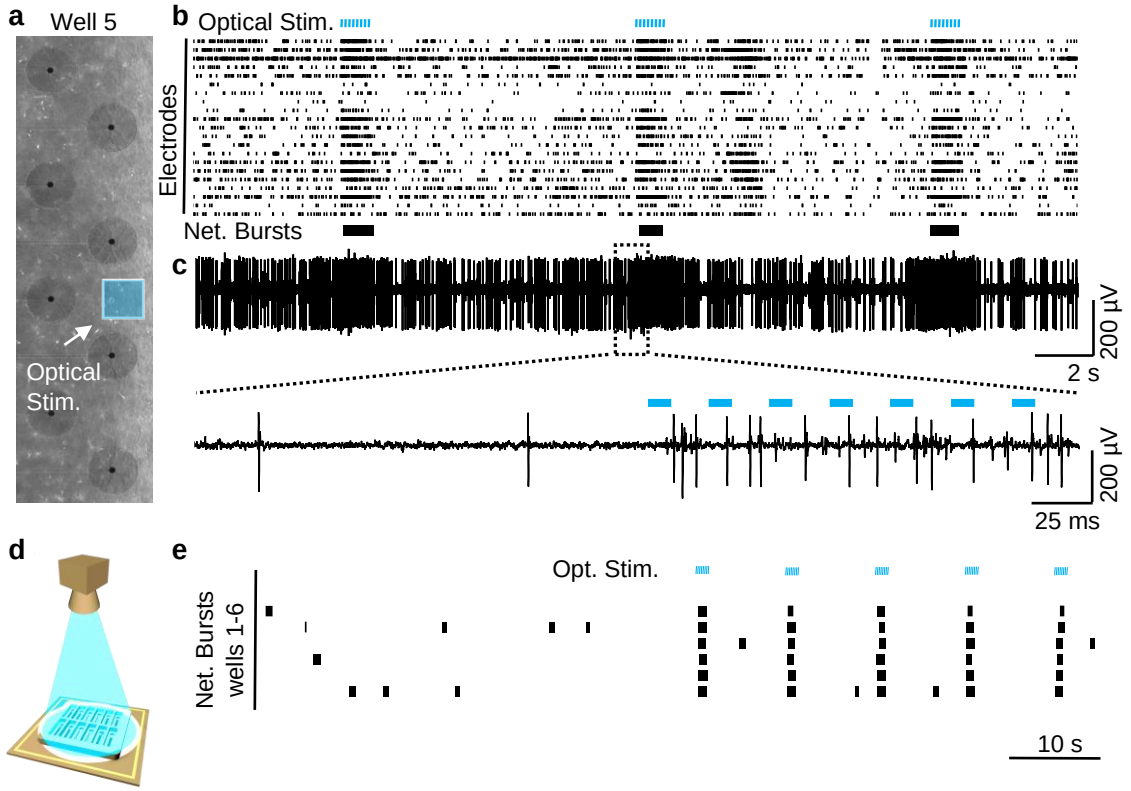

Figure 5.19: Optical stimulation of 3D neuronal networks transduced with Channelrhodopsin. The neuronal network in one well was stimulated with light in a defined area at 100 µm height (a) and recorded simultaneously (b and c). Neuronal circuits from 6 different wells were simultaneously stimulated with light (d) and recorded (e). Thick black lines indicate network bursts, blue lines indicate light stimulation.

5.2 Neuroinflammation

After the successful validation of 12nMPS, this study further focused on applications for the nMPS. Ultimately, it was evaluated if the device could be potentially employed for studies related to neuroinflammation. For this purpose, a new device was designed to contain 18 wells instead of 12 to increase the assay's throughput (figure 5.20). For this accomplishment, the number of CµE was reduced to 14 per well. However, this showed not to affect the assay. Furthermore, the same cell density (3k/µl) was seeded in a lower volume (7 µl), reducing the number of cells needed for each well. Cells could also survive up to 10 DIV without any shrinkage of the gel.

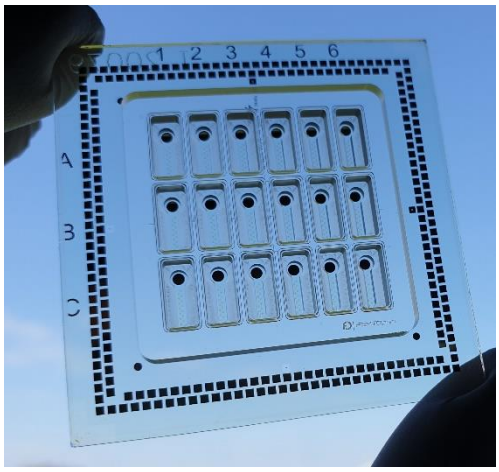

Figure 5.20: 18-well nMPS. Final device carrying 18 independent experiments and 14 electrodes per well.

5.2.1 Microfabrication of 18-well nMPS

The microfabrication process was performed identically to the procedure employed for the 12nMPS. Accordingly, the reproducibility of the CµE was similarly high as in the previous version (figure 5.21). Moreover, electrophysiological recordings showed the same quality even though electrodes in the 18nMPS were surrounded by fewer entries (12, instead of 24). The recording's quality was also corroborated by a previous study carried out by our former colleague (Molina-Martínez, 2020; Molina-Martínez et al., 2021). As well as in the 12nMPS, the cell seeding procedure was simple and could be carried out in all 18 wells at once while keeping the necessary cold temperatures. Ultimately, this upscale provided a higher throughput without affecting functional nor morphological readouts.

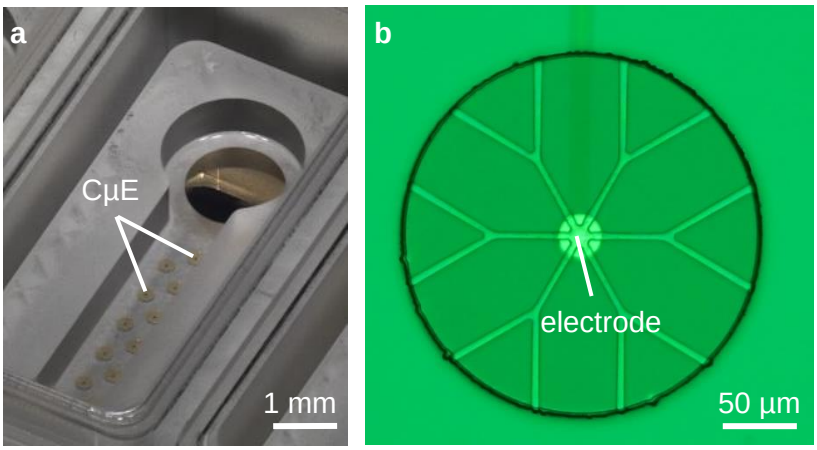

Figure 5.21: Updated CµE. Fourteen electrodes built on the substrate in the gel compartment. Image was taken by Dr Peter Jones (a). SU-8 structure with 12 entries leading towards the electrode. Image was taken by Fulya Ersoy (b).

5.2.2 Acquisition of microglia

Microglia were monitored every 2-3 days via the microscope. In the first days, remaining brain cells multiply until they built a more homogenous monolayer on top of which microglia started proliferating more obviously after 7 DIV (figure 5.22). After 11 DIV, microglia were abundant and therefore collected to be further processed for cell sorting and cell seeding in co-culture with neurons and astrocytes (N+AC).

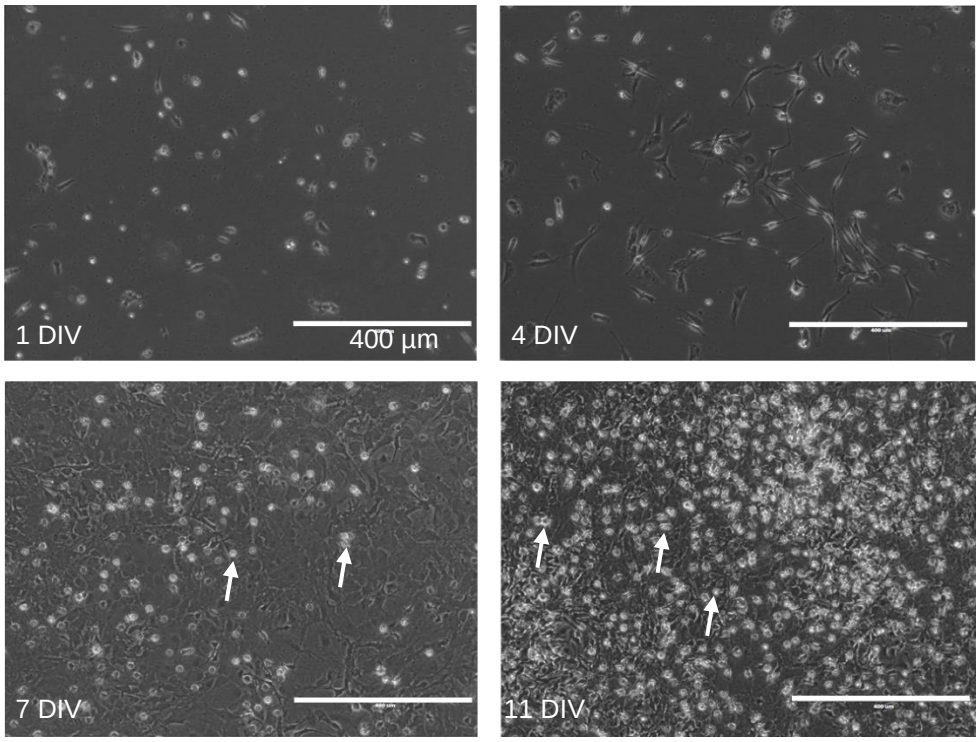

Figure 5.22: Microglia proliferation. Microglia multiply after 11 DIV by growing on top of other present CNS cell types. Microglia are indicated with white arrows.

After staining microglia with marker CD11b, cells were sorted. Here, five main graphs were set to classify CD11b-stained microglia. First, the area of the unstained control cells was defined. Then, singlets were categorised into surviving cells (P6) and then classified into stained (P8) vs unstained cells (P7). In control (figure 5.23), cells behaved as expected and demonstrated to be alive but not stained. Instead, surviving stained microglia were categorized accurately to be sorted (P8) (figure 5.24). Ultimately, approximately 500 K µG were acquired from 4 flasks with a 97-99% purity and a 92-98% viability. However, after centrifugation upon cell seeding, the number of cells was reduced to at least half, although still showing a 92-98% cell viability. Several protocols for reducing cell death during centrifugation were applied without any success. This issue significantly reduced the number of experiments of TriC, leading to more preparations. As demonstrated in section 5.1.3.1, this could potentially increase the variability

among experiments. This variability could also be increased by using different experimental animals for N+AC and microglial isolation. Despite this disadvantage, the employed protocol showed to be the most effective for acquiring pure murine microglia, as other tested approaches did either provide a low amount of microglia or demonstrated to produce a higher clamping in microglial cells.

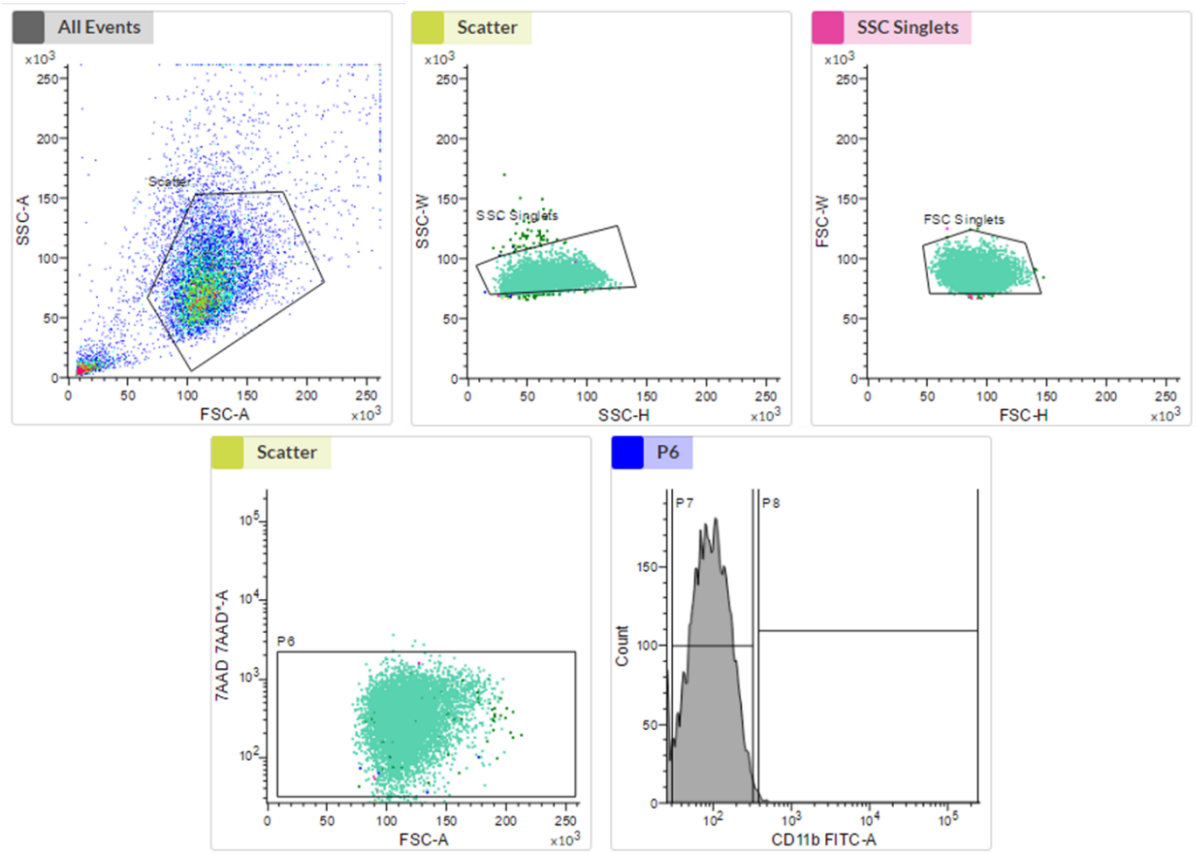

Figure 5.23: Characterisation of collected cells. Representation of collected cells (control) from the flask. Cells were selected from a defined area. Then, singlets were categorised into alive cells (P6) and then classified into stained (P8) vs unstained cells (P7). FSC= forward scatter channel; SSC= side scatter channel. Representation of 10.000 events.

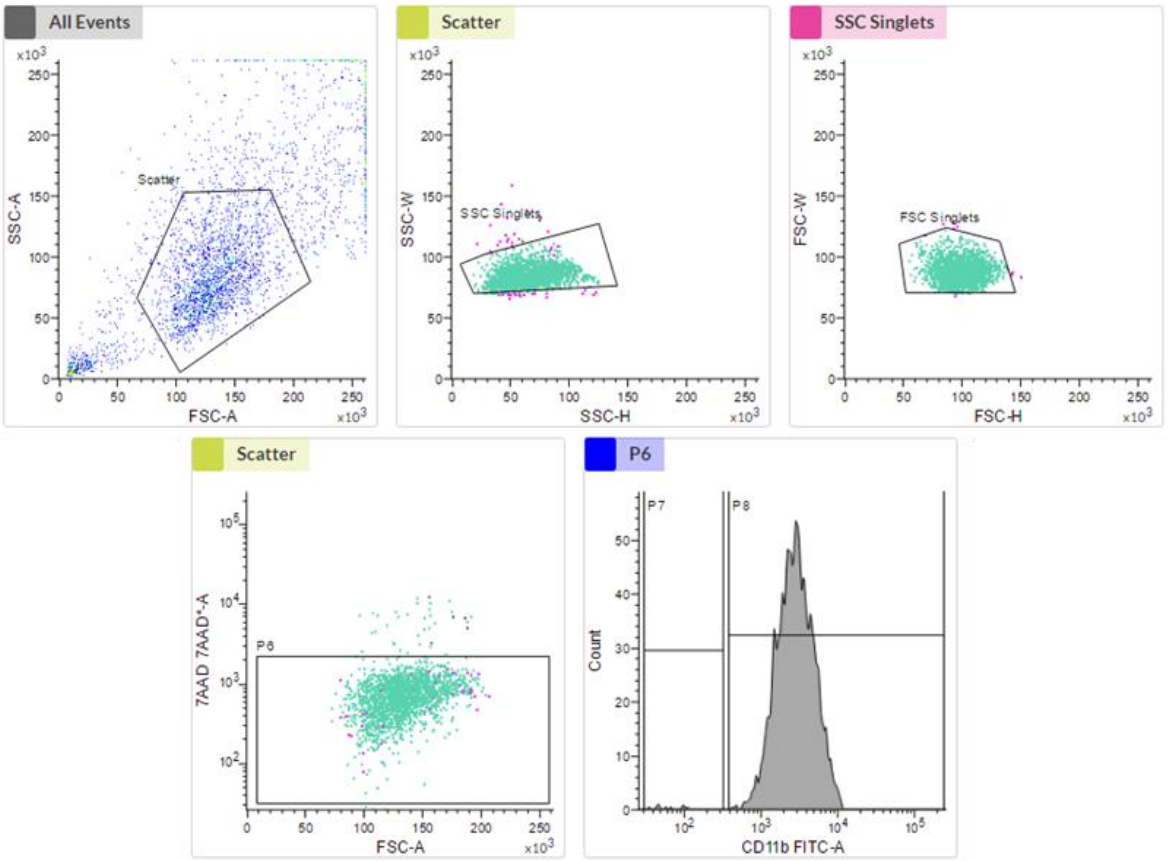

Figure 5.24: Characterisation of stained microglia. Representation of collected cells from the flask. Pre-defined area selected cells according to the control. Then, singlets were categorized into surviving cells (P6) and subsequently classified into stained (P8) vs unstained cells (P7). Stained cells represented microglia and were sorted out. FSC= forward scatter channel; SSC= side scatter channel. Representation of 4.000 events.

5.2.3 Morphology

Neurons, astrocytes and microglia were seeded in co-culture for up to 10 DIV. Bi-cultures (astrocytes and neurons, BiC) were either nurtured with media in the absence (BiC -/-) or presence (BiC +/+) of IL-34 and TGFβ2 (figure 5.25a and b). On the contrary, tri-cultures (neurons, astrocytes and exogenous microglia, TriC) were treated with both IL-34 and TGFβ2 (TriC +/+) (figure 5.25c and d). The basis of this procedure relies on the fact that microglia cannot survive in cell cultures without those compounds at a particular concentration (Bohlen et al., 2017). Throughout this study, microglial cell death was significantly increased after 5 DIV in TriC (data not shown) in the absence of supplemented IL-34 and TGFβ2. However, their survival was guaranteed when in the presence of the latter.

For a proper control to compare neuronal activity, morphology and protein release between both BiC and TriC, bi-cultures were also treated with the same medium as the tri-cultures (+/+). Nonetheless, this promoted the survival of endogenous microglia (figure 5.25b), obtained from

hippocampal cell isolation. Therefore, a second control was set, in which neurons and astrocytes remained untreated from IL-34 and TGFβ2. It is worth noting that even though both conditions are considered as a control, neither of them can be defined as an accurate control, as BiC -/- does grow in medium with different supplements, while BiC +/+ does also include few microglia and is not a pure bi-culture of neurons and astrocytes. However, by analysing the effect of stimulating factors on both samples, information about the effect on functionality, morphology and protein release can be gained.

As the number of surviving resident microglia were too homogenous and low, two ratios for exogenous microglia and N+AC were tested to evaluate which ratio was more physiologically relevant. Ratios 1 to 4 (1:4) indicate 1 microglia every 4 N+AC, while the ratio 1 to 8 (1:8) stands for the existence of 1 microglia every 8 neurons and astrocytes. Ideally, ratio 1:8 should evoke a physiological response, because it is closest to the biological ratio in the human brain (section 2.2).

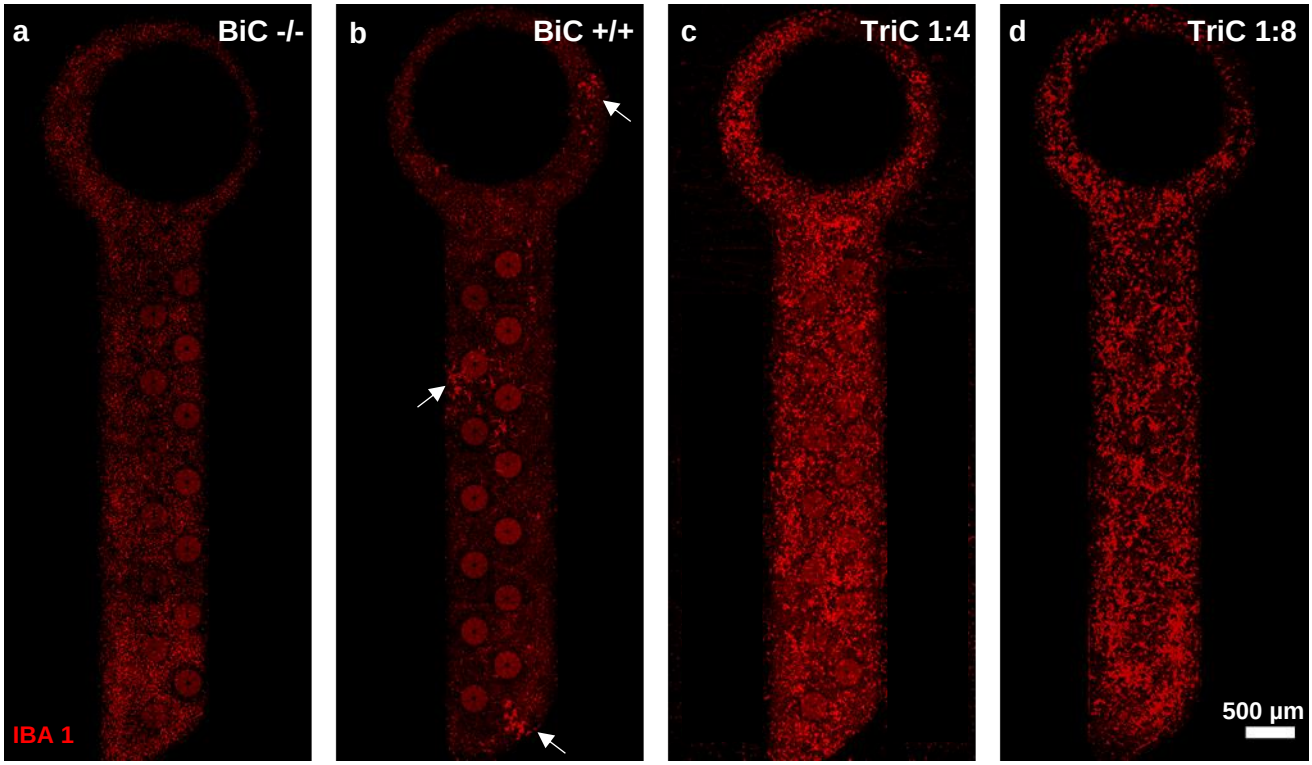

Figure 5.25: Microglial survival in wells of nMPS. Maximum intensity projections (MIPs) of entire gel of wells supporting microglial growth. Bi- or tri-cultures were supplemented with medium in the absence (a) or presence (b-d) of IL-34 and TGFβ2. Microglia survival in bi-cultures (a and b) and tri-cultures containing additionally introduced microglia in ratios 1:4 (c) and 1:8 (d) was analysed. Microglia were marked with IBA 1 (red). White arrows indicate surviving microglia in BiC +/+.

The survival of microglia was relevant for studying the effect of their presence when stimulating cultures with pro-inflammatory compounds IFNγ and TNFα for 24 and 48 hours. The morphological studies demonstrated that in the absence of microglia (BiC -/-), neurons and astrocytes seemed to present the same morphology and viability when unstimulated or stimulated (Figure 5.26). That property was also observed in bi-cultures +/+, where the few surviving microglia do not seem to influence the morphology of N+AC. However, when in higher amounts of microglia (TriC 1:4 and 1:8), a significant change in the astrocytic morphology is apparent after 24 hours (figure 5.26). Their branching seems to be thicker and shorter than in both BiC -/- and +/+. Moreover, microglia's presence led to significant cell death after 48 h, indicating that microglia at least enhance or elicit an inflammatory response when stimulated with I+T. This cell death could be related to either neurotoxicity or microglial phagocytosis, especially as it seems that astrocytes are being phagozised. It is worth noting that the neuronal cell death was not homogeneous in all samples at different preparations.

In some cases, cell death was evident, but not as much as in single experiments. This variability may be related to the health of the neuronal network, the cell density of N+AC and µG, and the accuracy of the introduced stimulation compounds I+T. The same concentration was applied across preparations, but technical issues, such as pipetting, could influence this. The cell density of all cell types is also relevant, as mentioned in section 5.1.3, especially the ones of astrocytes and microglia, as they significantly impact clearance functions. The cell concentration can vary for multiple reasons, such as the health of the sacrificed experimental animal, pipetting, or cell counting. To further evaluate this, cell types should be quantified before and after stimulation.

In order to confirm microglial activation, morphologies in unstimulated and stimulated samples were identified. Although most microglia presented a ramified morphology of up to 100 µm length in unstimulated samples, bushy, elongated, and amoeboid morphologies were also observed (figure 5.27, supplementary video 6). On the contrary, primarily 10 to 20 µm wide amoeboid forms were found in stimulated samples (figure 5.28), again indicating an inflammation response initiation. These data highlight the diversity in microglial morphologies. The multiple morphologies should be classified for more detailed information, and their percentage in each cell culture quantified. However, this was outside of this study's purpose but shall be carried out in the future.

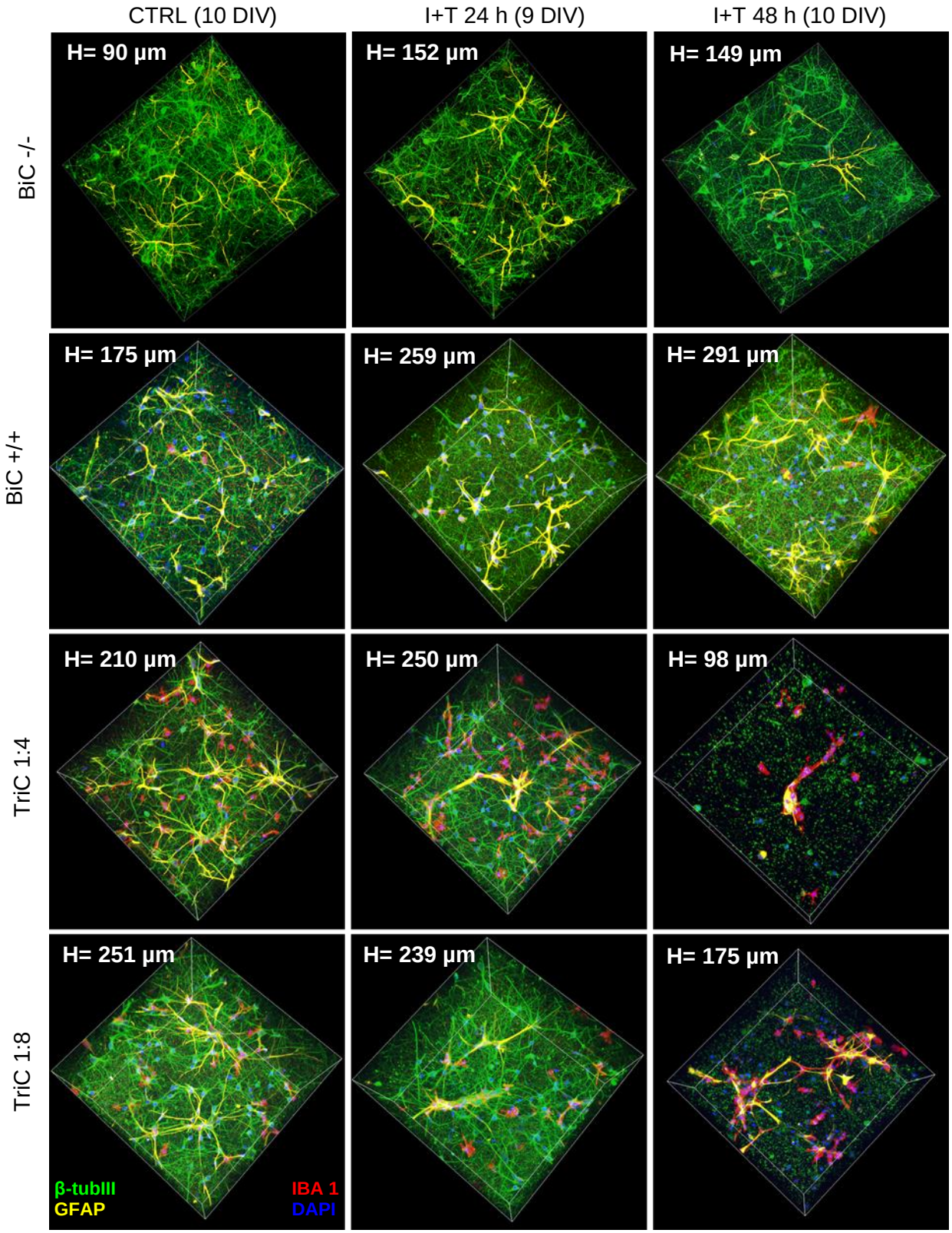

Figure 5.26: Immunostained 3D neuronal bi- and tri-cultures after 8 DIV. Cultures with or without supplemented IL-34 and TGFβ2 were maintained for 8 DIV to compare treated vs non-treated samples at different ratios (1:4 and 1:8) and time points (24 h and 48 h). Cells were stained for ß-tubIII (neurons, green), GFAP (astrocytes, yellow), IBA 1 (microglia, red) and DAPI (nuclei, blue). I + T indicates treatment with pro-inflammatory compounds IFNγ and TNFα. Area of 3D ICCs= 354 µm x 354 µm.

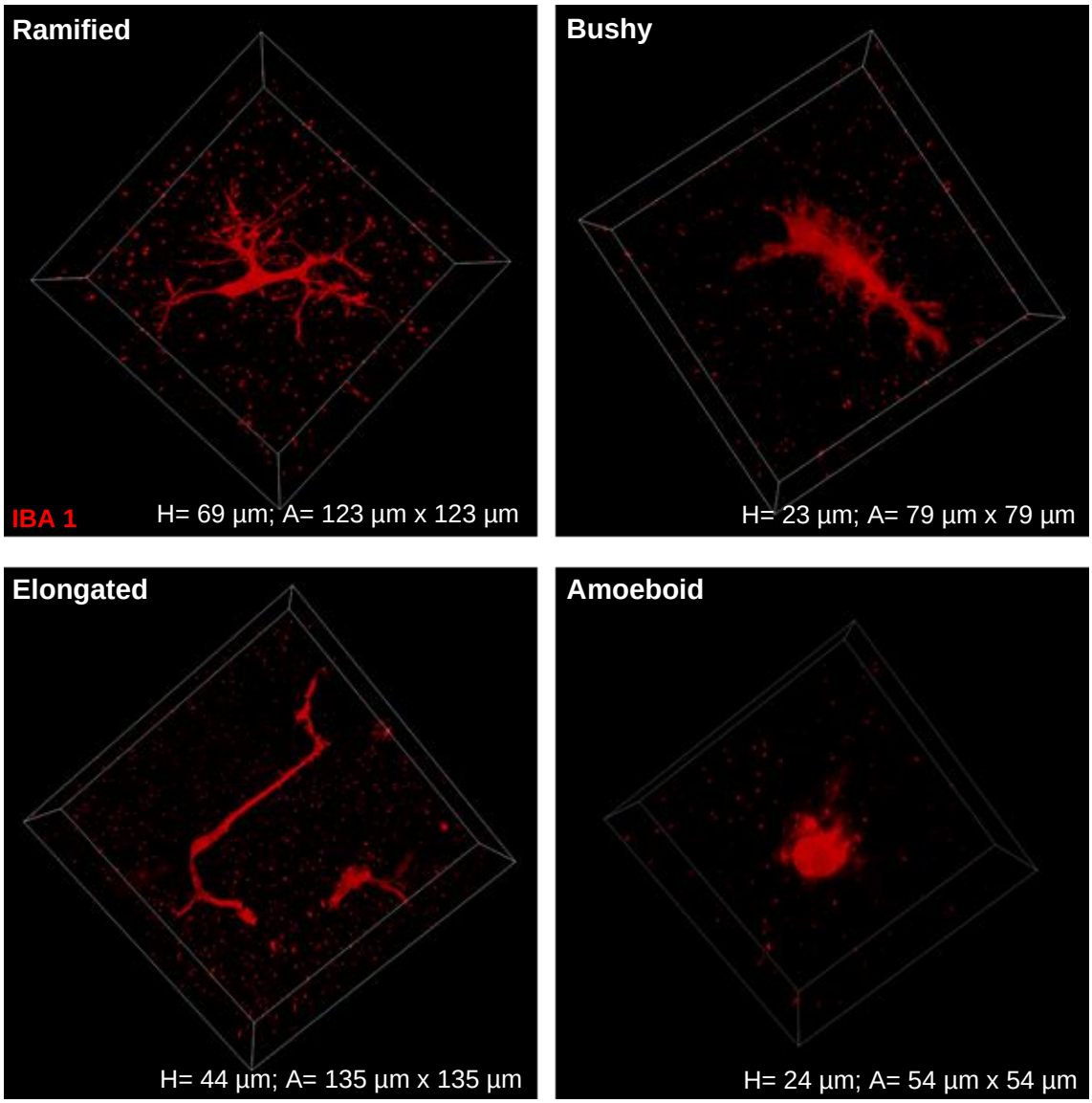

Figure 5.27: Microglia morphologies in non-treated samples after 8 DIV. Microglia showed multiple forms (ramified, bushy, elongated and amoeboid) in several non-stimulated samples. Microglia were marked for IBA 1.

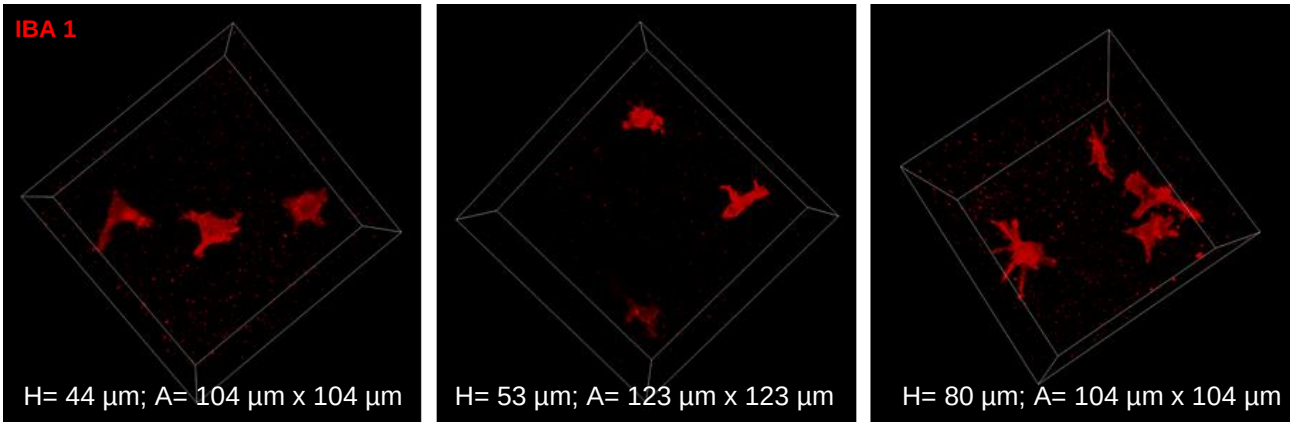

Figure 5.28: Microglia morphologies of samples treated with pro-inflammatory compounds IFNγ and TNFα for 24 h (7 DIV). Microglia showed smaller amoeboid forms after treatment with I+T. Microglia were marked for IBA 1.

One additional characteristic that needed to be identified was the presence of intercellular contacts. In both unstimulated and stimulated samples, neurons seemed to be joined with both microglia and astrocytes. In figure 5.29a (supplementary video 7), one of the microglia extensions is in very close proximity to a neuron's soma. Similarly, in figure 5.29b (supplementary video 8), extensions of an astrocyte, a neuron and a rather ramified microglia seem to be adjacent to each other, suggesting a link between them. This process is also visible in a stimulated sample (24 h) (figure 5.29c, supplementary video 9), where a hypertrophic astrocyte is in close contact with a neuron and a round-shaped µG. Although the perception of intercellular contacts may be clear, physical links between cells were only demonstrated with markers specific for cells and not junction connections. To confirm such claim, this should be further studied in detail by employing markers specific for connexions in gap junctions.

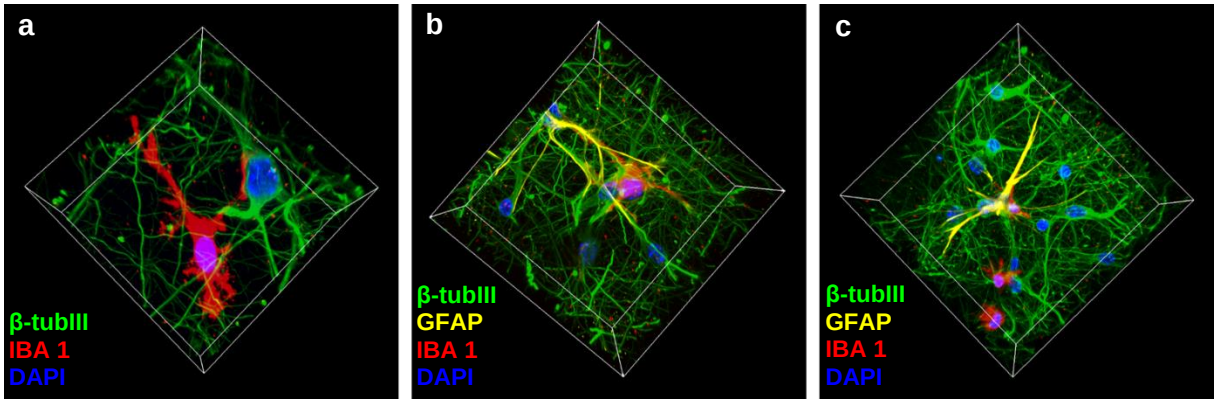

Figure 5.29: Direct neuron-glia cross-talk. Neurons (green) and microglia (red) are in tight contact with each other in non-treated samples. Scale: H= 34 µm; A= 61 µm x 61 µm. Suppl. video 7 (a). Microglia (red), neurons (green) and astrocytes (yellow) are expanding in close proximity in non-treated (Scale: H= 104 µm; A= 112 µm x 112 µm) (suppl. video 8) (b) and treated (24 h) samples (Scale: H= 67 µm; A= 135 µm x 135 µm) (suppl. video 9) (c).

5.2.4 Microglia migration

One of the most relevant features of microglia is their motility when they become active. In this study, microglia migration was highly complicated to evaluate. Live-cell imaging is primarily possible through the transduction with AAV. However, this technique would be inappropriate for inflammatory studies, as the virus itself could elicit particular unwanted behaviour in microglia, such as their activation. Moreover, tracking cells in 3D is more complex than in 2D cell cultures, where cells move in one focal plane. Therefore, microglia were seeded on top of a hydrogel that did or did not (control gel) contain pro-inflammatory compounds I+T. Microglia seeded on top of the control gel were fixed after 48 h, while microglia on top of gel containing stimulants were fixed after 24 and 48 h of cell seeding. All samples were nurtured

with control media (+/+) without additional pro-inflammatory compounds. If the microglia were motile, they would penetrate the gel to “fight” the sensed inflammatory cues.

The entire hydrogel of a random region was imaged to demonstrate the infiltration into the extracellular matrix. Surely, the settings for observing microglia migration was purposely designed to promote the relocation of microglia into the gel towards the pro-inflammatory cues. The readout revealed that samples seeded on top of the control gel for 48 h did not show any motility except for one or two µG (figure 5.30a). Similarly, microglia seeded on top of gel containing I+T for 24 h did not demonstrate to have penetrated the gel (figure 5.30b). Nonetheless, after 48 h, multiple microglia show to infiltrate up to 400 µm of the gel (figure 5.30c), suggesting that µG prevailing in TriC may also be motile. Ideally, this procedure should have been carried out by seeding astrocytes and neurons inside the gel. Although those experiments also indicated microglial motility (data not shown), the presence of surviving endogenous microglia inside the gel could not be excluded. Therefore, microglial motility could not be confirmed employing that method. To further evaluate this motility, microglia could be kept for 72 or 96 h on top of gel containing stimulating compounds I+T.

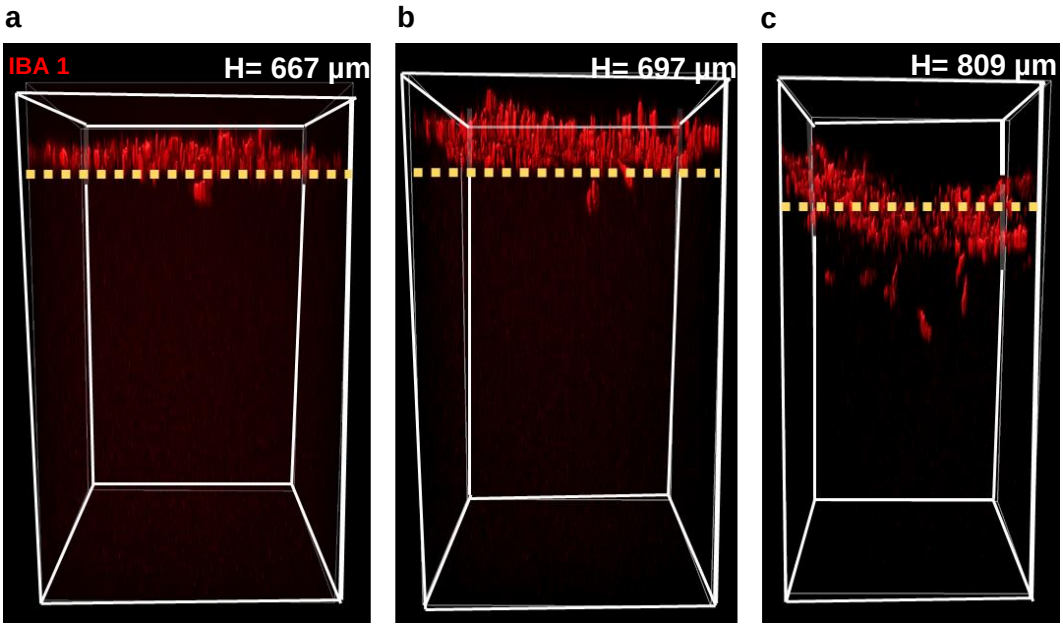

Figure 5.30: Frontal view of microglia seeded on top of hydrogel (1-2 DIV). Microglia seeded on top of the gel (2 DIV) (a). Microglia on top of gel containing pro-inflammatory compounds I+T for 24 h (1 DIV) (b) and 48 h (2 DIV) (c). Microglia are marked with IBA 1 (red) and posteriorly defined with iso-surfaces for better frontal visualisation. The entire gel was imaged in an area of A= 392 µm x 400 µm. The yellow discontinuous line indicates the top limit of the gel.

It is worth noticing that phagocytosis is a relevant aspect for this study. However, due to time constrains and difficulty for staining microglia and neurons for live cell imaging, such study is further being conducted by colleagues of the NMS group.

5.2.5 Electrophysiology

Through the morphological studies described above, it remained clear that active microglia in TriC affected neurons' health after 48 h. Nonetheless, although the astrocytic morphology was altered after a 24 h stimulation, neurons still seemed to be healthy. However, previous neuronal morphology analysis compared to the neurons' functionality seemed to differ significantly when treating with rotenone (see section 5.1.3.2). Therefore, the neuronal activity of stimulated and non-stimulated BiC and TriC was compared by performing six total recordings. Those were collected from three different preparations, which considerably increased the variability among the control recordings (BiC -/- and BiC +/+). Therefore, although data seem to indicate a clear tendency, a higher sample size for the stimulated controls is needed to confirm the following results. This is especially true for stimulated BiC +/+, as the number of surviving endogenous microglia was heterogeneous and could not be controlled. For comparing different conditions, several steps were taken.

Firstly, cells were recorded at three different time points, at 8 DIV (T= 0 h), 9 DIV (T= 24 h) and 10 DIV (T= 48 h). Chemical stimulants were added after the recordings of basal activity performed at 8 DIV. The timeline was defined upon the neurons' synchronicity and the shrinkage of the gel. As neurons were already synchronous after 8 DIV and the gel's shrinkage usually tended to happen after 10 DIV, the recordings of neurons at a cell density of 3k/ µl at 8, 9 and 10 DIV was appropriate. The relative change (%) was defined in reference to the basal activity recorded at T= 0 h (8 DIV) to evaluate the change of neuronal activity over time (24 and 48 hours, 9 DIV and 10 DIV, respectively). This decision was based on a previous electrical analysis (section 5.1.3) that demonstrated the considerable variability of absolute values at different preparations. Here, the variable of time-dependent analysis added up to the previously mentioned variabilities. Therefore, a percentage change aimed to show a more accurate change at different time points.

Secondly, conditions were classified into eight different groups. The first four groups corresponded to data obtained from BiC, where the first two groups (1 and 2) were not supplemented with IL-34 and TGFβ2 (BiC -/-), while groups 3 and 4 (BiC +/+) were. Groups 5 and 6 corresponded to TriC seeded at a ratio of 1:4, while groups 7 and 8 described data gained from TriC 1:8. Furthermore, uneven groups remained unstimulated, while even groups

were stimulated. The stimulation was carried out after the recordings at T= 0 h. Unstimulated samples were only supplied with fresh medium.

Table 5.2: Classified groups. BiC and TriC are categorized into groups depending on the addition of IL-34 and TGFβ2 or condition of stimulation. +=addition of compounds; -=no compounds added

Groups	Culture name	IL-34 and TGFβ2	IFNγ and TNFα (stimulation)
Group 1	BiC -/-	-	-
Group 2	BiC -/-	-	+
Group 3	BiC +/+	+	-
Group 4	BiC +/+	+	+
Group 5	TriC 1:4	+	-
Group 6	TriC 1:4	+	+
Group 7	TriC 1:8	+	-
Group 8	TriC 1:8	+	+

Thirdly, to understand the implications of microglia in the cell culture, several groups were compared to each other. Hence, four comparisons were made, i.e., differences between unstimulated conditions (groups 1 vs 3 vs 5 vs 7), stimulated conditions (groups 2 vs 4 vs 6 vs 8) and stimulated vs unstimulated within one condition (group 1 vs 2, group 3 vs 4, group 5 vs 6, group 7 vs 8). Those comparisons were always performed considering the time point at which the data were obtained (24 h or 48 h). Lastly, the activity at different time points within a group was compared to estimate the difference in activity after 24 and 48 h. For a simpler view of the data, only the significant differences are highlighted in a table under the graphs and in the graphs themselves. The rest of the values (not significant) are grouped in a table in the appendix section (tables 9.5-9.12).

Lastly, the same parameters as in section 5.1.3.2 were evaluated to define the neuronal circuit's alteration (MFR, BFR, %SiB, MBD, ISICoV, NBF, MFR in B, %B in NB) (figure.5.31). As expected, the neuronal circuits in BiC or TriC seemed to mature over time when unstimulated. The maturity was corroborated, especially by MFR, BFR, %SiB, NBF and the MFR in NB. It remains clear that the older the network is, the more mature it becomes. These data indicate that the number of synapses increases over time as the growing neuronal projections form more connections.

However, when stimulated with I+T, cultures seemed to behave differently. Stimulated BiC -/- showed an increased MFR, BFR, %SiB, MBD, and NBF compared to unstimulated BiC -/-.

Nonetheless, stimulated BiC +/+ showed the opposite tendency than unstimulated BiC +/+, especially on MFR, BFR and NBF, suggesting an influence of the few endogenous microglia. Furthermore, when comparing stimulated TriC 1:4 and 1:8 with their corresponding unstimulated control group and stimulated BiC -/- and +/+, all parameters exhibited a significant decrease in the neuronal activity of both stimulated TriC. Significances were generally observed after 48 h but sometimes even after 24 h (represented as red (24 h) and blue (48 h) dots in the table under graphs). Differences among groups suggested a substantial influence of microglia when active, which may have exacerbated the immune response leading to deteriorating the neuronal circuits. Dissimilarities in stimulated samples across time (24 and 48 h, represented with asterisks) were primarily observed in stimulated TriC 1:4 and 1:8, again highlighting the effect of activated microglia. Ultimately, the number of exogenous microglia did not seem to influence neuronal activity particularly. Therefore, in future studies, the lowest and more physiological ratio should be seeded (TriC 1:8).

Interestingly, the relative changes of ISICoV and NBF values observed in unstimulated TriC tend to be higher than in BiC. An increase in the percentage of ISICoV indicates that spikes incline to be more distributed into bursts rather than between them, suggesting a higher maturity level of the neuronal network. The matureness is corroborated by the absolute values of % of spikes in bursts (figure 5.32), which in both TriC is approximately 5-10 % higher than in any of the two BiC; however, not significantly. Instead, the absolute values of %B in NB (figure 5.33) demonstrate the networks in both TriC to be significantly more synchronous than in BiC, additionally corroborated by the significant increased relative change of NBF (figure 5.32).

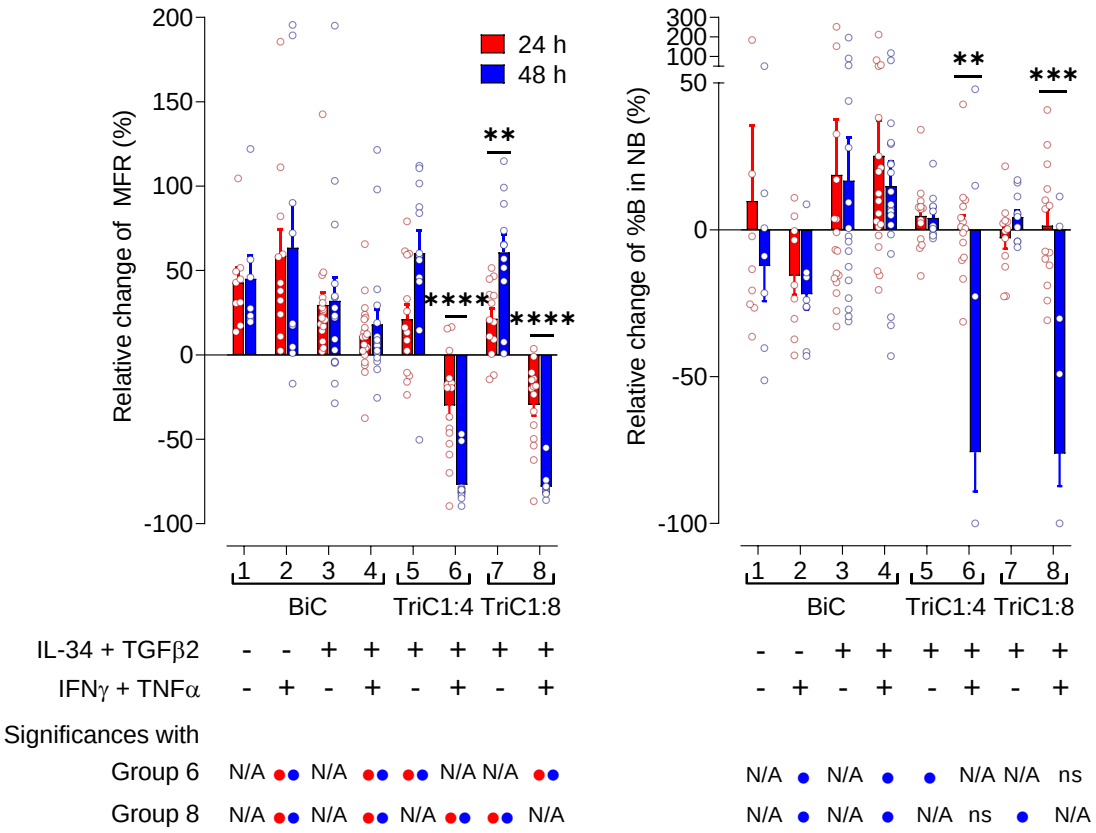
24 h
48 h
Relative change of MFR (%)
Relative change of %B in NB (%)
BiC
TriC1:4
TriC1:8
IL-34 + TGFβ2
IFNγ + TNFα
Significances with
Group 6
Group 8

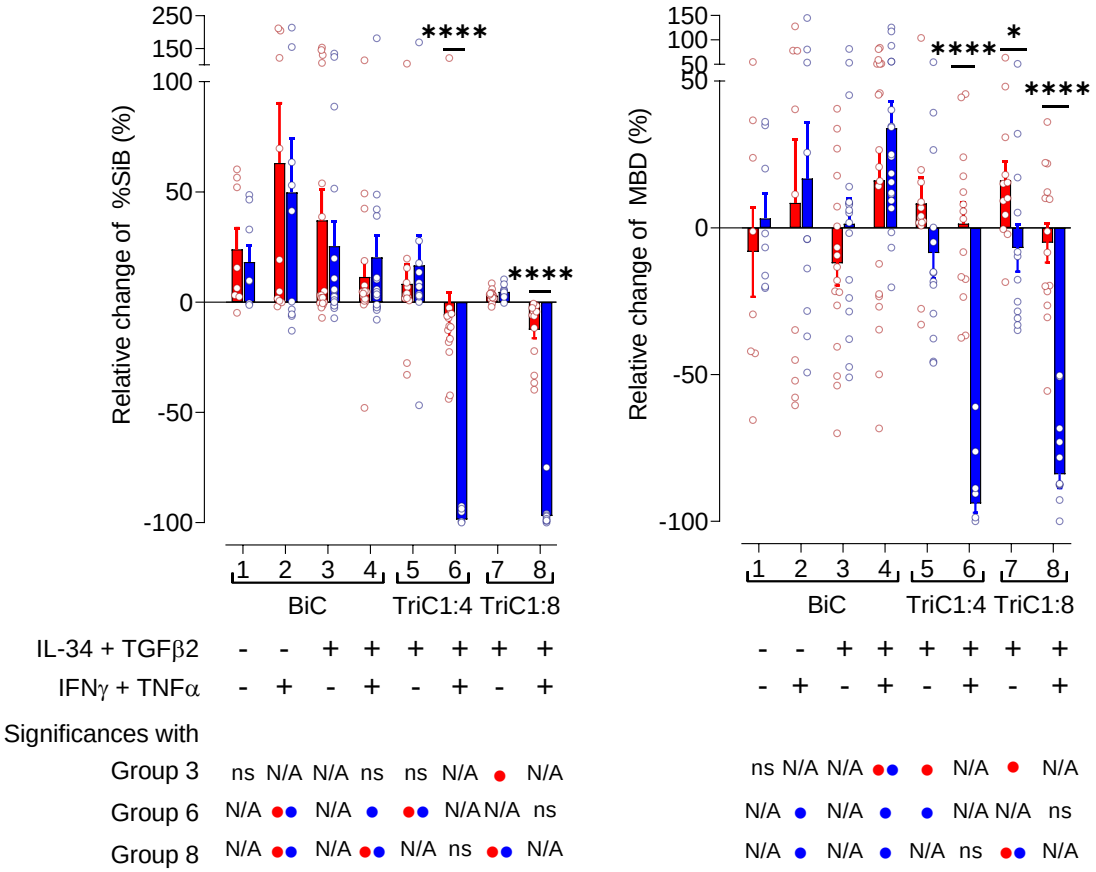
Relative change of %SiB (%)
Relative change of MBD (%)
BiC
TriC1:4
TriC1:8
IL-34 + TGFβ2
IFNγ + TNFα
Significances with
Group 3
Group 6
Group 8

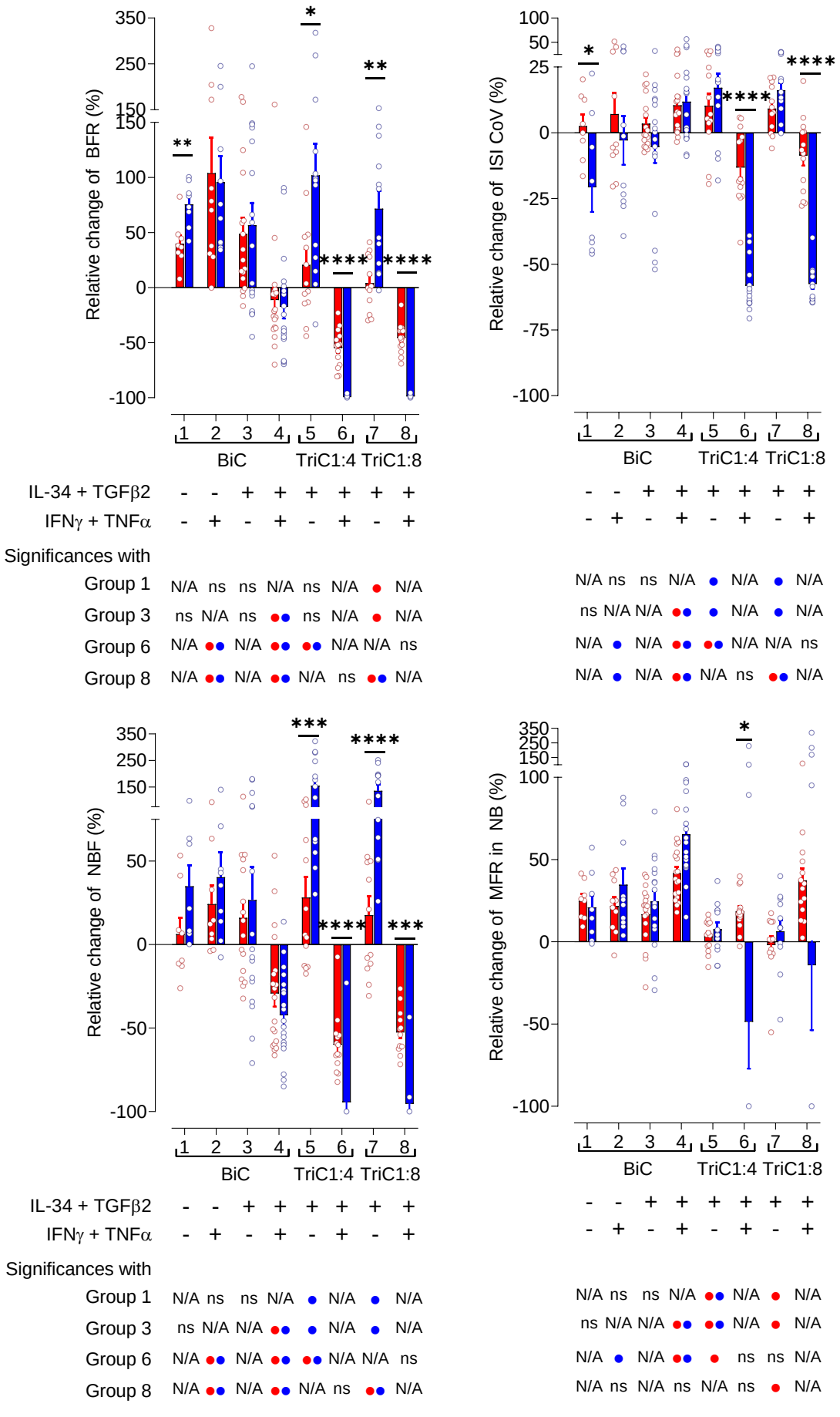
Relative change of BFR (%)
Relative change of ISI CoV (%)
Relative change of NBF (%)
Relative change of MFR in NB (%)
BiC
TriC1:4
TriC1:8
IL-34 + TGFβ2
IFNγ + TNFα
Significances with
Group 1
Group 3
Group 6
Group 8

Figure 5.31: Bi- and tri- cultures chemically stimulated with I+T for 24 and 48 h. Functional data were assessed and portrayed as the relative change (%) to data acquired before any treatment (T= 0 h). Data were compared upon 24 and 48 h treatment with pro-inflammatory compounds TNFα and IFNγ (I+T) and subsequently compared between non-treated conditions. Red bars and dots stand for samples treated for 24 h, while blue bars and dots represent cultures treated for 48 h. The following data are represented: Relative changes (%) of MFR, BFR, %SiB, BD, ISI CoV, NBF, MFR in NB and %B in NB. Error bars indicate SEM. Asterisks indicate significant differences between time points (24 h and 48 h) within different conditions: *p-value <0.05; **p-value <0.01; ***p-value <0.001; ****p-value <0.0001. Tables under graphs highlight the presence (+) or absence (-) of IL-34 + TGFβ2 and pro-inflammatory compounds IFNγ + TNFα. Significances among groups are summed in a table below with red and blue dots indicating significances between groups at 24 h and 48 h, respectively. “ns” stands for not significant while N/A stand for “not applicable”. Details of significances are listed in the appendix (**tables 9.5-9.12**).

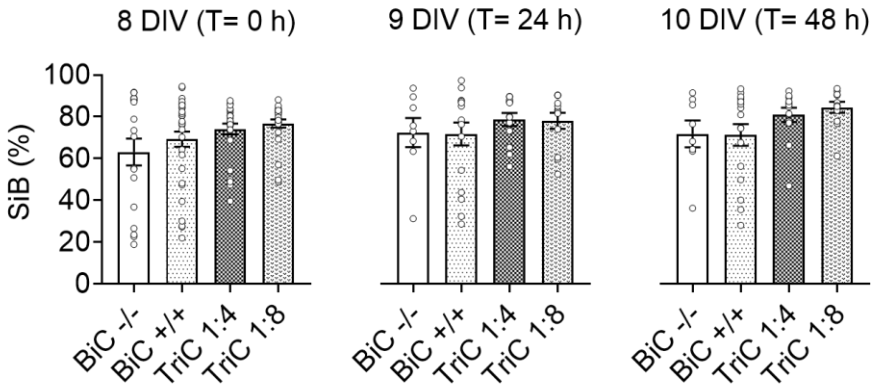

Figure 5.32: Representation of SiB (%) from untreated BiC and TriC. Graphs show values of wells collected at 8 DIV, 9 DIV and 10 DIV, which correspond to the time of analysis T= 0 h, T= 24 h, and T= 48 h, respectively. Bars represent SEM. Dots represent values of wells for each condition.

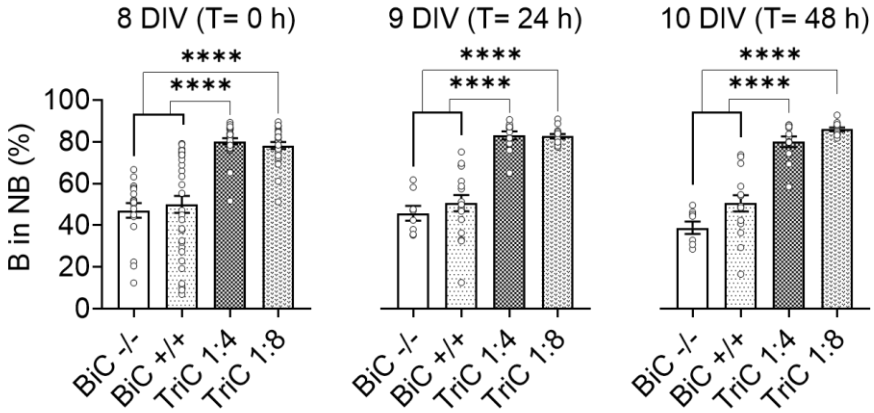

Figure 5.33: Representation of B in NB (%) from untreated BiC and TriC. Graphs show values of wells collected at 8 DIV, 9 DIV and 10 DIV, which correspond to the time of analysis T= 0 h, T= 24 h, and T= 48 h, respectively. Bars represent SEM. Dots represent values of wells for each condition. Significances are indicated by asterisks: ****p-value <0.0001.

Hence, these data suggest that supplemented microglia present in a physiological amount enhance the network's maturity. Likewise, the electrical activity is reduced drastically after microglia activation, which corroborates microglial extracellular signalling or phagocytosis function. To further shed light on this, analysis on pro-inflammatory proteins needed to be performed.

5.2.6 Protein expression

In order to confirm the significant impact microglia have on the inflammatory response, released proteins before and upon stimulation with I+T were measured. Hence, IL-1β, IL-6, CCL5/Rantes, CXCL2/MIP-2, Serpin E1/PAI-1, MMP9 were the molecules selected for further quantification. Interestingly, only values for Serpin E1, CCL5 and CXCL2 were high enough to be detected (figure 5.34). IL-1β and MMP9 were not detectable in any case, while IL-6 was only detectable when the values of CCL5 were above a specific range (data not shown). For simplicity, different groups remained classified equally to the structure explained in the previous section (groups 1 to 8) (table 5.2) and were stimulated correspondingly. Consequently, comparisons between groups were performed similarly as in the previous section. However, in this case, considering absolute values of 3 wells from one preparation acquired from the measurements at time points T=0 h, T= 24 h and T= 48 h.

Serpin E1/ PAI-1 was quantified in all conditions. However, it was higher in TriC than in BiC, even in unstimulated samples. Actually, Serpin E1 in unstimulated TriC were significantly higher at most time points when compared to BiC -/- and BiC +/+ (represented in the table under the graph as black (T= 0 h), green (T= 24 h) and pink (T= 48 h) dots). Moreover, as expected, the concentration of Serpin E1 was significantly higher after 48 h in both TriC with active microglia if compared to other stimulated samples. Interestingly, the rise of Serpin E1 is correlated to the cell death seen in the morphological studies and the significant decrease in neuronal activity observed after 48 h. These data suggest that the release of Serpin E1 is occurring even in the absence of microglia but exacerbated significantly through the latter's presence, especially when µG are activated with I+T.

CCL5/ Rantes was mainly detected after a 24 or 48 h stimulation, except for one value in unstimulated TriC 1:8 after 48 h. However, this value could also be considered an outlier, as most of the data in similar conditions remained undetectable. For the rest of the samples, CCL5 concentrations were below the standard curve (represented with a discontinuous blue line in the graph) and therefore not quantified but still considered for statistical evaluations. As aforementioned, concentrations increased significantly upon stimulation in all groups already

after 24 h, which indicates that the presence of microglia is not relevant to evoke the secretion of CCL5. However, the release of CCL5 in response to I+T is significantly faster when a relevant number of active microglia reside in the culture (TriC 1:4 or 1:8).

Similarly, concentrations of CXCL2/MIP-2 also indicated that the presence of microglia was not crucial to evoke its release after a 48 h stimulation with I+T. However, it did confirm that the presence of a physiologically relevant amount of microglia (TriC) does exacerbate the release of CXCL2 sooner than BiC.

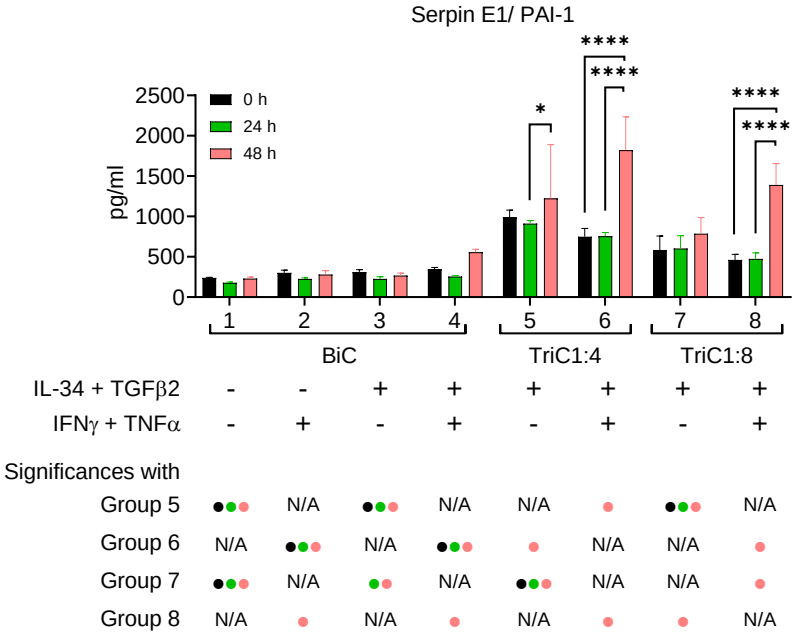

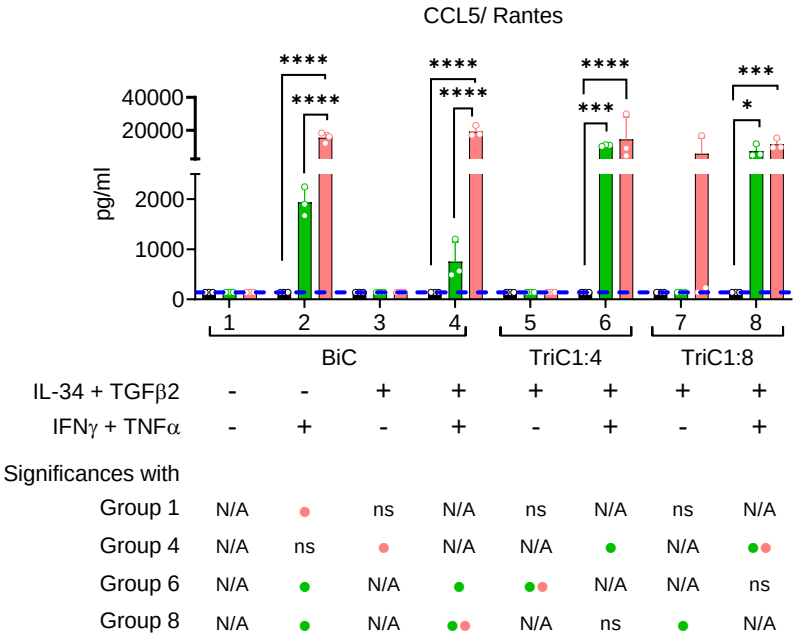

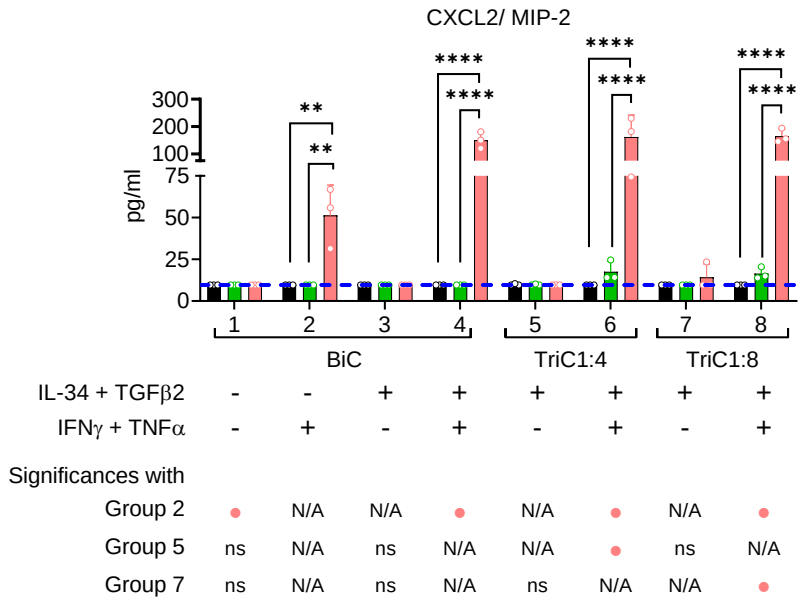

Figure 5.34: Molecule concentrations in bi- and tri- cultures chemically stimulated with TNFα and IFNγ for 24 and 48 h. Concentrations of molecules in the supernatant were assessed and compared before and after a 24 and 48 h treatment with pro-inflammatory compounds TNFα and IFNγ, and subsequently contrasted with multiple non-treated conditions. Bars and dots stand for compound concentrations at time 0 h (black), 24 h (green) and 48 h (pink). Error bars indicate SEM. Asterisks indicate significant differences between conditions at times 0, 24 and 48 h: *p-value <0.05; **p-value <0.01; ***p-value <0.001; ****p-value <0.0001. Tables under graphs highlight the presence (+) or absence (-) of IL-34 + TGFβ2 and pro-inflammatory compounds IFNγ + TNFα. Significances among groups are summed in a table below with black, green and pink dots indicating significances between groups at 0 h, 24 h and 48 h, respectively. “ns” stands for not significant while N/A stand for “not applicable”. Blue discontinuous lines indicate the values that were outside the dynamic range of the standard curve. Details of significances are listed in the appendix (**tables 9.13-9.15**).

To conclude, the collected data indicate a physiological behaviour of µG inside the nMPS that completes its function of extracellular signalling. Moreover, they show a rather ramified morphology when in homeostasis and ameboid features when stimulated with I+T. Furthermore, the electrophysiological recordings and quantitative protein assay confirm their increased sensitivity towards morphological analysis, indicating a reduction in activity in TriC when µG become active after 24 h. Interestingly, no significant differences were found between the two employed ratios, suggesting that a ratio of 1:8 accurately mimicks the brain environment.

6 Discussion

6.1 System validation

The CNS is a complex architecture organized into areas characterized by defining memory, sensory, motor and other functions. So far, most of the studies carried out to examine those neuronal phenomena imply using planar culture surfaces (Slanzi et al., 2020). 2D cell cultures have been beneficial to examine certain events. However, 2D environments do not exhibit essential cell signalling cues for normal nervous system development (Chandrasekaran et al., 2017). In order to precisely model the inherently 3D CNS, realistic microarchitectures need to be replicated. For this purpose, neurons are embedded in a 3D scaffold to present specific characteristics to promote neuronal connectivity and maturity (Wevers et al., 2016). As shown in previous work (Molina-Martínez, 2020), the best material that provides a rich environment for 3D neuronal outgrowth is Matrigel. Ideally, this system should provide the capacity of seeding the biological amount of neurons present in a murine hippocampus, which is approximately 21.000 neurons per mm^3 (Keller et al., 2018). However, the utilized gel carries the disadvantage of shrinking over time due to the presence of tensile forces caused by neural outgrowth (Molina-Martínez, 2020).

Consequently, a lower cell density as the one prevalent in a mouse hippocampus was employed. Ultimately, a cell concentration approximately 7 times lower than the physiological was seeded. Indeed, by establishing a viable cell density and an appropriate aspect ratio in the gel layer, primary neurons survived for up to ten days without presenting any shrinkage in the hydrogel. Despite this time-limiting factor, this hydrogel's properties allowed the development of the main neuronal features observed through classical imaging techniques. Those characteristics are neuronal arborisation, axonal growth and the presence of pre- and postsynaptic elements. Neuronal arborisation and nanometre-long dendritic spines were easily visible after transducing neurons with eGFP. Furthermore, immunostaining showed pre- and postsynaptic attributes in a dense 3D neuronal network and the survival of diverse cell types, such as neurons, astrocytes, inhibitory neurons and microglia. These data evidence the growth of healthy primary murine brain cells inside a 3D scaffold, accomplishing the first step to creating a physiologically relevant system.

Surely, these morphological aspects were assessed only due to the translucency of this platform. Choosing a transparent, stable, biocompatible and easily- reproducible material for an nMPS are several of the most relevant aspects fulfilled in this system. Also, to broaden this device's applications, glass materials were employed to avoid the absorbance of molecules utilised for toxicological analysis, allowing the reusability of the devices up to ten times. Moreover, the system allowed using a small number of cells due to compact geometrical

structures laser-etched in the piece of quartz. The flexible design compatible with ANSI/SLAS standards additionally permitted to image in an automated manner by employing a customised adapter, which allows morphological analysis in a large-scale fashion. Due to the mentioned characteristics, the device presented here demonstrated to be a novel, high-quality device to study detailed morphological aspects of neuronal cell cultures and glial cells present in the 3D scaffold. Astrocytes surviving in this platform were also shown to have brain-like outgrowth, making this system a potential platform to study morphological changes of brain cells affected by neurodegenerative diseases such as AD and PD.

Besides the advantageous feature of assessing healthy or unhealthy morphologies and cellular interactions, the neuronal activity could also be assessed by performing Ca^{2+}-imaging. The latter methodology is widely used among researchers for detecting neuronal activity (tables 3.1 and 3.2). Nonetheless, it does not give accurate and detailed information about the whole network when employing standard microscopy, as shown throughout this study, and represents transients of Ca^{2+} that cannot be considered for direct assessments of actions potentials. Hence, recent studies describe the ability to record from a 3D neuronal network via multiple electrodes. Although those studies are substantial for further optimizing 3D nMPS, besides presenting a low throughput, devices captured electrical activity in an invasive fashion or exhibited a platform with a low reproducibility and recording rate (tables 3.1 and 3.2).

Therefore, the innovative ad unique approach to capturing electrical activity in a non-invasive fashion showed to be the most essential characteristic added to the presented nMPS to enhance recordings of 3D neuronal networks. This study shows the easily reproducible production of a customised recording construction completed via lamination and photolithography. This assembly covered the electrode, which ultimately was enclosed by microtunnels branching out to the edge of the structure. Those microtunnels allowed the neurites' growth near the electrode that finally captured the electrical information travelling down the neurite. This feature proved to be substantial for registering an interconnected neuronal network (Molina-Martínez, 2020; Molina-Martínez et al., 2021). The organisation of a network was corroborated by evaluating the Ca^{2+}- transients in cell bodies spread in the upper part of the 3D scaffold. Neurons growing on the gel's upper section showed to be synchronous with neurites growing inside the microtunnels as they fired action potentials simultaneously. Exhibiting an equivalent activity in upper and lower portions of the hydrogel supported the idea of having a connected network.

Furthermore, the connectivity in distal and proximal areas of the gel layer was confirmed with optical stimulations of hCh2R-expressing neurons executed at different planes of the gel. Single blue light exposures in small regions evoked a synchronous response recorded from all

electrodes, which also supported the presence of developed ion channels and synapses between neurons. To further investigate this feature, several hCh2R-expressing cell cultures were triggered simultaneously. Despite displaying distinct firing patterns prior to stimulation, independent neuronal cell cultures seeded in one device exhibited synchronous network bursts after exposure to blue light. Indeed, this certifies the robustness and reproducibility of the 3D neuronal cultures by employing this platform. This characteristic opens the door to study phenomena underlying synaptic plasticity (LTP and LTD) and guarantees the possibility of studying synaptic impairments and cognitive disorders.

Nonetheless, it should be noted that the light stimuli were set to a certain intensity but still had to penetrate the gel and/or the glass substrate, making it impossible to determine the final intensity nor stimulate single cells across the gel. For this reason, some studies focused on including light stimulation within small electrodes (Shin et al., 2021; Park et al., 2021). However, this would require significant changes in this nMPS, which is why to facilitate the investigation, this platform could instead provide an alternative to light stimulation by electrically triggering the neurites through one of the capped microelectrodes (Haselier C. et al., 2017). Additionally, this would avoid the transduction of neurons. Together with optical and non-invasive techniques, this system demonstrates to be a device providing a synergy of multiple methodologies that allows the simultaneous combination of functional and morphological assessments.

As most of the platforms employed by any industry, this MPS also had to substantiate the stability and consistency across experiments besides presenting a high throughput. For this purpose, a methodology for interpreting the captured electrical activity from 3D recordings was implemented first. For this purpose, several methodologies were considered. As aforementioned, Poisson's surprise approach was thoroughly examined for studying the burst activity in single electrodes. This technique showed to be appropriate to investigate basal activity and the response to PTX. However, when studying the response of drugs that reduced or eliminated the activity completely, Poisson's surprise demonstrated not to be the most suitable method to study burst activity. The reason why this approach gave incoherent results was the Poisson's algorithm itself. The neuronal spike rate was considerably reduced after applying high concentrations of TTX (10 nM and 100 nM). Therefore, few action potentials detected within a time frame of approximately 30 to 60 seconds were erroneously interpreted as a burst. This outcome corroborated the imprecise detection of bursts as a consequence of employing the Poisson's surprise. Other researchers have also stated several inaccurate aspects when employing Poisson's surprise for burst detection (Baron et al., 2011), highlighting the discrepancies between research groups who employ diverse approaches to

evaluate electrophysiological data. So far, there is no unanimous rule for defining a burst (Cotterill et. Al., 2016). Nonetheless, by following the interval algorithm proposed by the Neuroexplorer software and other scientists (Charlesworth et al., 2015), the interpretation of bursts from data collected during this research showed to be accurate.

A disagreement also arises among researchers when defining a network burst (Pasquale et al., 2009; Shin et al., 2021). In this study, a custom-designed script employed Poisson's surprise method for NB detection (described in section 4.4.2). The script seemed to be more fitting, as defining the settings for an interval algorithm demonstrated an unreliable interpretation of NB in cultures treated with different compounds. Consequently, very clear network bursts were not identified among different recordings. Yet, the Poison's surprise approach employed for NB detection did not show significant inconsistencies for the analysis carried out in this study. However, it may show some variability if applied to studies holding different conditions, such as cell density or health state. Besides, it may also exhibit slight inconsistencies among recordings with similar conditions to the ones presented in this study, as the network bursts were defined by the firing pattern present in each burst of single electrodes. This firing pattern is dependent on many aspects, such as the number of neurites recorded from one electrode, the connectivity between neurites and the health of the network. As mentioned in a previous section (section 5.1.3), these qualities may differ when isolating cells at different time points.

Certainly, all these findings corroborate the complexity of defining a pooled analysis method suitable for each condition, cell type and specifically, different platforms. Few researchers suggest using different approaches to detect NB for MEA recordings (Kapucu et al., 2012; Gelfman et al., 2018). However, those are based on 2D cell cultures, where the neuronal activity is recorded from cell bodies and not neurites. To conclude, several aspects need to be considered to evaluate 3D neuronal networks accurately. Ultimately, a coherent and consistent approach for evaluating electrophysiological data of 3D murine neuronal networks was established during this study.

To reinforce the system's validation, interpreted electrophysiological activity was exhaustively scrutinised by examining the variability that may arise due to diverse biological, ambient or technical factors. It is worth noting that meaningful variabilities arose as a cause of utilising diverse biological samples gained from different preparations. As aforementioned, employed components during cell isolation, such as mice, the neuron isolation kit or different Matrigel batches, may induce differences in the neurons' viability. The utilized hydrogel may be one of the most significant sources for biological variability after the employment of various mice. Matrigel is extracted from Englebreth-Holm-Swarm tumours in mice (Orkin et al., 1977;

Kleiman and Martin, 2005; Hughes et al., 2010) and has different qualities across productions. Those qualities could imply variations during the gel's polymerisation, its elastic module, and the protein concentrations that optimize neuronal outgrowth. Therefore, to avoid additional deviations, the use of different batches of Matrigel should be avoided.

Furthermore, irregularities in cell counting and cell seeding might elicit variations in the final cell concentrations. The outcome of the indicated dissimilarities may be reflected in the health, connectivity and extension of the neuronal network. Consequently, more or fewer neurites are expanding into the microtunnels and then recorded. Most of the stated factors are unlikely to be controlled across different preparations; however, they can be reduced by employing multiple devices simultaneously. Undoubtedly, the reproducibility and consistency of this platform were verified by the acquisition of stable and robust data when employing several devices in parallel.

Interestingly, inter-well variations also demonstrated to be insignificant. As a result, the amount of wells in one device was increased from 12 independent compartments to 18. A higher throughput aimed to reduce the number of devices needed to complete a research, and, hence, the variability generated as a cause of multiple preparations.

With this system, pivotal characteristics are certain. Firstly, this nMPS guarantees the survival of neuronal networks, the examination of cell-to-cell interactions, and the assessment of morphological and non-invasive functional read-outs. Moreover, this platform certified to accurately investigate neuronal responses when treated with gold standard compounds PTX and TTX (Slikker et al., 2019). Those modified the neuronal activity by exhibiting an increase and decrease of the spike rate, respectively. Responses to those drug-dose dependent treatments showed the predicted electrophysiological behaviour, demonstrating a physiologically relevant neuronal network.

Moreover, this feature conveys direct and fast information about the networks' condition. It could, therefore, be highly efficient in anticipating the response to novel therapeutics by enhancing toxicity and efficacy tests (Watson et al., 2017; Marx et al., 2016). Consequently, by replacing low predictive 2D in vitro models with this simplified 3D system, drug discovery's success rate may increase (Dowden et al., 2019). The latter could be of major importance for treating neurological disorders, as medications for those are still lacking.

Nevertheless, despite characterising the neuron's functionality, both the morphology and physiological phenomena are essential to understand the mechanisms underlying unhealthy CNS in order to apply innovative therapies. Lately, nMPS have been utilized to evaluate key attributes of neuropathological conditions (Micccoli et al., 2018; Kim et al., 2019; Cairns et al.,

2020). Some studies focusing on AD demonstrated the aggregation of β-amyloids and neurofibrillary tangles in an extracellular matrix (Kim et al., 2015; Papadimitriou et al., 2018) and the up-take of artificial β-amyloids in 3D neuronal cultures (Park et al., 2015). Additionally, inflammatory responses caused by the presence of the former have been examined (Park et al., 2018). Although these studies gave a meaningful insight into brain processes by inducing an AD-like toxic environment, they disregard the impact on the neurons' electrophysiological behaviour. The examination of neuronal electrical patterns in parallel with the evaluation of morphological characteristics under such conditions could provide relevant and novel information concerning neurodegeneration in AD. Besides AD, this system could also provide a deeper insight into other neurodegenerative diseases, such as PD. Preliminary research performed by a collaborator (Dr Stella Donato, DZNE) demonstrated the survival of human-derived dopaminergic cell lines (neural precursor cells, NPCs) inside this platform for up to two weeks.

Additionally, functional read-out assessed electrically active NPCs (Molina-Martínez et al., 2021). Through further investigations, this cell line could provide a broader knowledge to the poorly understood pathogenesis of PD and additionally provide a disease model, as those systems aiming to recapitulate the underlying mechanisms forming the Lewis bodies and the α-synuclein pathology are lacking (Taylor-Whitleley et al., 2019). Presently, to overcome the absence of 3D PD models, many studies focus on inducing a PD-like behaviour by treating neurons with the pesticide rotenone (Betarbet et al., 2000; Pamies et al., 2018). This insecticide interferes with the creation of usable cellular energy by impairing complex I of the mitochondria and, consequently, the electron transport chain. In this study, the introduced nMPS showed to capture the immediate decrease in neural activity after application of low concentrations of rotenone for the first time in a non-invasive fashion. However, morphological changes in neurons were only appreciated after many hours, which is also characteristic of similar studies (Dexter et al., 1989). These alterations highlight the importance of multidisciplinary platforms that support morphological and especially functional traits to identify possible early effects.

To conclude, through the presented novel recording structure, the compatibility with automation for image processing, and the support of human-derived cell growth, this system qualifies as a high throughput platform with unique and multifaceted approaches for efficacy and toxicity tests as well as disease modelling for neurodegenerative diseases. These findings corroborate the versatility this device introduces to the organ-on-chip field. However, to optimize the study of neurological disorders affected by neuroinflammation, the role of glial

cells needs to be contemplated. Therefore, in further studies, microglia were co-cultured with astrocytes and neurons.

6.2 Neuroinflammation

Neuroinflammation is a complex process that requires a detailed analysis of multiple aspects to understand its underlying mechanisms, especially concerning neurological disorders, such as AD or PD. Those have been proved to be highly related to the increase of specific molecules that accumulate in the CNS, consequently increasing inflammatory compounds (Barcia et al., 2011; Belkhelfa et al., 2014). Therefore, to gain knowledge about the latter's effect on neuronal circuits in the presence of glial cells, the introduced multidisciplinary device was employed to support the growth of astrocytes, neurons and microglia, which completed *in vitro* the functions they carry out *in vivo*. The updated version of nMPS proved that the microfabrication and data assessment was as straightforward as in the previous version. As more wells were integrated into one platform, fewer devices were necessary to test different conditions. Ultimately, the device demonstrated that multiple assessments gave detailed information about 3D neurons co-cultured with astrocytes and microglia.

Multiple studies confirmed that neuroinflammation causes microglia to alter their predominantly ramified conformation to a round morphology (Kreutzberg, 1996). Therefore, MPS should most importantly provide platforms that allow the growth of multiple microglial morphologies, especially ramified, and the alteration of morphological properties when microglia become active. Moreover, previous research corroborated astrocytes' alteration, which become hypertrophic when active (Khakh and Sofroniew, 2015). In the presented study, most microglia were ramified and changed their form when stimulated with I+T already after 24 h. Moreover, other morphologies, such as bushy or elongated structures, were observed, which are generally more abundant in neuroinflammation states but are occasionally prevalent in homeostatic conditions (Bachstetter et al., 2015; Wyatt-Johnson et al., 2017). The various morphological properties observed in unstimulated µG proved that the employed system supported the growth of microglia in several functional states translated into diverse shapes.

Furthermore, astrocytes showed their extended and protracted projections when in homeostasis but shrinked in stimulated TriC, making the co-culture of dissociated neurons, astrocytes and microglia a more physiologically relevant system. Certainly, to this day, no 3D cell culture system studies have combined morphological, electrophysiological and proteomic

readouts to define the fitness of a TriC with dissociated brain cells. This singularity challenges the validation of this nMPS for potential neuroinflammation studies.

One of the major obstacles for applying this device to study neuroinflammation is the lack of a direct control to compare the network's activity and response to I+T of dissociated cell cultures co-cultured with microglia. Throughout the validation of the 12nMPS, neuronal circuits were scrutinised without considering microglia or other brain cells. Therefore, it is less physiologically relevant than assessing information about a tri-culture containing both astrocytes and neurons as well as microglia. However, it can be employed as a starting point to identify if tri-cultures responded similarly to bi-cultures. Hence, cultures containing neurons and astrocytes were employed as a control, only to supervise the effect of microglia in tri-cultures.

Initially, it was crucial to have a control only containing neurons and astrocytes that were growing in the same conditions as tri-cultures, i.e., nurtured with the same media. As aforementioned, cytokines IL-34 and TGFβ2 were essential for microglial survival (Bohlen et al., 2017). Yet, these cytokines do probably modify the environment of the 3D cultures, as they are involved in microglia differentiation and proliferation, but may also enhance neuronal development and circuitry through the microglia's maintenance and neuroprotection function (Suzumura and Ikenaka, 2013). By adding the mentioned proteins in the bi-culture (BiC +/+), some resident microglia survived or started proliferating (Whalley, 2014). Hence, the control that was supposed to include only neurons and astrocytes also promoted microglia's survival. Therefore, an additional control was nurtured with regular media (BiC -/-), which did not allow the survival of microglia. Still, the absence of additional IL-34 and TGFβ2 may not promote the same environmental condition and could not be considered as an accurate control either. However, by employing both controls, some crucial and accurate information could be extracted. Lastly, two concentrations of microglia inside the TriC were tested (ratio 1:4 and 1:8) but did not show significant differences among each other and are therefore going to be referred to as TriC in this section.

In TriC, the network's maturity seemed to be increased. Neuronal network maturity was shown by assessing the circuit's functionality. The % of spikes inside bursts and the % of bursts inside network bursts indicated that the maturity level in tri-cultures was increased compared to bi-cultures, especially through the %B in NB. Despite the addition of IL-34 and TGFβ2, the network of BiC +/+ demonstrated to be less developed than in TriC, confirming the need for a physiological amount of microglia to affect neuronal circuits. Therefore, the data suggest that microglia played a major role in promoting the network's maturity. This observation may be attributed to the previously mentioned function µG carry, i.e., protect the 3D culture from harm

and participate in the advantageous alteration of neuronal circuits. Although these are functions occurring *in vivo*, in this case, the process may be boosted due to the supplement of IL-34 and TGFβ2. Even though the latter are predominantly produced by neurons and astrocytes, the addition of both compounds was necessary as their production *in vitro* proved no to be enough to support microglial survival.

Moreover, a more mature neuronal network might originate through direct contact of microglia with neurons and astrocytes (Fróes et al., 1999.; Dobrenis et al., 2005). Morphological studies carried out in this research suggested the physical connection of microglia with neurons and astrocytes. Through this coupling, microglia may optimise neuronal circuits directly or indirectly by regulating astrocytic functionality in the “quad-partite synapse” (Araque et al., 1999; Pittaluga, 2017). To further understand the cross-talk between neurons, microglia, and astrocytes, gap junctions between those may be identified via morphological assays.

Microglia in TriC also seemed crucial to elicit a significant and faster immune response when stimulated with pro-inflammatory compounds IFNγ and TNFα. Morphological assays proved that in the presence of active µG, astrocytic hypertrophy and neuronal cell death rate increased. This effect was additionally corroborated by the functional assessment and the analysis of protein release. Moreover, astrocytes became denser and shorter after a 24 h stimulation. Neuronal cell death was observed after a 48 h treatment. Through functional readouts, it remained clear that the previously very active and synchronous network was significantly reduced in stimulated TriC after 48 h, which correlated with the observed higher cell death.

Furthermore, the neuronal activity in TriC was also declining before an apparent cell death, suggesting that the immune response enhanced by microglia was already affecting the neuronal network’s health at T= 24 h. Once more, the combination of morphological and functional readouts provided a deeper insight into the effect of chemical stimulants. Certainly, the mentioned observations were supported by the detection of molecules involved in a neuronal response, especially through the release of CCL5. The latter is detectable when an immune response occurs and is expressed by neurons and microglia, but especially by astrocytes at high levels (Pittaluga et al., 2017). Its presence causes the release of large amounts of glutamate from neurons if in high concentrations. As aforementioned, high concentrations of glutamate can lead to cell death by promoting a neurotoxic environment (Suzumura and Ikenaka, 2013). Although measured quantities of CCL5 are relatively high in stimulated BiC -/- after 24 h, the effect of a toxic condition was not noticeable at different time points in any of the other assessed readouts. Instead, a decrease of neuronal activity after 24 and 48 h stimulation was noticed in BiC +/+ (MFR, BFR, and NBF), but still, the amount of the

few surviving active microglia seemed not to be enough to cause morphological alterations in astrocytes nor neurons at any of the studied time points. On the other hand, morphological and functional alterations were observed in TriC after a 24 h stimulation. Accordingly, CCL5 values were equally significantly high at T= 24 h and T= 48 h, demonstrating that in the presence of abundant active microglia, CCL5 release is increased more rapidly, and therefore probably glutamate. Consequently, these increased values result in the activation or conformational alteration of astrocytes at an earlier stage than if microglia remained inactive or were not present. As neurons, astrocytes, and microglia release CCL5, these data suggest that all known to be present brain cells in the TriC are actively responding to the inflammatory cues. This hypothesis, however, should be further corroborated by assessing the levels of mRNA expression in each cell type.

CXCL2 is released by all cultures when stimulated mainly after 48 h. Although the quantities secreted at T= 48 h by BiC +/+ are very similar to those released by TriC at equal time points, values in the former are under the detection curve at T= 24 h. In contrast, in TriC, the freed quantity of CXCL2 increases after 24 h, although not significantly. Values measured between 24 and 48 h may show a time-dependent increase of CXCL2 values in both BiC and TriC, providing information about the transcription speed of CXCL2 under the named conditions. In this manner, the influence of the presence and amount of microglia might be assessed. So far, these data suggest, once more, that the presence of a physiological amount of microglia accelerates the immune response and its consequences when not attenuated rapidly enough.

Similar effects are shown when quantifying Serpin E1. Although, in this case, the cited molecule was detected in all conditions at all time points, which is expected because Serpin E1 is also found in the hippocampus at higher levels in homeostasis (Sallés and Strickland, 2002). Our observations indicated that even without microglia, astrocytes directly or indirectly regulate the CNS by secreting Serpin E1. Interestingly, in bi-cultures, even when stimulated, the concentration of Serpin E1 was significantly lower than in unstimulated TriC. Indeed, values in the latter could be correlated with the higher maturity of the neuronal network. As previously suggested, neuronal circuits in TriC may develop better than BiC through the presence of microglia, and this may also be attributed to the “quad-partite synapse”, where neurons, microglia, and astrocytes communicate to regulate the environment in the brain (Pittaluga et al., 2017). Therefore, when in homeostasis, astrocytes secrete more regulatory molecules such as Serpin E1 than in the absence of microglia. Furthermore, as expected (Sallés and Strickland, 2002), Serpin E1 release increased in TriC after stimulated with I+T for 48 h, demonstrating, again, that the presence of microglia is promoting the increase pro-inflammatory Serpin E1 secretion after stimulation with I+T.

It is worth noticing that the release of Serpin E1 and CXCL2 in TriC increases significantly after 48 h of stimulation, whereas CCL5 is significantly increased after 24 h due to the addition of I+T. This dynamic displays the incapability of the brain cells to attenuate further the inflammatory response, even if in the presence of supplementary anti-inflammatory compounds TGFβ2 and IL-34 (Zhang et al., 2019; Lelios et al., 2020). Certainly, the observed outcome is, more importantly, to be attributed to the direct interaction of INFγ and TFNα with brain cells, which caused the release of pro-inflammatory compounds, more obviously CCL5. In response to the former, CCL5 may have enhanced neuronal cell death by causing the release of neurotoxic glutamate. Nonetheless, it cannot be discarded that IFNγ may have promoted neuronal cell death sooner than CCL5.

IFNγ directly affects the neuronal health by binding to neuronal NMDA receptors in the pre-synaptic terminal, leading to the entry of calcium and, if in high amounts, to cell death and release of toxins that affect the state of neighbouring glial and neuronal cells (Suzumura and Ikenaka, 2013). Consequently, the neuronal health could be influenced by IFNγ itself, and not necessarily solely by the elicited immune response. However, this was not corroborated by morphological nor functional readouts of BiC -/- after 48 h. Therefore, this rapid cell death may be attributed to the combination of employed stimulants (I+T), phagocytosis and exacerbated release of pro-inflammatory and toxic compounds due to the presence of higher amounts of microglia. Undoubtedly, the second stimulant, TNFα, worsens the neuronal health state by causing the release of glutamate, which probably promoted a neurotoxic environment and the entry of Ca2+ inside the neuron. Indeed, I+T led to the release of toxic NO and ROS, incrementing the chance of cell death in a short period and reducing the possibility to study the release of further anti- or pro-inflammatory cues. For supporting this statement, anti-inflammatory compounds should be evaluated in unstimulated and stimulated cultures at further time points. Additionally, anti-inflammatory components could be added to cell cultures with the aim to reduce the pro-inflammatory response and evaluate a possible recovery process by quantifying protein levels released to the supernatant. Although IFNγ did not show an enormous influence on direct neuronal cell death after 48 h, it might be that it does if incubated with BiC for more extended periods. Therefore, other compounds that do not promote direct neuronal cell death could be employed. One possibility is LPS from *E. coli*, although the hydrogel's diffusion rate should be considered and evaluated. This would add additional strength to the claim that our system supports biologically relevant microglia in co-existence with astrocytes and neurons.

Unfortunately, some of the targeted pro-inflammatory molecules (IL-1β, IL-6, and MMP9) were not detected by employing the Luminex multiplex assay. Nonetheless, this does not

necessarily mean that they were not secreted. One of the reasons why they remained undetected may be that the short time frame cells had to produce enough quantities of the named molecules before cells started deteriorating. For instance, Kiefer et al. (1993) detected high mRNA levels of IL-6 after 8 hours of stimulation, with a peak after 24 h in rats *in vivo* (Kiefer et al., 1993). Surely, mRNA levels assessed in the mentioned study do not represent the levels of ultimately secreted protein levels but the genetic regulation upon the initiation of inflammation. Therefore, it might be that even *in vivo*, and especially in 3D *in vitro* models like this, it takes more time to release fully transcribed IL-6 molecules. Also, although the system presented here mimics neuronal networks, it does not fully imitate brain structures. Therefore, the response to hazardous stimuli may be delayed, and therefore, some molecules are only detectable after a certain amount of time.

Furthermore, while the Luminex multiplex assay is a very accurate system, it could be that most of the pro-inflammatory compounds were prevalent in the hydrogel and not in the supernatant from which the molecules were measured. Other methodologies, such as the RT-PCR or Western blot, may provide more details about the secretion or expression of these molecules by also examining the quantity inside the gel.

Moreover, failure to determine IL-1β, IL-6, and MMP9 could also be attributed to the number of brain cells seeded in our device. As mentioned in the section above (section 6.1), the shrinkage of the matrigel and the supply of nutrients displays a complex issue for seeding 3D brains cells at a physiological amount in this nMPS for more extended periods. As explained, murine hippocampal neurons in the brain are approximately seven times more abundant than the number of seeded cells in this system (Keller et al., 2018), which is consequently correlated to the number of astrocytes and microglia. Hence, this might have considerably reduced the amount of some of the cues secreted by the brain cells after 24 and 48 h and, consequently, reduced the chance for those to be detected. To corroborate this hypothesis, the immune response should be analysed over longer periods. Apart from the increased cell death after application of I+T, this may not be feasible with this nMPS, as 3D cell cultures at a particular cell density start presenting hydrogel shrinkage after 10 DIV. Besides, neuronal maturity is achieved between 6 and 7 DIV.

Lastly, as shown by the motility experiments, microglia showed to migrate up to 400 µm inside the gel that contained I+T but only after 48 h. This observation may indicate that brain cells secrete less pro-inflammatory compounds at 24 h since the cues released by microglia may be perceived better only 48 h later when microglial motility is increased. However, this may be disputed, as the motility test did not accurately resemble the conditions present in our TriC. Apart from including neurons, microglia and astrocytes inside the gel in TriC, I+T was solely

introduced through the medium, leading to an extensive reach inside the gel via diffusion. In contrast, in the motility experiments, I+T was only added to the gel containing no cells. Moreover, freshly collected microglia were seeded on top of the gel surface and fixed after 1 or 2 DIV, which did not resemble the 3D conformation of microglia seeded inside the gel for at least 8 DIV. For both reasons, 2D less-ramified microglia prevailed at one focal plane, which may have decreased the probability of sensing I+T compared to 8-day-old 3D microglia extending their ramifications in 3D, which can be correlated to a study comparing microglia in growing in 2D and 3D (Cuní-López et al., 2020). Ultimately, 3D microglia were more widespread and had a higher probability of sensing any cues diffusing through the gel. Consequently, microglia in TriC may displace much earlier than in the observed data. This migration could additionally be related to the microglia function of phagocytosis. It could relevantly be correlated to the increased cell death after 48 h of stimulation. Further studies should focus on NO and ROS detecting assays and time laps morphological readouts that confirm phagocytosis in this TriC. Therefore, microglia should be ideally tracked in real-time, but as stated above, this was a relatively complex task. As an alternative, phagocytic traits can also be proven by targeting microglia with CD68 and MHC class II, which are markers known to be expressed by phagocytic microglia (Graber et al., 2010).

Microglia-specific transductions with AAV containing fluorophores were not feasible without initiating an immune response against the virus. Moreover, the dye tomato lectin was also tested for live-cell imaging (data not shown) but did not dye microglia later identified with ICC, indicating a low diffusion rate through the gel. Alternatively, microglia may be marked before cell seeding in 3D, as demonstrated by Park et al. (2018), where microglia were labelled with a red fluorescent dye (Park et al., 2018). Nonetheless, in the mentioned study, immortalized cell types were employed, which are generally more stable than primary murine cells. Other studies use mice lines where µG are genetically encoded to be fluorescent (McKinsey et al., 2020). This methodology has also been transferred to microglia iPSC lines (Pandya et al., 2017). Although the 3D conformation of the cell culture system challenges any tracking of microglia motility occurring in several focal planes, it could be feasible to image several Z-stacks every certain amount of time and detect microglia migration. This was accomplished recently by Cuní-López et al. (2020), where 3D microglial iPSCs were tracked in a 45 µm thick hydrogel without the necessity of staining the cells. Nonetheless, tracking unmarked microglia might not be feasible in a 900 µm thick gel.

To conclude, the assessed data during this study demonstrate that this nMPS supports the growth of microglia in co-culture with astrocytes and neurons in a physiologically relevant fashion. This statement has been corroborated by the combination of morphological, functional

and protein analysis. Whether this system is appropriate to study neuroinflammation still needs to be corroborated by more detailed analysis, such as cell counting of different brain cells, presence and effect of anti-inflammatory compounds, physical connections of brain cells, and accurate motility and phagocytosis experiments. Moreover, several crucial factors in neuroinflammation have not been considered here, such as the lymphatic system, other brain cells (e.g. oligodendrocytes), or the blood-brain-barrier. Nonetheless, this study's goal was to observe the physiological response of microglia in our nMPS, which was possible to determine via the use of this multidisciplinary nMPS.

7 Outlook

The relevance and novelty of this model are introduced by ground-breaking biological and technological advances. Those promoted the validation and application of the novel nMPS that supports the growth of a 3D murine tri-culture and allows the synergy of morphological, functional, and proteomic readouts. Nonetheless, by integrating more techniques, further neurotoxicity studies, drug screening, and disease modelling, the TriC may be more physiologically relevant.

7.1 Current results

Via the combination of nanoengineering techniques of MEA, photolithography, and ISLE, the presented nMPS showed to be highly reproducible and scalable. Through the extracellular recordings in which the adapted 256MEA format and lithographed CµE were combined, this system provided functional readouts of 3D growing neurons in a non-invasive manner. Moreover, the employed glass materials constituting the substrate and microfluidic piece entailed high biocompatibility that supported the survival and morphological readout of at least three brain cell types, i.e., neurons, microglia, and astrocytes. The open and versatile design of the MF piece additionally allowed the retrieval of the supernatant medium, ultimately allowing the analysis of protein levels. Due to its robust fabrication, when both the substrate and the MF piece were assembled via biocompatible glue, a novel transparent *in vitro* platform with either 12 or 18 single experiments could be employed for acquiring readouts at a morphological, functional, and proteomic level. This platform's validation via hippocampal cells confirmed the high informative value about neuronal circuits and their morphology. At the same time, the addition of microglia stimulated with pro-inflammatory compounds highlighted the impact of conditions at proteomic levels.

Additionally, through its compatibility with ANSI/SLAS standards, applying a custom-designed adapter allows the monitoring and imaging of 3D cultures in an automated manner, partly fulfilling the requirements for high-throughput screening studies (HTS) (Seo et al., 2018). However, extracellular recordings are restricted by the number of electrodes, highly dependent on the recording systems available. To this day, recordings of up to 256 microelectrodes may be performed with the employed system. Indeed, this limits the throughput of the platforms. Nonetheless, by updating the current device, the capacity may be enhanced by increasing the amount of individual experiments and reducing the number of electrodes in each of the wells without compromising the assay.

Ultimately, by combining engineering techniques, this nMPS allowed the combination of multiple neurobiological technical readouts of 3D dissociated brain cells. Accordingly, this system can be considered one of the most relevant in vitro platforms to study neuronal circuits developed in the last years. However, to further increase the physiological relevance and broaden our knowledge about brain mechanisms, other components may be implemented.

7.2 Further implementations

The presented system proved versatile and allowed multi-parametric approaches to defining 3D cell cultures at a morphological, functional, and proteomic level. However, further implementations would make this nMPS more relevant.

7.2.1 Human-derived cell lines

The main goal of microphysiological technologies is to simulate *in vivo* situations occurring *in vitro*. During this study, using experimental animals eased the production of the introduced device as it accelerated the latter's validation. However, to implement the 3R principle (replacement, reduction, and refinement) and follow the OoC requirements, human derived-cells are being employed. In collaboration with Prof. Dr Peter Heutink (DZNE), the nMPS was utilized to perform morphological and functional readouts of neural precursor cells differentiated by Dr Stella Donato. The latter survived for approximately two weeks in culture without observing any gel shrinkage. Additionally, those iPSCs may be modified to mimic the physiology of Parkison's disease and are planned to be co-cultured with microglial iPSCs that integrate a GFP fluorophore to facilitate the monitoring in real-time. In this manner, neuronal circuits of human-derived cell lines may be evaluated in physiological and neuropathological conditions.

Although the mentioned cell lines partly represent human physiology, they still do not recapitulate human brain architectures. Therefore, in collaboration with Dr Udo Kraushaar, neurospheres (HeLa cells) were introduced into this system. Ultimately, the activity could be recorded, indicating that this nMPS may be suitable to characterise neurospheres.

7.2.2 Parkinson's disease

Rotenone elicits PD-like behaviour. Hence, it is employed in multiple studies to evoke neuronal dysfunction similar to the one occurring in PD. During this study, BiC treated with rotenone revealed the importance of multiple assessments to identify the former's early or late

effects. However, no proteomic, genetic or mitochondrial studies were carried out during this study. Implementing those would give even more detailed information about the released proteins or toxins. Likewise, the microglial function was not contemplated in this section, although it may play a more significant role in response to rotenone or protein aggregates occurring in PD. Ultimately, further experiments should consider using lower concentrations of rotenone to avoid both fast cell death and neuronal activity reduction. Accordingly, potential outcomes assessed via the diverse readouts may be correlated to PD.

Nonetheless, for higher accuracy, current studies performed in the NMS lab related to PD employ α-synuclein instead of rotenone. The latter will be added to the gel's upper surface to assess the propagation across 3D neurons inside the gel. Likely, neuronal degeneration and higher microglial motility may be observed.

7.2.3 Long-term potentiation

The optical stimulation of specific cell types has been one of the most considerable advances in neurobiological techniques in the last decade. Through this methodology, not only excitatory or inhibitory neurons may be manipulated, but also astrocytes or microglia (Xie et al., 2019; Laprell et al., 2021). In this study, the nMPS demonstrated to be compatible with optogenetics. Channelrhodopsin-expressing neurons changed the electrophysiological firing pattern after light stimulation. Further studies carried out by colleagues of the NMS are aiming to alter neuronal networks to induce LTP. Likely, this will give a more detailed insight into synaptic modulation.

Indeed, the above-mentioned technique could be used to modulate microglia or astrocytes via light stimulation. In this manner, the impact of each cell type in neuromodulation could be evaluated. Additionally, instead of employing chemical stimulants to elicit an inflammatory response, glia cells could be activated via optical stimulation. However, a viral transduction would alter the microglial activation state. Therefore, genetically modified mice or cell lines are required to perform the mentioned experiments.

7.2.4 Neuroinflammation

Currently, the presented nMPS proved to be suitable to evoke physiological responses of microglia in co-culture with astrocytes and neurons. However, further studies need to be carried out to confirm the microglia migration and phagocytosis. For this purpose, a particular

area of the cell culture could be damaged via light toxicity. Subsequently, the region of interest could be imaged with a constant frequency to determine the migration of fluorophore-expressing microglia. In this manner, the damaged tissue is located in a defined area, where microglia should migrate towards. Additionally, phagocytic traits can also be proven by targeting microglia with CD68 and MHC class II, which are markers known to be expressed by phagocytic microglia (Graber et al., 2010).

Moreover, to assess the regulatory response to any stimuli, mRNA expression should be correlated to the transcribed proteins. Currently, the gel in which the cells are prevailing can be degraded and could potentially be used to measure mRNA levels. However, cell-specific mRNA levels for each sample may not be feasible to acquire, as this system is designed to support cell cultures with low cell densities. However, several samples could be merged and then evaluated. This suggestion could also help estimate the amount of time needed to transcribe and secrete specific molecules and further confirm the regulation of compounds not detected in our samples' supernatant.

In this study, three CNS cell types were evaluated after evoking an inflammatory response. However, other components of the CNS, such as oligodendrocytes, were not contemplated. Physiologically, the interplay between oligodendrocytes and axons is acutely affected by neuroinflammation, especially if the latter induces demyelination (Dulamea, 2017). Nonetheless, myelination has never been evaluated in this 3D tri-culture system. Most probably, oligodendrocytes are not growing in the presented tri-culture, as mature oligodendrocytes develop at stage P7 in mice (Flores-Obando et al., 2017), and neurons and astrocytes during this study were isolated from embryonic mice. Also, microglia are isolated and sorted from P2 mice. However, it could be that some of the precursors present in embryonic stages did ultimately survive but did not develop to become functional and mature oligodendrocytes. Regardless, oligodendrocytes may be isolated from postnatal mice (P5-P7) (Flores-Obando et al., 2017) and characterised in the already viable 3D tri-culture to form a tetra-culture. Likely, their functionality may be estimated via morphological and molecular analysis.

7.2.5 Blood-brain barrier

With the ability to study the consequences of either neuronal or glial alteration by employing this nMPS, the repercussions of those in the blood-brain barrier (BBB) may be evaluated. Through the easily modifiable design of the femtoprint piece, a third layer was added to promote the growth of endothelial cells on top of the gel embedding the brain cells.

Consequently, a barrier could be formed between the 3D tri-culture and the medium, which would act as the circulatory system in the CNS (Maoz et al., 2018). Here, the barrier's tightness could be studied with visual methods or by integrating TEER electrodes (see tables 3.1 and 3.2) into the device. However, this might not be necessary, as neural activity captured by the MEA might give accurate information about compounds crossing the BBB by examining the neurons' physiological behaviour. For instance, GABA and glutamate are thought to be impermeable to the BBB (Boonstra et al., 2015; Purves et al., 2004) and could therefore be employed as an indicator for BBB tightness. Those compounds could be added to the medium, which is separated from the cell culture by the BBB. As explained, PTX is an antagonist of GABA. Therefore, the addition of GABA should evoke the reduction of neuronal activity. Consequently, if GABA were to penetrate the BBB, the decrease of neuronal activity would indicate BBB impermeability. Instead, glutamate would induce the opposite response.

7.3 Future applications

As required by the EuroOoC, the designed nMPS demonstrated to be suitable for diverse studies and showed low variability among devices (Mastrangeli et al., 2019). Moreover, the introduced assay proved to be highly reproducible and supported the growth and readout of human-derived cells in preliminary results (section 7.2.1). Therefore, this *in vitro* platform may be applied for neuronal disease modelling, drug development and neurotoxicity tests.

7.3.1 Neurological disorders

Neurological disorders are highly prevalent in the human population worldwide and are expected to increase in developed countries (United Nations, 2019). In an effort to overcome this threat, neuro-microphysiological systems have emerged in the last years (see tables 3.1 and 3.2). nMPS have shown to be promising by allowing better control, manipulation and readout of 3D brain cells. Accordingly, these systems assure a more accurate recapitulation of brain processes, thereby increasing the brain cell cultures' physiological relevance. The latter is also the case for the presented nMPS. The introduced device has shown to be suitable for studying the effects of several chemical compounds via multiple readout possibilities. Ultimately, it also promoted NPCs' survival and the potential of morphological and functional analysis, demonstrating the usability to complete research employing human-derived cell lines.

Induced pluripotent stem cells have been a crucial factor to imitate human neuronal pathophysiology in the CNS. In recent years several cell lines that mimic PD or AD behaviour

have been developed (Park et al., 2018; Chen et al., 2020). Through the various readouts that this nMPS provides, those iPSCs may be characterized. Processes such as protein aggregations and the effect on neuronal circuits or glial activation can be evaluated and better understood.

More importantly, iPSCs technology allows the engineering of patient-derived cells, practical to determine the pathological cause of patient-specific disorders or correct a present mutation for posterior cell therapy. Certainly, cell therapy is one of the best options in slowing or ceasing the progression of PD. According to Stoddard- Bennett and Pera (2019), in 2018, a study was started to complete a transplantation trial (Takahashi Lab, Kyoto University Hospital, Japan, 2018). Here, patient-specific fibroblasts carrying a mutation that causes familial PD are obtained and reprogrammed to dopaminergic iPSCs in which the mutation is corrected. After safety and quality checks, those lineages are introduced into the brain-specific areas of the patient. Before applying this methodology in humans, the functioning of human dopaminergic iPSCs was tested on a PD model in primates (Kikuchi et al., 2017). The results showed considerable improvements without tumour formations in an observation period of two years. In order to determine the quality of the cell lines, the presented nMPS could be employed before initiating primate or human trials. Pre-clinical testing would aid to discard cell lineages that do not behave as expected and characterise them further.

7.3.2 Drug development

The fabrication of nMPS intends to fill the gap between traditional 2D platforms and animal models as they do not fully represent the complexity of brain physiology (Walker et al., 2018). Physiological relevance is especially crucial for drug development. As aforementioned, the failure to determine the drug efficacy and unpredicted toxicity effects is the major reason for the high attrition rates in CNS drugs (Schuler, 2017). This issue does not only increase the costs significantly but also causes a lack of medicine for certain neurological disorders. By providing an interdisciplinary high-throughput nMPS, efficacy and toxicity testing of novel drugs could be more efficiently tested and, therefore, reduce the rate of previously undetected toxic effects upon testing in 2D platforms or animal models (Watson et al., 2017). Additionally, through the increased predictability, the testing of novel compounds may lead to identifying new drug targets or disease mechanisms. Consequently, pharmacokinetics and – dynamics might be determined more quickly.

Furthermore, as explained above, new genetic technologies allow the possibility of creating patient-specific induced pluripotent cell lines with a specific gender or genetic background (Bhatia and Ingber, 2014). Through the utilisation of this nMPS, personalized medicine may be developed. Accordingly, cell lines could be tested for efficacy of already existing compounds. More importantly, the nMPS opens the possibility for the development and efficiency testing of new drugs to treat rare neuronal diseases.

7.3.3 Neurotoxicity screenings

Neurotoxicity tests are crucial during drug development. Nonetheless, they are also performed for detecting environmental toxicity (Roberts et al., 2015). For this purpose, metals, pesticides, and organometals are tested to determine the damage they can cause to the CNS. Presently, the chemical risk is assessed with animal models. However, those are rarely translatable to humans (Roberts et al., 2015), especially when evaluating the seizure or sedation side effects of chemical compounds (Kumlien and Lundberg, 2010). To fill this gap, the use of MEA technology integrated into simplified 2D platforms demonstrated to be highly stable and suitable for testing multiple targets at once and is therefore thought to be the most appropriate technique to estimate seizures or sedation effects (Slikker et al., 2019).

Consequently, MEA technology has been employed for functional screening of compounds (Johnstone et al., 2010; Novellino et al., 2011). Also, it has been developed in the last years to allow the assessment of multiple dosage and compounds simultaneously by providing devices with higher throughput (see tables 3.1 and 3.2). Nevertheless, monolayers do not fully recapitulate *in vivo* situations and are therefore replaced by 3D cell cultures in nMPS. Indeed, some studies have already employed 3D nMPS to corroborate the effect of certain pesticides, such as rotenone, and actually classified the latter as a potential environmental risk factor for PD (Pamies et al., 2017; Pamies et al., 2018). Still, those studies did not evaluate the functionality of 3D neurons, which reduces the possibility of earlier detection of side effects. Therefore, this study primarily focused on providing a multidisciplinary device that allowed the assessment of neuronal functionality. Additionally, it gives insights at morphological and molecular levels of 3D cell cultures. Ultimately, by employing the presented nMPS, neurotoxicity screenings can be carried out to assess the risk of novel chemicals employed in agriculture, cosmetics and others.

7.4 nMPS market: challenges and forecast

Lately, several companies have expanded the MPS technology commercialisation focused on the neuronal system. Some examples are the XonaChipsTM (Dr Noo Li Jeon, Xona LLC microfluidics), the MicroBrain Biotech (Dr Bernadette Bung), the OrganoPlateTM (Dr Paul Vito and Dr Jos, mimetas), or Nerve-on-chip TM (AxoSim, Dr Michael Moore, Tulane University). It started with the compartmentalisation of the cell body and axons (Taylor et al., 2005; Li et al., 2019) and continued with the fabrication of microfluidics containing microtunnels, most effective in controlling and evaluating axonal direction growth (Courte et al., 2018; Lassus et al., 2018). Subsequently, a phase guide microfluidic configuration was fabricated that allows the perfusion and growth of 3D neurons (Wevers et al., 2016). Undoubtedly, those platforms' success did not depend only on the technology itself but instead on the usability, unique assays and informative analyses able to be performed by employing standard laboratory techniques (Junaid et al., 2017). Those are requirements fulfilled by the presented nMPS.

Certainly, the system employed during this study, above all, aimed to fulfil the suggestions proposed by the ORCHID (organ-on-chip in development) community to produce a brain-on-a-chip (Mastrangeli et al., 2019). Through the nMPS components, especially the microfluidic design, the introduced system is a ready-to-use platform that facilitates the cell seeding of homogeneously distributed cells and uncomplicated media change due to the absence of perfusion systems. Moreover, the unique possibility of performing high-throughput non-invasive extracellular recordings from dissociated murine or human-derived neurons and neurospheres simultaneously to Ca^{2+}-imaging and optogenetics makes this platform exclusive compared to most existing systems. Furthermore, standard techniques, such as live-cell imaging, ICC, LMA or large-scale imaging, increases the adaptability for end-users. For the mentioned reasons, this nMPS could potentially be commercialised. Otherwise, as other small OoC corporations do (Mastrangeli et al., 2019), the NMS could offer a full-service in house employing this nMPS to help comprehend the end-users needs.

Indeed, some reports estimate MPS technology, especially OoCs, to become a multi-billion market in the upcoming years. The basis for that is the capacity to improve the transition from pre-clinical to clinical studies in pharmaceutical companies (Li et al., 2019). Nonetheless, for accurate estimation, the production of new devices and the demand for more predictive *in vitro* models need to be evaluated. For this reason, more devices, like the one presented here, aim for compatibility with human-derived cells and higher throughput. These implementations would profit their adoption for drug discovery and testing of diverse compounds and ultimately increase the life quality of that part of the population suffering from neurological disorders.

8 Statement of contributions

Part of this work has been submitted for publication (Molina-Martínez et al., 2021). Both Dr Beatriz Martínez Molina and I are the first co-authors of the mentioned publication. The latter describes the production of a novel neuro microphysiological system that allows the characterisation of 3D neuronal networks via morphological and functional readouts. Additionally, the publication shows the possibility of simultaneously recording electrophysiological data while performing Ca^{2+}-imaging and optogenetics. The following table aims to disclose the contributions of colleagues in the different sections. Some of those materials and results are also included in the published manuscript. Data or methodologies included in the manuscript but not throughout this specific work are not included in the table.

Statement of contributions	LVJ	BBM	FE	MvdM	SD	KS	AK	MM	LFGA	MJ	NSM	PH	PDJ	PC
Conceptualization: Experimental design (**System validation**)														
Conceptualization: Experimental design (**Microglia**)														
Methodology: Microfluidic design (**sections 4.2.3.2, 5.1 and 5.2**)														
Methodology: CμE design (**sections 4.2.3.1 and 5.1**)														
Methodology: Device fabrication (**sections 4.2.3.1, 4.2.3.2, 5.1.1 and 5.2.1**)														
Investigation: CμE-recording efficiency (**sections 4.2.3.1 and 5.1.3**)														
Investigation: SEM images (**section 5.1.1**)														
Investigation: Morphological readouts (**sections 5.1.2, 5.1.3.2, 5.2.3 and 5.2.4**)														
Investigation: Microglia cell sorting and acquisition (**sections 4.1.2, 5.1.2, 5.2.2 and 5.2.3**)														
Investigation: Electrophysiological recordings (**sections 5.1.3 and 5.2.5**)														
Investigation: Ca++-imaging and optogenetics (**sections 4.4.4, 4.4.5 and 5.1.3.3**)														
Investigation: Cytokine quantification (**section 4.4.7, 5.2.6**)														
Automation system: microscopy (**sections 4.4.6 and 5.1.2**)														
Automation system adapter: design (**sections 4.4.6 and 5.1.2**)														
Formal analysis: Statistics system validation (**sections 4.4.3, 5.1.3.1 and 5.1.3.2**)														
Formal analysis: Statistics microglia (**sections 4.4.3, 5.2.5 and 5.2.6**)														
Formal analysis: Electrophysiology (**sections 4.4.2, 5.1.3 and 5.2.5**)														
Visualization: Data presentation system validation (**section 5.1**)														
Visualization: Data presentation microglia (**section 5.2**)														

LVJ= Laura-Victoria Jentsch; BMM= Beatriz Martínez Molina; FE= Fulya Ersoy; MvdM= Matthijs van der Moolen; SD= Stella Donato; AK= Alex Kirillov; KS= Kathrin Stadelmann; MM= Mathew McDonald; Laura Fernández García-Agudo; MJ= Meike Jakobi; NSM= Nicole Schneiderhan-Marra; PH= Peter Heutink; PDJ= Peter D. Jones; PC= Paolo Cesare. Dark green= significant contribution; Light green= less significant contribution; White= no contribution.

9 Bibliography

Accardi, M. V., Pugsley, M. K., Forster, R., Troncy, E., Huang, H., and Authier, S. (2016). The emerging role of in Vitro electrophysiological methods in Cns Safety pharmacology. Journal of Pharmacological and Toxicological Methods, 81, 47-59. doi:10.1016/j.vascn.2016.03.008.

Adamsky, A., Kol, A., Kreisel, T., Doron, A., Ozeri-Engelhard, N., Melcer, T., Refaeli, R., Horn, H., Regev, L., Groysman, M., London, M., and Goshen, I. (2018). Astrocytic Activation Generates De Novo Neuronal Potentiation and Memory Enhancement. Cell, 174(1). doi:10.1016/j.cell.2018.05.002.

Adriani, G., Ma, D., Pavesi, A., Kamm, R. D., and Goh, E. L. (2017). A 3D neurovascular microfluidic model consisting of neurons, astrocytes and cerebral endothelial cells as a blood–brain barrier. Lab on a Chip, 17(3), 448-459. doi:10.1039/c6lc00638h.

Alwine, J. C., Kemp, D. J., and Stark, G. R. (1977). Method for detection of specific RNAs in agarose gels by transfer to diazobenzyloxymethyl-paper and hybridization with DNA probes. Proceedings of the National Academy of Sciences, 74(12), 5350-5354. doi:10.1073/pnas.74.12.5350.

Amin, N. D., and Paşca, S. P. (2018). Building models of brain disorders with three-dimensional organoids. Neuron, 100(2), 389-405. doi:10.1016/j.neuron.2018.10.007.

Amor, S., Puentes, F., Baker, D., and Van der Valk, P. (2010). Inflammation in neurodegenerative diseases. Immunology, 129(2), 154-169. doi:10.1111/j.1365-2567.2009.03225.x.

Araque, A., Parpura, V., Sanzgiri, R. P., and Haydon, P. G. (1999). Tripartite synapses: Glia, the unacknowledged partner. Trends in Neurosciences, 22(5), 208-215. doi:10.1016/s0166-2236(98)01349-6.

Arellano, G., Ottum, P. A., Reyes, L. I., Burgos, P. I., and Naves, R. (2015). Stage-specific role of interferon-gamma in experimental autoimmune encephalomyelitis and multiple sclerosis. Frontiers in Immunology, 6. doi:10.3389/fimmu.2015.00492.

Bachstetter, A. D., Van Eldik, L. J., Schmitt, F. A., Neltner, J. H., Ighodaro, E. T., Webster, S. J., J., Patel, E., Abner, E. L., Kryscio, R. J., and Nelson, P. T. (2015). Disease-related microglia heterogeneity in the hippocampus of alzheimer's disease, dementia with Lewy bodies, and hippocampal sclerosis of aging. Acta Neuropathologica Communications, 3(1). doi:10.1186/s40478-015-0209-z.

Bae, J. H., Lee, J. M., and Chung, B. G. (2016). Hydrogel-encapsulated 3D microwell array for neuronal differentiation. Biomedical Materials, 11(1), 015019. doi:10.1088/1748-6041/11/1/015019.

Baëtens, T., Begard, S., Pallecchi, E., Thomy, V., Arscott, S., and Halliez, S. (2020). The effect of thermal treatment on the neuronal cell biocompatibility of su-8. Materials Today Communications, 24, 101073. doi:10.1016/j.mtcomm.2020.101073.

Bak, L. K., Schousboe, A., and Waagepetersen, H. S. (2006). The glutamate/gaba-glutamine cycle: Aspects of transport, neurotransmitter homeostasis and ammonia transfer. Journal of Neurochemistry, 98(3), 641-653. doi:10.1111/j.1471-4159.2006.03913.x.

Baltimore, D. (1970). Viral RNA-dependent DNA Polymerase: RNA-dependent DNA polymerase In Virions of RNA tumour viruses. Nature, 226(5252), 1209-1211. doi:10.1038/2261209a0.

Barcia, C., Ros, C. M., Annese, V., Gómez, A., Ros-Bernal, F., Aguado-Llera, D., D., Martínez-Pagán, M. E., de Pablos, V., Fernandez-Villalba, E., and Herrero, M. T. (2011). Ifn-γ

signaling, with the synergistic contribution of tnf-α, mediates cell specific microglial and astroglial activation in experimental models of parkinson's disease. Cell Death and Disease, 2(4). doi:10.1038/cddis.2011.17.

Baron, M. S., Chaniary, K. D., Rice, A. C., and Shapiro, S. M. (2011). Multi-Neuronal recordings in the basal ganglia in normal AND Dystonic Rats. Frontiers in Systems Neuroscience, 5. doi:10.3389/fnsys.2011.00067

Basu, A., Krady, J. K., and Levison, S. W. (2004). Interleukin-1: A master regulator of neuroinflammation. Journal of Neuroscience Research, 78(2), 151-156. doi:10.1002/jnr.20266.

Batzoglou, S. (2000). Human and Mouse Gene Structure: Comparative Analysis and Application to Exon Prediction. Genome Research, 10(7), 950-958. doi:10.1101/gr.10.7.950.

Bavli, D., Prill, S., Ezra, E., Levy, G., Cohen, M., Vinken, M., Vanfleteren, J., Jaeger, M., and Nahmias, Y. (2016). Real-time monitoring of metabolic function in liver-on-chip microdevices tracks the dynamics of mitochondrial dysfunction. Proceedings of the National Academy of Sciences, 113(16). doi:10.1073/pnas.1522556113.

Belkhelfa, M., Rafa, H., Medjeber, O., Arroul-Lammali, A., Behairi, N., Abada-Bendib, M., Makrelouf, M., Belarbi, S., Masmoudi, A. N., Tazir, M., and Touil-Boukoffa, C. (2014). IFN-γ and TNF-α Are Involved During Alzheimer Disease Progression and Correlate with Nitric Oxide Production: A Study in Algerian Patients. Journal of Interferon and Cytokine Research, 34(11), 839–847. doi:10.1089/jir.2013.0085

Bellouard, Y. (2012). The Femtoprint Project. Journal of Laser Micro/Nanoengineering, 7(1), 1-10. doi:10.2961/jlmn.2012.01.0001.

Benveniste, E. N., and Benos, D. J. (1995). TNF-alpha- and IFN-gamma-mediated signal transduction pathways: effects on glial cell gene expression and function. The FASEB Journal, 9(15), 1577–1584. https://doi.org/10.1096/fasebj.9.15.8529837.

Bertholet, A. M., Delerue, T., Millet, A. M., Moulis, M. F., David, C., Daloyau, M., Arnauné-Pelloquin, L., Davezac, N., Mils, V., Miquel, M. C., Rojo, M., and Belenguer, P. (2016). Mitochondrial fusion/fission dynamics in neurodegeneration and neuronal plasticity. Neurobiology of Disease, 90, 3–19. doi:10.1016/j.nbd.2015.10.011.

Betarbet, R., Sherer, T. B., MacKenzie, G., Garcia-Osuna, M., Panov, A. V., and Greenamyre, J. T. (2000). Chronic systemic pesticide exposure reproduces features of Parkinson's disease. Nature Neuroscience, 3(12), 1301-1306. doi:10.1038/81834

Bhatia, S. N., and Ingber, D. E. (2014). Microfluidic organs-on-chips. Nature Biotechnology, 32(8), 760-772. doi:10.1038/nbt.2989.

Biffi, E., Regalia, G., Menegon, A., Ferrigno, G., and Pedrocchi, A. (2013). The influence of neuronal density and maturation on network activity of hippocampal cell cultures: A methodological study. PLoS ONE, 8(12). doi:10.1371/journal.pone.0083899.

Bohlen, C. J., Bennett, F. C., Tucker, A. F., Collins, H. Y., Mulinyawe, S. B., and Barres, B. A. (2017). Diverse requirements for microglial survival, specification, and function revealed by defined-medium cultures. Neuron, 94(4). doi:10.1016/j.neuron.2017.04.043.

Boonstra, E., De Kleijn, R., Colzato, L. S., Alkemade, A., Forstmann, B. U., and Nieuwenhuis, S. (2015). Neurotransmitters as food supplements: The effects of gaba on brain and behavior. Frontiers in Psychology, 6. doi:10.3389/fpsyg.2015.01520.

Boullay, PF (1812). "Analyse chimique de la Coque du Levant, Menispermum cocculus". Bulletin de Pharmacie (in French). 4: 5–34. Menispermum cocculus" has been renamed "Anamirta cocculus".

Bourke, J. L., Quigley, A. F., Duchi, S., O'Connell, C. D., Crook, J. M., Wallace, G. G., Cook, M. J., and Kapsa, R. M. I. (2017). Three-dimensional neural cultures produce networks that mimic native brain activity. Journal of Tissue Engineering and Regenerative Medicine, 12(2), 490–493. https://doi.org/10.1002/term.2508.

Brodal, P. (2010). Central Nervous System: Structure and Function. Cary: Oxford University Press, USA.

Bronisz, E., and Kurkowska-Jastrzębska, I. (2016). Matrix metalloproteinase 9 In Epilepsy: The role of NEUROINFLAMMATION in Seizure Development. Mediators of Inflammation, 2016, 1-14. doi:10.1155/2016/7369020.

Brown, J. A., Codreanu, S. G., Shi, M., Sherrod, S. D., Markov, D. A., Neely, M. D., Britt, C. M., Hoilett, O. S., Reiserer, R. S., Samson, P. C., McCawley, L. J., Webb, D. J., Bowman, A. B., McLean, J. A., and Wikswo, J. P. (2016). Metabolic consequences of inflammatory disruption of the blood-brain barrier in an organ-on-chip model of the human neurovascular unit. Journal of Neuroinflammation, 13(1). doi:10.1186/s12974-016-0760-y.

Brunello, C. A., Jokinen, V., Sakha, P., Terazono, H., Nomura, F., Kaneko, T., Lauri, S. E., Franssila, S., Rivera, C., Yasuda, K., and Huttunen, H. J (2013). Microtechnologies to FUEL neurobiological research with nanometer precision. Journal of Nanobiotechnology, 11(1), 11. doi:10.1186/1477-3155-11-11.

Buisson, A., Nicole, O., Docagne, F., Sartelet, H., Mackenzie, E. T., and Vivien, D. (1998). Up-regulation of a serine protease inhibitor in astrocytes mediates the neuroprotective activity of transforming growth factor β1. The FASEB Journal, 12(15), 1683-1691. doi:10.1096/fasebj.12.15.1683.

Burns, A., and Iliffe, S. (2009). Alzheimer's disease. BMJ, 338(Feb05 1). doi:10.1136/bmj.b158.

Cairns, D. M., Rouleau, N., Parker, R. N., Walsh, K. G., Gehrke, L., and Kaplan, D. L. (2020). A 3d human brain–like tissue model of herpes-induced alzheimer's disease. Science Advances, 6(19). doi:10.1126/sciadv.aay8828.

Cajal, S. R., and May, R. M. (1928). Degeneration and regeneration of the nervous system. Oxford: Oxford University Press.

Cannell M.B., Berlin J.R. and Lederer W.J. (1987). Intracellular calcium in cardiac myocytes: calcium transients measured using fluorescence imaging. Soc Gen Physiol Ser.42:201-14. PMID: 3505361.

Carbone, L. (2004). What animals want: Expertise and advocacy in laboratory animal welfare policy. Choice Reviews Online, 42(04). doi:10.5860/choice.42-2227

Carter M., Shieh J.C. (2010). Guide to Research Techniques in Neuroscience: Elsevier Inc.

Cesare P., Jones P., Molina-Martínez, B. (2017). Device for the examination of neurons. In: WO 2019/115320 A1. Germany.

Chandrasekaran, A., Avci, H. X., Ochalek, A., Rösingh, L. N., Molnár, K., László, L., Teglasi A, Pesti K, Mike A et al (2017). Comparison of 2D and 3D neural induction methods for the generation of Neural progenitor cells from human induced pluripotent stem cells. Stem Cell Research, 25, 139-151. doi:10.1016/j.scr.2017.10.010.

Chang, W., Wu, J., Lee, C., Vogt, B. A., and Shyu, B. (2011). Spatiotemporal organization and thalamic modulation of seizures in the mouse medial thalamic-anterior cingulate slice. Epilepsia, 52(12), 2344-2355. doi:10.1111/j.1528-1167.2011.03312.x.

Charlesworth, P., Cotterill, E., Morton, A., Grant, S., and Eglen, S. J. (2015). Quantitative differences in developmental profiles of spontaneous activity in cortical and hippocampal cultures. Neural Development, 10(1), 1. doi:10.1186/s13064-014-0028-0.

Chen, H. J., Miller, P., and Shuler, M. L. (2018). A pumpless body-on-a-chip model using a primary culture of human intestinal cells and a 3d culture of liver cells. Lab on a Chip, 18(14), 2036-2046. doi:10.1039/c8lc00111a.

Chen, M., Maimaitili, M., Buchholdt, S. H., Jensen, U. B., Febbraro, F., and Denham, M. (2020). Generation of eight human induced pluripotent stem cell lines from Parkinson's disease patients carrying familial mutations. Stem Cell Research, 42, 101657. doi:10.1016/j.scr.2019.101657.

Chen, X., and Pan, W. (2015). The treatment strategies for neurodegenerative diseases BY integrative medicine. Integrative Medicine International, 1(4), 223-225. doi:10.1159/000381546.

Choi, S. H., Kim, Y. H., Quinti, L., Tanzi, R. E., and Kim, D. Y. (2016). 3D culture models of Alzheimer's disease: A road map to a "cure-in-a-dish". Molecular Neurodegeneration, 11(1). doi:10.1186/s13024-016-0139-7

Chwalek, K., Tang-Schomer, M. D., Omenetto, F. G., and Kaplan, D. L. (2015). In vitro bioengineered model of cortical brain tissue. Nature Protocols, 10(9), 1362-1373. doi:10.1038/nprot.2015.091.

Cirit, M., and Stokes, C. L. (2018). Maximizing the impact of microphysiological systems with in vitro–in vivo translation. Lab on a Chip, 18(13), 1831-1837. doi:10.1039/c8lc00039e.

Coombs, J. S., Eccles, J. C., and Fatt, P. (1955). The specific ionic conductances and the ionic movements across the motoneuronal membrane that produce the inhibitory post-synaptic potential. The Journal of Physiology, 130(2), 326-373. doi:10.1113/jphysiol.1955.sp005412.

Coquinco A., Cynader M. (2015) Use of a 3-Compartment Microfluidic Device to Study Activity Dependent Synaptic Competition. In: Biffi E. (eds) Microfluidic and Compartmentalized Platforms for Neurobiological Research. Neuromethods, vol 103. Humana Press, New York, NY. https://doi.org/10.1007/978-1-4939-2510-0_8

Cotterill, E., Charlesworth, P., Thomas, C. W., Paulsen, O., and Eglen, S. J. (2016). A comparison of computational methods for detecting bursts in neuronal spike trains and their application to human stem cell-derived neuronal networks. Journal of Neurophysiology, 116(2), 306-321. doi:10.1152/jn.00093.2016.

Courte, J., Renault, R., Jan, A., Viovy, J., Peyrin, J., and Villard, C. (2018). Reconstruction of directed neuronal networks in a microfluidic device with asymmetric microchannels. Methods in Cell Biology, 71-95. doi:10.1016/bs.mcb.2018.07.002.

Cugola, F. R., Fernandes, I. R., Russo, F. B., Freitas, B. C., Dias, J. L., Guimarães, K. P., et al. (2016). The Brazilian Zika virus strain causes birth defects in experimental models. Nature, 534(7606), 267-271. doi:10.1038/nature18296.

Cuní-López, C., Quek, H., Oikari, L. E., Stewart, R., Nguyen, T. H., Sun, Y. et al. (2021). 3D models of Alzheimer's disease patient microglia recapitulate disease phenotype and show differential drug responses compared to 2d. doi:10.1101/2021.03.17.435758.

De Paola, M., Buanne, P., Biordi, L., Bertini, R., Ghezzi, P., and Mennini, T. (2007). Chemokine MIP-2/CXCL2, acting on Cxcr2, Induces motor neuron death in primary cultures. Neuroimmunomodulation, 14(6), 310-316. doi:10.1159/000123834.

del Río Hortega P, Penfield W (1892). "Cerebral Cicatrix: the Reaction of Neuroglia and Microglia to Brain Wounds". Bulletin of the Johns Hopkins Hospital. 41: 278–303.

Deuschl, G., Beghi, E., Fazekas, F., Varga, T., Christoforidi, K. A., Sipido, E. et al. (2020). The burden of neurological diseases in Europe: An analysis for the Global burden of Disease Study 2017. The Lancet Public Health, 5(10). doi:10.1016/s2468-2667(20)30190-0.

Dexter, D. T., Carter, C. J., Wells, F. R., Javoy-Agid, F., Agid, Y., Lees, A. et al. (1989). Basal Lipid Peroxidation in Substantia Nigra Is Increased in Parkinson's Disease. Journal of Neurochemistry, 52(2), 381-389. doi:10.1111/j.1471-4159.1989.tb09133.x.

Dobrenis, K., Chang, H., Pina-Benabou, M., Woodroffe, A., Lee, S., Rozental, R. et al. (2005). Human and mouse microglia express connexin36, and functional gap junctions are formed between rodent microglia and neurons. Journal of Neuroscience Research, 82(3), 306-315. doi:10.1002/jnr.20650.

Dowden H., Munro J. (2019). Trends in clinical success rates and therapeutic focus. Nat Rev Drug Discov, 18(7):495-496.

Dulamea, A. O. (2017). Role of oligodendrocyte dysfunction in demyelination, remyelination and neurodegeneration in multiple sclerosis. Multiple Sclerosis: Bench to Bedside, 91-127. doi:10.1007/978-3-319-47861-6_7

Ehrenberger, K., Benkoe, E., and Felix, D. (1982). Suppressive action of picrotoxin, a GABA antagonist, on labyrinthine spontaneous nystagmus and vertigo in man. Acta Oto-Laryngologica, 93(1-6), 269-273. doi:10.3109/00016488209130882.

Elliott, A. C., and Woodward, W. A. (2007). Statistical analysis quick reference guidebook: With SPSS examples. Thousand Oaks, CA: Sage Publications.

Elshal, M., and McCoy, J. (2006). Multiplex bead array assays: Performance evaluation and comparison of sensitivity to ELISA. Methods, 38(4), 317-323. doi:10.1016/j.ymeth.2005.11.010.

Engvall, E., Jonsson, K., and Perlmann, P. (1971). Enzyme-linked immunosorbent assay. ii. quantitative assay of protein antigen, immunoglobulin g, by means of enzyme-labelled antigen and antibody-coated tubes. Biochimica Et Biophysica Acta (BBA) - Protein Structure, 251(3), 427-434. doi:10.1016/0005-2795(71)90132-2

Erta, M., Quintana, A., and Hidalgo, J. (2012). Interleukin-6, a major cytokine in the central nervous system. International Journal of Biological Sciences, 8(9), 1254-1266. doi:10.7150/ijbs.4679

Esch, M. B., Ueno, H., Applegate, D. R., and Shuler, M. L. (2016). Modular, pumpless body-on-a-chip platform for THE co-culture of GI TRACT epithelium and 3D Primary liver tissue. Lab on a Chip, 16(14), 2719-2729. doi:10.1039/c6lc00461j.

Fan, Y., Nguyen, D. T., Akay, Y., Xu, F., and Akay, M. (2016). Engineering a Brain Cancer Chip for High-throughput Drug Screening. Scientific Reports, 6(1). https://doi.org/10.1038/srep25062.

Fang, Y., and Eglen, R. M. (2017). Three-Dimensional cell cultures in drug discovery and development. Slas Discovery: Advancing the Science of Drug Discovery, 22(5), 456-472. doi:10.1177/1087057117696795.

Filiano, A. J., Gadani, S. P., and Kipnis, J. (2015). Interactions of innate and adaptive immunity in brain development and function. Brain Research, 1617, 18-27. doi:10.1016/j.brainres.2014.07.050.

Flores-Obando, R. E., Freidin, M. M., and Abrams, C. K. (2018). Rapid and specific immunomagnetic isolation of mouse primary oligodendrocytes. Journal of Visualized Experiments, (135). doi:10.3791/57543.

Fogel, D.B. (2018). Factors associated with clinical trials that fail and opportunities for improving the likelihood of success: A review. Contemp Clin Trials Commun, 11:156-164.

Foster, M. and Sherrington, C.S. (1897). Textbook of Physiology, volume 3 (7th ed.). London: Macmillan, p.929.

Franzen, N., van Harten, W. H., Retèl, V. P., Loskill, P., van den Eijnden-van Raaij, J., and Ijzerman, M. (2019). Impact of organ-on-a-chip technology on pharmaceutical RandD costs. Drug Discovery Today, 24(9), 1720–1724. https://doi.org/10.1016/j.drudis.2019.06.003.

Frega, M., Tedesco, M., Massobrio, P., Pesce, M., and Martinoia, S (2014): Network dynamics of 3D engineered neuronal cultures: a new experimental model for in-vitro electrophysiology. Sci Rep, 4:5489

Fróes, M. M., Correia, A. H., Garcia-Abreu, J., Spray, D. C., Campos de Carvalho, A. C., and Neto, V. M. (1999). Gap-junctional coupling between neurons and astrocytes in primary central nervous system cultures. Proceedings of the National Academy of Sciences, 96(13), 7541-7546. doi:10.1073/pnas.96.13.7541.

Fujioka, H., Dairyo, Y., Yasunaga, K., and Emoto, K. (2012). Neural functions of matrix Metalloproteinases: Plasticity, neurogenesis, and disease. Biochemistry Research International, 2012, 1-8. doi:10.1155/2012/789083.

Gall, J. G., and Pardue, M. L. (1969). Formation and detection of rna-dna hybrid molecules in cytological preparations. Proceedings of the National Academy of Sciences, 63(2), 378-383. doi:10.1073/pnas.63.2.378

Garcez, P.P; Loiola, E. C.,da Costa, R. M., Higa, L. M., Trindade, P., Delvecchio, R., Nascimento, J. M., Brindeiro, R., Tanuri, A., Rehen, S. K. (2016). Zika virus impairs growth in human neurospheres and brain organoids. Science 352, 816–818.

Garcia-Agudo, L. F., Janova, H., Sendler, L. E., Arinrad, S., Steixner, A. A., Hassouna, I., . . . Ehrenreich, A. H. (2019). Genetically induced brain inflammation by cnp deletion transiently benefits from microglia depletion. The FASEB Journal, 33(7), 8634-8647. doi:10.1096/fj.201900337r.

GBD 2015 Neurological Disorders Collaborator Group. Global, regional, and national burden of neurological disorders during 1990-2015: a systematic analysis for the Global Burden of Disease Study 2015. Lancet Neurol 2017; 16: 877-97.

Gelfman S, Wang Q, Lu YF, Hall D, Bostick CD, Dhindsa R, Halvorsen M, McSweeney KM, Cotterill E, Edinburgh T et al. (2018). meaRtools: An R package for the analysis of neuronal networks recorded on microelectrode arrays. PLoS Comput Biol, 14(10):e1006506.

Göbel, K., Ruck, T., and Meuth, S. G. (2018). Cytokine signaling in multiple sclerosis: Lost in translation. Multiple Sclerosis Journal, 24(4), 432-439. doi:10.1177/1352458518763094.

Godbe, J. M., Freeman, R., Burbulla, L. F., Lewis, J., Krainc, D., and Stupp, S. I. (2020). Gelator length Precisely TUNES Supramolecular Hydrogel stiffness and NEURONAL phenotype in 3D culture. ACS Biomaterials Science and Engineering, 6(2), 1196-1207. doi:10.1021/acsbiomaterials.9b01585.

Gottmann, J., Hermans, M., and Ortmann, J. (2012). Digital photonic production of Micro structures in glass by In-volume Selective laser-induced etching using a high SPEED Micro scanner. Physics Procedia, 39, 534-541. doi:10.1016/j.phpro.2012.10.070.

Götz, J., Bodea, LG. and Goedert, M. Rodent models for Alzheimer disease. Nat Rev Neurosci 19, 583–598 (2018). https://doi.org/10.1038/s41583-018-0054-8.

Graber, D. J., Hickey, W. F., and Harris, B. T. (2010). Progressive changes in microglia and macrophages in spinal cord and peripheral nerve in the transgenic rat model of amyotrophic lateral sclerosis. Journal of Neuroinflammation, 7(1), 8. doi:10.1186/1742-2094-7-8.

Grosberg, A., Alford, P. W., McCain, M. L., and Parker, K. K. (2011). Ensembles of engineered cardiac tissues for physiological and pharmacological study: Heart on a chip. Lab on a Chip, 11(24), 4165. doi:10.1039/c1lc20557a.

Gurney K. (2004). An introduction to neural networks. London, UK: University College London Press.

Habibey, R., Golabchi, A., Latifi, S., Difato, F., and Blau, A. (2015). A microchannel device tailored to laser axotomy and long-term microelectrode array electrophysiology of functional regeneration. Lab on a Chip, 15(24), 4578-4590. doi:10.1039/c5lc01027f.

Hackam, D. G., and Redelmeier, D. A. (2006). Translation of research evidence from animals to humans. JAMA, 296(14), 1727. doi:10.1001/jama.296.14.1731.

Hämmerle, H., Egert, U., Mohr, A., and Nisch, W. (1994). Extracellular recording in neuronal networks with substrate integrated Microelectrode arrays. Biosensors and Bioelectronics, 9(9-10), 691-696. doi:10.1016/0956-5663(94)80067-7.

Hancock, M. K., Kopp, L., Kaur, N., and Hanson, B. J. (2015). A facile method for simultaneously measuring neuronal cell viability and neurite outgrowth. Current Chemical Genomics and Translational Medicine, 9(1), 6-16. doi:10.2174/2213988501509010006.

Haselier, C., Biswas, S., Rösch, S., Thumann, G., Müller, F., and Walter, P. (2017). Correlations between specific patterns of spontaneous activity and stimulation efficiency in degenerated retina. PLOS ONE, 12(12). doi:10.1371/journal.pone.0190048.

Herland, A., Van der Meer, A. D., FitzGerald, E. A., Park, T., Sleeboom, J. J., and Ingber, D. E. (2016). Distinct contributions of astrocytes And Pericytes to Neuroinflammation identified in a 3d Human blood-brain barrier on a chip. PLOS ONE, 11(3). doi:10.1371/journal.pone.0150360.

Heuschkel, M. O., Fejtl, M., Raggenbass, M., Bertrand, D., and Renaud, P. (2002). A three-dimensional multi-electrode array for multi-site stimulation and recording in acute brain slices. Journal of Neuroscience Methods, 114(2), 135-148. doi:10.1016/s0165-0270(01)00514-3.

Hodgkin, A. L., and Huxley, A. F. (1952). A quantitative description of membrane current and its application to conduction and excitation in nerve. The Journal of Physiology, 117(4), 500-544. doi:10.1113/jphysiol.1952.sp004764.

Hughes, C. S., Postovit, L. M., and Lajoie, G. A. (2010). Matrigel: A complex protein mixture required for optimal growth of cell culture. PROTEOMICS, 10(9), 1886-1890. doi:10.1002/pmic.200900758.

Huh, D., Matthews, B. D., Mammoto, A., Montoya-Zavala, M., Hsin, H. Y., and Ingber, D. E. (2010). Reconstituting organ-level lung functions on a chip. Science, 328(5986), 1662-1668. doi:10.1126/science.1188302.

Idris, F., Hanna Muharram, S., Zaini, Z., and Diah, S. (2018). Establishment of murine in vitro blood-brain barrier models using immortalized cell lines: Co-cultures of brain endothelial cells, astrocytes, and neurons. doi:10.1101/435990.

Ionescu, A., Zahavi, E. E., Gradus, T., Ben-Yaakov, K., and Perlson, E. (2016). Compartmental microfluidic system for studying muscle–neuron communication and neuromuscular

junction maintenance. European Journal of Cell Biology, 95(2), 69-88. doi:10.1016/j.ejcb.2015.11.004.

Irons, H. R., Cullen, D. K., Shapiro, N. P., Lambert, N. A., Lee, R. H.,and LaPlaca, M. C. (2008). Three-dimensional neural constructs: A novel platform for Neurophysiological investigation. Journal of Neural Engineering, 5(3), 333-341. doi:10.1088/1741-2560/5/3/006.

Jang, K., Mehr, A. P., Hamilton, G. A., McPartlin, L. A., Chung, S., Suh, K., and Ingber, D. E. (2013). Human kidney proximal tubule-on-a-chip for drug transport and nephrotoxicity assessment. Integrative Biology, 5(9), 1119-1129. doi:10.1039/c3ib40049b.

Jo, J., Xiao, Y., Sun, A., Cukuroglu, E., Tran, H., Göke, J., .et al. (2016). Midbrain-like Organoids from Human pluripotent stem cells contain FUNCTIONAL dopaminergic And Neuromelanin-producing neurons. Cell Stem Cell, 19(2), 248-257. doi:10.1016/j.stem.2016.07.005.

Johnstone, A. F., Gross, G. W., Weiss, D. G., Schroeder, O. H., Gramowski, A., and Shafer, T. J. (2010). Microelectrode arrays: A Physiologically Based neurotoxicity testing platform for the 21st century. NeuroToxicology, 31(4), 331-350. doi:10.1016/j.neuro.2010.04.001.

Jones, P.D. (2017). Nanofluidic technology for chemical neurostimulation. Eberhard Karls Universität Tübingen.

Junaid, A., Mashaghi, A., Hankemeier, T., and Vulto, P. (2017). An end-user perspective on organ-on-a-chip: Assays and usability aspects. Current Opinion in Biomedical Engineering, 1, 15-22. doi:10.1016/j.cobme.2017.02.002.

Kaech, S., and Banker, G. (2006). Culturing hippocampal neurons. Nature Protocols, 1(5), 2406-2415. doi:10.1038/nprot.2006.356.

Kalia, L. V., and Lang, A. E. (2015). Parkinson's disease. The Lancet, 386(9996), 896-912. doi:10.1016/s0140-6736(14)61393-3.

Kamei, K., Koyama, Y., Tokunaga, Y., Mashimo, Y., Yoshioka, M., Fockenberg, C., et al. (2016). Characterization of phenotypic and transcriptional differences in human pluripotent stem cells under 2d and 3d culture conditions. Advanced Healthcare Materials, 5(22), 2951-2958. doi:10.1002/adhm.201600893.

Kandell, E. R., Koester, J. D., Mack, S. H., and Siegelbaum, S. (2021). Principles of neural science. New York: McGraw-Hill.

Kapucu, F. E., Tanskanen, J. M., Mikkonen, J. E., Ylä-Outinen, L., Narkilahti, S., and Hyttinen, J. A. (2012). Burst analysis tool for developing neuronal networks exhibiting highly varying action potential dynamics. Frontiers in Computational Neuroscience, 6. doi:10.3389/fncom.2012.00038.

Keller, D., Erö, C., and Markram, H. (2018). Cell densities in the mouse brain: A systematic review. Frontiers in Neuroanatomy, 12. doi:10.3389/fnana.2018.00083.

Kempermann, Gerd. Adult Neurogenesis. Oxford University Press, 2006, p. 66-78.

Khakh, B. S. and Sofroniew, M. V. (2015). Diversity of astrocyte functions and phenotypes in neural circuits. Nature Neuroscience, 18(7), 942–952. https://doi.org/10.1038/nn.4043.

Kiefer, R., Lindholm, D., and Kreutzberg, G. W. (1993). Interleukin-6 and transforming Growth Factor-β1 mRNAs are induced in rat facial nucleus following Motoneuron Axotomy. European Journal of Neuroscience, 5(7), 775-781. doi:10.1111/j.1460-9568.1993.tb00929.x.

Kikuchi, T., Morizane, A., Doi, D., Magotani, H., Onoe, H., Hayashi, T. et al. (2017). Human ips cell-derived dopaminergic neurons function in a primate parkinson's disease model. Nature, 548(7669), 592-596. doi:10.1038/nature23664

Kilic, O., Pamies, D., Lavell, E., Schiapparelli, P., Feng, Y., Hartung, T., et al. (2016). Brain-on-a-chip model enables analysis of human neuronal differentiation and chemotaxis. Lab on a Chip, 16(21), 4152-4162. doi:10.1039/c6lc00946h.

Kim, Y. H., Choi, S. H., D'Avanzo, C., Hebisch, M., Sliwinski, C., Bylykbashi, E., et al. (2015). A 3D human neural cell culture system for modeling Alzheimer's Disease. Nature Protocols, 10(7), 985-1006. doi:10.1038/nprot.2015.065.

Kim, H., Park, H. J., Choi, H., Chang, Y., Park, H., Shin, J., et al. (2019). Modeling G2019S-LRRK2 Sporadic Parkinson's disease in 3D Midbrain organoids. Stem Cell Reports, 12(3), 518-531. doi:10.1016/j.stemcr.2019.01.020.

Kim, J. W., Lee, S. H., Ko, H. M., Kwon, K. J., Cho, K. S., Choi, C. S., et al. (2011). Biphasic regulation of tissue plasminogen activator activity in ischemic rat brain and in cultured neural cells: Essential role of astrocyte-derived plasminogen activator inhibitor-1. Neurochemistry International, 58(3), 423-433. doi:10.1016/j.neuint.2010.12.020.

Kleinman, H. K., and Martin, G. R. (2005). Matrigel: Basement membrane matrix with biological activity. Seminars in Cancer Biology, 15(5), 378-386. doi:10.1016/j.semcancer.2005.05.004.

Kreutzberg, G. W. (1996). Microglia: A sensor for pathological events in the CNS. Trends in Neurosciences, 19(8), 312-318. doi:10.1016/0166-2236(96)10049-7.

Kumlien, E., and Lundberg, P. O. (2010). Seizure risk associated with neuroactive drugs: Data from the who adverse drug reactions database. Seizure, 19(2), 69-73. doi:10.1016/j.seizure.2009.11.005.

Kunze, A., Giugliano, M., Valero, A., and Renaud, P. (2011). Micropatterning neural cell cultures in 3D with a multi-layered scaffold. Biomaterials, 32(8), 2088-2098. doi:10.1016/j.biomaterials.2010.11.047.

Kyoto University Hospital (2018). Announcement of Physician-Initiated Clinical Trials for Parkinson's Disease. [(accessed on 16 April 2020)]; Available online: https://www.cira.kyoto-u.ac.jp/e/pressrelease/news/180730-170000.html

Lancaster, M. A., Renner, M., Martin, C., Wenzel, D., Bicknell, L. S., Hurles, M. E., et al. (2013). Cerebral organoids model human brain development and microcephaly. Nature, 501(7467), 373-379. doi:10.1038/nature12517.

Lanfranco, M. F., Mocchetti, I., Burns, M. P., and Villapol, S. (2018). Glial- and Neuronal-specific expression OF CCL5 mRNA in the rat brain. Frontiers in Neuroanatomy, 11. doi:10.3389/fnana.2017.00137.

Laplaca, M., Vernekar, V., Shoemaker, J., Cullen, D.K., Coulter, W. (2010). Three-Dimensional Neuronal Cultures. Methods in Bioengineering: 3D Tissue Engineering.

Laprell, L., Schulze, C., Brehme, M., and Oertner, T. G. (2021). The role of microglia membrane potential in chemotaxis. Journal of Neuroinflammation, 18(1). doi:10.1186/s12974-020-02048-0.

Lassus, B., Naudé, J., Faure, P., Guedin, D., Von Boxberg, Y., Mannoury la Cour, C., et al. (2018). Glutamatergic and Dopaminergic modulation OF cortico-striatal CIRCUITS probed by dynamic calcium imaging of networks reconstructed in microfluidic chips. Scientific Reports, 8(1). doi:10.1038/s41598-018-35802-9.

Lau, L. T., and Yu, A. C. (2001). Astrocytes produce and release interleukin-1, Interleukin-6, tumor necrosis factor alpha And Interferon-Gamma following traumatic and Metabolic Injury. Journal of Neurotrauma, 18(3), 351-359. doi:10.1089/08977150151071035.

Lawson, L., Perry, V., and Gordon, S. (1992). Turnover of resident microglia in the normal adult mouse brain. Neuroscience, 48(2), 405-415. doi:10.1016/0306-4522(92)90500-2.

Legendy, C. R., and Salcman, M. (1985). Bursts and recurrences of bursts in the spike trains of spontaneously active striate cortex neurons. Journal of Neurophysiology, 53(4), 926-939. doi:10.1152/jn.1985.53.4.926.

Lelios, I., Cansever, D., Utz, S. G., Mildenberger, W., Stifter, S. A., and Greter, M. (2020). Emerging roles of il-34 in health and disease. Journal of Experimental Medicine, 217(3). doi:10.1084/jem.20190290

Li, C., Zhang, Y., Levin, A. M., Fan, B. Y., Teng, H., Ghannam, M. M., et al. (2018). Distal axonal proteins and their Related MiRNAs in Cultured cortical neurons. Molecular Neurobiology, 56(4), 2703-2713. doi:10.1007/s12035-018-1266-7.

Ling, E., and Wong, W. (1993). The origin and nature of ramified and amoeboid microglia: A historical review and current concepts. Glia, 7(1), 9-18. doi:10.1002/glia.440070105.

Lock, C., Oksenberg, J., and Steinman, L. (1999). The role of TNFalpha AND LYMPHOTOXIN In demyelinating disease. Annals of the Rheumatic Diseases, 58(Supplement 1), I121-I128. doi:10.1136/ard.58.2008.i121.

Łopacińska, J. M., Emnéus, J., and Dufva, M. (2013). Poly(Dimethylsiloxane) (PDMS) affects gene expression in PC12 Cells differentiating INTO neuronal-like cells. PLoS ONE, 8(1). doi:10.1371/journal.pone.0053107.

LoTurco, S., Osellame, R., Ramponi, R., & Vishnubhatla, K. C. (2013). Hybrid chemical etching of femtosecond laser irradiated structures for engineered microfluidic devices. Journal of Micromechanics and Microengineering, 23(8), 085002. doi:10.1088/0960-1317/23/8/085002.

Low, L. A., Mummery, C., Berridge, B. R., Austin, C. P., and Tagle, D. A. (2020). Organs-on-chips: Into the next decade. Nature Reviews Drug Discovery. doi:10.1038/s41573-020-0079-3.

Lucas, S., Rothwell, N. J., and Gibson, R. M. (2006). The role of inflammation in CNS injury and disease. British Journal of Pharmacology, 147(S1). doi:10.1038/sj.bjp.0706400.

Malishev, E., Pimashkin, A., Gladkov, A., Pigareva, Y., Bukatin, A., Kazantsev, V., Mukhina, I., Dubina, M. (2015) Microfluidic device for unidirectional axon growth. Journal of Physics: Conference Series 2015, 643:012025.

Maoz, B. M., Herland, A., FitzGerald, E. A., Grevesse, T., Vidoudez, C., Pacheco, A. R., et al. (2018). A linked organ-on-chip model of the human neurovascular unit reveals the metabolic coupling of endothelial and neuronal cells. Nature Biotechnology, 36(9), 865-874. doi:10.1038/nbt.4226.

Mariani, J., Simonini, M. V., Palejev, D., Tomasini, L., Coppola, G., Szekely, A. M., et al. (2012). Modeling human cortical development in vitro using induced pluripotent stem cells. Proceedings of the National Academy of Sciences, 109(31), 12770-12775. doi:10.1073/pnas.1202944109.

Martinez, A. D., Acuna, R., Figueroa, V., Maripillan, J., and Nicholson, B. (2009). Gap-junction channels dysfunction in deafness and hearing loss. Antioxid. Redox Signal. 11, 309–322. doi: 10.1089/ars.2008.2138.

Marx, U. (2016). Biology-inspired microphysiological system approaches to solve the prediction dilemma of substance testing. ALTEX. doi:10.14573/altex.1603161.

Mastrangeli, M., Millet, S., Mummery, C., Loskill, P., Braeken, D., Eberle, W., Cipriano, M., Fernandez, L., Graef, M., Gidrol, X., Picollet-D'Hahan, N., van Meer, B., Ochoa, I., Schutte, M. and van den Eijnden-van Raaij, J. (2019). Building blocks for a European Organ-on-Chip roadmap. ALTEX - Alternatives to animal experimentation, 36(3), pp. 481-492. doi: 10.14573/altex.1905221.

Matejuk, A., and Ransohoff, R. M. (2020). Crosstalk between astrocytes and Microglia: An overview. Frontiers in Immunology, 11. doi:10.3389/fimmu.2020.01416.

McCoy, M. K., and Tansey, M. G. (2008). TNF signaling inhibition in the CNS: Implications for normal brain function and neurodegenerative disease. Journal of Neuroinflammation, 5(1), 45. doi:10.1186/1742-2094-5-45.

McDonald, M., Sebinger, D., Brauns, L., Gonzalez-Cano, L., Menuchin-Lasowski, Y., Mierzejewski, M., . . . Jones, P. D. (2020). A mesh microelectrode array for non-invasive electrophysiology within neural organoids. doi:10.1101/2020.09.02.279125.

McKinsey, G. L., Lizama, C. O., Keown-Lang, A. E., Niu, A., Santander, N., Larpthaveesarp, A., et al. (2020). A new genetic strategy for targeting microglia in development and disease. ELife, 9. doi:10.7554/elife.54590.

Mehling, M., and Tay, S. (2014). Microfluidic cell culture. Current Opinion in Biotechnology, 25, 95-102. doi:10.1016/j.copbio.2013.10.005.

Mehra, A., Ali, C., Parcq, J., Vivien, D., and Docagne, F. (2016). The plasminogen activation system in neuroinflammation. Biochimica Et Biophysica Acta (BBA) - Molecular Basis of Disease, 1862(3), 395-402. doi:10.1016/j.bbadis.2015.10.011.

Mertz, D. R., Ahmed, T., and Takayama, S. (2018). Engineering cell heterogeneity into organs-on-a-chip. Lab on a Chip, 18(16), 2378-2395. doi:10.1039/c8lc00413g.

Miccoli, B., Braeken, D., and Li, Y. E. (2019). Brain-on-a-chip devices for drug screening and disease modeling applications. Current Pharmaceutical Design, 24(45), 5419-5436. doi:10.2174/1381612825666190220161254.

Mizuno, T., Zhang, G., Takeuchi, H., Kawanokuchi, J., Wang, J., Sonobe, Y., et al. (2008). Interferon-γ directly INDUCES neurotoxicity through a NEURON specific, calcium-permeable complex OF IFN-γ receptor and AMPA GLURL RECEPTOR. The FASEB Journal, 22(6), 1797-1806. doi:10.1096/fj.07-099499

Mofazzal Jahromi, M. A., Abdoli, A., Rahmanian, M., Bardania, H., Bayandori, M., Moosavi Basri, S. M., et al. (2019). Microfluidic Brain-on-a-Chip: Perspectives for MIMICKING neural system disorders. Molecular Neurobiology, 56(12), 8489-8512. doi:10.1007/s12035-019-01653-2.

Mohs, R. C., and Greig, N. H. (2017). Drug discovery and development: Role of basic biological research. Alzheimer's and Dementia: Translational Research and Clinical Interventions, 3(4), 651-657. doi:10.1016/j.trci.2017.10.005.

Molina-Martínez, B. (2020). Development of a novel 3D microphysiological system for functional and morphological assessment of neuronal networks. Eberhard Karls Universität Tübingen.

Molina-Martínez, B., Jentsch, L.V., Ersoy, F., Van der Moolen, M., Donato, S., Ness, T. V., et al. (2021). A multimodal 3D neuro-microphysiological system WITH neurite-trapping microelectrodes. doi:10.1101/2021.04.16.436793.

Mosig A, Nawroth J, Loskill P: Organs-on-a-Chip: Neue Perspektiven in der Medikamenten-entwicklung und Personalisierten Medizin. Deutsche Zeitschrift für Klinische Forschung (DZKF).

Musick, K., Khatami, D., and Wheeler, B. C. (2009). Three-dimensional micro-electrode array for recording DISSOCIATED neuronal cultures. Lab on a Chip, 9(14), 2036. doi:10.1039/b820596e.

Negri, J., Menon, V., and Young-Pearse, T. L. (2020). Assessment of spontaneous neuronal activity in vitro using multi-well multi-electrode arrays: Implications for assay development. Eneuro, 7(1). doi:10.1523/eneuro.0080-19.2019.

Neher, E., and Sakmann, B. (1976). Single-channel currents recorded from membrane of denervated frog muscle fibres. Nature, 260(5554), 799-802. doi:10.1038/260799a0.

Nex Technologies: Neuroexplorer Manual. 2019.

Novellino, A., Scelfo, B., Palosaari, T., Price, A., Sobanski, T., Shafer, T. J., et al. (2011). Development of micro-electrode array based tests for neurotoxicity: assessment of interlaboratory reproducibility with neuroactive chemicals. Frontiers in Neuroengineering, 4. doi:10.3389/fneng.2011.00004.

Obata K, Oide M and Tanaka H (1978). Excitatory and inhibitory actions of GABA and glycine on embryonic chick spinal neurons in culture. Brain Res 144, 179–184.

Obien, M. E., Deligkaris, K., Bullmann, T., Bakkum, D. J., and Frey, U. (2015). Revealing neuronal function through microelectrode array recordings. Frontiers in Neuroscience, 8. doi:10.3389/fnins.2014.00423.

Odawara, A., Gotoh, M., and Suzuki, I. (2013). A three-dimensional neuronal culture technique that controls the direction of neurite elongation and the position of soma to mimic the layered structure of the brain. RSC Advances, 3(45), 23620. https://doi.org/10.1039/c3ra44757j.

Orkin, R. W., Gehron, P., McGoodwin, E. B., Martin, G. R., Valentine, T., and Swarm, R. (1977). A murine tumor producing a matrix of basement membrane. Journal of Experimental Medicine, 145(1), 204-220. doi:10.1084/jem.145.1.204.

Pamies, D., Barreras, P., Block, K., Makri, G., Kumar, A., Wiersma, D., Smirnova, L., Zang, C., Bressler, J., Christian, K.M. et al. (2017). A human brain microphysiological system derived from induced pluripotent stem cells to study neurological diseases and toxicity. ALTEX 34(3):362-376. doi:10.14573/altex.1609122

Pamies, D., Block, K., Lau, P., Gribaldo, L., Pardo, C. A., Barreras, P., et al. (2018). Rotenone exerts developmental neurotoxicity in a human brain spheroid model. Toxicology and Applied Pharmacology, 354, 101-114. doi:10.1016/j.taap.2018.02.003.

Pan, L., Alagapan, S., Franca, E., Brewer, G. J., and Wheeler, B. C. (2011). Propagation of action potential activity in a predefined microtunnel neural network. Journal of Neural Engineering, 8(4), 046031. doi:10.1088/1741-2560/8/4/046031.

Pandya, H., Shen, M. J., Ichikawa, D. M., Sedlock, A. B., Choi, Y., Johnson, K. R., et al. (2017). Differentiation of human and murine induced pluripotent stem cells to microglia-like cells. Nature Neuroscience, 20(5), 753-759. doi:10.1038/nn.4534

Papadimitriou, C., Celikkaya, H., Cosacak, M. I., Mashkaryan, V., Bray, L., Bhattarai, P., . . . Kizil, C. (2018). 3D culture method for alzheimer's disease modeling reveals interleukin-4 rescues aβ42-induced loss of human neural stem cell plasticity. Developmental Cell, 46(1). doi:10.1016/j.devcel.2018.06.005.

Papadimitriou, C., Cosacak, M. I., Mashkaryan, V., Celikkaya, H., Bray, L., Bhattarai, P., et al. (2017). Instructive starpeg-heparin biohybrid 3d cultures for modeling human neural stem cell plasticity, neurogenesis, and neurodegeneration. doi:10.1101/225243.

Pardue, M. L., and Gall, J. G. (1969). Molecular hybridization of radioactive dna to the dna of cytological preparations. Proceedings of the National Academy of Sciences, 64(2), 600-604. doi:10.1073/pnas.64.2.600

Park, J., Lee, B. K., Jeong, G. S., Hyun, J. K., Lee, C. J., and Lee, S. (2015). Three-dimensional Brain-on-a-chip with an interstitial level of flow and its application as an in Vitro model of Alzheimer's disease. Lab on a Chip, 15(1), 141-150. doi:10.1039/c4lc00962b.

Park, J., Wetzel, I., Marriott, I., Dréau, D., D'Avanzo, C., Kim, D. Y., et al. (2018). A 3d human triculture system modeling neurodegeneration and neuroinflammation in alzheimer's disease. Nature Neuroscience, 21(7), 941-951. doi:10.1038/s41593-018-0175-4.

Park, Y., Franz, C. K., Ryu, H., Luan, H., Cotton, K. Y., Kim, J. U., et al. (2021). Three-dimensional, multifunctional neural interfaces for cortical spheroids and engineered assembloids. Science Advances, 7(12). doi:10.1126/sciadv.abf9153.

Paşca, A. M., Sloan, S. A., Clarke, L. E., Tian, Y., Makinson, C. D., Huber, N., et al. (2015). Functional cortical neurons and astrocytes from human pluripotent stem cells in 3d culture. Nature Methods, 12(7), 671-678. doi:10.1038/nmeth.3415.

Pasquale, V., Martinoia, S., and Chiappalone, M. (2009). A self-adapting approach for the detection of bursts and network bursts in neuronal cultures. Journal of Computational Neuroscience, 29(1-2), 213-229. doi:10.1007/s10827-009-0175-1.

Patel, A. B., De Graaf, R. A., Mason, G. F., Rothman, D. L., Shulman, R. G., and Behar, K. L. (2005). The contribution of Gaba TO glutamate/glutamine cycling and energy metabolism in the rat cortex in vivo. Proceedings of the National Academy of Sciences, 102(15), 5588-5593. doi:10.1073/pnas.0501703102.

Personius, K. E., Chang, Q., Mentis, G. Z., O'donovan, M. J., and Balice-Gordon, R. J. (2007). Reduced gap junctional coupling leads to uncorrelated motor neuron firing and precocious neuromuscular synapse elimination. Proc. Natl. Acad. Sci. U.S.A. 104, 11808–11813. doi: 10.1073/pnas.0703357104.

Peyrin, J., Deleglise, B., Saias, L., Vignes, M., Gougis, P., Magnifico, S., . . . Brugg, B. (2011). Axon diodes for the reconstruction of oriented neuronal networks in microfluidic chambers. Lab on a Chip, 11(21), 3663. doi:10.1039/c1lc20014c.

Phillips, K. A., Bales, K. L., Capitanio, J. P., Conley, A., Czoty, P. W., 't Hart, B. A., et al. (2014). Why primate models matter. American Journal of Primatology, 76(9), 801-827. doi:10.1002/ajp.22281.

Piondron P, Piguet P, Förster E. (2005). New Methods for Culturing Cells from Nervous Tissues. ISBN: 978-3-8055-7831-8.

Pistollato, F., Ohayon, E. L., Lam, A., Langley, G. R., Novak, T. J., Pamies, D., et al. (2016). Alzheimer disease research in the 21st century: past and current failures, new perspectives and funding priorities. Oncotarget, 7(26), 38999-39016. doi:10.18632/oncotarget.9175.

Pittaluga, A. (2017). Ccl5–glutamate cross-talk in astrocyte-neuron communication in multiple sclerosis. Frontiers in Immunology, 8. doi:10.3389/fimmu.2017.01079.

Prevedel, R., Yoon, Y., Hoffmann, M., Pak, N., Wetzstein, G., Kato, S., et al. (2014). Simultaneous whole-animal 3d imaging of neuronal activity using light-field microscopy. Nature Methods, 11(7), 727-730. doi:10.1038/nmeth.2964

Probert, L. (2015). TNF and its receptors in the CNS: The essential, the desirable and the deleterious effects. Neuroscience, 302, 2-22. doi:10.1016/j.neuroscience.2015.06.038.

Purves DA, G.J.; Fitzpatrick, D.; Hall, W.C.: Neuroscience. Sunderland, Massachusetts U.S.A.: Sinauer Associates, Inc; 2004.

Qian, X., Nguyen, H., Song, M., Hadiono, C., Ogden, S., Hammack, C., et al. (2016). Brain-Region-Specific Organoids Using MINI-BIOREACTORS for Modeling Zikv exposure. Cell, 165(5), 1238-1254. doi:10.1016/j.cell.2016.04.032.

Quiroga, R. Q., Nadasdy, Z., and Ben-Shaul, Y. (2004). Unsupervised spike detection and sorting with wavelets and superparamagnetic clustering. Neural Computation, 16(8), 1661-1687. doi:10.1162/089976604774201631.

Regehr, W., Delaney, K., and Tank, D. (1994). The role of presynaptic calcium in short-term enhancement at the hippocampal mossy fiber synapse. The Journal of Neuroscience, 14(2), 523-537. doi:10.1523/jneurosci.14-02-00523.1994.

Rempe, R. G., Hartz, A. M., and Bauer, B. (2016). Matrix metalloproteinases in the brain and blood-brain barrier: versatile breakers and makers. journal of cerebral blood flow and metabolism, 36(9), 1481-1507. doi:10.1177/0271678x16655551.

Ren, K., Zhou, J., and Wu, H. (2013). Materials for Microfluidic chip fabrication. Accounts of Chemical Research, 46(11), 2396-2406. doi:10.1021/ar300314s.

Renart, J., Reiser, J., and Stark, G. R. (1979). Transfer of proteins from gels to diazobenzyloxymethyl-paper and detection with antisera: A method for studying antibody specificity and antigen structure. Proceedings of the National Academy of Sciences, 76(7), 3116-3120. doi:10.1073/pnas.76.7.3116

Renault, R., Sukenik, N., Descroix, S., Malaquin, L., Viovy, J., Peyrin, J., et al. (2015). Combining microfluidics, Optogenetics and calcium imaging to Study Neuronal communication in vitro. PLOS ONE, 10(4). doi:10.1371/journal.pone.0120680.

Roberts, R. A., Aschner, M., Calligaro, D., Guilarte, T. R., Hanig, J. P., Herr, D. W., et al. (2015). Translational biomarkers of Neurotoxicity: A health and environmental Sciences Institute perspective on the way forward. Toxicological Sciences, 148(2), 332-340. doi:10.1093/toxsci/kfv188.

Rubin H. (1966). Altering bacteriological plastic Petri dishes for tissue culture use. Public Heal Rep 81, 843. Medline, Google Scholar.

Sallés, F. J., and Strickland, S. (2002). Localization and regulation of the Tissue Plasminogen Activator–plasmin system in the hippocampus. The Journal of Neuroscience, 22(6), 2125-2134. doi:10.1523/jneurosci.22-06-02125.2002.

Sambrook, J. and Russel, D. W. Molecular Cloning. (2001). A Laboratory Manual (Cold Spring Harbor Laboratory Press, Cold Spring Harbor, 2001).

Schafer, D. P., Lehrman, E. K., and Stevens, B. (2012). The “quad-partite” synapse: Microglia-synapse interactions in the developing and mature CNS. Glia, 61(1), 24-36. doi:10.1002/glia.22389.

Scherer, W. F., Syverton, J. T., and Gey, G. O. (1953). Studies on the propagation in vitro of poliomyelitis viruses. Journal of Experimental Medicine, 97(5), 695-710. doi:10.1084/jem.97.5.695

Schmieder, F., Klapper, S., Koukourakis, N., Busskamp, V., and Czarske, J. (2018). Optogenetic stimulation of human neural networks using fast ferroelectric spatial light modulator—based holographic illumination. Applied Sciences, 8(7), 1180. doi:10.3390/app8071180.

Schork, N. J. (2015). Personalized medicine: Time for One-person trials. Nature, 520(7549), 609-611. doi:10.1038/520609a.

Seibenhener, M. L., and Wooten, M. W. (2012). Isolation and culture of hippocampal neurons from prenatal mice. Journal of Visualized Experiments, (65). doi:10.3791/3634.

Semple, B. D., Kossmann, T., and Morganti-Kossmann, M. C. (2009). Role of CHEMOKINES in CNS health and Pathology: A focus on The Ccl2/ccr2 And Cxcl8/cxcr2 networks.

Journal of Cerebral Blood Flow and Metabolism, 30(3), 459-473. doi:10.1038/jcbfm.2009.240.

Seo, J., Shin, J., Leijten, J., Jeon, O., Camci-Unal, G., Dikina, A. D., et al. (2018). High-throughput approaches for screening and analysis of cell behaviors. Biomaterials, 153, 85-101. doi:10.1016/j.biomaterials.2017.06.022

Shin, H., Jeong, S., Lee, J., Sun, W., Choi, N., and Cho, I. (2021). 3D high-density microelectrode array with optical stimulation and drug delivery for investigating neural circuit dynamics. Nature Communications, 12(1). doi:10.1038/s41467-020-20763-3.

Shuler, M. L. (2017). Organ-, body- and disease-on-a-chip systems. Lab on a Chip, 17(14), 2345-2346. doi:10.1039/c7lc90068f.

Sidor, M. M., Davidson, T. J., Tye, K. M., Warden, M. R., Diesseroth, K., and McClung, C. A. (2015). In vivo optogenetic stimulation of the rodent central nervous system. Journal of Visualized Experiments, (95). doi:10.3791/51483.

Siracusa, R., Fusco, R., and Cuzzocrea, S. (2019). Astrocytes: Role and functions in Brain Pathologies. Frontiers in Pharmacology, 10. doi:10.3389/fphar.2019.01114.

Slanzi, A., Iannoto, G., Rossi, B., Zenaro, E., and Constantin, G. (2020). In vitro models of neurodegenerative diseases. Frontiers in Cell and Developmental Biology, 8. doi:10.3389/fcell.2020.00328.

Slikker W, Roberts R, Pierson JB: Translational Biomarkers of Neurotoxicity (NeuTox). In.: HESI global org; 2019.

Soscia, D. A., Lam, D., Tooker, A. C., Enright, H. A., Triplett, M., Karande, P., et al. (2020). A flexible 3-dimensional microelectrode array for in vitro brain models. Lab on a Chip, 20(5), 901-911. doi:10.1039/c9lc01148j.

Stoddard-Bennett, T., and Reijo Pera, R. (2019). Treatment of parkinson's disease through personalized medicine and induced pluripotent stem cells. Cells, 8(1), 26. doi:10.3390/cells8010026.

Strohmeyer, R., and Rogers, J. (2001). Molecular and cellular mediators of alzheimer's disease inflammation. Journal of Alzheimer's Disease, 3(1), 131-157. doi:10.3233/jad-2001-3118.

Sun G, Liu W, Fan Z, Zhang D, Han Y, Xu L, Qi J, Zhang S, Gao BT, Bai X et al: The Three-Dimensional Culture System with Matrigel and Neurotrophic Factors Preserves the Structure and Function of Spiral Ganglion Neuron In Vitro. Neural Plast 2016, 2016:4280407.

Suntsova, M. V., and Buzdin, A. A. (2020). Differences between human and Chimpanzee genomes and their implications in gene expression, protein functions and biochemical properties of the two species. BMC Genomics, 21(S7). doi:10.1186/s12864-020-06962-8.

Suzumura, A., and Ikenaka, K. (2013). Neuron-Glia Interaction in Neuroinflammation. Springer.

Takagi, Hiroshi. "Roles of Ion Channels in EPSP Integration at Neuronal Dendrites." Neuroscience Research, vol. 37, no. 3, 2000, pp. 167–171., doi:10.1016/s0168-0102(00)00120-6.

Takahashi, K., and Yamanaka, S. (2006). Induction of pluripotent stem cells from MOUSE embryonic and Adult Fibroblast cultures by Defined Factors. Cell, 126(4), 663-676. doi:10.1016/j.cell.2006.07.024.

Taylor, A. M., Blurton-Jones, M., Rhee, S. W., Cribbs, D. H., Cotman, C. W., and Jeon, N. L. (2005). A microfluidic CULTURE platform for CNS axonal injury, regeneration and transport. Nature Methods, 2(8), 599-605. doi:10.1038/nmeth777.

Taylor-Whiteley, T. R., Le Maitre, C. L., Duce, J. A., Dalton, C. F., and Smith, D. P. (2019). Recapitulating Parkinson's disease pathology in a three-dimensional human neural cell culture model. Disease Models and Mechanisms, 12(4), Dmm038042. doi:10.1242/dmm.038042.

Tekin, H., Simmons, S., Cummings, B., Gao, L., Adiconis, X., Hession, C. C., et al. (2018). Effects of 3d culturing conditions on the transcriptomic profile of stem-cell-derived neurons. Nature Biomedical Engineering, 2(7), 540-554. doi:10.1038/s41551-018-0219-9.

Temin, H. M., and Mizutani, S. (1970). Viral rna-dependent DNA Polymerase: RNA-dependent DNA polymerase In Virions of ROUS Sarcoma Virus. Nature, 226(5252), 1211-1213. doi:10.1038/2261211a0.

Terrasso, A. P., Silva, A. C., Filipe, A., Pedroso, P., Ferreira, A. L., Alves, P. M., and Brito, C. (2017). Human neuron-astrocyte 3d co-culture-based assay for evaluation of neuroprotective compounds. Journal of Pharmacological and Toxicological Methods, 83, 72-79. doi:10.1016/j.vascn.2016.10.001.

Thode, H. C. (2002). Testing for normality. New York: Dekker.

Thomasjr, C., Springer, P., Loeb, G., Berwaldnetter, Y., and Okun, L. (1972). A miniature microelectrode array to monitor the bioelectric activity of cultured cells. Experimental Cell Research, 74(1), 61-66. doi:10.1016/0014-4827(72)90481-8.

TierSchG: Tierschutzgesetz. In: BGBl I S 1626. Bundesministerium der Justiz und für Verbraucherschutz; 2019.

Timmerman, R., Burm, S. M., and Bajramovic, J. J. (2018). An overview of in vitro methods to study microglia. Frontiers in Cellular Neuroscience, 12. doi:10.3389/fncel.2018.00242.

Todd, G. K., Boosalis, C. A., Burzycki, A. A., Steinman, M. Q., Hester, L. D., Shuster, P. W., and Patterson, R. L. (2013). Towards neuronal organoids: A method for long-term culturing of high-density hippocampal neurons. PLoS ONE, 8(4). doi:10.1371/journal.pone.0058996.

Towlson, E. K., Vértes, P. E., Yan, G., Chew, Y. L., Walker, D. S., Schafer, W. R., and Barabási, A. (2018). Caenorhabditis elegans and the network Control framework—faqs. Philosophical Transactions of the Royal Society B: Biological Sciences, 373(1758), 20170372. doi:10.1098/rstb.2017.0372.

Umpierre, A. D., Bystrom, L. L., Ying, Y., Liu, Y. U., Worrell, G., and Wu, L. (2020). Microglial calcium signaling is attuned to neuronal activity in awake mice. ELife, 9. doi:10.7554/elife.56502.

Uzel, S. G., Platt, R. J., Subramanian, V., Pearl, T. M., Rowlands, C. J., Chan, V et al. (2016). Microfluidic device for the formation of optically EXCITABLE, Three-dimensional, compartmentalized motor units. Science Advances, 2(8). doi:10.1126/sciadv.1501429.

Volpato, V., and Webber, C. (2020). Addressing variability in ipsc-derived models of human disease: Guidelines to promote reproducibility. Disease Models and Mechanisms, 13(1), Dmm042317. doi:10.1242/dmm.042317.

Von Bartheld, C. S., Bahney, J., and Herculano-Houzel, S. (2016). The search for true numbers of neurons and glial cells in the human brain: A review of 150 years of CELL COUNTING. Journal of Comparative Neurology, 524(18), 3865-3895. doi:10.1002/cne.24040.

Wake, H., and Fields, R. D. (2011). Physiological function of microglia. Neuron Glia Biology, 7(1), 1-3. doi:10.1017/s1740925x12000166.

Walker, A. L., Imam, S. Z., and Roberts, R. A. (2018). Drug discovery and development: Biomarkers of neurotoxicity and neurodegeneration. Experimental Biology and Medicine, 243(13), 1037-1045. doi:10.1177/1535370218801309.

Wang, Y., Wang, L., Guo, Y., Zhu, Y., and Qin, J. (2018). Engineering stem cell-derived 3d brain organoids in a perfusable organ-on-a-chip system. RSC Advances, 8(3), 1677-1685. doi:10.1039/c7ra11714k.

Wang, X., and Suzuki, Y. (2007). Microglia produce IFN-γIndependently from T cells during ACUTE toxoplasmosis in the brain. Journal of Interferon and Cytokine Research, 27(7), 599-605. doi:10.1089/jir.2006.0157.

Wang, X., Takano, T., and Nedergaard, M. (2009). Astrocytic calcium Signaling: Mechanism and implications for functional brain imaging. Methods in Molecular Biology, 93-109. doi:10.1007/978-1-59745-543-5_5

Wang, X., Tan, M., Yu, J., and Tan, L. (2014). Matrix metalloproteinases and their multiple roles in alzheimer's disease. BioMed Research International, 2014, 1-8. doi:10.1155/2014/908636.

Watson, D. E., Hunziker, R., and Wikswo, J. P. (2017). Fitting tissue chips and microphysiological systems into the grand scheme of medicine, biology, pharmacology, and toxicology. Experimental Biology and Medicine, 242(16), 1559-1572. doi:10.1177/1535370217732765.

Wevers, N. R., Van Vught, R., Wilschut, K. J., Nicolas, A., Chiang, C., Lanz, H. L., et al. (2016). High-throughput compound evaluation on 3d networks of neurons and glia in a microfluidic platform. Scientific Reports, 6(1). doi:10.1038/srep38856.

Whalley, K. (2014). Microglial maintenance. Nature Reviews Neuroscience, 15(6), 353-353. doi:10.1038/nrn3759.

World Population Prospects. (2019). In. New York: United Nations; 2019.

Wyatt-Johnson, S. K., Herr, S. A., and Brewster, A. L. (2017). Status epilepticus TRIGGERS Time-dependent alterations in Microglia abundance and MORPHOLOGICAL phenotypes in the hippocampus. Frontiers in Neurology, 8. doi:10.3389/fneur.2017.00700.

Xie, Y., Jackson, M. F., and MacDonald, J. F. (2013). Optogenetics and synaptic plasticity. Acta Pharmacologica Sinica, 34(11), 1381-1385. doi:10.1038/aps.2013.150.

Xie, Z., Yang, Q., Song, D., Quan, Z., and Qing, H. (2019). Optogenetic manipulation of Astrocytes from synapses to neuronal networks: A potential therapeutic strategy for neurodegenerative diseases. Glia, 68(2), 215-226. doi:10.1002/glia.23693.

Xu, T., Molnar, P., Gregory, C., Das, M., Boland, T., and Hickman, J. J. (2009). Electrophysiological characterization of embryonic hippocampal neurons cultured in a 3D collagen hydrogel. Biomaterials, 30(26), 4377-4383. doi:10.1016/j.biomaterials.2009.04.047.

Xu, R., Boreland, A. J., Li, X., Erickson, C., Jin, M., Atkins, C, et al. (2020). Developing human pluripotent Stem CELL-BASED cerebral Organoids with a Controllable Microglia ratio for modeling brain development and pathology. doi:10.1101/2020.10.09.331710.

Ylä-Outinen, L., Joki, T., Varjola, M., Skottman, H., and Narkilahti, S. (2012). Three-dimensional growth matrix for human embryonic stem CELL-DERIVED neuronal cells. Journal of Tissue Engineering and Regenerative Medicine, 8(3), 186-194. doi:10.1002/term.1512.

Zemelman, B. V., Lee, G. A., Ng, M., and Miesenböck, G. (2002). Selective photostimulation of genetically charged neurons. Neuron, 33(1), 15-22. doi:10.1016/s0896-6273(01)00574-8.

Zengel, P., Nguyen-Hoang, A., Schildhammer, C., Zantl, R., Kahl, V., and Horn, E. (2011). M-Slide chemotaxis: A new chamber for long-term chemotaxis studies. BMC Cell Biology, 12(1). doi:10.1186/1471-2121-12-21.

Zhang, S., Wang, Q., Yang, Q., Gu, H., Yin, Y., Li, Y., et al. (2019). NG2 glia REGULATE brain innate Immunity via TGF-B2/TGFBR2 AXIS. BMC Medicine, 17(1). doi:10.1186/s12916-019-1439-x

Zheng, C., Zhou, X., and Wang, J. (2016). The dual roles of cytokines in Alzheimer's Disease: Update on interleukins, TNF-α, TGF-B AND IFN-γ. Translational Neurodegeneration, 5(1). doi:10.1186/s40035-016-0054-4.

10 Appendix

Table 10.1: Values of three different recordings grouped in wells (10-12). Represented parameters in recordings no.9 (device A), 10 (device C) and 11 (device D) of preparation 4: MFR, BFR, %SiB, BD and ISICoV.

MFR (Hz)

Wells recording no. 9	1	2	3	4	5	6	7	8	9	10	11	12	All data
Mean	4,97	4,66	4,33	3,87	4,83	5,52	6,02	6,49	5,21	3,68	3,72	4,35	4,82
Std. Deviation	2,38	2,34	2,04	1,86	2,17	2,21	1,75	2,68	1,51	1,55	1,49	1,28	2,12
Std. Error of Mean	0,52	0,51	0,45	0,42	0,47	0,48	0,38	0,58	0,33	0,35	0,34	0,28	0,13
p-value	>0,9999	>0,9999	0,9964	0,6161	>0,9999	0,9646	0,1955	0,2709	0,9952	0,1608	0,1882	0,9389	
Number of values	21	21	21	20	21	21	21	21	21	20	19	21	248

BFR (Hz)

Wells recording no. 9	1	2	3	4	5	6	7	8	9	10	11	12	All data
Mean	0,1465	0,1193	0,1173	0,1148	0,1363	0,1587	0,1825	0,1852	0,1472	0,09775	0,09009	0,1076	0,1342
Std. Deviation	0,08442	0,09383	0,0699	0,0788	0,07749	0,104	0,07577	0,1006	0,07795	0,06372	0,04908	0,05492	0,0832
Std. Error of Mean	0,01842	0,02048	0,01525	0,01762	0,01691	0,02269	0,01654	0,02195	0,01701	0,01425	0,01126	0,01199	0,005283
p-value	0,9998	0,8747	0,999	0,9986	>0,9999	0,9485	0,2149	0,5017	0,9995	0,5606	0,0844	0,2252	
Number of values	21	21	21	20	21	21	21	21	21	20	19	21	248

SiB (%)

Wells recording no. 9	1	2	3	4	5	6	7	8	9	10	11	12	All data
Mean	77,49	75,92	74,68	67,72	73,83	76,9	77,17	80,3	74,44	70,35	67,53	77,64	74,84
Std. Deviation	7,469	7,887	9,543	10,97	6,753	6,877	4,943	6,694	4,941	6,311	9,235	5,141	7,741
Std. Error of Mean	1,63	1,721	2,134	2,453	1,474	1,538	1,079	1,461	1,078	1,411	2,119	1,122	0,4956
p-value	0,7735	0,9998	>0,9999	0,101	0,9996	0,9181	0,4844	0,0182	>0,9999	0,0673	0,0343	0,2836	
Number of values	21	21	21	20	21	21	21	21	21	20	19	21	248

BD (s)

Wells recording no. 9	1	2	3	4	5	6	7	8	9	10	11	12	All data
Mean	0,9693	0,9764	0,9755	0,9259	0,9962	1,013	0,9821	1,039	0,985	0,9952	0,89	1,136	0,995
Std. Deviation	0,2032	0,1778	0,1967	0,2118	0,1761	0,1486	0,1891	0,1811	0,2099	0,1838	0,171	0,2112	0,1977
Std. Error of Mean	0,04434	0,0388	0,04399	0,04992	0,03843	0,03243	0,04127	0,03951	0,0458	0,0411	0,03923	0,04846	0,01263
p-value	0,9994	0,9996	0,9996	0,8381	>0,9999	0,9996	0,9997	0,9888	0,9998	>0,9999	0,2408	0,0276	
Number of values	21	21	21	20	21	21	21	21	21	20	19	21	248

ISI CoV

Wells recording no. 9	1	2	3	4	5	6	7	8	9	10	11	12	All data
Mean	3,961	3,878	3,432	3,319	3,335	3,355	3,339	3,63	3,584	3,427	3,176	3,895	3,54
Std. Deviation	1,064	0,6898	0,8721	0,7958	0,6443	0,7568	0,6458	0,5926	0,6852	0,5195	0,7643	0,8386	0,7882
Std. Error of Mean	0,2323	0,1505	0,1903	0,178	0,1406	0,1651	0,1409	0,1325	0,1495	0,1162	0,1753	0,183	0,05005
p-value	0,1802	0,4822	0,9993	0,9436	0,9613	0,9833	0,9666	0,9995	0,9997	0,9993	0,438	0,4063	
Number of values	21	21	21	20	21	21	21	21	21	20	19	21	248

MFR (Hz)

Wells recording no. 10	1	2	3	4	5	6	7	8	9	10	11	12	All data
Mean	4,224	5,481	5,694	3,722	3,515	3,088	6,614	5,178	3,109	3,586	2,258	2,528	4,069
Std. Deviation	1,083	1,134	2,962	1,847	1,577	1,672	2,276	1,547	0,8801	1,581	0,6247	0,937	1,935
Std. Error of Mean	0,2364	0,2475	0,6463	0,413	0,3441	0,3738	0,4966	0,3375	0,1921	0,345	0,1433	0,2095	0,1231
p-value	>0,9999	0,001	0,4379	0,9997	0,9388	0,421	0,0028	0,1561	0,0081	0,9771	<0,0001	<0,0001	
Number of values	21	21	21	20	21	20	21	21	21	21	19	20	247

BFR (Hz)

Wells recording no. 10	1	2	3	4	5	6	7	8	9	10	11	12	All data
Mean	0,1089	0,1825	0,1683	0,09035	0,095	0,08258	0,1771	0,1535	0,08444	0,101	0,04965	0,05426	0,1061
Std. Deviation	0,04861	0,08103	0,111	0,05649	0,06589	0,05315	0,08209	0,07537	0,04613	0,05844	0,02454	0,02331	0,06571
Std. Error of Mean	0,01061	0,01768	0,02423	0,01296	0,01438	0,01188	0,01791	0,01645	0,01007	0,01307	0,00563	0,005495	0,004268
p-value	>0,9999	0,0165	0,4067	0,9916	0,9999	0,7997	0,0353	0,2722	0,7349	>0,9999	<0,0001	<0,0001	
Number of values	21	21	21	20	21	20	21	21	21	21	19	20	247

SiB (%)

Wells recording no. 10	1	2	3	4	5	6	7	8	9	10	11	12	All data
Mean	76,54	77,05	76,03	71,68	71,23	67,56	82,51	74,87	66,84	72	68,17	69,61	72,88
Std. Deviation	4,78	4,994	9,751	8,824	9,06	12,88	5,936	7,157	8,77	6,287	11,44	7,84	9,151
Std. Error of Mean	1,069	1,09	2,128	1,926	1,977	2,88	1,327	1,562	1,914	1,372	2,624	1,711	0,5811
p-value	0,1696	0,0771	0,9576	>0,9999	0,9997	0,8249	<0,0001	0,9895	0,1806	>0,9999	0,8503	0,8287	
Number of values	21	21	21	20	21	20	21	21	21	21	19	20	247

BD (s)

Wells recording no. 10	1	2	3	4	5	6	7	8	9	10	11	12	All data
Mean	0,9683	0,9124	0,9099	1	1,037	0,958	0,9447	0,8801	0,9368	1,006	1,032	0,9478	0,9624
Std. Deviation	0,1368	0,1402	0,1239	0,1605	0,2149	0,2182	0,1018	0,1025	0,188	0,2102	0,2326	0,1732	0,1763
Std. Error of Mean	0,02986	0,0306	0,02842	0,0359	0,04689	0,0488	0,02399	0,02236	0,04102	0,04587	0,05337	0,03779	0,01129
p-value	>0,9999	0,9349	0,8702	0,9975	0,9274	>0,9999	>0,9999	0,0973	>0,9999	0,9989	0,98	>0,9999	
Number of values	21	21	21	20	21	20	21	21	21	21	19	20	247

ISI CoV

Wells recording no. 10	1	2	3	4	5	6	7	8	9	10	11	12	All data
Mean	3,87	3,795	3,94	3,582	3,726	3,394	4,598	4,026	3,38	3,351	3,509	3,316	3,71
Std. Deviation	0,7686	0,7296	0,7557	0,8426	0,7812	0,8293	1,174	0,59	0,6773	0,6625	0,861	0,5707	0,8461
Std. Error of Mean	0,1677	0,1592	0,1649	0,1839	0,1705	0,1854	0,2562	0,1287	0,1478	0,1446	0,1975	0,1245	0,05362
p-value	0,996	0,9996	0,9412	0,9992	>0,9999	0,6958	<0,0001	0,6635	0,6015	0,4758	0,9854	0,335	
Number of values	21	21	21	20	21	20	21	21	21	21	19	20	247

MFR (Hz)

Wells recording no. 11	1	2	3	4	5	6	7	8	9	10	All data
Mean	4,529	4,215	5,396	4,077	3,915	4,303	2,49	3,7	4,675	4,735	4,257
Std. Deviation	1,734	1,397	1,786	1,457	1,799	1,437	1,279	1,976	1,623	2,08	1,845
Std. Error of Mean	0,3784	0,3124	0,3898	0,318	0,4023	0,3135	0,286	0,4312	0,3542	0,454	0,1276
p-value	0,9972	>0,9999	0,0492	0,9996	0,9927	0,9999	0,0002	0,8343	0,97	0,9289	
Number of values	21	20	21	21	20	21	20	21	21	21	209

BFR (Hz)

Wells recording no. 11	1	2	3	4	5	6	7	8	9	10	All data
Mean	0,1262	0,1235	0,145	0,1122	0,1137	0,1098	0,03042	0,09367	0,1075	0,1182	0,1152
Std. Deviation	0,06391	0,06168	0,07077	0,04945	0,08206	0,0513	0,01853	0,08846	0,05025	0,05008	0,07182
Std. Error of Mean	0,01395	0,01346	0,01544	0,01079	0,01835	0,01147	0,004634	0,01978	0,01096	0,01149	0,004968
p-value	0,9995	>0,9999	0,7491	>0,9999	>0,9999	>0,9999	<0,0001	0,9901	0,9999	>0,9999	
Number of values	21	20	21	21	20	21	20	21	21	21	209

SiB (%)

Wells recording no. 11	1	2	3	4	5	6	7	8	9	10	All data
Mean	76,53	78,21	79,08	75,24	73,13	79,49	69,85	70,09	83,13	80,69	76,65
Std. Deviation	6,533	5,018	7,775	6,043	6,378	4,525	11,95	9,075	4,851	6,938	7,82
Std. Error of Mean	1,426	1,095	1,697	1,351	1,426	1,012	2,607	1,98	1,113	1,514	0,5462
p-value	>0,9999	0,9667	0,947	0,9952	0,4602	0,3585	0,329	0,1049	0,0007	0,3452	
Number of values	21	20	21	21	20	21	20	21	21	21	209

BD (s)

Wells recording no. 11	1	2	3	4	5	6	7	8	9	10	All data
Mean	0,9881	0,9196	0,996	0,8946	0,8926	0,9069	0,8246	0,8634	1,086	1,034	0,9398
Std. Deviation	0,137	0,2005	0,143	0,1568	0,1737	0,1963	0,1782	0,1962	0,1458	0,149	0,1832
Std. Error of Mean	0,02991	0,04375	0,03282	0,03423	0,03986	0,04283	0,03889	0,04281	0,0326	0,03252	0,01279
p-value	0,9246	0,9994	0,8632	0,9501	0,9506	0,9932	0,0453	0,4519	0,0047	0,1827	
Number of values	21	20	21	21	20	21	20	21	21	21	209

ISI CoV

Wells recording no. 11	1	2	3	4	5	6	7	8	9	10	All data
Mean	4,017	4,357	4,244	4,327	3,993	4,18	3,756	3,391	4,925	4,342	4,14
Std. Deviation	0,9774	0,8514	1,17	0,7523	0,7097	0,7395	0,7513	0,9108	1,055	0,8591	0,9756
Std. Error of Mean	0,2133	0,1858	0,2553	0,1642	0,1628	0,1614	0,1639	0,1987	0,2302	0,1875	0,06749
p-value	0,9994	0,9737	0,9995	0,991	0,9974	0,9998	0,5273	0,0052	0,0028	0,9848	
Number of values	21	20	21	21	20	21	20	21	21	21	209

Table 10.2. Values grouped in preparations (10). Represented parameters in preparations 1-10: MFR, BFR, %SiB, BD, ISICoV, NBF, MFR in NB, B in NB.

Preparation (MFR)	1	2	3	4	5	6	7	8	9	10	All data
Mean	7,50	7,02	5,98	4,40	4,80	5,02	3,98	7,97	4,82	8,55	5,84
Std. Deviation	2,52	1,30	1,29	1,05	1,08	0,84	1,15	0,87	2,28	1,39	1,99
Std. Error of Mean	0,43	0,41	0,19	0,18	0,33	0,24	0,41	0,29	0,66	0,42	0,15
p-value	0,0078	0,16	0,9997	<0,0001	0,093	0,082	0,017	0,0002	0,74	0,0004	
Number of values	34	10	46	34	11	12	8	9	12	11	187

Preparation (BFR)	1	2	3	4	5	6	7	8	9	10	All data
Mean	0,09061	0,204	0,148	0,1325	0,1217	0,1035	0,1762	0,1381	0,1576	0,1915	0,1372
Std. Deviation	0,02732	0,03055	0,03806	0,06739	0,01912	0,01273	0,05331	0,02423	0,03453	0,04053	0,05175
Std. Error of Mean	0,004685	0,009659	0,005611	0,01156	0,005764	0,003674	0,01885	0,008075	0,009968	0,01222	0,003784
p-value	<0,0001	0,0009	0,7071	0,7291	0,6135	<0,0001	0,5942	>0,9999	0,5961	0,0231	
Number of values	34	10	46	34	11	12	8	9	12	11	187

Preparation (SiB)	1	2	3	4	5	6	7	8	9	10	All data
Mean	45,57	86,88	84,7	74,04	91,19	84,83	67,95	93,45	80,68	86,48	75,71
Std. Deviation	16,63	2,918	6,351	4,267	2,526	4,245	5,361	2,309	11,81	4,208	17,71
Std. Error of Mean	2,853	0,9227	0,9365	0,7317	0,7616	1,225	1,895	0,7696	3,41	1,269	1,295
p-value	<0,0001	0,0002	<0,0001	<0,0001	<0,0001	0,0689	<0,0001	<0,0001	0,482	0,0089	
Number of values	34	10	46	34	11	12	8	9	12	11	187

Preparation (BD)	1	2	3	4	5	6	7	8	9	10	All data
Mean	1,024	1,153	1,274	0,9889	1,122	1,434	0,6897	2,328	1,071	1,887	1,22
Std. Deviation	0,3503	0,1462	0,2145	0,1046	0,1824	0,2794	0,1059	0,2189	0,3282	0,9545	0,4697
Std. Error of Mean	0,06008	0,04624	0,03162	0,01794	0,05499	0,08065	0,03744	0,07297	0,09475	0,2878	0,03435
p-value	0,7387	>0,9999	0,1301	<0,0001	>0,9999	0,0945	<0,0001	<0,0001	0,9991	0,034	
Number of values	34	10	46	34	11	12	8	9	12	11	187

Preparation (ISI CoV)	1	2	3	4	5	6	7	8	9	10	All data
Mean	3,917	4,233	4,834	3,774	5,844	5,089	2,986	5,88	4,223	3,195	4,354
Std. Deviation	1,76	0,3468	0,9171	0,4239	0,5013	0,7952	0,3638	1,163	0,7621	0,3482	1,241
Std. Error of Mean	0,3018	0,1097	0,1352	0,0727	0,1511	0,2295	0,1286	0,3877	0,22	0,105	0,09073
p-value	0,9445	0,9983	0,1251	<0,0001	<0,0001	0,1875	<0,0001	<0,0001	>0,9999	<0,0001	
Number of values	34	10	46	34	11	12	8	9	12	11	187

Preparation (NBF)	1	2	3	4	5	6	7	8	9	10	All data
Mean	0,09884	0,1302	0,1215	0,07198	0,1058	0,07433	0,1007	0,1048	0,122	0,1432	0,1043
Std. Deviation	0,03729	0,02296	0,02618	0,02435	0,01223	0,00911	0,02766	0,01233	0,0313	0,01701	0,03369
Std. Error of Mean	0,006396	0,007259	0,00386	0,004175	0,003689	0,00263	0,009778	0,004109	0,009036	0,00538	0,00247
p-value	0,9992	0,0517	0,0135	<0,0001	>0,9999	<0,0001	>0,9999	>0,9999	0,716	0,0006	
Number of values	34	10	46	34	11	12	8	9	12	11	187

Preparation (MFR in NB)	1	2	3	4	5	6	7	8	9	10	All data
Mean	117,4	136,4	132,3	221,5	152,5	149,4	128,7	127,8	96,54	110,4	144,5
Std. Deviation	47,75	13,02	20,25	28,36	12,86	21,1	23,35	10,35	19,61	21,97	47,66
Std. Error of Mean	8,189	4,118	2,986	4,864	3,877	6,09	8,256	3,448	5,661	6,948	3,495
p-value	0,1653	0,976	0,3962	<0,0001	0,7074	0,9948	0,8587	0,1059	<0,0001	0,0256	
Number of values	34	10	46	34	11	12	8	9	12	11	187

Preparation (B in NB)	1	2	3	4	5	6	7	8	9	10	All data
Mean	31,54	43,54	57,7	39,86	74,72	60,27	46,46	56,65	52,66	53,36	48,98
Std. Deviation	17,87	7,092	9,866	8,064	4,728	7,169	13,71	8,34	10,03	18,87	16,64
Std. Error of Mean	3,065	2,243	1,455	1,383	1,425	2,069	4,847	2,78	2,896	5,966	1,22
p-value	0,0002	0,5767	0,0005	0,0002	<0,0001	0,005	>0,9999	0,3776	0,9769	0,9992	
Number of values	34	10	46	34	11	12	8	9	12	11	187

Table 10.3: Values grouped in devices (A-E). Represented parameters of devices A-E: MFR, BFR, %SiB, BD, ISICoV, NBF, MFR in NB, B in NB.

nMPS (MFR)	A	B	C	D	E	All data
Mean	5,81	5,716	8,267	5,062	6,604	5,844
Std. Deviation	2,109	1,655	2,45	1,365	2,669	1,994
Std. Error of Mean	0,2658	0,1992	0,7073	0,3052	0,5565	0,1507
p-value	>0,9999	0,9957	0,0506	0,2272	0,7725	
Number of values	63	69	12	20	23	187

nMPS (BFR)	A	B	C	D	E	All data
Mean	0,1247	0,139	0,1121	0,144	0,1738	0,1372
Std. Deviation	0,05924	0,04855	0,01568	0,04099	0,04054	0,05175
Std. Error of Mean	0,007463	0,005845	0,004525	0,009166	0,008453	0,003784
p-value	0,0192	0,9956	0,0038	0,951	0,0028	
Number of values	63	34	47	20	23	187

nMPS (SiB)	A	B	C	D	E	All data
Mean	76	76,33	48,1	80,27	83,46	75,71
Std. Deviation	12,84	21,54	16,59	5,78	9,305	17,71
Std. Error of Mean	1,618	2,593	4,788	1,292	1,94	1,295
p-value	0,3291	0,0035	0,0004	0,9993	<0,0001	
Number of values	63	34	47	20	23	187

nMPS (BD)	A	B	C	D	E	All data
Mean	1,319	1,138	0,9173	1,098	1,461	1,22
Std. Deviation	0,5308	0,2422	0,3047	0,1807	0,8011	0,4697
Std. Error of Mean	0,06688	0,02916	0,08796	0,04041	0,167	0,03435
p-value	0,2358	>0,9999	0,1971	0,9199	0,4511	
Number of values	63	34	47	20	23	187

nMPS (ISI CoV)	A	B	C	D	E	All data
Mean	4,72	4,412	3,921	3,976	3,731	4,354
Std. Deviation	1,285	1,249	1,85	0,4497	0,7884	1,241
Std. Error of Mean	0,1619	0,1503	0,5342	0,1006	0,1644	0,09073
p-value	0,3653	0,9995	0,9621	0,073	0,0233	
Number of values	63	34	47	20	23	187

nMPS (NBF)	A	B	C	D	E	All data
Mean	0,09366	0,105	0,117	0,09766	0,1316	0,1043
Std. Deviation	0,02444	0,03793	0,02177	0,03814	0,02747	0,03369
Std. Error of Mean	0,003079	0,004566	0,006283	0,008528	0,005856	0,00247
p-value	0,0827	>0,9999	0,4485	0,9737	0,0022	
Number of values	63	34	47	20	23	187

nMPS (MFR in NB)	A	B	C	D	E	All data
Mean	156,2	147,6	92,92	174	102,8	144,5
Std. Deviation	36,65	42,66	27,88	71,89	21,41	47,66
Std. Error of Mean	4,618	5,135	8,049	16,08	4,564	3,495
p-value	0,1747	0,9695	0,0005	0,4287	<0,0001	
Number of values	63	34	47	20	23	187

nMPS (B in NB)	A	B	C	D	E	All data
Mean	50,94	48,45	41,22	44,88	52,97	48,98
Std. Deviation	14,78	19,22	20,6	9,964	14,33	16,64
Std. Error of Mean	1,863	2,314	5,946	2,228	3,056	1,22
p-value	0,9505	>0,9999	0,7909	0,5972	0,8259	
Number of values	63	34	47	20	23	187

Table 10.4. Data grouped into devices of preparations 1, 3 and 4. Represented parameters: MFR, BFR, %SiB, BD, ISICoV, NBF, MFR in NB, B in NB.

MFR

Preparation 1	**A**	**B**	**C**	**All data**
Mean	8,789	5,663	8,267	7,502
Std. Deviation	1,877	2,079	2,45	2,519
Std. Error of Mean	0,5935	0,6002	0,7073	0,4321
p-value	0,335	0,0658	0,6909	
Number of values	10	12	12	34

Preparation 3	**A**	**B**	**C**	**D**	**All data**
Mean	4,728	6,135	6,699	5,869	5,857
Std. Deviation	1,381	1,024	0,9474	1,406	1,373
Std. Error of Mean	0,3986	0,2956	0,2735	0,4447	0,2025
p-value	0,0325	0,9359	0,1704	>0,9999	
Number of values	12	12	12	10	46

Preparation 4	**A**	**C**	**D**	**All data**
Mean	4,802	4,124	4,256	4,402
Std. Deviation	0,8962	1,34	0,714	1,048
Std. Error of Mean	0,2587	0,3868	0,2258	0,1797
p-value	0,5713	0,8008	0,9695	
Number of values	12	12	10	34

BFR

Preparation 1	**A**	**B**	**C**	**All data**
Mean	0,08218	0,07617	0,1121	0,09061
Std. Deviation	0,02973	0,02181	0,01568	0,02732
Std. Error of Mean	0,009402	0,006295	0,004525	0,004685
p-value	0,7155	0,2419	0,0389	
Number of values	10	12	12	34

Preparation 3	**A**	**B**	**C**	**D**	**All data**
Mean	0,09842	0,1657	0,1594	0,1727	0,148
Std. Deviation	0,01934	0,01864	0,02196	0,03495	0,03806
Std. Error of Mean	0,005582	0,00538	0,006341	0,01105	0,005611
p-value	<0,0001	0,1749	0,6707	0,3182	
Number of values	12	12	12	10	46

Preparation 4	**A**	**C**	**D**	**All data**
Mean	0,1631	0,1163	0,1152	0,1325
Std. Deviation	0,09857	0,04395	0,02206	0,06739
Std. Error of Mean	0,02846	0,01269	0,006976	0,01156
p-value	0,5901	0,9269	0,9078	
Number of values	12	12	10	34

SiB

Preparation 1	A	B	C	All data
Mean	56,18	34,19	48,1	45,57
Std. Deviation	8,384	15,71	16,59	16,63
Std. Error of Mean	2,651	4,535	4,788	2,853
p-value	0,9554	0,1077	0,2409	
Number of values	10	12	12	34

Preparation 3	A	B	C	D	All data
Mean	78,26	86,39	89,66	84,46	84,7
Std. Deviation	8,179	2,366	2,332	3,802	6,351
Std. Error of Mean	2,361	0,683	0,6732	1,202	0,9365
p-value	0,0637	0,9398	0,0015	0,9024	
Number of values	12	12	12	10	46

Preparation 4	A	C	D	All data
Mean	73,71	72,67	76,09	74,04
Std. Deviation	3,919	4,389	4,138	4,267
Std. Error of Mean	1,131	1,267	1,309	0,7317
p-value	0,169	0,0929	0,9444	
Number of values	12	12	10	34

BD

Preparation 1	A	B	C	All data
Mean	1,264	0,9318	0,9173	1,024
Std. Deviation	0,3831	0,2849	0,3047	0,3503
Std. Error of Mean	0,1211	0,08223	0,08796	0,06008
p-value	0,1437	0,7875	0,706	
Number of values	10	12	12	34

Preparation 3	A	B	C	D	All data
Mean	1,202	1,282	1,366	1,241	1,274
Std. Deviation	0,2901	0,135	0,2403	0,1211	0,2145
Std. Error of Mean	0,08374	0,03898	0,06938	0,0383	0,03162
p-value	0,9845	0,9426	0,5142	>0,9999	
Number of values	12	12	12	10	46

Preparation 4	A	C	D	All data
Mean	1,03	0,9758	0,9555	0,9889
Std. Deviation	0,1404	0,05297	0,09427	0,1046
Std. Error of Mean	0,04052	0,01529	0,02981	0,01794
p-value	0,8441	>0,9999	0,7916	
Number of values	12	12	10	34

ISI CoV

Preparation 1	A	B	C	All data
Mean	5,256	2,797	3,921	3,917
Std. Deviation	0,9642	1,451	1,85	1,76
Std. Error of Mean	0,3049	0,4189	0,5342	0,3018
p-value	0,0742	0,1258	>0,9999	
Number of values	10	12	12	34

Preparation 3	A	B	C	D	All data
Mean	5,371	4,506	5,474	3,813	4,834
Std. Deviation	1,045	0,397	0,453	0,4412	0,9171
Std. Error of Mean	0,3017	0,1146	0,1308	0,1395	0,1352
p-value	0,5037	0,0687	0,0132	0,0001	
Number of values	12	12	12	10	46

Preparation 4	A	C	D	All data
Mean	3,538	3,707	4,138	3,774
Std. Deviation	0,2689	0,3723	0,4164	0,4239
Std. Error of Mean	0,07762	0,1075	0,1317	0,0727
p-value	0,2045	0,936	0,0347	
Number of values	12	12	10	34

NBF

Preparation 1	A	B	C	All data
Mean	0,1121	0,06963	0,117	0,09884
Std. Deviation	0,02891	0,03956	0,02177	0,03729
Std. Error of Mean	0,009143	0,01142	0,006283	0,006396
p-value	0,6218	0,0403	0,3078	
Number of values	10	12	12	34

Preparation 3	A	B	C	D	All data
Mean	0,0981	0,1253	0,136	0,1274	0,1215
Std. Deviation	0,01969	0,01766	0,02751	0,024	0,02618
Std. Error of Mean	0,005685	0,005099	0,007943	0,007588	0,00386
p-value	0,0161	0,9789	0,2413	0,9231	
Number of values	12	12	12	10	46

Preparation 4	A	C	D	All data
Mean	0,08014	0,06723	0,06788	0,07198
Std. Deviation	0,02325	0,02638	0,02289	0,02435
Std. Error of Mean	0,006712	0,007616	0,00724	0,004175
p-value	0,67	0,909	0,9494	
Number of values	12	12	10	34

MFR in NB

Preparation 1	A	B	C	All data
Mean	161	105,6	92,92	117,4
Std. Deviation	35,44	50,01	27,88	47,75
Std. Error of Mean	11,21	14,44	8,049	8,189
p-value	0,0145	0,335	0,2227	
Number of values	10	12	12	34

Preparation 3	A	B	C	D	All data
Mean	143,1	131,6	140,5	110,2	132,3
Std. Deviation	22,59	15,47	10,48	14,48	20,25
Std. Error of Mean	6,522	4,466	3,026	4,579	2,986
p-value	0,258	0,9999	0,5109	0,0038	
Number of values	12	12	12	10	46

Preparation 4	A	C	D	All data
Mean	212	217,4	237,8	221,5
Std. Deviation	17,42	20,07	40,56	28,36
Std. Error of Mean	5,029	5,793	12,83	4,864
p-value	0,8601	0,9972	0,3315	
Number of values	12	12	10	34

B in NB

Preparation 1	A	B	C	All data
Mean	34,25	19,6	41,22	31,54
Std. Deviation	10,26	13,54	20,6	17,87
Std. Error of Mean	3,244	3,908	5,946	3,065
p-value	0,9554	0,1077	0,2409	
Number of values	10	12	12	34

Preparation 3	A	B	C	D	All data
Mean	66,83	52,59	60,47	49,57	57,7
Std. Deviation	7,045	7,395	7,199	8,152	9,866
Std. Error of Mean	2,034	2,135	2,078	2,578	1,455
p-value	0,0074	0,2602	0,7885	0,0362	
Number of values	12	12	12	10	46

Preparation 4	A	C	D	All data
Mean	38,33	41,13	40,19	39,86
Std. Deviation	6,031	8,785	9,708	8,064
Std. Error of Mean	1,741	2,536	3,07	1,383
p-value	0,9168	0,9511	0,9992	
Number of values	12	12	10	34

Table 10.5: Significances in the relative change of MFR (%). Comparison between BiC -/- , BiC +/+, TriC 1:4, and TriC 1:8 while untreated or stimulated with I+T. Red indicate difference across groups at T= 24 h, while blue indicates those at T= 48 h.

Relative change MFR (%)	**Group 1** BiC -/- Untreated	**Group 2** BiC -/- Stimulated	**Group 3** BiC +/+ Untreated	**Group 4** BiC +/+ Stimulated	**Group 5** TriC 1:4 Untreated	**Group 6** TriC 1:4 Stimulated	**Group 7** TriC 1:8 Untreated	**Group 8** TriC 1:8 Stimulated
Group 1	N/A	ns	ns	N/A	ns	N/A	ns	N/A
Group 2	ns	N/A	N/A	ns	N/A	p<0.001 p<0.0001	N/A	p<0.001 p<0.001
Group 3	ns	N/A	N/A	ns	ns	N/A	ns	N/A
Group 4	N/A	ns	ns	N/A	N/A	p<0.001 p<0.0001	N/A	p<0.0001 p<0.0001
Group 5	ns	N/A	ns	N/A	N/A	p<0.001 p<0.0001	ns	N/A
Group 6	N/A	p<0.001 p<0.0001	N/A	p<0.001 p<0.0001	p<0.001 p<0.0001	N/A	N/A	ns
Group 7	ns	N/A	ns	N/A	ns	N/A	N/A	p<0.0001 p<0.0001
Group 8	N/A	p<0.001 p<0.001	N/A	p<0.0001 p<0.0001	N/A	ns	p<0.0001 p<0.0001	N/A

Table 10.6: Significances in the relative change of BFR (%). Comparison between BiC -/-, BiC +/+, TriC 1:4, and TriC 1:8 while untreated or stimulated with I+T. Red indicate difference across groups at T= 24 h, while blue indicates those at T= 48 h.

Relative change BFR (%)	**Group 1** BiC -/- Untreated	**Group 2** BiC -/- Stimulated	**Group 3** BiC +/+ Untreated	**Group 4** BiC +/+ Stimulated	**Group 5** TriC 1:4 Untreated	**Group 6** TriC 1:4 Stimulated	**Group 7** TriC 1:8 Untreated	**Group 8** TriC 1:8 Stimulated
Group 1	N/A	ns	ns	N/A	ns	N/A	p<0.01 ns	N/A
Group 2	ns	N/A	N/A	ns	N/A	p<0.001 p<0.0001	N/A	p<0.01 p<0.0001
Group 3	ns	N/A	N/A	p<0.01 p<0.01	ns	N/A	p<0.05 ns	N/A
Group 4	N/A	ns	p<0.01 p<0.01	N/A	N/A	p<0.01 p<0.0001	N/A	p<0.01 p<0.0001
Group 5	ns	N/A	ns	N/A	N/A	p<0.001 p<0.0001	ns	N/A
Group 6	N/A	p<0.001 p<0.0001	N/A	p<0.01 p<0.0001	p<0.001 p<0.0001	N/A	N/A	ns
Group 7	p<0.01 ns	N/A	p<0.05 ns	N/A	ns	N/A	N/A	p<0.0001 p<0.0001
Group 8	N/A	p<0.01 p<0.0001	N/A	p<0.01 p<0.0001	N/A	ns	p<0.0001 p<0.0001	N/A

Table 10.7: Significances in the relative change of %SiB (%). Comparison between BiC -/-, BiC +/+, TriC 1:4, and TriC 1:8 while untreated or stimulated with I+T. Red indicate difference across groups at T= 24 h, while blue indicates those at T= 48 h.

Relative change %SiB (%)	**Group 1** BiC -/- Untreated	**Group 2** BiC -/- Stimulated	**Group 3** BiC +/+ Untreated	**Group 4** BiC +/+ Stimulated	**Group 5** TriC 1:4 Untreated	**Group 6** TriC 1:4 Stimulated	**Group 7** TriC 1:8 Untreated	**Group 8** TriC 1:8 Stimulated
Group 1	N/A	ns	ns	N/A	ns	N/A	ns	N/A
Group 2	ns	N/A	N/A	ns	N/A	p<0.05 p<0.001	N/A	p<0.05 p<0.001
Group 3	ns	N/A	N/A	ns	ns	N/A	p<0.05 ns	N/A
Group 4	N/A	ns	ns	N/A	N/A	ns p<0.0001	N/A	p<0.01 p<0.0001
Group 5	ns	N/A	ns	N/A	N/A	p<0.001 p<0.0001	ns	N/A
Group 6	N/A	p<0.05 p<0.001	N/A	ns p<0.0001	p<0.001 p<0.0001	N/A	N/A	ns
Group 7	ns	N/A	p<0.05 ns	N/A	ns	N/A	N/A	p<0.01 p<0.0001
Group 8	N/A	p<0.05 p<0.001	N/A	p<0.01 p<0.0001	N/A	ns	p<0.01 p<0.0001	N/A

Table 10.8: Significances in the relative change of BD (%). Comparison between BiC -/-, BiC +/+, TriC 1:4, and TriC 1:8 while untreated or stimulated with I+T. Red indicate difference across groups at T= 24 h, while blue indicates those at T= 48 h.

Relative change BD (%)	**Group 1** BiC -/- Untreated	**Group 2** BiC -/- Stimulated	**Group 3** BiC +/+ Untreated	**Group 4** BiC +/+ Stimulated	**Group 5** TriC 1:4 Untreated	**Group 6** TriC 1:4 Stimulated	**Group 7** TriC 1:8 Untreated	**Group 8** TriC 1:8 Stimulated
Group 1	N/A	ns	ns	N/A	ns	N/A	ns	N/A
Group 2	ns	N/A	N/A	ns	N/A	ns p<0.001	N/A	ns p<0.001
Group 3	ns	N/A	N/A	p<0.05 p<0.05	p<0.05 ns	N/A	p<0.05 ns	N/A
Group 4	N/A	ns	p<0.05 p<0.05	N/A	N/A	ns p<0.0001	N/A	ns p<0.0001
Group 5	ns	N/A	p<0.05 ns	N/A	N/A	ns p<0.0001	ns	N/A
Group 6	N/A	ns p<0.001	N/A	ns p<0.0001	ns p<0.0001	N/A	N/A	ns
Group 7	ns	N/A	p<0.05 ns	N/A	ns	N/A	N/A	p<0.05 p<0.0001
Group 8	N/A	ns p<0.001	N/A	ns p<0.0001	N/A	ns	p<0.05 p<0.0001	N/A

Table 10.9: Significances in the relative change of ISI CoV (%). Comparison between BiC -/-, BiC +/+, TriC 1:4, and TriC 1:8 while untreated or stimulated with I+T. Red indicate difference across groups at T= 24 h, while blue indicates those at T= 48 h.

Relative change ISI CoV (%)	**Group 1** BiC -/- Untreated	**Group 2** BiC -/- Stimulated	**Group 3** BiC +/+ Untreated	**Group 4** BiC +/+ Stimulated	**Group 5** TriC 1:4 Untreated	**Group 6** TriC 1:4 Stimulated	**Group 7** TriC 1:8 Untreated	**Group 8** TriC 1:8 Stimulated
Group 1	N/A	ns	ns	N/A	ns p<0.01	N/A	ns p<0.01	N/A
Group 2	ns	N/A	N/A	ns	N/A	p<0.05 p<0.001	N/A	ns p<0.001
Group 3	ns	N/A	N/A	p<0.05 p<0.05	ns p<0.01	N/A	ns p<0.01	N/A
Group 4	N/A	ns	p<0.05 p<0.05	N/A	N/A	p<0.0001 p<0.0001	N/A	p<0.001 p<0.0001
Group 5	ns p<0.01	N/A	ns p<0.01	N/A	N/A	p<0.001 p<0.0001	ns	N/A
Group 6	N/A	p<0.05 p<0.001	N/A	p<0.0001 p<0.0001	p<0.001 p<0.0001	N/A	N/A	ns
Group 7	ns p<0.01	N/A	ns p<0.01	N/A	ns	N/A	N/A	p<0.001 p<0.0001
Group 8	N/A	ns p<0.001	N/A	p<0.001 p<0.0001	N/A	ns	p<0.001 p<0.0001	N/A

Table 10.10: Significances in the relative change of NBF (%). Comparison between BiC -/-, BiC +/+, TriC 1:4, and TriC 1:8 while untreated or stimulated with I+T. Red indicate difference across groups at T= 24 h, while blue indicates those at T= 48 h.

Relative change NBF (%)	**Group 1** BiC -/- Untreated	**Group 2** BiC -/- Stimulated	**Group 3** BiC +/+ Untreated	**Group 4** BiC +/+ Stimulated	**Group 5** TriC 1:4 Untreated	**Group 6** TriC 1:4 Stimulated	**Group 7** TriC 1:8 Untreated	**Group 8** TriC 1:8 Stimulated
Group 1	N/A	ns	p<0.01 p<0.01	N/A	ns p<0.01	N/A	ns p<0.01	N/A
Group 2	ns	N/A	N/A	ns	N/A	p<0.0001 p<0.0001	N/A	p<0.0001 p<0.0001
Group 3	ns	N/A	N/A	p<0.01 p<0.01	ns p<0.01	N/A	ns p<0.01	N/A
Group 4	N/A	ns	ns	N/A	N/A	p<0.01 p<0.0001	N/A	p<0.05 p<0.0001
Group 5	ns p<0.01	N/A	ns p<0.01	N/A	N/A	p<0.0001 p<0.0001	ns	N/A
Group 6	N/A	p<0.0001 p<0.0001	N/A	p<0.01 p<0.0001	p<0.0001 p<0.0001	N/A	N/A	ns
Group 7	ns p<0.01	N/A	ns p<0.01	N/A	ns	N/A	N/A	p<0.001 p<0.0001
Group 8	N/A	p<0.0001 p<0.0001	N/A	p<0.05 p<0.0001	N/A	ns	p<0.001 p<0.0001	N/A

Table 10.11: Significances in the relative change of MFR in NB (%). Comparison between BiC -/-, BiC +/+, TriC 1:4, and TriC 1:8 while untreated or stimulated with I+T. Red indicate difference across groups at T= 24 h, while blue indicates those at T= 48 h.

Relative change MFR in NB (%)	Group 1 BiC -/- Untreated	Group 2 BiC -/- Stimulated	Group 3 BiC +/+ Untreated	Group 4 BiC +/+ Stimulated	Group 5 TriC 1:4 Untreated	Group 6 TriC 1:4 Stimulated	Group 7 TriC 1:8 Untreated	Group 8 TriC 1:8 Stimulated
Group 1	N/A	ns	ns	N/A	p<0.001 ns	N/A	p<0.001 ns	N/A
Group 2	ns	N/A	N/A	ns	N/A	ns p<0.05	N/A	ns
Group 3	ns	N/A	N/A	p<0.001 p<0.0001	p<0.05 p<0.05	N/A	p<0.05 ns	N/A
Group 4	N/A	ns	p<0.001 p<0.0001	N/A	N/A	p<0.0001 p<0.01	N/A	ns
Group 5	p<0.001 ns	N/A	p<0.05 p<0.05	N/A	N/A	p<0.01 ns	ns	N/A
Group 6	N/A	ns p<0.05	N/A	p<0.0001 p<0.01	p<0.01 ns	N/A	N/A	ns
Group 7	p<0.001 ns	N/A	p<0.05 ns	N/A	ns	N/A	N/A	p<0.001 ns
Group 8	N/A	ns	N/A	ns	N/A	ns	p<0.001 ns	N/A

Table 10.12: Significances in the relative change of %B in NB (%). Comparison between BiC -/-, BiC +/+, TriC 1:4, and TriC 1:8 while untreated or stimulated with I+T. Red indicate difference across groups at T= 24 h, while blue indicates those at T= 48 h.

Relative change %B in NB (%)	Group 1 BiC -/- Untreated	Group 2 BiC -/- Stimulated	Group 3 BiC +/+ Untreated	Group 4 BiC +/+ Stimulated	Group 5 TriC 1:4 Untreated	Group 6 TriC 1:4 Stimulated	Group 7 TriC 1:8 Untreated	Group 8 TriC 1:8 Stimulated
Group 1	N/A	ns	ns	N/A	ns	N/A	ns	N/A
Group 2	ns	N/A	N/A	ns p<0.05	N/A	ns p<0.01	N/A	ns p<0.001
Group 3	ns	N/A	N/A	ns	ns	N/A	ns	N/A
Group 4	N/A	ns p<0.05	ns	N/A	N/A	ns p<0.0001	N/A	ns p<0.0001
Group 5	ns	N/A	ns	N/A	N/A	ns p<0.0001	ns	N/A
Group 6	N/A	ns p<0.01	N/A	ns p<0.0001	ns p<0.0001	N/A	N/A	ns
Group 7	ns	N/A	ns	N/A	ns	N/A	N/A	ns p<0.0001
Group 8	N/A	ns p<0.001	N/A	ns p<0.0001	N/A	ns	ns p<0.0001	N/A

Table 10.13: Significances of Serpin E1/PAI-1 release into the supernatant. Comparison between BiC -/-, BiC +/+, TriC 1:4, and TriC 1:8 while untreated or stimulated with I+T. Black p-values indicate differences across groups at T= 0 h, while green indicates those at T= 24 h and pink at T= 48 h.

Serpin E1/ PAI-1	**Group 1** BiC -/- Untreated	**Group 2** BiC -/- Stimulated	**Group 3** BiC +/+ Untreated	**Group 4** BiC +/+ Stimulated	**Group 5** TriC 1:4 Untreated	**Group 6** TriC 1:4 Stimulated	**Group 7** TriC 1:8 Untreated	**Group 8** TriC 1:8 Stimulated
Group 1	N/A	ns	ns	N/A	p<0.0001 p<0.0001 p<0.0001	N/A	p<0.05 p<0.01 p<0.001	N/A
Group 2	ns	N/A	N/A	ns	N/A	p<0.01 p<0.001 p<0.0001	N/A	ns
Group 3	ns	N/A	N/A	ns	p<0.0001 p<0.0001 p<0.0001	N/A	ns p<0.05 p<0.01	N/A
Group 4	N/A	ns	ns	N/A	N/A	p<0.05 p<0.01 p<0.0001	N/A	ns ns p<0.0001
Group 5	p<0.0001 p<0.0001 p<0.0001	N/A	p<0.0001 p<0.0001 p<0.0001	N/A	N/A	ns ns p<0.05	p<0.05 p<0.05 p<0.01	N/A
Group 6	N/A	p<0.01 p<0.001 p<0.0001	N/A	p<0.05 p<0.01 p<0.0001	ns ns p<0.05	N/A	N/A	ns ns p<0.01
Group 7	p<0.05 p<0.01 p<0.001	N/A	ns p<0.05 p<0.01	N/A	p<0.05 p<0.05 p<0.01	N/A	N/A	ns ns p<0.001
Group 8	N/A	ns ns p<0.0001	N/A	p<0.05 p<0.05 p<0.01	N/A	ns ns p<0.01	ns ns p<0.001	N/A

Table 10.14: Significances of CCL5/ Rantes release into the supernatant. Comparison between BiC -/-, BiC +/+, TriC 1:4, and TriC 1:8 while untreated or stimulated with I+T. Black p-values indicate differences across groups at T= 0 h, while green indicates those at T= 24 h and pink at T= 48 h.

CCL5/ Rantes	**Group 1** BiC -/- Untreated	**Group 2** BiC -/- Stimulated	**Group 3** BiC +/+ Untreated	**Group 4** BiC +/+ Stimulated	**Group 5** TriC 1:4 Untreated	**Group 6** TriC 1:4 Stimulated	**Group 7** TriC 1:8 Untreated	**Group 8** TriC 1:8 Stimulated
Group 1	N/A	ns ns p<0.0001	ns	N/A	ns	N/A	ns	N/A
Group 2	ns ns p<0.0001	N/A	N/A	ns	N/A	ns p<0.01 ns	N/A	ns
Group 3	ns	N/A	N/A	ns ns p<0.01	ns	N/A	ns	N/A
Group 4	N/A	ns	ns ns p<0.01	N/A	N/A	ns p<0.01 ns	N/A	ns p<0.05 p<0.05
Group 5	ns	N/A	ns	N/A	N/A	ns p<0.001 p<0.0001	ns	N/A
Group 6	N/A	ns p<0.01 ns	N/A	ns p<0.01 ns	ns p<0.001 p<0.0001	N/A	N/A	ns
Group 7	ns	N/A	ns	N/A	ns	N/A	N/A	ns p<0.01 ns
Group 8	N/A	ns	N/A	ns p<0.05 p<0.05	N/A	ns	ns p<0.01 ns	N/A

Table 10.15: Significances of CXCL2 release into the supernatant. Comparison between BiC -/-, BiC +/+, TriC 1:4, and TriC 1:8 while untreated or stimulated with I+T. Black p-values indicate differences across groups at T= 0 h, while green indicates those at T= 24 h and pink at T= 48 h.

CXCL2	Group 1 BiC -/- Untreated	Group 2 BiC -/- Stimulated	Group 3 BiC +/+ Untreated	Group 4 BiC +/+ Stimulated	Group 5 TriC 1:4 Untreated	Group 6 TriC 1:4 Stimulated	Group 7 TriC 1:8 Untreated	Group 8 TriC 1:8 Stimulated
Group 1	N/A	ns ns p<0.01	ns	N/A	ns	N/A	ns	N/A
Group 2	ns ns p<0.01	N/A	N/A	ns ns p<0.0001	N/A	ns ns p<0.0001	N/A	ns ns p<0.0001
Group 3	ns	N/A	N/A	ns	ns	N/A	ns	N/A
Group 4	N/A	ns ns p<0.0001	ns	N/A	N/A	ns	N/A	ns
Group 5	ns	N/A	ns	N/A	N/A	ns ns p<0.0001	ns	N/A
Group 6	N/A	ns ns p<0.0001	N/A	ns	ns ns p<0.0001	N/A	N/A	ns
Group 7	ns	N/A	ns	N/A	ns	N/A	N/A	ns ns p<0.0001
Group 8	N/A	ns ns p<0.0001	N/A	ns	N/A	ns	ns ns p<0.0001	N/A

Supplementary video 1: Cell culture in 12nMPS. Bird perspective of 12nMPS and zoom into one well. Neurons (green) are embedded in hydrogel (pink).

Supplementary video 2: Immunofluorescence staining of a 3D tri-culture. Primary neurons co-cultured with astrocytes and microglia growing in 3D were immunolabeled for nucleus-related marker DAPI (blue), IBA1 (red), GFAP (yellow), and neurite related marker β-tubulin III (green). Scale: H= 112; A= 112 µm × 109 µm.

Supplementary video 3: Spontaneous intracellular calcium oscillations in GCaMP6f-transduced neurons growing in the nMPS. Synchronized oscillations of primary untreated neurons expressing GCaMP6f were captured by calcium imaging after 10 DIV. Images of 200×200 µm were acquired at 5 frames per second and at 560 µm from the bottom of the device.

Supplementary video 4: Intracellular calcium oscillations in GCaMP6f-transduced neurons treated with PTX. Large synchronous oscillations in intracellular calcium observed in 3D neuronal networks following application of PTX (10 µM). Images were taken at 5 frames per second, 10 minutes after applying PTX. The region of the nMPS imaged had an area of 200×200 µm and was at 560 µm from the bottom of the device.

Supplementary video 5: Intracellular calcium oscillations in GCaMP6f-transduced neurons treated with TTX. Intracellular calcium oscillations in 3D neuronal networks were almost completely abolished by application of TTX (10 nM). Images were taken at 5 frames per second, 10 minutes after applying TTX. The region of the nMPS imaged had an area of 200×200 µm and was at 560 µm from the bottom of the device.

Supplementary video 6. Ramified microglia. Iba1 labeled microglia growing in three dimensions. Nucleus is stained with DAPI. Scale: H= 69 µm; A= 123 µm x 123 µm.

Supplementary video 7: Microglia extensions on neuronal soma. Physical contact of non-stimulated microglia (Iba1, red) and neurons (ß-tubulin III, green) in three dimensions. Scale: H= 34 µm; A= 61 µm x 61 µm.

Supplementary video 8: Entangled non-stimulated tri-cultures. Physical contact between unstimulated microglia (Iba1, red), neurons (ß-tubulin III, green), and astrocytes (GFAP, yellow). Scale: H= 104 µm; A= 112 µm x 112 µm.

Supplementary video 9: Entangled stimulated tri-cultures. Physical contact between stimulated microglia (Iba1, red), neurons (ß-tubulin III, green), and astrocytes (GFAP, yellow). Scale: H= 67 µm; A= 135 µm x 135 µm.